Dynamics of Temporal Dissipative Solitons in Time-Delayed Systems with Large Delay

Dissertation
zur Erlangung des Grades eines
Doktor der Naturwissenschaften

eingereicht am
Fachbereich Mathematik und Informatik
der Freien Universität Berlin

vorgelegt von

Mina Stöhr

Berlin, April 2024

Dynamics of Temporal Dissipative Solitons in Time-Delayed Systems with Large Delay

Erstgutachterin: Prof. Dr. Isabelle Schneider, Freie Universität Berlin
Zweitgutachter: Prof. Dr. Jan Sieber, University of Exeter

Datum der Disputation: 17. Juli 2024

Abstract

Dynamical effects in time-delayed systems with large delay have captivated researchers for many decades. These systems exhibit a wide range of intriguing phenomena. Particularly the emergence of pulse-like solutions, known as **Temporal Dissipative Solitons (TDSs)**, have been a central point of research, as they are highly relevant in various domains such as optical and neural systems.

This thesis is dedicated to the understanding of the bifurcations and instabilities of TDSs. By scutinizing the singular limit of large delay, it is possible to derive a desingularized equation with an advanced argument in which the TDSs appear as homoclinic solutions. In our investigation, we show how we can employ classical homoclinic bifurcation theory as an effective tool to gain insights into the dynamics of these types of solutions. We demonstrate our results based on two systems from neural and laser dynamics.

We present a formal definition of TDSs supporting the analogy of the TDSs and homoclinic solutions in the desingularized equation. We derive a novel equation with an advanced argument featuring an innate symmetry allowing us to study alternating pulse solutions in the context of homoclinic bifurcation theory as well as square wave solutions.

As a prototypical system displaying different kinds of excitability, we investigate the emergence of TDSs and their dynamics in the Morris-Lecar model under time-delayed feedback. We successfully link the underlying dynamics to homoclinic bifurcations in the desingularized equation. Thereby, we discuss a homoclinic orbit flip, leading to the coexistence of stable TDSs with stable pulse packages and their disappearance by the collision of their profiles with an unstable equilibrium in a Bykov T-point, which induces a delocalization. Additionally, we relate the period-doubling bifurcation of TDSs to the unfolding of a degenerate homoclinic with a symmetry breaking.

We present an application of our theory by investigating square waves in the Kerr-Gires-Tournois interferometer. We show that our methodology supports the study of square waves as heteroclinic solutions, revealing that the mechanisms driving the collapsed snaking phenomenon are connected to a Bykov T-point shedding light on the underlying intricate dynamics.

Our studies are supported by a numerical analysis using the path-continuation package DDE-BIFTOOL.

Zusammenfassung

Dynamische Effekte in zeitverzögerten Systemen mit großer Verzögerung faszinieren Forscher seit vielen Jahrzehnten. Diese Systeme zeigen eine Vielzahl von interessanten Phänomenen. Insbesondere das Auftreten von Puls-Lösungen, bekannt als **Temporäre Dissipative Solitonen (TDSs)**, sind ein zentraler Forschungspunkt, da sie in verschiedenen Bereichen wie optischen und neuronalen Systemen äußerst relevant sind.

Diese Dissertation widmet sich dem Verständnis der Verzweigungsszenarien und Instabilitäten von TDSs. Durch die Untersuchung des singulären Grenzwerts gegeben durch die große zeitliche Verzögerung, ist es möglich eine desingularisierte Gleichung mit einem vorauseilendem Argument herzuleiten, in der die TDSs als homokline Lösungen auftauchen. In unserer Untersuchung zeigen wir, dass wir homokline Verzweigungstheorie als ein effektives Werkzeug nutzen können um Einblicke in die Dynamik dieser Art von Lösungen zu gewinnen.

Wir präsentieren eine formale Definition von TDSs, die die Analogie der TDSs und homoklinen Lösungen in der desingularisierten Gleichung unterstützt. Durch die Einführung einer neuen Gleichung, welche eine Symmetrie beinhaltet, können wir auch alternierende Pulslösungen im Kontext der homoklinen Verzweigungstheorie untersuchen, sowie Rechtecksschwingungen.

Als prototypisches System, das verschiedene Arten von Anregbarkeit zeigt, untersuchen wir das Auftreten von TDSs und ihre Dynamik im Morris-Lecar-Modell unter zeitverzögerter Rückkopplung. Wir verknüpfen erfolgreich die zugrunde liegende Dynamik mit homoklinen Verzweigungen in der desingularisierten Gleichung. Dabei diskutieren wir einen homoklinen Orbit-Flip, der zur Koexistenz stabiler TDSs mit stabilen Pulspaketen führt, und ihr Verschwinden durch die Kollision ihrer Profile mit einem instabilen Gleichgewicht in einem Bykov-T-Punkt, der eine Delokalisierung induziert. Zudem können wir auch die Periodenverdoppelung von TDSs mit der Entfaltung eines degenerierten Homoklinen mit Symmetriebrechung in Verbindung bringen.

Wir präsentieren eine Anwendung unserer Theorie auf Rechtecksschwingungen im Kerr-Gires-Tournois-Interferometer und studieren diese als heterokline Lösungen. Wir zeigen, dass die Mechanismen, die das sogenannte "collapsed snaking" erzeugen, mit einem Bykov-T-Punkt verbunden sind, was zu tieferen Einblicken in die zugrunde liegenden Dynamiken führt.

Unsere Studien werden durch eine numerische Bifurkationsanalyse mit dem Pfadverfolgungspaket DDE-BIFTOOL unterstützt.

Acknowledgments

I would like to extend my heartfelt appreciation and gratitude to Matthias Wolfrom, my supervisor, for his support, invaluable expertise, and countless insightful discussions throughout my doctoral studies. Thank you for taking me on as a PHD student.

I am also deeply grateful to Isabelle Schneider for her support and invaluable feedback during the preparation of this thesis. I sincerely appreciate her willingness to serve as my supervisor throughout the doctoral process.

I would also like to thank Jan Sieber at the University of Exceter for agreeing to be the second reader.

My sincere thanks go out to all my colleagues at WIAS for their support and fostering a warm and conducive atmosphere.

I would also like to express my gratitude to Elias Koch and Svetlana Gurevich at the University of Münster, as well as Julien Javaloyes in Mallorca, for their collaboration and contributions to our joint work.

Special gratitude is owed to my friends and family and all the people who have supported me during my doctoral studies and throughout my entire life.

Finally, I am grateful for the financial support provided by the Collaborative Research Center 910 Project A4 and the Weierstrass Institute Berlin, which made this research possible.

Contents

CHAPTER 1

Preamble

Dynamical effects in DDEs with large delay have been studied extensively. They hold significance in various fields including optical and optoelectronic systems. These systems exhibit a wide range of intriguing phenomena, such as the generation of pulse solutions, known as temporal dissipative solitons.

This thesis is devoted to the study of the bifurcation scenarios and instabilities of temporal dissipative solitons. In our investigation, we show how we can employ classical homoclinic bifurcation theory as a powerful tool to gain insights into the bifurcation behaviour and instabilites of these types of solutions. To illustrate our findings, we provide concrete examples involving the Morris-Lecar model under time-delayed feedback and the Kerr-Gires-Tournois interferometer.

The following chapter serves as an introduction to temporal dissipative solitons by giving a historical review of the phenomenon and finishes by providing an outline of the thesis.

1.1 Historical review on soliton solutions in spatially extended systems

The fascination with solitons dates back to the early 19th century when John Scott Russell's serendipitous observation of a solitary water wave in a canal stirred scientific curiosity. While executing experiments to determine the most efficient design for canal boats, he discovered a phenomenon that he described as the wave of translation, see Figure 1.1.1. His observation, published in the report [Rus45], has since been quoted excessively and hence shall not be missed here:

> *I was observing the motion of a boat which was rapidly drawn along a narrow channel by a pair of horses, when the boat suddenly stopped – not so the mass of water in the channel which it had put in motion; it accumulated round the prow of the vessel in a state of violent agitation, then suddenly leaving it behind, rolled forward with great velocity, assuming the form of a large solitary elevation, a rounded, smooth and well-defined heap of water, which continued its course along the channel apparently without change of form or diminution of speed. I followed it on horseback, and overtook it still rolling on at a rate of some eight or nine miles an hour, preserving its original figure some thirty feet long and a foot to a foot and a half in height. Its height gradually diminished, and after a chase of one or two miles I lost it in the windings of the channel. Such, in the month of August 1834, was my first chance interview with that singular and beautiful phenomenon which I have called the Wave of Translation.*

These localized waves or wave packets essentially preserve their shape and localization even after collisions with other solitons. This observation seemed to disagree at that time with the contemporary theory on water waves as it contradicts the superposition principle of waves describing the concept of interference: when two waves propagating in space meet, the amplitude of the resulting wave is equal to the sum of the amplitudes of each wave. Theoretical investigations were then continued by Joseph Boussinesq [Bou71] and Lord Rayleigh [Ray76],

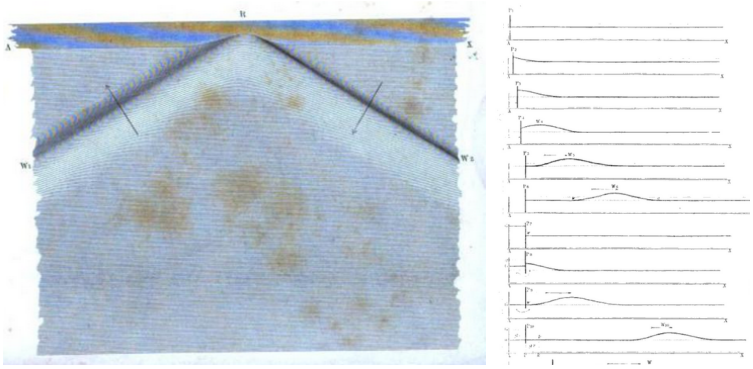

Figure 1.1.1: Drawings of a solitary wave from Russel's publication in [Rus45].

and finally by Korteweg and de Vries in 1895 leading to the eponymous mathematical model describing waves on shallow water surfaces, [KDV95]. The system is a prototypical model for an integrable PDE possessing infinitely many conserved quantities despite the nonlinearity. Especially, it provides for explicit soliton solutions. However, solitons are not only linked to fluid dynamics but in fact, can be associated with the wider field of conservative spatially extended systems and found, thereby, an important field of application in optical fibres, [KA03]. Being a key phenomenon in these systems, they arise due to a delicate balance between dispersive and nonlinear effects of the medium. A principal example of their appearance is the nonlinear Schrödinger equation, [KA03], which is a classical field equation that can be used to describe the propagation of light in nonlinear optical fibres.

However, solitons should not only be linked exclusively to conservative systems, since localized solutions with similar properties can also be observed in nonlinear spatially extended systems that are dissipative, [AA08]. In order to avoid ambiguity, they are referred to as autosolitons, spots, pulses, oscillons or dissipative solitons, expanding upon the notion of solitons in conservative systems. Coexisting with a stable stationary homogeneous state, they deviate from it only in a localized region and form stable solutions. Unlike their conservative counterparts, the occurrence of these dissipative solitons does not only depend on the balance of nonlinearity and dispersion. Additionally, their

emergence is due to underlying mechanisms of self-organization, relying on a balance between energy gain and loss. Their remarkable ability to retain their shape and localization, even after collisions, has positioned them at the forefront of innovations, particularly in optical or optoelectronic systems, where they play a crucial part for data transmission using optical pulses, see for example [AA08; KA03; PBA10]. On that account, they can be found as travelling pulse solutions in systems modelled by reaction-diffusion systems, as much as systems of Ginzburg-Landau or Swift-Hohenberg type. But they manifest not only in optically active materials. Also dissipative models of optically passive materials, like the nonlinear Schrödinger equation with an external driving force or Lugiato-Lefever equation, exhibit solitons. Moreover, diverse other systems such as models describing neural signal propagation and other chemical reactions or biological processes can feature solutions that can be characterized as dissipative solitons. For example in neuronal systems modelling action potentials, they play a crucial role for a reliant communication between neurons. As action potentials are sharp changes in the electrical field in the cell membrane, which travel then in virtually constant shape from the cell along axons to synaptic connections with other cells, they also qualify for soliton-type solutions in the corresponding models.

1.2 Temporal dissipative solitons in time-delayed systems

Recent experimental and theoretical findings indicate that dissipative solitons can even manifest in systems incorporating a time delay, devoid of explicit spatial variables. In this context, the delay time significantly exceeds the internal time scales of the system and the localization occurs then in time. These localized states in time-delayed systems are referred to as temporal dissipative solitons (TDSs). An intuitive example is presented by a ring laser, see [VT05], where the delay corresponds physically to the ring cavity. A time-delayed feedback results from a signal that gets reinjected into the laser after performing a round-trip through the cavity. The pulse is then localized within the delay line and the temporal localization pattern repeats itself with a period slightly

exceeding the delay time. The TDSs are hence periodic solutions which spend most of the time near a stable background equilibrium, except for a short time interval, in which the pulse is developed. This intriguing phenomenon has found diverse applications, with a pronounced presence in a wide range of fields, especially within the realm of optoelectronic systems. For instance, one finds them in models of passively mode-locked semiconductor lasers with saturable absorber, like the above-mentioned ring laser, whose mode-locked pulse solutions are a particular case for TDSs, [MJBG14; SJG18; VT05]. Beyond this intriguing area of application, they can also be found as cavity solitons in vertical-cavity surface-emitting lasers with delays, [GJTB15; Gus+15; RKB20; SPVJG19; TKB17; TPKBB21]. Other examples include bistable systems with feedback [MGB14; SM18] or neuronal models [RAFBJ16].

It is also possible to find several pulses within a delay line. These types of localized solutions are known as pulse packages or bound states and soliton molecules like in spatially extended systems. The interaction dynamics of the individually addressable pulses were analysed in [MJG20; NRVW06; Vla22]. Other specific instabilites have been examined as well, see [HGJ21; Sch+19]. However, a profound, yet comprehensive mathematical theory for TDSs including their bifurcations and instabilities, is still lacking.

An important role in the creation of TDSs play excitable systems subjected to a time-delayed feedback. As a prototypical example of the rising of TDSs due to mechanisms related to excitability, the phase oscillator and the FitzHugh-Nagumo system under time-delayed feedback have been examined in [YRSW19]. For sufficiently large time-delayed feedback, the excitation pulse can be replicated after a time that is marginally larger than the delay time. This gives rise to the appearance of periodic patterns displaying localized structures. The interaction dynamics of TDSs in the excitable phase oscillator under time-delayed feedback have been analysed in [MJG20].

Temporal dissipative solitons have an innate relation to spatially localized states. This has been studied by introducing a spatio-temporal representation, see [GP96; YG17]. Whereas in spatially extended systems, the pulse is localized in space, in this representation it is localized within the delay line. This analogy could also be extended to systems with two time-delayed feedback loops, for

the case of two delays that are significantly different, see [YG14; YG15].

For time-delayed systems, the limit of large delay acts like a singular perturbation on the system. In this way, it gives rise to dynamics on multiple time scales, [AJMRJ95; Fen79; Kue+15]. This has been scrutinized for the analysis of the eigenvalue spectrum of equilibria [LWY11], of the Floquet spectrum of rapidly oscillating solutions [SWLY13], but also of chaotic dynamics in nonlinear networks with time-delayed couplings [Hei+11]. Beyond that, the limit of large delays could also prove to be an effective approach for the classification and computation of the Floquet spectrum of TDSs. In [YRSW19], a theory was developed, classifying the spectrum of a TDS into a pseudo-continuous part which is determined by the background equilibrium of the soliton and a point spectrum, that can be deduced by the profile of the soliton. Lastly, the authors derive a desingularized equation incorporating an advanced argument, the so called *profile equation*, in which the TDSs can be found as homoclinics suggesting the description of their bifurcations and instabilities in the context of homoclinic bifurcation theory. This proposition motivated the work presented in this thesis.

In our research, we show how we can employ classical homoclinic bifurcation theory as an effective tool to gain insights into the bifurcation behaviour of temporal dissipative solitons. To illustrate our findings, we provide concrete examples involving the Morris-Lecar model under time-delayed feedback and a delay-algebraic model of the Kerr-Gires-Tournois interferometers. Our studies are supported by a numerical analysis using the continuation package DDE-BIFTOOL [ELR02; SELSR16].

1.3 Outline of the thesis

We will give now an outline of the thesis.

Chapter 2 and **3** are review chapters, clarifying notations and important background theory to the topic of temporal dissipative solitons and homoclinic bifurcation theory.

In **Chapter 2**, we commence with a phenomenological introduction to temporal dissipative solitons and undertake a review of the existing theory concerning these solutions within time-delayed systems. In particular, we derive an equation with an advanced argument, termed the profile equation, wherein solitons manifest as homoclinic solutions.

In **Chapter 3**, we provide an overview on homoclinic bifurcation theory within finite-dimensional vector fields. In particular, we investigate genericity conditions intrinsic to homoclinics, whose violations induce bifurcations of these structures. We demonstrate how under parameter variations periodic solutions can bifurcate from homoclinic solutions and conclude by discussing some homoclinic bifurcations that find application in the main part of the thesis.

Chapters 4 to **8** form the core of this thesis and contain the results of our research on bifurcations of temporal dissipative solitons in the context of homoclinic bifurcation theory. In Chapter 4, we present our theoretical results and continue then with a demonstration of our research from the application of our theory.

In **Chapter 4**, we present a mathematical framework for temporal dissipative solitons, allowing us to prove their relation to homoclinic solutions in the profile equation. We derive an equation similar to the profile equation, in which also alternating pulse solutions can be treated as homoclinic solutions. We analyse the Floquet spectrum in this system and show how it moreover accomodates the period-doubling bifurcation. Finally, we demonstrate that also square waves can be studied as connecting orbits in the newly derived system.

In **Chapter 5**, we introduce the Morris-Lecar model used for the subsequent analyses of TDSs and their bifurcations in Chapter 6 and Chapter 7.

In **Chapter 6**, we explore temporal dissipative solitons in the time-delayed Morris-Lecar model. As a prototypical example underscoring that excitability is an important factor for the emergence of solitons, we display how the addition of a time-delayed feedback induces the generation of solitons. We demonstrate that the underlying mechanisms of excitability in this system lead to a destabilization of equidistant multi-pulse solutions, giving rise to stable pulse packages and show how this is linked to a homoclinic orbit flip bifurcation. Beyond that,

we discuss the role of a heteroclinic bifurcation, called Bykov T-point, for the delocalization of the solitons.

In **Chapter 7**, we study the period-doubling of solitons in the context of homoclinic bifurcation theory. By making use of our previously developed framework, we are able to relate this bifurcation to the unfolding of a degenerate homoclinic together with a symmetry breaking.

In **Chapter 8**, we apply our theory to square waves, by making use of an equation, in which these solutions can be identified with connecting orbits. In a delay-algebraic system modelling Kerr-Gires-Tournois interferometers, we present how the formation of complex coexisting square-wave patterns that are organized in a structure of snaking branches can be explained using homoclinic bifurcation theory, relating this snaking scenario to a Bykov T-point.

In **Chapter 9**, we give a summary of the presented results from our study on the bifurcations of temporal dissipative solitons with the help of homoclinic bifurcation theory. We finish with an outlook and conclusive remarks.

Additionally, in **Appendix A**, we give an overview of the determining systems used for the numerical computations of the various homoclinic bifurcations used in the preceding chapters. We review the boundary value problem for the numerical computation of homoclinics and develop an extension for certain complex cases. Finally, we present a condition in order to compute a homoclinic orbit flip bifurcation.

CHAPTER 2

Temporal dissipative solitons

In this chapter, we provide a phenomenological introduction to temporal dissipative solitons and conduct a review of the current theoretical landscape surrounding these solutions within time-delayed systems. The relation between time-delayed and spatially extended systems is reviewed using a pseudo-spatial representation. We discuss how the large delay limit acts as a singular perturbation on the system. A key focus involves deriving an equation with an advanced argument, referred to as the profile equation, in which solitons emerge as homoclinic solutions. We present a review of the Floquet spectrum of temporal dissipative solitons, showing its subdivision into a pseudo-continuous spectrum and an interface spectrum. The chapter concludes with a reappearance rule involving the Floquet spectrum, showing a characteristic property for periodic solutions in DDE systems with respect to certain critical Floquet multipliers. To illustrate the ideas reviewed in this chapter, the phase oscillator and the FitzHugh-Nagumo system under the influence of a time-delayed feedback are investigated.

2.1 Fundamental notions

Consider a Delay Differential Equation (DDE)

$$\dot{x}(t) = f(x(t), x(t-\tau)),\ x(t) \in \mathbb{R}^n, \tag{2.1.1}$$

where $f \in \mathcal{C}^1(\mathbb{R}^n \times \mathbb{R}^n, \mathbb{R}^n)$ is nonlinear, and the delay τ is assumed to be large. The phase space of these types of dynamical systems is an infinite-dimensional Banach space. A point in the phase space is a function $x_t(\theta), -\tau \leq \theta \leq 0$ with $x_t(\theta) := x(t+\theta)$. Hence, in order to solve (2.1.1) for $t \geq \sigma$, one needs to provide an initial value in the sense of a function x_σ defined on a history interval $[\sigma - \tau, \sigma]$. Accordingly, the phase space is given by $\mathcal{C}^0([-\tau, 0], \mathbb{R}^n)$. Theory on delay differential equations can be, for example, reviewed in [DVGLW95; HL93].

The theory discussed in this chapter is based on the paper by Yanchuk et al. [YRSW19] unless otherwise indicated. The results presented in that paper form the foundation and starting point of our research.

Suppose the system (2.1.1) possesses an equilibrium x_0, that is stable for large delays τ. An equilibrium x_0 is said to be stable, if all roots λ of the corresponding characteristic equation have negative real parts. The characteristic equation is obtained by linearizing (2.1.1) at x_0 and is then given by

$$\det(\lambda \mathbb{I} - A_0 - B_0 e^{-\lambda\tau}) = 0, \tag{2.1.2}$$

where $A_0 := \partial_1 f(x_0, x_0)$ and $B_0 := \partial_2 f(x_0, x_0)$. Furthermore, we denote the identity matrix in $\mathbb{R}^{n\times n}$ with $\mathbb{I}$. Additionally, note that in DDE systems, linear stability implies asymptotic exponential stability [HL93]. For a detailed analysis of the eigenvalue spectrum of equilibria in DDEs, see [LWY11]. Moreover, in [YWPT22] it was demonstrated, that stability of an equilibrium of (2.1.1) for large delays τ implies stability for all delays $\tau \geq 0$.

Definition 1. *An equilibrium of the system* (2.1.1) *is said to be absolutely stable, if it is stable for all delays* $\tau \geq 0$.

We commence now by introducing certain properties concerning temporal dissipative solitons providing us with a phenomenological definition.

Based on the observations in [YRSW19], we say a periodic solution of the DDE system (2.1.1) for large delay τ is a *temporal dissipative soliton (TDS)*, if it satisfies the following characteristics. A TDS is a solution that spends most of the time near an absolutely stable equilibrium x_0. The delay value τ is considered to be much larger than the other time scales of the system and a temporal localization arises, when the TDS leaves abruptly the vicinity of x_0 such that a pulse is developed. We call x_0 the *background* of the soliton. Moreover, if the system provides for a TDS, it appears as a family of periodic solutions of (2.1.1) for all large enough delays τ. Moreover, a particular characteristic pertaining to TDSs can be observed when introducting an additional parameter. Denoting the corresponding period of a TDS at delay τ with $T(\tau)$, one can define the *response time* as

$$\delta(\tau) := T(\tau) - \tau. \tag{2.1.3}$$

TDSs are solutions having a period, that is slightly larger than the delay, which makes δ a positive and finite value. This expresses the natural time lag related to a causality principle in time-delayed systems, see [YG17], and intuitively corresponds to the time that the system needs to create another pulse. Especially, for $\tau \longrightarrow \infty$, for their corresponding periods, it is $T(\tau) \longrightarrow \infty$, but the response time $\delta(\tau)$ of the TDSs stays bounded and has a limit, that we denote with δ_∞.

Note, that the soliton only approaches the stable background equilibrium in the sense of the finite dimensional space of the system variables. However, in the infinite-dimensional phase space, the trajectory never comes close to the background, as there is always a pulse contained in the history interval.

Analogously to [YRSW19], we consider the following two excitable systems as prototypical examples for the generation of TDSs under time-delayed feedback. The first example is given by the time-delayed phase oscillator

$$\dot{\phi}(t) = d - \sin\phi(t) + \kappa \sin(\phi(t-\tau) - \phi(t)), \tag{2.1.4}$$

which can be seen as a reduced model for a general injected Ginzburg-Landau equation with time-delayed feedback [GJTB15]. Without feedback, it serves as

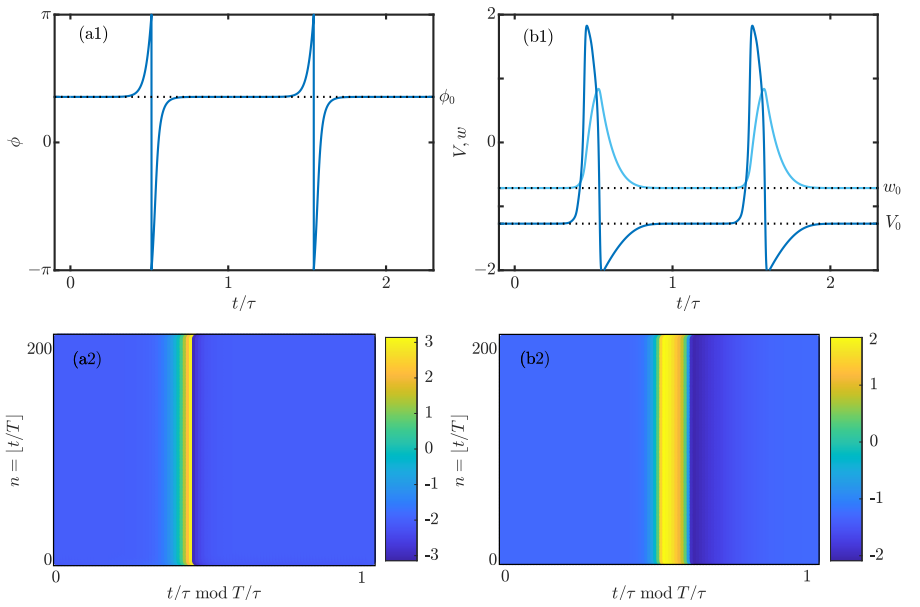

Figure 2.1: Examples of TDSs: (a1), (a2) in the phase oscillator (2.1.4); (b1), (b2) FitzHugh-Nagumo system (2.1.5a)–(2.1.5b) under time-delayed feedback. (a1), (a2) profiles of the TDSs: ϕ, resp. V (blue), w (light blue), stable background (black dotted); (a2), (b2) spatio-temporal representation of the TDSs. Parameters: (a1), (a2) $d = 0.9$, $\kappa = 1$, $\tau = 30$; (b1), (b2) $a = 0.7$, $b = 0.8$, $\epsilon = 0.08$, $\kappa = 0.1$, $\tau = 100$.

a prototypical example for the *saddle-node bifurcation on an invariant circle (SNIC)*. The second example is the FitzHugh-Nagumo neuron which is a simplified neuronal system modelling spike generation, [Izh07]. We add a time-delayed feedback such that the system is given by

$$\dot{V}(t) = V(t) - (V^3(t)/3) - w(t) + \kappa V(t-\tau), \tag{2.1.5a}$$

$$\dot{w}(t) = \epsilon(V(t) + a - bw(t)). \tag{2.1.5b}$$

If the parameters of the two systems are chosen in their respective excitable regimes, both systems can generate TDSs. Figure 2.1 displays the profiles (blue) of the TDS in the time-delayed phase oscillator (Panel (a1)) and FitzHugh-

Nagumo (Panel (b1)) with large delay. Note, that the phase oscillator is defined on the unit sphere leading to the sharp transition in the middle of the pulse due to the 2π-modulation. One can see that both TDSs spend most of the time near their corresponding background equilibrium (dashed black lines), denoted with ϕ_0 and (V_0, w_0), for respectively the phase oscillator and FitzHugh-Nagumo system, which are given by the stable equilibrium in each system. They can be computed by setting $\dot{\phi}(t) = 0$ in the case of the phase oscillator, or by computing the intersection of $\dot{V}(t) = 0$ and $\dot{w}(t) = 0$ in the FitzHugh-Nagumo system.

2.2 Pseudo-spatial representation

TDSs display a heuristic equivalence to spatially localized states in PDEs, see [GP96; YG17]. This can be seen by introducing new coordinates: the pseudo-spatial variable representing the delay-line along the horizontal axis $t \bmod T$ and the pseudo-temporal variable along the vertical axis defined as the number of round-trips $n = \lfloor t/T \rfloor$. This gives us a spatio-temporal representation of the time trace. In these new coordinates, the TDSs appear as standing waves in a spatially extended system, given by the parameter transformation $t = \sigma + nT$, $\sigma \in [0, T]$. In Figure 2.1, Panels (a2) and (b2), we plot the time series obtained by a numerical integration represented in a normalized spatio-temporal representation for respectively the time-delayed phase oscillator (2.1.4), and FitzHugh-Nagumo system (2.1.5a)–(2.1.5b).

However, this transformation has the disadvantage that it depends on the period of the solution and thus a solution parameter. Instead, one can use a similar one with $t = \sigma + n\tau$, $\sigma \in [0, \tau]$, and $n = \lfloor t/\tau \rfloor$. In these coordinates, the solution displays a drift. The pulse recurs in every consecutive time interval shifted by a constant δ. This reveals the time lag in a system with time-delay related to the causality principle, see [YG17], manifesting in a positive response time of the system given by δ (2.1.3).

2.3 Large delay limit

Since solitons are a phenomenon for all large delays, we are especially interested in analyzing the limit $\tau \longrightarrow \infty$, which is a singular limit and hence acts like a singular perturbation in the infinite delay limit. Indeed, rescaling time in Eq. (2.1.1) by $t' = t/\tau$ leads to

$$\frac{1}{\tau}\frac{dx(t')}{dt'} = f\left(x(t'), x(t'-1)\right).$$

Setting $\epsilon = 1/\tau$ and applying formally the limit $\tau \longrightarrow \infty$ corresponds then to $\epsilon \longrightarrow 0$, revealing the singular nature of the equation. One obtains then

$$0 = f(x(t'), x(t'-1)) =: f(x_{k+1}, x_k). \tag{2.3.1}$$

This equation gives a discrete map for times $k \in \mathbb{Z}$, where the state x_{k+1} is determined by an implicit function of x_k. This map is called the *singular map* of Eq. (2.1.1).

Note, that the fixed points of the singular map (2.3.1) correspond to equilibria of the DDE (2.1.1). In particular, following [YWPT22], a stable fixed point x_0 of the singular map (2.3.1) is also an absolutely stable equilibrium of the DDE (2.1.1) and can serve as a background for TDSs. In contrast to that, nonconstant solutions of the DDE system (2.1.1) for $\tau \longrightarrow \infty$ are very different from solutions of the singular map (2.3.1).

The presence of a large delay gives rise to dynamics on multiple time scales, see [AJMRJ95; Fen79; Kue+15] for ordinary differential equations. Theory for the analytical tools in case of DDE systems are provided in [BLZ98; DVGLW95; HMO06].

In the next section, we will introduce an equation, which replaces the singular limit with a finite one, that enables us to study the soliton solutions for $\tau \longrightarrow \infty$ as homoclinic solutions.

2.4 Reappearance rule and profile equation

We now make use of the reappearance rule, introduced in [YP09], pertaining to periodic solutions of delay equations. Any T-periodic solution $x_*(t)$ of equation (2.1.1) at delay time τ is also a solution of (2.1.1) replacing τ by

$$\tau_m := \tau + mT, \qquad \text{for all } m \in \mathbb{Z}. \tag{2.4.1}$$

I.e. periodic solutions reappear when adding integer multiples of the period to the delay. Indeed, inserting $x_*(t)$ into (2.1.1) and taking into account that a T-periodic solution $x_*(t)$ satisfies $x_*(t+T) = x_*(t)$, we obtain

$$\begin{aligned} \dot{x}_*(t) =& f(x_*(t), x_*(t-\tau)) = f(x_*(t), x_*(t-\tau-mT)) \\ =& f(x_*(t), x_*(t-\tau_m)), \end{aligned} \tag{2.4.2}$$

for all $m \in \mathbb{Z}$.

Recall the parameter $\delta(\tau) := T(\tau) - \tau$ (2.1.3) referring to the response time of the system linked to solitons. Together with the reappearance rule (2.4.1) for $m = -1$, we can see now from Equation (2.4.2) that the profiles of the soliton solutions can be found as a family of periodic solutions of the DDE (2.1.1) with τ replaced by $\tau_{-1} = -\delta$:

$$\dot{x}(t) = f\left(x(t), x(t+\delta)\right). \tag{2.4.3}$$

This equation is referred to as *profile equation* (PE). In contrast to the large delay DDE (2.1.1), the profile equation (2.4.3) is a differential equation with an advanced argument. Note that any advanced system can be turned into a regular DDE system under the time reversal $t \longmapsto -t$. Opposing to DDE systems, initial value problems can only be solved backwards in time in systems with an advanced argument.

We have seen in the preceding section, that the large delay limit is a singular limit. Moreover, recall that solitons are a family of periodic solutions, such that for $\tau \longrightarrow \infty$, for their corresponding period it is $T(\tau) \longrightarrow \infty$. However, for solitons the limit of the response times (2.1.3) remains finite, and for $\tau \longrightarrow \infty$ it is $\delta(\tau) = T(\tau) - \tau \longrightarrow \delta_\infty$, by the initial assumptions made for TDSs in Section 2.1. Due to the reappearance rule, the family of soliton solutions

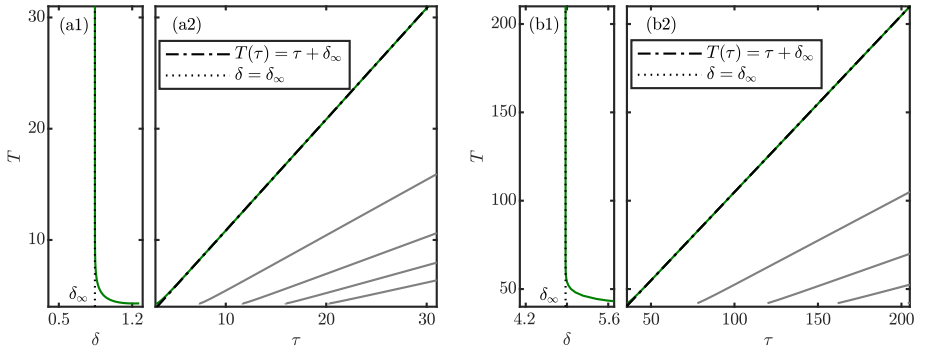

Figure 2.2: Branches of periodic solutions related to TDSs: (a1), (a2) in the phase oscillator (2.1.4); (b1), (b2) in the FitzHugh-Nagumo system (2.1.5a)–(2.1.5b). Branches of periodic solutions (green): (a2), (b2) in the large delay DDE (2.1.1); (a1), (b1) in the profile equation (2.4.3). In the large delay DDE, the branches approach a line $T(\tau) = \tau + \delta_\infty$ (dashed-dotted) for $\tau \longrightarrow \infty$. Secondary branches with multiple pulses per delay interval are displayed in grey. In the profile equation, the branches approach a vertical line (dotted) for $\delta \longrightarrow \delta_\infty$. Parameters as in Fig. 2.1.

reappears in the profile equation to a family of periodic solutions with periods $T \longrightarrow \infty$, for $\delta \longrightarrow \delta_\infty$ remaining finite. This way, we can replace the singular limit $\tau \longrightarrow \infty$ in the large delay DDE with the finite limit $\delta \longrightarrow \delta_\infty$ in the profile equation.

Figure 2.2 illustrates the relation between the branches of periodic solutions displaying TDSs (green) the large delay DDE (Panels (a2), (b2)) and the corresponding branches under the reappearance rule (2.4.1) in the profile equation (Panels (a1), (b1)). Panels (a1), (a2) correspond to the phase oscillator (2.1.4) and Panels (b1), (b2) to the FitzHugh-Nagumo system (2.1.5a)–(2.1.5b). In the large delay DDE of each system, the branches lie asymptotically to a line $T(\tau) = \tau + \delta_\infty$ (dashed-dotted) for $\tau, T \longrightarrow \infty$. To avoid ambiguity, note that in either system, the values of the corresponding limiting response times δ_∞ are different. The branches featuring soliton solutions reappear to branches in the profile equation, where the periods $T \longrightarrow \infty$ for $\delta \longrightarrow \delta_\infty$ (dotted). Panels

(a2), (b2) show also the secondary branches (grey) obtained by the reappearance rule for $m \geq 1$. The solitons on these branches display $m+1$ equidistant pulses per delay interval.

By applying the reappearance rule, the profiles of the periodic solutions are preserved. Yet, the stability of the solutions can change under the reappearance rule. This can already be observed when comparing the stability of equilibria in the DDE with their stability in the profile equation and leads to an essential consequence for the family of soliton solutions. Consider the background equilibrium x_0, which is assumed to be stable for all positive delays $\tau \geq 0$. For details on the eigenvalue spectrum of equilibria in DDEs, see [LWY11]. For $\tau \longrightarrow 0$ most of the eigenvalues disappear to $-\infty$ and a finite number of eigenvalues, equal to the dimension of the state space, remain and have negative real parts. The real parts of the stable eigenvalues at $\tau = 0$ remain negative, also for small negative delays $\tau < 0$. Since for $\tau < 0$ the DDE has turned into an equation with an advanced argument, there are now infinitely many unstable eigenvalues, i.e. eigenvalues with positive real parts, appearing from $+\infty$ for small $\tau < 0$, turning x_0 into an equilibrium of saddle-type for small negative delays. That implies that a stable background equilibrium x_0 turns naturally into an equilibrium of saddle-type in the profile equation (2.4.3) for small $\delta > 0$.

Figure 2.3 illustrates the eigenvalue spectrum for the soliton's background in the phase oscillator (2.1.4) (Panels (a1), (a2)) and in the FitzHugh-Nagumo system (2.1.5a)–(2.1.5b) (Panels (b1), (b2)). Panels (a2), (b2) show the eigenvalue spectrum of the respective stable background equilibria in the DDE (2.1.1) for delays $\tau \geq 0$. Note that for $\tau \longrightarrow \infty$ the eigenvalues λ accumulate along the imaginary axis $\mathrm{Re}(\lambda) = 0$. This can also be seen in the inlets of the panels, showing the spectrum of the backgrounds for a selected large delay. On the other hand for $\tau \longrightarrow 0$, they vanish to $-\infty$. In the case of the phase oscillator only one and in the FitzHugh-Nagumo system a complex conjugate pair (see zoom in subpanel) of eigenvalues remain and have negative real parts at $\tau = 0$. Panels (a1), (b1) show the spectrum in the corresponding profile equation (2.4.3) of the respective system. Conversely to the DDE, infinitely many eigenvalues with positive real parts appear for $\delta \longrightarrow 0$ and accumulate

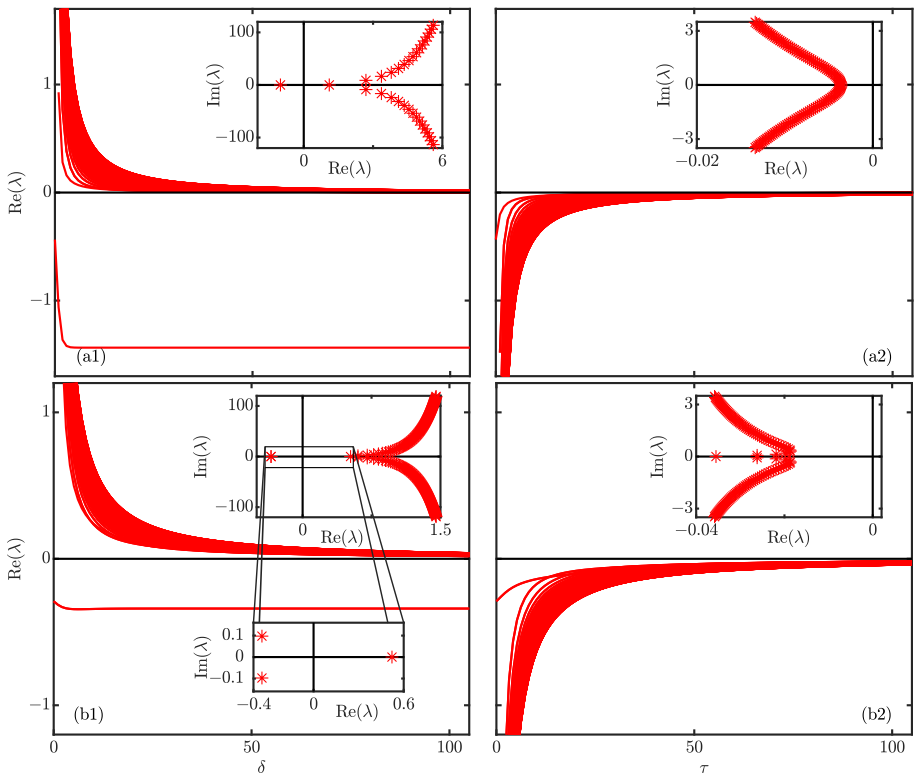

Figure 2.3: Eigenvalue spectrum of the background equilibrium: (a1), (a2) in the phase oscillator; (b1), (b2) in the FitzHugh-Nagumo system. Numerically computed eigenvalues (red): (a1), (b1) in the profile equation (2.4.3) for varying δ. Subpanels: spectrum at $\delta = \delta_\infty$. (a2), (b2) in the large delay DDE (2.1.1) for varying τ. Subpanels: spectrum at $\tau = 100$. Parameters: For the phase oscillator $\delta_\infty \approx 0.8443$; FitzHugh-Nagumo $\delta_\infty \approx 4.8758$. Other parameters as in Fig. 2.1.

along the imaginary axis for $\delta \longrightarrow \infty$. Note, that those eigenvalues show positive real parts also for large δ. On the other hand, the stable eigenvalues from $\tau = \delta = 0$ continue to have negative real parts and we can even observe that they remain negative for all $\delta > 0$. The subpanels show the spectrum of the

backgrounds at the respective values of the limiting response times δ_∞.

We have seen, that in the profile equation, the solitons appear as a family of T-periodic solutions with $T \longrightarrow \infty$, for $\delta \longrightarrow \delta_\infty$ remaining finite. Also, recall that the background x_0 is stable and turns into an equilibrium of saddle-type in the profile equation (2.4.3). Then in the profile equation, the family of periodic solutions approach a homoclinic solution $x_h(t)$ at $\delta = \delta_\infty$, i.e. a solution satisfying

$$\lim_{t \longrightarrow \pm\infty} x_h(t) = x_0, \tag{2.4.4}$$

where x_0 is an equilibrium of saddle-type. Thus, with the profile equation, we have now derived an equation that allows us to examine solitons and their bifurcations in the context of homoclinic bifurcation theory.

2.5 Floquet spectrum of TDS: pseudo-continuous spectrum and interface spectrum

In [YRSW19], a theory has been presented for the classification of the Floquet spectrum of TDSs using the large delay limit. In this section, we will present a short review of its derivation.

Suppose $x_*(t)$ is a T-periodic TDS solution of a DDE system (2.1.1). In general, the spectrum of a periodic solution is given by solutions to the Floquet problem: For a T-periodic solution $x_*(t)$ of (2.1.1) at a fixed value of τ, the Floquet problem is given by

$$\dot{v}(t) = A(t)v(t) + B(t)v(t-\tau), \tag{2.5.1}$$

$$v(t+T) = \mu v(t), \tag{2.5.2}$$

where $A(t) = \partial_1 f\left(x_*(t), x_*(t-\tau)\right)$ and $B(t) = \partial_2 f\left(x_*(t), x_*(t-\tau)\right)$ are T-periodic matrices. Solutions $v_*(t)$ satisfying (2.5.1)–(2.5.2) are called Floquet eigenfunctions to the Floquet multiplier μ_* of the solution $x_*(t)$ of (2.1.1). The solutions (μ_*, v_*) to (2.5.1)–(2.5.2) are in general complex with $\mu_* \in \mathbb{C}$ and

$v_*(t) \in \mathbb{C}^n$. While the multipliers are unique, the eigenfunctions are unique up to a complex scalar multiple. This has to be taken into account when investigating the spectrum numerically. Periodic solutions have generically one trivial multiplier given by $\mu = 1$, delivered by the mode $\dot{x}_*(t)$. The solution is said to be stable, if all multipliers lie inside the complex unit circle $|\mu| < 1$, except the trivial one.

In order to obtain an equation devoid of the large delay, we make use of the definition of the response time $\delta = T - \tau$ (2.1.3). Together with the Floquet condition (2.5.2), it is then

$$v(t-\tau) = \mu^{-1} v(t-\tau+T) = \mu^{-1} v(t+\delta). \tag{2.5.3}$$

Hence, with (2.5.3) the Floquet problem (2.5.1)–(2.5.2) turns into

$$\dot{v}(t) = A(t)v(t) + \mu^{-1} B(t) v(t+\delta), \tag{2.5.4}$$

$$v(t+T) = \mu v(t). \tag{2.5.5}$$

Using that a TDS spends most of the time near its corresponding background x_0, the time interval of localization can be shifted, such that $x_*(t) \approx x_0$ for all $t_0 < |t| < T/2$. The lower bound $t_0 \in [0, T/2]$ has to be chosen sufficiently large and note that, the larger the value is chosen, the better the approximation. Then also $A(t) \approx A_0 := \partial_1 f(x_0, x_0)$ and $B(t) \approx B_0 := \partial_2 f(x_0, x_0)$ for all $t_0 < |t| < T/2$. The asymptotics of $v(t)$ can hence be described by the system

$$\dot{v}(t) = A_0 v(t) + \mu^{-1} B_0 v(t+\delta).$$

Applying now the limit $\delta \longrightarrow \delta_\infty$, yields

$$\dot{v}(t) = A_0 v(t) + \mu^{-1} B_0 v(t+\delta_\infty)$$

and the corresponding characteristic equation of the linearization is given by

$$\chi(\mu, \rho) := \det(\rho \mathbb{I} - A_0 - \mu^{-1} e^{\rho \delta_\infty} B_0). \tag{2.5.6}$$

Then, the *pseudo-continuous spectrum (PCS)* is defined as

$$\chi(\mu, i\omega) := \det(i\omega \mathbb{I} - A_0 - \mu^{-1} e^{i\omega\delta_\infty} B_0) = 0. \tag{2.5.7}$$

Hence, it is determined by those multipliers μ for which the characteristic equation has roots with vanishing real parts. In the absense of singularities, this defines a curve $\mu(\omega)$ in $\mathbb{C}$ and we can see that the pseudo-continuous spectrum is entirely determined by the background. If the system (2.1.1) is one-dimensional, i.e. $x(t) \in \mathbb{R}$, this curve can be brought into the explicit form

$$\mu(\omega) = e^{i\omega\delta_\infty} B_0/(i\omega - A_0).$$

In higher dimensions, the curve is a complex polynomial of degree rank B_0 in μ^{-1}. The multiplier μ accumulate along the curve for $\tau \longrightarrow \infty$. Assume the multiplier $\mu(\omega_*)$ is contained in the PCS, i.e. the characteristic equation (2.5.6) has a purely imaginary root $\rho = i\omega_*$. Then the eigenfunction $y(t)$ corresponding to $\mu(\omega_*)$ is not localized, as it is a multiple of $e^{i\omega_* t} v_*$, where v_* denotes the corresponding eigenvector of the matrix $i\omega_* \mathbb{I} - A_0 - \mu^{-1} e^{i\omega_* \delta_\infty} B_0$ given in (2.5.6).

The *interface spectrum* is composed of those multipliers whose corresponding eigenfunctions are localized at the interface of the soliton and decay to 0 outside of that region, i.e. when the soliton is near the background. It consists of a finite number of multipliers that do not have purely imaginary roots $\rho = i\omega$ and can be obtained by deriving a function similar to the Evans function for localized states in spatially extended systems, see [AA08; San02]. For a full derivation, see supplementary material of [YRSW19]. Consider the case where the characteristic equation (2.5.6) has no purely imaginary roots $i\omega$. Since it was derived from (2.5.4), an equation with an advanced argument, it can have at most a finite number N_s of stable eigenvalues. We are looking for those multipliers whose corresponding eigenfunctions decay outside of their region of localization. To this end, the authors derive an $N_s \times N_s$-matrix $E(\mu)$ whose entries consist of projections of the N_s propagated stable eigenfunctions on each one of the N_s stable eigenvectors in the phase space. Then the multipliers μ belonging to the interface spectrum are given by the roots of $\det E(\mu) = 0$. All entries are independent of the large delay τ and period T.

In Figure 2.4 we show the Floquet spectrum and eigenfunctions of a stable TDS in the phase oscillator (2.1.4) (Panels (a1), (a2)) and the FitzHugh-Nagumo system (2.1.5a)–(2.1.5b) (Panels (b1), (b2)). Panels (a1) and (b1) show the Floquet spectrum in the respective system. The numerically com-

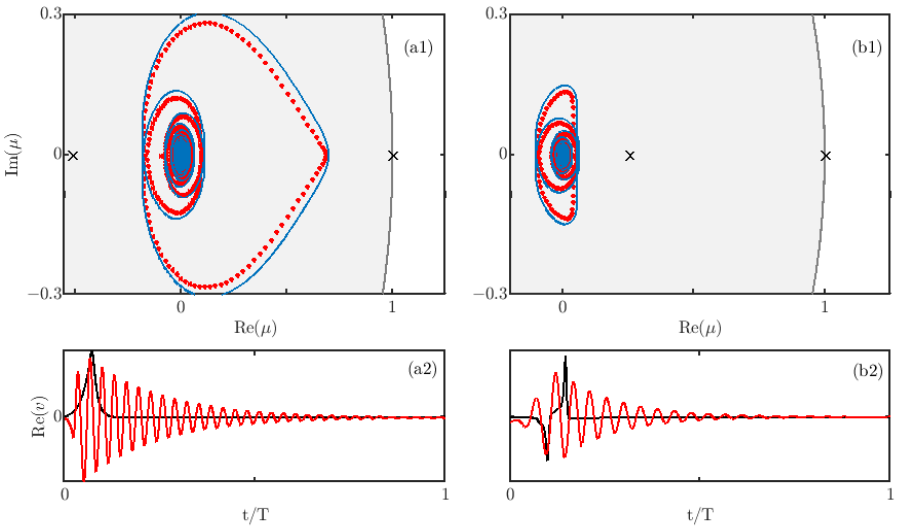

Figure 2.4: Floquet spectrum and eigenfunctions of a stable TDS: (a1), (a2) in the phase oscillator; (b1), (b2) in the FitzHugh-Nagumo system. (a1), (b1) Numerically computed Floquet spectrum (red asterisks and black crosses) and the limiting curve given by the PCS (blue). The multipliers approaching the PCS are indicated by the red crosses, the interface spectrum by the black crosses. The unit circle in $\mathbb{C}$ is displayed in grey. (a2), (b2) selected eigenfunctions corresponding to multipliers from the PCS (red) and interface spectrum (black). Parameters: (a1), (a2) $\tau = 60$; (b1), (b2) $\tau = 200$ and as in Fig. 2.1.

puted multipliers are given by the red asterisks and black crosses. The multipliers indicated by the black crosses correspond to the multipliers from the interface spectrum. As the multiplier $\mu = 1$ gives trivially a localized eigenmode, it is always part of the interface spectrum. For $\tau \longrightarrow \infty$ we find an increasing number of multipliers (red asterisks) approaching the pseudo-continuous spectrum (blue). Recall, that the stable backgrounds are denoted with ϕ_0 and (V_0, w_0) in the respective systems. The pseudo-continuous spectrum can be computed explicitly from (2.5.7) and is then given by

$$\mu(\omega) = \kappa e^{i\omega\delta_\infty}/(i\omega + \cos(\phi_0) + \kappa)$$

in the case of the phase oscillator (2.1.4), and by

$$\mu(\omega) = \kappa e^{i\omega\delta_\infty}(i\omega + \epsilon b)/(\epsilon + (i\omega + \epsilon b)(i\omega + V_0^2 - 1))$$

for the FitzHugh-Nagumo system (2.1.5a)–(2.1.5b). Note, that all multipliers except the trivial one lie inside the unit circle in $\mathbb{C}$ (grey), implying that the TDSs are stable. Panels (a2) and (b2) show exemplary eigenfunctions corresponding to a multiplier from the pseudo-continous spectrum (red) and interface spectrum (black). One can see that an eigenfunction corresponding to a multiplier from the interface spectrum is localized, while an eigenfunction corresponding to a multiplier from the pseudo-continuous spectrum is not.

2.6 Reappearance of resonant Floquet multipliers

A direct consequence of applying the reappearance rule (2.4.1) on the Floquet problem (2.5.1)–(2.5.2) leads to a reappearance rule of certain Floquet multipliers together with the periodic solution, cf. Lemma 1 in [GR23].

Suppose $x_*(t)$ is a T-periodic solution of the DDE system (2.1.1) at fixed delay τ. Suppose further that $x_*(t)$ possesses a critical Floquet multiplier μ, such that

$$\mu^l = 1 \text{ for some } l \in \mathbb{N}, \text{ and } \mu^j \neq 1 \text{ for all } j = 1, \dots, l-1. \tag{2.6.1}$$

Such a mulitplier is called *resonant*. Then, $x_*(t)$ is a T-periodic solution of the DDE system (2.1.1) with the resonant Floquet multiplier μ for all

$$\tau_{ml} = \tau + mlT, \quad \text{for all } m \in \mathbb{Z}. \tag{2.6.2}$$

Indeed, recalling the Floquet condition $v(t+T) = \mu v(t)$ (2.5.2) in the variational equation (2.5.1) of (2.1.1) at $x_*(t)$ yields

$$\begin{aligned}\dot{v}(t) &= A(t)v(t) + B(t)v(t-\tau) = A(t)v(t) + \mu\, B(t)v(t-\tau\, -\, T)\\ &= A(t)v(t) + \mu^m\, B(t)v(t-\tau - m\,T) = A(t)v(t) + \mu^{ml} B(t)v(t-\tau - mlT).\end{aligned}$$

Note, that for the calculation, we also exploited the T-periodicity of the matrices $A(t) = \partial_1 f\left(x_*(t), x_*(t-\tau)\right)$ and $B(t) = \partial_2 f\left(x_*(t), x_*(t-\tau)\right)$.

Trivially, for $l = 1$ one obtains the general reappearance rule (2.4.1), for the multiplier $\mu = 1$ with the corresponding Floquet mode $\dot{x}_*(t)$. In general, a resonant multiplier μ corresponds for $l = 2$ to a period-doubling bifurcation, and for $l > 2$, the critical multiplier μ corresponds to a resonant Neimark-Sacker bifurcation. Suppose $x_*(t)$ is a soliton solution for a fixed large delay τ and recall that solitons lie on a branch $T(\tau) = \tau + \delta(\tau)$ with $\delta(\tau) \longrightarrow \delta_\infty$. The entire branch reappears to $T_m(\tau) := \tau + \delta(\tau) + mT(\tau)$ for all $m \in \mathbb{Z}$. Hence, if $x_*(t)$ has a resonant mulitplier μ with $l > 1$, the soliton solution together with the critical mutliplier μ then reappears on every l-th reappearing branch.

We have now reviewed the current theory on temporal dissipative solitons in DDE systems. In particular, we have introduced the profile equation, an equation with an advanced argument, in which the solitons appear as periodic solutions approaching a homoclinic solution. Our goal is to analyse the bifurcations and instabilities of TDSs by studying the corresponding homoclinics and accompanying family of large-period periodic solutions in the profile equation. To this end, we will give an overview of homoclinic bifurcation theory in the next chapter.

CHAPTER 3

Homoclinic bifurcation theory

This chapter reviews important concepts of the theory on homoclinic solutions and their bifurcations within finite-dimensional vector fields. In particular, conditions for the genericity of these types of solutions are discussed. To extend our understanding of homoclinic bifurcations into higher dimensions, we introduce the centre manifold reduction technique, which serves to effectively reduce dimensionality. Emphasizing the practical implications of our theoretical discussions, we show how the unfolding of a homoclinic solution always comes along with the formation of periodic solutions. We conclude by exploring certain bifurcations induced by the unfolding of degenerate configurations of homoclinics that play a significant role in the main part of the thesis.

3.1 Homoclinic and heteroclinic solutions

This chapter is a summary of the theory on homoclinic and heteroclinic bifurcations in ordinary differential equations based on the review by [HS10].

Consider an autonomous ordinary differential equation (ODE)

$$\dot{x}(t) = f(x(t), \eta), \tag{3.1.1}$$

where f is a nonlinear function depending on the state variable $x(t) \in \mathbb{R}^n$ and parameters $\eta \in \mathbb{R}^p$. For the various results presented in this chapter, different

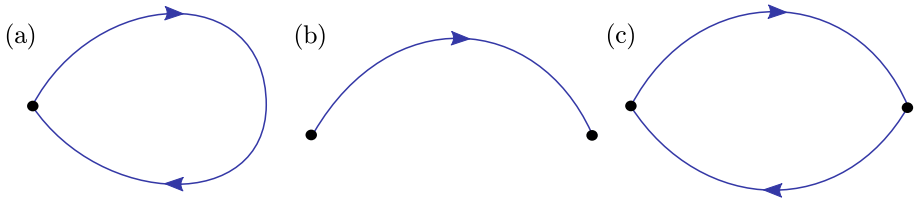

Figure 3.1: Sketches of connecting orbits: (a) homoclinic orbit, (b) heteroclinic orbit, (c) heteroclinic cycle.

orders of differentiability on the vector field are required and can be gathered from the corresponding literature, see references in [HS10]. For simplicity, assume f to be smooth enough in order to satisfy the conditions for every assumption presented here, i.e. $f \in \mathcal{C}^k(\mathbb{R}^n \times \mathbb{R}^p, \mathbb{R}^n)$, for $k \in \mathbb{N}$ sufficiently large.

Definition 2. *A solution $h(t)$ of (3.1.1) at $\eta = \eta_*$ is called* heteroclinic *if it satisfies*

$$\lim_{t\to-\infty} h(t) = x_0 \quad \text{and} \quad \lim_{t\to\infty} h(t) = x_1,$$

where x_0 and x_1 are two distinct equilibria of (3.1.1).

A solution $h(t)$ of (3.1.1) at $\eta = \eta_*$ is called homoclinic *if it satisfies*

$$\lim_{t\to\pm\infty} h(t) = x_0.$$

A heteroclinic cycle *of (3.1.1) at $\eta = \eta_*$ consists of several heteroclinic solutions $h_j(t)$, $j = 1, \ldots, l$, such that*

$$\lim_{t\to\infty} h_j(t) = x_{(j+1) \bmod l} = \lim_{t\to-\infty} h_{(j+1) \bmod l}(t), \quad j = 1, \ldots, l,$$

where x_j, $j = 1, \ldots, l$, are pairwise distinct equilibria of (3.1.1).

Heteroclinic and homoclinic orbits are also often referred to as *connecting orbits*. Figure 3.1 displays a schematic representation of the different types of connecting orbits presented above in Definition 2. Panel (a) displays a trajectory connecting an equilibrium to itself, corresponding to a homoclinic

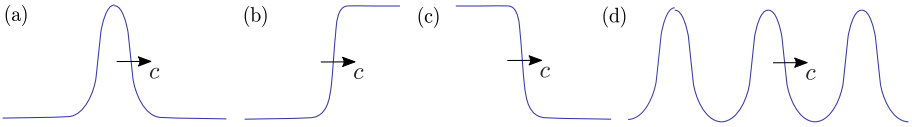

Figure 3.2: Sketches of travelling wave solutions moving with constant speed c: (a) pulse, (b) front, (c) back, (d) periodic pattern.

orbit. Panel (b) gives a sketch of a heteroclinic orbit, where the trajectory connects to two distinct equilibria. In Panel (c), there is a heteroclinic cycle consisting of two heteroclinic connections.

Examples of the appearance of homoclinic or heteroclinic solutions can be found in various nonlinear dynamical systems. A particular instance are travelling-wave solutions of partial differential equations (PDEs) with unbounded domains that have an intrinsic relation to homoclinic solutions. Consider the following reaction-diffusion system given by

$$\partial_t u(t,x) = D\partial_{xx} u(t,x) + F(u(t,x)), \quad u(t,x) \in \mathbb{R}. \tag{3.1.2}$$

The real variables t and x represent, respectively, the time and space of the system. Furthermore, let $F \in \mathcal{C}^1(\mathbb{R},\mathbb{R})$ and D be a real parameter. A solution of (3.1.2) of the form $u(t,x) = u_*(x-ct)$ is called a *travelling wave* and describes a solution with a fixed profile u_* that moves in forward time with a speed $c \in \mathbb{R}$ to the left for $c < 0$ or to the right for $c > 0$. Applying the travelling wave ansatz $u(t,x) = u_*(x-ct)$, with $\xi := x - ct$ to (3.1.2), we obtain

$$\frac{d}{d\xi}\begin{pmatrix} U \\ V \end{pmatrix} = \begin{pmatrix} V \\ -D^{-1}(cV + F(U)) \end{pmatrix}, \tag{3.1.3}$$

an ODE for the new coordinates $(U,V) := (u_*, \partial_\xi u_*)$. Solutions of this reduced system (3.1.3) give travelling waves to the original PDE (3.1.2). What is more, homoclinics of this ODE give rise to travelling pulse solutions in the PDE (3.1.2). These correspond to travelling waves that are localized in space. Subsequently, heteroclinics give rise to fronts and backs, which are travelling waves that become constant for $x \longrightarrow \pm\infty$. Note, that these travelling pulses correspond to dissipative solitons emerging in nonlinear dissipative systems,

like the reaction-diffusion system discussed here. Figure 3.2 gives an overview of the above-mentioned travelling wave solutions in the PDE.

3.2 Homoclinics to hyperbolic equilibria: stable and unstable manifolds

Suppose $h(t)$ is a homoclinic solution of (3.1.1) given by

$$\dot{x}(t) = f(x(t), \eta),$$

at parameters $\eta = \eta_*$. Denote with x_0 the corresponding equilibrium to which the homoclinic converges for $t \longrightarrow \pm\infty$. We will restrict ourselves to equilibria satisfying the following assumption.

Hypothesis 1 (Hyperbolicity of equilibrium)**.** *The equilibrium x_0 of* (3.1.1) *is* hyperbolic *at $\eta = \eta_*$, i.e. the linearization of the vector field* (3.1.1) *at x_0, which is given by the matrix $\dfrac{\partial f}{\partial x}(x_0; \eta_*)$ has no eigenvalues with vanishing real part. Suppose further, that there is at least one eigenvalue which has a real part of the opposite sign than the other eigenvalues, i.e., x_0 is a* saddle *equilibrium.*

The hyperbolicity assumption here excludes bifurcations induced by the equilibrium. Theory on homoclinics to nonhyperbolic saddles, i.e. the case where the linearization of (3.1.1) at x_0 has eigenvalues on the imaginary axis, can be reviewed in Section 2.2. of [HS10]. In the following, we will suppose that x_0 satisfies Hypothesis 1. The stable and unstable manifolds of x_0 at $\eta = \eta_*$ are given by

$$W^{\mathrm{s}}(x_0; \eta_*) = \{x(t_0) : x(t) \text{ satisfies (3.1.1) and } x(t) \longrightarrow x_0 \text{ as } t \longrightarrow \infty\},$$
$$W^{\mathrm{u}}(x_0; \eta_*) = \{x(t_0) : x(t) \text{ satisfies (3.1.1) and } x(t) \longrightarrow x_0 \text{ as } t \longrightarrow -\infty\}.$$

Both sets are immersed manifolds of class $\mathcal{C}^k$, which are invariant under the flow. They converge towards the equilibrium x_0 in their respective time limits

and the rate of convergence is exponential in t, [GH83; TV10]. The homoclinic solution must lie in the intersection of the stable and unstable manifold. Indeed, if there is a time t at which $h(t) \in W^{\mathrm{s}}(x_0;\eta_*) \cap W^{\mathrm{u}}(x_0;\eta_*)$, then this is satisfied for all $t \in \mathbb{R}$, because of the invariance of the flow in a dynamical system. Hence the entire orbit must lie in the intersection of the stable and unstable manifold of x_0.

Consider now the corresponding tangent spaces. The variational equation of (3.1.1) at $h(t)$ is given by

$$\dot{v}(t) = \frac{\partial f}{\partial x}(h(t);\eta_*)v(t), \tag{3.2.1}$$

At each point along $h(t)$ one can define the tangent space to the stable and unstable manifold of x_0. They are given, respectively, by

$$\begin{aligned} T_{h(t)}W^{\mathrm{s}}(x_0;\eta_*) &= \{v(t) : v(\cdot) \text{ satisfies (3.2.1) and } v(s) \longrightarrow 0 \text{ as } s \longrightarrow \infty\}, \\ T_{h(t)}W^{\mathrm{u}}(x_0;\eta_*) &= \{v(t) : v(\cdot) \text{ satisfies (3.2.1) and } v(s) \longrightarrow 0 \text{ as } s \longrightarrow -\infty\}. \end{aligned}$$

Since $\dot{h}(t)$ lies in $T_{h(t)}W^{\mathrm{s}}(x_0;\eta_*)$ as well as $T_{h(t)}W^{\mathrm{u}}(x_0;\eta_*)$, the intersection is at least one dimensional. Assume that it is exactly one dimensional and hence spanned only by $\dot{h}(t)$.

The adjoint system of the variational equation (3.2.1) is given by

$$\dot{w}(t) = -\frac{\partial f}{\partial x}(h(t);\eta_*)^{\mathrm{tr}}w(t), \tag{3.2.2}$$

where M^{tr} denotes the transpose of the matrix M. Let $\langle \cdot\,,\,\cdot \rangle$ be the euclidean scalar product in $\mathbb{R}^n$. We denote with $V^{\perp}$ the space of vectors that are perpendicular to V with respect to $\langle \cdot\,,\,\cdot \rangle$. The adjoint linearized eigenspaces of x_0 are then given by

$$\begin{aligned} T_{h(t)}W^{\mathrm{s}}(x_0;\eta_*)^{\perp} &= \{w(t) : w(\cdot) \text{ satisfies (3.2.2) and } w(s) \longrightarrow 0 \text{ as } s \longrightarrow \infty\}, \\ T_{h(t)}W^{\mathrm{u}}(x_0;\eta_*)^{\perp} &= \{w(t) : w(\cdot) \text{ satisfies (3.2.2) and } w(s) \longrightarrow 0 \text{ as } s \longrightarrow -\infty\}. \end{aligned}$$

Solutions $v(t)$ of (3.2.1) and $w(t)$ of (3.2.2) satisfy

$$\frac{\mathrm{d}}{\mathrm{d}t}\langle w(t), v(t)\rangle = 0.$$

Consider now the spaces

$$\begin{aligned} &T_{h(t)}W^{\mathrm{s}}(x_0;\eta_*) \ \cap \ T_{h(t)}W^{\mathrm{u}}(x_0;\eta_*) \\ &\qquad = \{\ v(t) : v(\cdot) \text{ satisfies (3.2.1) and } v(s) \longrightarrow 0 \text{ as } |s| \longrightarrow \infty\ \}, \\ &[T_{h(t)}W^{\mathrm{s}}(x_0;\eta_*) \ + \ T_{h(t)}W^{\mathrm{u}}(x_0;\eta_*)]^{\perp} \\ &\qquad = \{\ w(t) : w(\cdot) \text{ satisfies (3.2.2) and } w(s) \longrightarrow 0 \text{ as } |s| \longrightarrow \infty\ \}, \end{aligned}$$

where we denote with $A+B$ the direct sum of two vector spaces A and B. Since we assumed $T_{h(t)}W^{\mathrm{s}}(x_0;\eta_*)\cap T_{h(t)}W^{\mathrm{u}}(x_0;\eta_*)$ to be a one dimensional subspace spanned by $\dot{h}(t)$, also $[T_{h(t)}W^{\mathrm{s}}(x_0;\eta_*)+T_{h(t)}W^{\mathrm{u}}(x_0;\eta_*)]^{\perp}$ is one-dimensional. We denote with $\psi(t)$ the element spanning $[T_{h(t)}W^{\mathrm{s}}(x_0;\eta_*)+T_{h(t)}W^{\mathrm{u}}(x_0;\eta_*)]^{\perp}$. The two vectors $\dot{h}(t)$ and $\psi(t)$ lie orthogonally with respect to $\langle\cdot\ ,\ \cdot\rangle$.

3.3 Nondegeneracy condition for the homoclinic solution

An important factor guaranteeing the persistence of a homoclinic orbit under varying parameters is a transversality condition on the stable and unstable manifold. In order to ensure a generic unfolding of the homoclinic, we will use the so called Melnikov integral. This tool was developed for the detection of chaos in non-autonomous dynamical systems, see for example [GH83] for a mechanical system under periodic perturbations, and can reveal the existence of homoclinic tangles in the Poincaré-map.

Consider a homoclinic solution $h(t)$ of (3.1.1) to the equilibrium x_0 at $\eta = \eta_*$. In this section, we set $\eta_* = 0$ for simplicity. The equilibrium is assumed to be of saddle-type, i.e. it satisfies Hypothesis 1. Remember that $h(t) \in W^{\mathrm{s}}(x_0;0) \cap W^{\mathrm{u}}(x_0;0)$. Varying the parameter, the homoclinic possibly dissolves. The unstable and stable manifold split and no longer intersect. Consider now the following Lemma.

Lemma 1 (see [HS10] Lemma 2.1 and Proof)**.** *Assume the equilibrium x_0 satisfies Hypothesis 1 and $T_{h(t)}W^{\mathrm{s}}(x_0;0)\cap T_{h(t)}W^{\mathrm{u}}(x_0;0) = \mathbb{R}\dot{h}(t)$. Then for each η close to 0, there are orbits $h^{\mathrm{s}}(\cdot;\eta) \in W^{\mathrm{s}}(x_0(\eta);\eta)$ and $h^{\mathrm{u}}(\cdot;\eta) \in W^{\mathrm{u}}(x_0(\eta);\eta)$,*

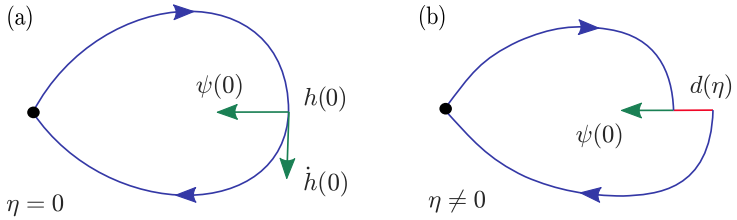

Figure 3.3: A homoclinic structure $h(t)$ at $\eta = 0$ (Panel (a)) dissolves for $\eta \neq 0$ (Panel (b)). The distance between the stable and unstable manifold is then given by d.

that are unique and $h^{\mathrm{s}}(0;0) = h^{\mathrm{u}}(0;0) = h(0)$*, such that*

$$h^{\mathrm{u}}(0;\eta) - h^{\mathrm{s}}(0;\eta) \in \mathbb{R}\psi(0) \text{ for all } \eta.$$

The functions $h^{\mathrm{s}}(\cdot;\eta)$ *and* $h^{\mathrm{u}}(\cdot;\eta)$*, considered with values in* $\mathcal{C}^0(\mathbb{R}^+, \mathbb{R}^n)$ *and* $\mathcal{C}^0(\mathbb{R}^-, \mathbb{R}^n)$*, respectively, are smooth in* η*.*

One can now define the distance d between the stable and unstable manifold as

$$d(\eta) := \langle \psi(0), h^{\mathrm{u}}(0;\eta) - h^{\mathrm{s}}(0;\eta) \rangle.$$

Since for homoclinic solutions, the unstable and stable manifold coincide, it is $d(\eta) = 0$ at $\eta = 0$, see Figure 3.3. Applying Taylor at $\eta = 0$ gives

$$d(\eta) = d(0) + d'(0)\eta + \mathcal{O}(|\eta|^2).$$

It can be shown that

$$d'(0) = \int_{\mathbb{R}} \langle \psi(t), \frac{\partial}{\partial \eta} f(h(t);0) \rangle \, \mathrm{d}t,$$

see [Mel63; Wig03]. This integral is called the *Melnikov integral* $\mathcal{M}$.

Since $d(0) = 0$, it is $d(\eta) = \mathcal{M}\eta + \mathcal{O}(|\eta|^2)$ and one can now make the assumption that the homoclinic orbit will not persist under parameter variations if $\mathcal{M} \neq 0$. Hence, we can make the following nondegeneracy condition for homoclinics:

Hypothesis 2 (Nondegeneracy of homoclinics, see [HS10] Hypothesis 2.2)**.** *A nondegeneracy condition for the homoclinic solution $h(t)$ in (3.1.1) to the saddle equilibrium x_0 at parameter $\eta = (\eta_1, \dots, \eta_p) = \eta_*$ is given by:*

1. (transverse intersection) *The stable and unstable manifold of x_0 intersect transversely:*

$$T_{h(t)}W^{\mathrm{s}}(x_0;\eta_*) \cap T_{h(t)}W^{\mathrm{u}}(x_0;\eta_*) = \mathbb{R}\dot{h}(0).$$

2. (generic unfolding) *The stable and unstable manifold of x_0 unfold generically with respect to the parameter η_j, for $j \in \{1, \dots, p\}$:*

$$\mathcal{M}_j = \int_{\mathbb{R}} \langle \psi(t), \frac{\partial}{\partial \eta_j}\Big|_{\eta=\eta_*} f(h(t);\eta)\rangle \, \mathrm{d}t \neq 0.$$

3.4 Nondegeneracy conditions for the saddle equilibrium

For certain tools needed to examine homoclinics and their bifurcation scenarios discussed later, it becomes evident that conditions on the spectrum of the saddle equilibrium x_0 are crucial, as it is responsible for the asymptotic behaviour of the homoclinic. The dynamics at the tails of the homoclinic are governed by the linearization around its corresponding equilibrium given by

$$\dot{v}(t) = \frac{\partial}{\partial x} f(x_0, \eta_*) v(t), \tag{3.4.1}$$

and thereby depend on the spectrum of the equilibrium.

Suppose the equilibrium x_0 is of saddle-type (Hypothesis 1). Then there is an $l \in \{1, \dots n\}$, such that the n eigenvalues of the matrix $\frac{\partial}{\partial x} f(x_0, \eta_*)$ denoted with λ_j, $j = 1, \dots, n$, repeated with multiplicity, can be arranged by increasing real part:

$$\mathrm{Re}(\lambda_1) \leq \mathrm{Re}(\lambda_2) \leq \cdots \leq \mathrm{Re}(\lambda_l) < 0 < \mathrm{Re}(\lambda_{l+1}) \leq \cdots \leq \mathrm{Re}(\lambda_n).$$

The eigenvalues closest to the imaginary axis are called the *leading stable* and *leading unstable eigenvalues*, denoted with λ^{ls} and λ^{lu}, respectively. The

eigenvalues λ_j, $j = 1, \ldots, n$, satisfying $\mathrm{Re}(\lambda_j) = \mathrm{Re}(\lambda_l)$ are the leading stable eigenvalues and those satisfying $\mathrm{Re}(\lambda_j) = \mathrm{Re}(\lambda_{l+1})$ are the leading unstable eigenvalues. Generically, they dominate the dynamics at the tails, as they give the slowest exponential decay rates. Thereby, the asymptotics at the tail for $t \longrightarrow -\infty$ are order $\mathcal{O}(\mathrm{Re}(e^{\lambda^{\mathrm{lu}} t}))$, and of order $\mathcal{O}(\mathrm{Re}(e^{\lambda^{\mathrm{ls}} t}))$ for $t \longrightarrow \infty$.

We consider the following generic configurations of saddle-type equilibria.

Hypothesis 3 (saddle-type configurations, see [HS10] Hypothesis 2.3)**.** *Generic configurations of the equilibrium are given by:*

1. (tame saddle) *The unique leading unstable eigenvalue λ^{lu} is real and simple and the leading stable eigenvalue satisfy $|\mathrm{Re}(\lambda^{\mathrm{ls}})| > \lambda^{\mathrm{lu}}$.*

2. (simple saddle) *The leading stable and unstable eigenvalues are unique, real and simple.*

3. (saddle focus) *The leading unstable eigenvalue is unique, real and simple. There are precisely two leading stable eigenvalues λ^{ls} and $\overline{\lambda^{\mathrm{ls}}}$, and these are simple with nonvanishing real parts.*

4. (double focus) *The leading stable and unstable eigenvalues are unique (up to complex conjugation) and simple.*

Note that for case (*1.*), the leading stable eigenvalue λ^{ls} of the saddle does not have to be unique or simple. Consider the case where the leading stable eigenvalue is unique, real, and simple, and there are precisely two leading unstable eigenvalues, λ^{lu} and $\overline{\lambda^{\mathrm{lu}}}$, which are complex conjugate with nonvanishing real parts and are likewise simple. This configuration qualifies as a saddle focus in the time-reversed version of system (3.1.1).

The *saddle value* σ is given by

$$\sigma := \mathrm{Re}(\lambda^{\mathrm{ls}}) + \mathrm{Re}(\lambda^{\mathrm{lu}}). \tag{3.4.2}$$

If $\sigma > 0$, we call the saddle x_0 *wild*. If $\sigma < 0$, we call the saddle *tame*.

The spectrum of an equilibrium can be further subdivided, if there are spectral gaps given in the following way: If there is a $\lambda^{\mathrm{ss}} \in \mathbb{R}$, and a natural number $n_s < l$ such that

$$\mathrm{Re}(\lambda_1) \leq \cdots \leq \mathrm{Re}(\lambda_{n_s}) < \lambda^{\mathrm{ss}} < \mathrm{Re}(\lambda^{\mathrm{ls}}) < 0,$$

then λ^{ss} is called *strong stable eigenvalue*. Analogously, if there is a $\lambda^{\mathrm{uu}} \in \mathbb{R}$, and a natural number $n_u > l+1$ such that

$$0 < \mathrm{Re}(\lambda^{\mathrm{lu}}) < \lambda^{\mathrm{uu}} \leq \mathrm{Re}(\lambda_{n_u}) \leq \cdots \leq \mathrm{Re}(\lambda_n),$$

then λ^{uu} is called *strong unstable eigenvalue*.

In the following chapters, we will discuss the possible influences of the strong spectrum and the size of the spectral gaps on the dynamics of the homoclinic.

3.5 Inclination and orbit flip configurations

In the previous section, we discussed that the asymptotic behaviour of the homoclinic is determined by the spectrum of the corresponding saddle equilibrium x_0 and presented conditions on the saddle equilibrium. We will now continue with our discussion on the asymptotic behaviour of the homoclinic in more detail.

In the generic configurations, the homoclinic approaches its saddle along the leading eigendirections and the decay rate of the left and right tails are respectively of order $\mathcal{O}(\mathrm{Re}(e^{\lambda^{\mathrm{lu}}t}))$ and $\mathcal{O}(\mathrm{Re}(e^{\lambda^{\mathrm{ls}}t}))$. Define $W^{\mathrm{ls,u}}(x_0;\eta_*)$ as the set whose tangent space at x_0 is given by the leading stable eigendirections plus the generalized unstable eigenspace of $\frac{\partial}{\partial x}f(x_0;\eta_*)$. Let $W^{\mathrm{lu,s}}(x_0;\eta_*)$ be analogously the set whose tangent space consists of the leading unstable eigendirections plus the generalized stable eigenspace. These are invariant manifolds, whose differentiability depends on spectral gap conditions, provided by invariant manifold theory [TV10]. In general, they can only be assumed to be continuously differentiable. Note, that although their tangent space at x_0 is unique, the manifolds themselves are not uniquely defined. Generically, the manifolds $W^{\mathrm{ls,u}}(x_0;\eta_*)$ and $W^{\mathrm{s}}(x_0;\eta_*)$ and, analogously, the manifolds $W^{\mathrm{s,lu}}(x_0;\eta_*)$ and $W^{\mathrm{u}}(x_0;\eta_*)$ intersect transversally. This is visualized in Figure 3.4, where a generic homoclinic $h(t)$ (blue) in three dimensions is displayed with a corresponding equilibrium x_0 having respectively one real leading unstable, leading stable (single arrows) and strong stable eigendirection (double arrow). The

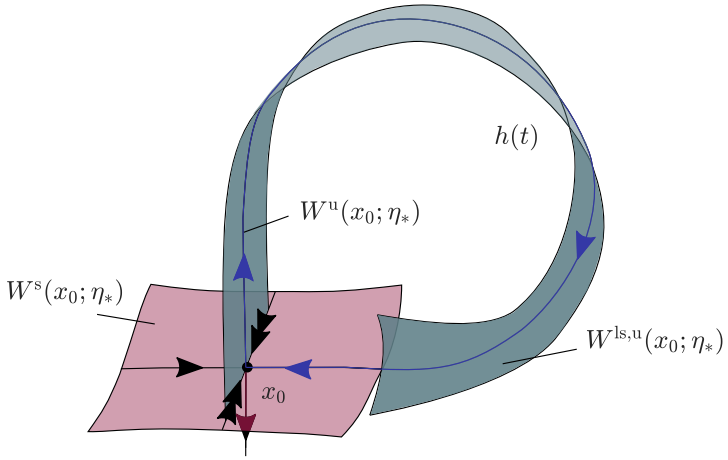

Figure 3.4: Exemplary generic homoclinic orbit $h(t)$ in $\mathbb{R}^3$ (blue) to a corresponding saddle equilibrium x_0 with a real leading stable and unstable eigendirection (single arrows), and a real strong stable eigendirection (double arrow). The homoclinic approaches x_0 along the leading stable eigendirection and the manifolds $W^{\mathrm{ls,u}}(x_0;\eta_*)$ (grey) and $W^{\mathrm{s}}(x_0;\eta_*)$ (red) intersect transversally.

homoclinic approaches its saddle along the leading eigendirections. Moreover, the manifolds $W^{\mathrm{ls,u}}(x_0;\eta_*)$ (grey) and $W^{\mathrm{s}}(x_0;\eta_*)$ (red) intersect transversally.

Nevertheless, these conditions may be violated. In the following, we discuss the case when the strong spectrum rules over the asymptotics.

Orbit flip. Assume that there is a strong stable and unstable eigenvalue, denoted with λ^{ss} and λ^{uu}. Define the *strong stable manifold* $W^{\mathrm{ss}}(x_0;\eta_*)$ as the set of all solutions $x(t)$ of the ODE (3.1.1) satisfying $||x(t)-x_0|| \in \mathcal{O}(e^{\lambda^{\mathrm{ss}}t})$. We then say that the stable manifold of the homoclinic lies in an *orbit flip* configuration, if $h(t) \in W^{\mathrm{ss}}(x_0;\eta_*)$. That is, the homoclinic approaches the equilibrium x_0 for $t \longrightarrow \infty$ along the strong stable manifold $W^{\mathrm{ss}}(x_0;\eta_*)$. This scenario is displayed in Figure 3.5 for a homoclinic $h(t)$ in three dimensions, with a corresponding saddle equilibrium x_0, having again, respectively, one real unstable, leading stable and strong stable eigendirection. Note that for a generic orbit flip configuration, the manifolds $W^{\mathrm{ss,u}}(x_0;\eta_*)$ (grey) and $W^{\mathrm{s}}(x_0;\eta_*)$

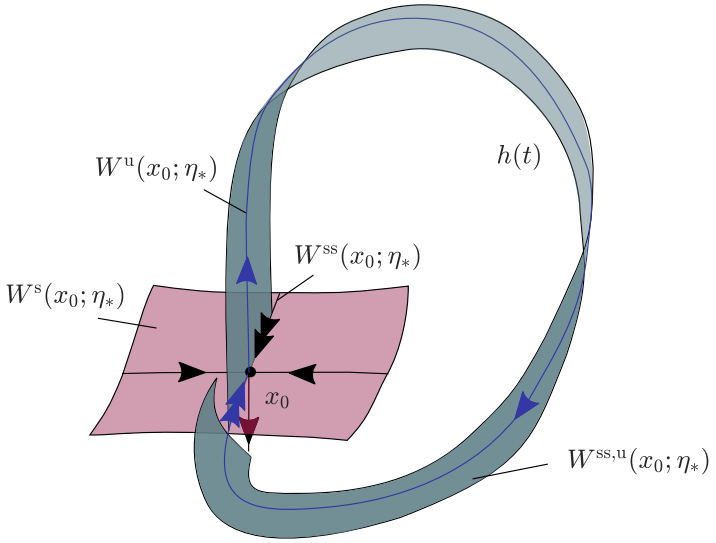

Figure 3.5: Homoclinic orbit $h(t)$ (blue) in $\mathbb{R}^3$ with stable manifold in orbit flip configuration. The corresponding saddle equilibrium x_0 has a real leading stable and unstable eigendirection (single arrows), and a real strong stable eigendirection (double arrow). The homoclinic approaches x_0 along the strong stable eigendirection and the manifolds $W^{\mathrm{ss,u}}(x_0;\eta_*)$ (grey) and $W^{\mathrm{s}}(x_0;\eta_*)$ (red) intersect transversally.

(red) intersect transversally. The manifold $W^{\mathrm{ss,u}}(x_0;\eta_*)$ is defined analogously as the manifold, whose tangent space at x_0 is given by the strong stable eigendirections plus the generalized unstable eigenspace of $\frac{\partial}{\partial x}f(x_0;\eta_*)$. Analogously, the *strong unstable manifold* $W^{\mathrm{uu}}(x_0;\eta_*)$ can be defined as the set of all solutions $x(t)$ of (3.1.1) satisfying $||x(t)-x_0|| \in \mathcal{O}(e^{\lambda^{\mathrm{uu}}t})$. We then say that the unstable manifold of the homoclinic lies in an orbit flip configuration if $h(t) \in W^{\mathrm{uu}}(x_0;\eta_*)$.

Suppose for simplicity that x_0 is a simple saddle, i.e. the leading stable and unstable eigenvalue are unique, real and simple (Hypothesis 3 (*2.*)). Recalling Lemma 1, there are solutions $h^{\mathrm{s}}(t;\eta)$ and $h^{\mathrm{u}}(t;\eta)$ lying in the stable, and respectively unstable manifold $W^{\mathrm{s}}(x_0(\eta);\eta)$ and $W^{\mathrm{u}}(x_0(\eta);\eta)$. We can now

define the following vectors

$$\nu^{\mathrm{s}}(\eta) := \lim_{t\to\infty} \; e^{-\lambda^{\mathrm{ls}}(\eta)t} \; \left(h^{\mathrm{s}}(t;\eta) - x_0(\eta)\right),$$
$$\nu^{\mathrm{u}}(\eta) := \lim_{t\to-\infty} e^{-\lambda^{\mathrm{lu}}(\eta)t} \; \left(h^{\mathrm{u}}(t;\eta) - x_0(\eta)\right),$$

where we indicate with $x_0(\eta)$, $\lambda^{\mathrm{ls}}(\eta)$ and $\lambda^{\mathrm{lu}}(\eta)$ the possible parameter dependencies of the equilibrium and the leading eigenvalues. Note, that in the more general case where the eigenvalues are not real, the limits can be computed in complex coordinates. It can be verified that the limits exist and are of order $\mathcal{C}^k$ in η. The vectors $\nu^{\mathrm{s}}(\eta)$ and $\nu^{\mathrm{u}}(\eta)$ are multiples of the eigenvectors of the linearization $\frac{\partial}{\partial x} f(x_0(\eta);\eta)$ corresponding to the leading eigenvalues $\lambda^{\mathrm{ls}}(\eta)$ and $\lambda^{\mathrm{lu}}(\eta)$, respectively. Especially, it is $\nu^{\mathrm{s}} = 0$ if and only if the homoclinic approaches the equilibrium x_0 for $t \longrightarrow \infty$ along the strong stable manifold $W^{\mathrm{ss}}(x_0;\eta_*)$. Analogously it is $\nu^{\mathrm{u}} = 0$, if and only if the homoclinic approaches the equilibrium x_0 for $t \longrightarrow -\infty$ along the strong unstable manifold $W^{\mathrm{uu}}(x_0;\eta_*)$. Beyond that, there is a constant $\epsilon > 0$, such that

$$h^{\mathrm{s}}(t;\eta) = x_0(\eta) + e^{\lambda^{\mathrm{ls}}(\eta)t}\nu^{\mathrm{s}}(\eta) + \mathcal{O}(e^{(\mathrm{Re}\lambda^{\mathrm{ls}}(\eta)-\epsilon)t}), \quad t \longrightarrow \infty,$$

and analogously for $h^{\mathrm{u}}(t;\eta)$, [HS10]. Thereby, if $\nu^{\mathrm{s}}(\eta_*)$ or $\nu^{\mathrm{u}}(\eta_*)$ vanish, the leading stable or unstable eigendirection do not appear in the asymptotic decay rates of the homoclinic.

But not only the generic asymptotics of the homoclinic solution along the leading eigendirections might not be realized. Another nongeneric configuration can appear involving features of the stable and unstable eigenvectors of the saddle equilibrium when they are transported along the homoclinic orbit.

Inclination flip. Generically, the manifolds $W^{\mathrm{ls,u}}(x_0;\eta_*)$ and $W^{\mathrm{s}}(x_0;\eta_*)$ intersect transversally along the homoclinic orbit. However, it can happen, that the intersection is not transversal. Then the stable manifold is in an *inclination flip* configuration. This is sketched in Figure 3.6 for a homoclinic in $\mathbb{R}^3$ that has a corresponding saddle with three real eigenvalues, with one being positive. Analogously, the unstable manifold is in an inclination flip, if the manifolds $W^{\mathrm{s,lu}}(x_0;\eta_*)$ and $W^{\mathrm{u}}(x_0;\eta_*)$ do not intersect transversally along the homoclinic orbit.

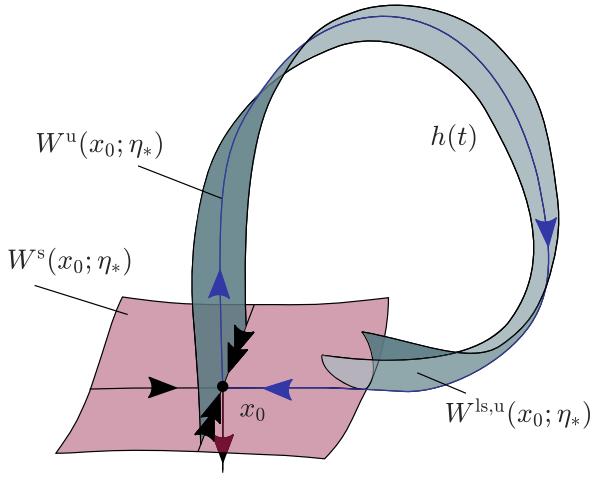

Figure 3.6: Homoclinic orbit $h(t)$ (blue) in $\mathbb{R}^3$ with stable manifold in inclination flip configuration. The corresponding saddle equilibrium x_0 has a real leading stable and unstable eigendirection (single arrows), and a real strong stable eigendirection (double arrow). The homoclinic approaches x_0 along the leading stable eigendirection and the manifolds $W^{\mathrm{ls,u}}(x_0;\eta_*)$ (grey) and $W^{\mathrm{s}}(x_0;\eta_*)$ (red) do not intersect transversally.

We would like to formalize these statements, in a similar manner as for the orbit flip case. Denote with v^{ls} and v^{lu} the leading stable and unstable eigenvectors corresponding to the leading eigenvalues λ^{ls} and λ^{lu} of the matrix $\frac{\partial}{\partial x} f(x_0;\eta_*)$. Consider the solutions of (3.2.1) lying in $T_{h(t)}W^{\mathrm{s}}(x_0;\eta_*)$. For $t \longrightarrow -\infty$, they converge generically to the sum of the tangent space of the strong stable manifold $T_{x_0}W^{\mathrm{ss}}(x_0;\eta_*)$ and the eigendirection defined by the leading unstable eigenvector v^{lu}. Conversely, the stable manifold is in an inclination flip configuration, then the tangent space $T_{h(t)}W^{\mathrm{s}}(x_0;\eta_*)$ along the homoclinic for $t \longrightarrow -\infty$ converges to the sum of the tangent space of the leading stable manifold at $T_{x_0}W^{\mathrm{ls}}(x_0;\eta_*)$ and the eigendirection defined by the leading unstable eigendirection v^{lu}.

This works similarly for the unstable manifold. The solutions of (3.2.1) lying in $T_{h(t)}W^{\mathrm{u}}(x_0;\eta_*)$ converge generically for $t \longrightarrow \infty$ to the sum of the tangent space of the strong unstable manifold $T_{x_0}W^{\mathrm{uu}}(x_0;\eta_*)$ and the eigendirection defined by the leading stable eigenvector v^{ls}. Then, the unstable manifold is in an inclination flip configuration, if the tangent space $T_{h(t)}W^{\mathrm{u}}(x_0;\eta_*)$ along the homoclinic for $t \longrightarrow \infty$ converges to the sum of the tangent space of the leading unstable manifold at $T_{x_0}W^{\mathrm{lu}}(x_0;\eta_*)$ and the eigendirection given by the leading stable eigendirection v^{ls}.

Recall from Section 3.2 the solution $\psi(t)$ of (3.2.2) spanning the space $[T_{h(t)}W^{\mathrm{s}}(x_0;\eta_*) + T_{h(t)}W^{\mathrm{u}}(x_0;\eta_*)]^{\perp}$. Similarly to Lemma 1 presented in Section 3.3, we give the following lemma.

Lemma 2 (see [HS10] Lemma 2.3)**.** *Assume that Hypotheses 1 and 2. (1.) are met. For $j = \mathrm{s},\mathrm{u}$ there are unique solutions $\psi_j(\cdot;\eta)$ of*

$$\dot{w}(t) = -\partial_x f(h^j(t;\eta);\eta)^{\mathrm{tr}} w(t), \qquad j = \mathrm{s},\mathrm{u},$$

with $||\psi^j(0;\psi)|| = 1$ and $\psi^j(t;\eta) \perp T_{h^j(t;\eta)}W^j(x_0(\eta);\eta)$, so that

$$\psi^{\mathrm{u}}(0;\eta) - \psi^{\mathrm{s}}(0;\eta) \in \mathbb{R}\dot{h}(0).$$

The functions $\psi^{\mathrm{s}}(\cdot;\eta)$ and $\psi^{\mathrm{u}}(\cdot;\eta)$, considered with values in $\mathcal{C}^0(\mathbb{R}^+,\mathbb{R}^n)$ and $\mathcal{C}^0(\mathbb{R}^-,\mathbb{R}^n)$, respectively, are smooth in η.

Define then the vectors

$$\nu_*^{\mathrm{s}}(\eta) := \lim_{t\longrightarrow-\infty} e^{\lambda^{\mathrm{ls}}(\eta)t}\psi^{\mathrm{s}}(t;\eta), \quad \text{and} \quad \nu_*^{\mathrm{u}}(\eta) := \lim_{t\longrightarrow\infty} e^{\lambda^{\mathrm{lu}}(\eta)t}\psi^{\mathrm{u}}(t;\eta).$$

It can again be shown that these limits exist and are of class $\mathcal{C}^k$ in η. The vectors $\nu_*^{\mathrm{s}}(\eta_*)$ and $\nu_*^{\mathrm{u}}(\eta_*)$ are multiples of the leading stable and unstable eigendirections of the adjoint linearization $\partial_x f(x_0;\eta_*)^{\mathrm{tr}}$ of (3.1.1) at x_0. In particular, the stable manifold does not lie in an inclination flip configuration if and only if $\nu_*^{\mathrm{s}}(\eta_*) \neq 0$. Analogously, the unstable manifold does not lie in an inclination flip configuration if and only if $\nu_*^{\mathrm{u}}(\eta_*) \neq 0$.

We can now state the following Hypothesis excluding orbit and inclination flip configurations.

Hypothesis 4 (Inclination and orbit properties, see [HS10] Hypothesis 2.4)**.** *The following conditions exclude inclination flip and orbit flip configurations:*

1. *The stable manifold along the homoclinic orbit is not in an inclination flip configuration, i.e.* $\nu_*^{\mathrm{s}} \neq 0$.
2. *The unstable manifold along the homoclinic orbit is not in an inclination flip configuration, i.e.* $\nu_*^{\mathrm{u}} \neq 0$.
3. *The homoclinic orbit is not in an orbit flip configuration within the stable manifold, i.e.* $\nu^{\mathrm{s}} \neq 0$.
4. *The homoclinic orbit is not in an orbit flip configuration within the unstable manifold, i.e.* $\nu^{\mathrm{u}} \neq 0$.

Assuming the leading eigenvalues are real and simple (Hypothesis 3 (*2.*) (simple saddle)), we can define the orientation index with

$$O(\eta) := \mathrm{sign}\{\langle \nu_*^{\mathrm{s}}(\eta), \nu^{\mathrm{s}}(\eta)\rangle \langle \nu_*^{\mathrm{u}}(\eta), \nu^{\mathrm{u}}(\eta)\rangle\}. \tag{3.5.1}$$

A homoclinic orbit at $\eta = \eta_*$ is orientable if $O(\eta_*) = 1$ and non-orientable, when $O(\eta_*) = -1$. Especially, if Hypothesis 4 is satisfied, it is $O(\eta_*) = \pm 1$. If at a parameter $\eta = \eta_*$ it is $O(\eta_*) = 0$, the homoclinic is either in an inclination or orbit flip configuration and Hypothesis 4 fails. This suggests that, in the three-dimensional case given in Figures 3.4–3.6, the unfolding of an orbit or inclination flip leads to a change in the orientation of the two-dimensional manifold $W^{\mathrm{ls,u}}(x_0;\eta)$.

3.6 Homoclinic centre manifolds

Since the analysis of homoclinics in higher dimensions can be tedious, it makes sense to analyse a reduced system, containing the homoclinic orbit and all recurring dynamics. To this end, suppose again that $h(t)$ is a homoclinic orbit of (3.1.1) at $\eta = \eta_*$ that limits to the saddle equilibrium x_0.

Hypothesis 5 (Linear normal hyperbolicity, see [HS10] Hypothesis 3.1)**.** *The spectrum of the saddle x_0 and the corresponding eigenspaces can be decomposed in the following way:*

$$\operatorname{spec}\{\frac{\partial}{\partial x} f(x_0, \eta_*))\} = \sigma^{\mathrm{u}} \cap \sigma^{\mathrm{c}} \cap \sigma^{\mathrm{s}},$$
$$\text{with } \max(\operatorname{Re}(\sigma^{\mathrm{s}})) < \min(\operatorname{Re}(\sigma^{\mathrm{c}})) \quad \text{and} \quad \max(\operatorname{Re}(\sigma^{\mathrm{c}})) < \min(\operatorname{Re}(\sigma^{\mathrm{u}})).$$

The eigenspaces corresponding to the subsets of the spectrum are denoted with $E^{\mathrm{s}}_{x_0}$, $E^{\mathrm{c}}_{x_0}$ and $E^{\mathrm{u}}_{x_0}$, respectively, and their direct sum is $E^{\mathrm{s}}_{x_0} + E^{\mathrm{c}}_{x_0} + E^{\mathrm{u}}_{x_0} = \mathbb{R}^n$. Additionally, the subspaces $E^{\mathrm{s}}(t)$, $E^{\mathrm{c}}(t)$ and $E^{\mathrm{u}}(t)$ are continuous in $t \in \mathbb{R}$ and their direct sum $E^{\mathrm{s}}(t) + E^{\mathrm{c}}(t) + E^{\mathrm{u}}(t) = \mathbb{R}^n$ for all $t \in \mathbb{R}$. It is $E^j(t) \longrightarrow E^j_{x_0}$ for $|t| \longrightarrow \infty$, such that the flow $\Phi(t, r)$ of

$$\dot{v}(t) = \frac{\partial}{\partial x} f(h(t); \eta_*) v(t)$$

maps $E^j(r)$ into $E^j(t)$ for all $t, r \in \mathbb{R}$ and each $j = \mathrm{s}, \mathrm{c}, \mathrm{u}$. Furthermore, the derivative $\dot{h}(t)$ lies in $E^{\mathrm{c}}(t)$.

Under these conditions, the homoclinic possesses a centre manifold. Its differentiability is influenced by the size of the spectral gaps between the leading eigenvalues and the strong spectrum. This has been demonstrated in [Hom96; San00; San93].

Theorem 1 (Homoclinic centre manifold, see [HS10] Theorem 3.3)**.** *Suppose Hypothesis 5 is satisfied. For any $K \in \mathbb{N}$ and $\alpha \in (0, 1)$, such that*

$$K + \alpha < \min\{\frac{\min \operatorname{Re}(\sigma^{\mathrm{c}})}{\max \operatorname{Re}(\sigma^{\mathrm{s}})}, \frac{\min \operatorname{Re}(\sigma^{\mathrm{u}})}{\max \operatorname{Re}(\sigma^{\mathrm{c}})}\},$$

there are a constant $\epsilon > 0$ and a locally invariant, normally hyperbolic homoclinic centre manifold $W^{\mathrm{c}}_{\mathrm{hom}}(\eta)$ associated with $h(t)$ and defined for $|\eta - \eta_*| < \epsilon$, with the following properties: $W^{\mathrm{c}}_{\mathrm{hom}}(\eta)$ is of class $\mathcal{C}^{K,\alpha}$ jointly in (x, η) and has dimension equal to $\dim E^{\mathrm{c}}_{x_0}$.

The notation $\mathcal{C}^{K,\alpha}$ denotes the Höder space, containing all K-times continuously differentiable functions, whose K-th partial derivatives are Hölder continuous with exponent α. Hypothesis 5 providing for normal hyperbolicity

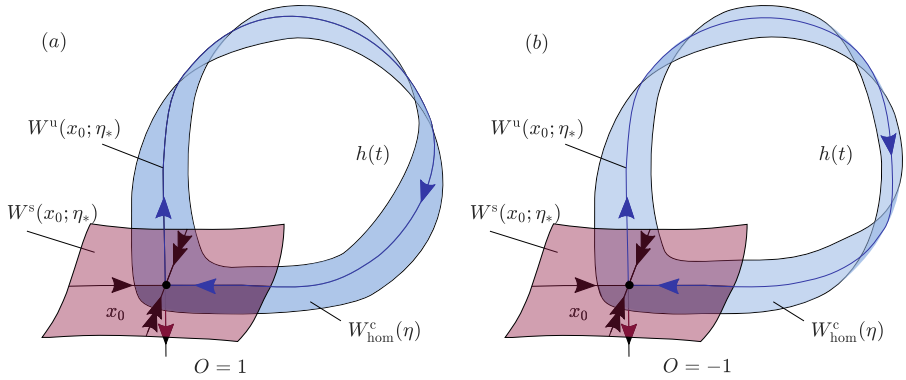

Figure 3.7: Exemplary two-dimensional centre manifold (blue) of a generic homoclinic solution (blue) to a saddle with real eigenvalues in $\mathbb{R}^3$ with one being positive: the centre manifold is either diffeomorphic to (a) an annulus or (b) a Möbius strip; the respective orientation index is $O = 1$ or $O = -1$.

of the centre manifold is necessary in order to yield robustness under perturbations in η. Moreover, the centre manifold is locally invariant under the flow. Not only the homoclinic is contained in the centre manifold, but also all recurring solutions, that is, all solutions that are close to it for all times.

The space $E^{\mathrm{c}}(t)$ is the tangent bundle of the centre manifold along the homoclinic at $\eta = \eta_*$ and it is uniquely defined. Indeed, consider $W^{\mathrm{s,lu}}(x_0;\eta_*)$, the manifold whose tangent bundle is given by the stable and leading unstable eigendirection and $W^{\mathrm{ls,u}}(x_0;\eta_*)$ the manifold, whose tangent bundle is given by the leading stable and unstable eigendirection of the equilibrium. Then $E^{\mathrm{c}}(t)$ is the intersection of the tangent spaces of both manifolds. Note, that if the centre manifold exists, it is not necessarily uniquely defined. Moreover, the centre manifold is tangent to $E^{\mathrm{c}}(t)$ and since $E^{\mathrm{c}}(t) \longrightarrow E^{\mathrm{c}}_{x_0}$ for $|t| \longrightarrow \infty$, the centre manifold at $\eta = \eta_*$ is tangent to $E^{\mathrm{c}}_{x_0}$ at x_0, consisting of the leading stable and leading unstable eigendirection of x_0.

Suppose a homoclinic satisfies the nondegeneracy condition given in Hypothesis 2 (*1.*) and is neither in an orbit or inclination flip configuration (Hypothesis 4). Suppose that the corresponding equilibrium is of simple saddle-type (Hypothesis 3 (*2.*)), i.e. its linearization has two real leading eigenvalues. Then

$E^{\mathrm{c}}(t)$ satisfies Hypothesis 5, since it is a continuous vector bundle limiting to the eigenspace of $\partial_x f(h(t);\eta_*)$ corresponding to the leading eigenvalues. Therefore, a two-dimensional centre manifold exists. The centre manifold is either diffeomorphic to an annulus or a Möbius strip, depending on the orientation index O (3.5.1). A sketch of a two-dimensional centre manifold for the two possible orientations is depicted in Figure 3.7. In both situations of this example, note that at x_0, the centre manifold is tangent to the unstable eigendirection and the leading stable eigendirection of x_0.

The existence of a centre manifold can already reveal key information about the dynamics. For example, this can uncover the possible existence of so called N-homoclinics or N-periodic solutions. We understand by that solutions that pass N-times around the primary homoclinic or periodic solution. Analogously to the period-doubling bifurcation, the bifurcation of a 2-homoclinic is called homoclinic doubling and can be responsible for the existence of chaotic dynamics, see [GH83]. We associate with chaos the presence of shift dynamics in the Poincaré map. Especially, chaotic dynamics imply the existence of N-periodic solutions for each N in a tubular neighbourhood of the homoclinic.

An application for a two-dimensional centre manifold can be found in the so called resonant homoclinic orbit, examined in detail in [CDF90]. This treats the case of a homoclinic solution limiting to a simple saddle with vanishing saddle value σ and the unfolding of this configuration. Under the before-made non-degeneracy assumptions and disallowing orbit or inclination flip scenarios, the homoclinic possesses a two-dimensional centre manifold. Its existence immediately excludes the occurrence of N-homoclinics and N-periodic solutions with $N > 1$ in the orientable case and $N > 2$ in the non-orientable one. Therefore, looking at the dimension or topology of the centre manifold can help to exclude, a priori, certain solutions.

On the other side, in orientation-changing bifurcations, like the orbit flip or inclination flip bifurcations, the two-dimensional centre manifold itself bifurcates and switches between an annulus and a Möbius strip. This demands for a three-dimensional centre manifold in which the flip can be executed. This can induce the generation of N-homoclinics and shift dynamics. The unfolding of an orbit flip will be presented in Section 3.8.

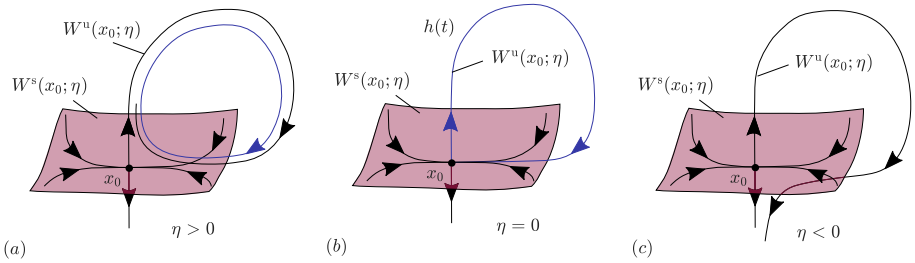

Figure 3.8: Birth of a periodic orbit in a homoclinic bifurcation. The sketch displays a saddle equilibrium x_0 with a one-dimensional unstable eigendirection and a two-dimensional stable manifold (red). (a) The unstable manifold splits above the stable manifold for $\eta > 0$ and the system possesses a stable periodic solution (blue). (b) The manifolds intersect and thus create a homoclinic connection (blue) for $\eta = 0$. (c) The unstable manifold splits below the stable manifold for $\eta < 0$. The homoclinic dissolves and there is also no periodic solution.

3.7 Bifurcation of periodic orbits from a homoclinic

Generic homoclinics appear in codimension-one bifurcations in which periodic solutions disappear by colliding with an equilibrium x_0 of saddle-type. The birth of periodic solutions from a homoclinic solution in a planar equation was studied in [ALGM73]. In particular, this topic has been scrutinized by Shilnikov for vector fields in $\mathbb{R}^n$, [Shi63; Shi68; SSTC01]. In this section, we discuss the birth of a periodic solution from a homoclinic connecting to an equilibrium x_0 under the various possible saddle-type configurations. In particular, we discuss the proof for the case, where the equilibrium x_0 is a tame saddle (Hypothesis 3 (*1.*)).

Figure 3.8 gives an idea of the bifurcation. Panel (a) displays a three-dimensional vector field with a periodic solution for a parameter $\eta > 0$. For $\eta \longrightarrow 0$, the periodic solution approaches the saddle equilibrium x_0 and thereby the corresponding period goes to infinity. At $\eta = 0$, see Panel (b), it collides with the saddle equilibrium x_0. The stable (red) and unstable manifold intersect and thereby create a homoclinic solution $h(t)$. For $\eta < 0$, see Panel (c),

the stable and unstable manifold split up again, leading to the break-up of the homoclinic structure and there are no periodic orbits in a small neighbourhood of the homoclinic loop. We want to give a summary of the proof based on [SSTC01] using so called *Shilnikov variables* in order to present a standard technique for the analysis of homoclinics. Another popular Ansatz is Lin's method [Lin90] based on a Lyapunov-Schmidt reduction.

Suppose the equation (3.1.1)

$$\dot{x}(t) = f(x(t), \eta),$$

with $f \in \mathcal{C}^1$, $x(t) \in \mathbb{R}^n$ and $\eta \in \mathbb{R}$, possesses a homoclinic solution $h(t)$ at parameter $\eta = 0$. The homoclinic approaches the equilibrium x_0 for $t \longrightarrow \pm\infty$. Without loss of generality, the equilibrium x_0 is at the origin for all η. We suppose that Hypotheses 1 and 3 (*1.*) are satisfied; so x_0 is of saddle-type and the leading unstable eigenvalue λ^{lu} is unique, real and simple and the saddle value $\sigma := \mathrm{Re}(\lambda^{\mathrm{ls}}) + \lambda^{\mathrm{lu}}$ (3.4.2) is negative, where λ^{ls} denotes the leading stable eigenvalue. Additionally, we assume that it has exactly one eigenvalue to the right of the imaginary axis, which is λ^{lu}. Moreover, we assume Hypothesis 2 is satisfied, i.e. the homoclinic unfolds generically with respect to the parameter η. The stable and unstable manifold $W^{\mathrm{s}}(x_0; \eta)$ and $W^{\mathrm{u}}(x_0; \eta)$ split for parameter values $\eta \neq 0$ and only intersect at $\eta = 0$. Without loss of generality, assume that the unstable manifold splits inward, i.e. above $W^{\mathrm{s}}(x_0; \eta)$ for $\eta > 0$ and outward, i.e. below $W^{\mathrm{s}}(x_0; \eta)$ for $\eta < 0$ (c.f. Figure 3.8).

The dynamics in a sufficiently small neighbourhood around the saddle x_0 can be described by

$$\begin{aligned} \dot{u}(t) &= a(\eta)u + r(u, w, \eta), \\ \dot{w}(t) &= \lambda(\eta)y + s(u, w, \eta), \end{aligned}$$

where $u(t) = (u_1, \ldots, u_{n-1})(t) \in \mathbb{R}^{n-1}, w(t) \in \mathbb{R}$. This is due to the Hartman-Grobman Theorem, see for example[SSTC98]. The functions r and s vanish at the origin, together with their first derivative with respect to (u, w). Hence the unstable manifold lies tangentially to the w-axis and the stable manifold to the u-coordinates at the origin 0. The eigenvalues of the matrix $a(\eta) \in \mathbb{R}^{(n-1)\times(n-1)}$ coincide with the stable eigenvalues of the linearization of x_0 at

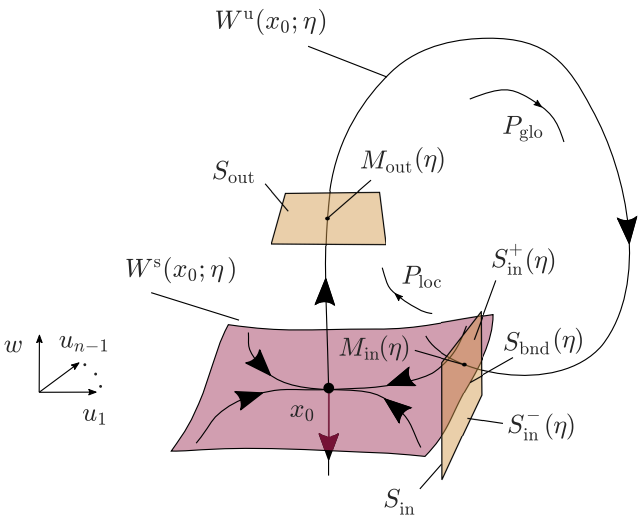

Figure 3.9: Schematic representation of the proof for the situation with $\eta < 0$: the unstable manifold $W^{\mathrm{u}}(x_0;\eta)$ of x_0 splits inward and the intersection with the cross-section S_{in} (yellow) in $M_{\mathrm{in}}(\eta)$ lies above the stable manifold $W^{\mathrm{s}}(x_0;\eta)$ (red).

$\eta = 0$ and are all assumed to have negative real parts. Similarly $\lambda(\eta)$ is real, positive and equal to λ^{lu} at $\eta = 0$.

Pick two points M_{in} and M_{out} on the homoclinic in a neighbourhood of x_0, such that M_{in} lies on $W^{\mathrm{s}}(x_0;0)$ and M_{out} on $W^{\mathrm{u}}(x_0;0)$. We construct two cross-sections, S_{in} and S_{out}, transverse to the homoclinic through, respectively, M_{in} and M_{out}. They can be chosen in a manner, such that $\dot{u}(t) \neq 0$ and also $\dot{u}_1(t) \neq 0$. The cross-section through M_{in} is then given by a planar area at $u_1 = \mathit{constant}$. On the other hand, the cross-section through M_{out} is chosen such that $w = \mathit{constant}$. This provides coordinates $(w^0, u^0) = (w, u_2, \ldots, u_{n-1})$ on S_{in} and $u^1 = (u_1, \ldots, u_{n-1})$ on S_{out}. Define now the local map from S_{in} to S_{out} as P_{loc} and the global map P_{glo} from S_{out} to S_{in}. The composition $P := P_{\mathrm{glo}} \circ P_{\mathrm{loc}}$ maps S_{in} onto itself. The trajectory starting from (w^0, u^0) intersects S_{out} in u^1. The negative saddle value implies that the linearized flow near the saddle contracts two-dimensional areas and the local map P_{loc}

is a contraction, see Lemma 13.2. in [SSTC01]. Furthermore, we gather from Section 6.2 in [SSTC98], that

$$\left\| \frac{\partial}{\partial(w^0, u^0)} P_{\mathrm{loc}}(w^0, u^0) \right\| \leq C e^{(\sigma+\epsilon)\tau},$$

for a flight time τ between corresponding points on the cross-sections, which can be considered to become larger the closer the corresponding trajectory comes to x_0. Moreover, the value ϵ is positive, small and depends on the distance of the cross-sections to the origin. Since the saddle quantity σ is smaller than zero, the map P_{loc} is strongly contracting. The map P_{glo} is a diffeomorphism from a small neighbourhood M_{in} into a small neighbourhood of M_{out} and has hence a bounded derivative. Thus, $P = P_{\mathrm{glo}} \circ P_{\mathrm{loc}}$, which is the Poincaré map, is strongly contracting as well.

The intersection of the stable manifold with the cross-section S_{in} subdivides S_{in} into an upper part S_{in}^+ and lower part S_{in}^-. Trajectories beginning at S_{in}^- leave the neighbourhood of the homoclinic close to the origin and never intersect with S_{out}. Note, that the flight time τ is infinite for points on the boundary $S_{\mathrm{bnd}} = W^{\mathrm{s}}(x_0; 0) \cap S_{\mathrm{in}}$. Still, due to continuity, an image on S_{in} can be defined. Choose a point $M \in S_{\mathrm{in}}^+$. Its image under P_{loc} lies in S_{out} per definiton. As M approaches the boundary $S_{\mathrm{bnd}} = W^{\mathrm{s}}(x_0; 0) \cap S_{\mathrm{in}}$, its image $P_{\mathrm{loc}}(M)$ tends to M_{out}. By continuity, we can hence define

$$P(S_{\mathrm{bnd}}) = M_{\mathrm{in}} = P_{\mathrm{glo}}(M_{\mathrm{out}}).$$

These points can be also defined for varying parameters and thereby, this also holds for small $\eta \neq 0$. Note that the coordinates are chosen such that the saddle and the sections S_{in}, S_{out} are independent of small parameter variations. In contrast to that, the stable and unstable manifold are not and hence the subsections S_{bnd} vary with η. However, this doesn't change the result. Due to our assumption of the splitting of the homoclinic for parameters $\eta \neq 0$, it is then

$$M_{\mathrm{in}}(\eta) \in \begin{cases} S_{\mathrm{in}}^+(\eta) & \text{if } \eta > 0, \\ S_{\mathrm{bnd}}(\eta) & \text{if } \eta = 0, \\ S_{\mathrm{in}}^-(\eta) & \text{if } \eta < 0. \end{cases}$$

Figure 3.9 gives an overview of the situation for $\eta > 0$. The system possesses periodic solutions if and only if the map P has fixed points. We want to show that if $M_{\text{in}}(\eta) \in S^+_{\text{in}}$, then P has a fixed point. To this end, we consider the following Lemma. The proof can be reviewed in [SSTC01].

Lemma 3 (see [SSTC01] Lemma 13.4)**.** *Let V be a closed convex set in $\mathbb{R}^{n-1}$ and U be a closed subset of V. Let P be a contracting map $P : U \to V$. Assume also that the boundary ∂U of U in V is mapped by T into a single point M^+. Then, if $M_{\text{in}} \in U$, the map has a unique fixed point M^* in U, which is the limit of the iterations of M_{in} by P. All trajectories which do not enter $V \setminus U$ tend to the fixed point in U. On the contrary, if $M_{\text{in}} \in V \setminus U$, then there is no fixed point in U; moreover any orbit leaves U after a finite number of iterations of the map.*

Taking now $V = S_{\text{in}}$, $U = S^+_{\text{in}}$ with $\partial U = S_{\text{bnd}}$ and $V \setminus U = S^-_{\text{in}}$ immediately gives us the desired result.

Remark 1. *In the case of x_0 being a wild saddle focus (Hypothesis 3 (3.)), i.e. x_0 is of saddle focus type with saddle value σ (3.4.2) being positive, the map P is no longer a contraction. In particular, it contains infinitely many horseshoes. This leads to the coexistence of infinitely many periodic solutions with the homoclinic. This is also discussed in detail in [SSTC01].*

We give now the results for the different possible saddle configurations. The proofs can be found in the corresponding literature, see [HS10; SSTC01] and references therein. Note, that for the respective proofs, different kinds of differentiability of the vector fields are required. The cases of a tame saddle and double focus require $f \in \mathcal{C}^1$, whereas the proof for a wild saddle equilibrium demands for $f \in \mathcal{C}^2$.

Theorem 2 (Homoclinic bifurcation with tame saddle, see [HS10] Theorem 5.1)**.** *Suppose the system (3.1.1) has a homoclinic solution $h(t)$ to x_0 at $\eta = \eta_*$. Assume the non-degeneracy condition Hypothesis 2 for $h(t)$ is met.*

Suppose that the equilibrium x_0 is a tame saddle (Hypothesis 3 (1.)): The unique leading unstable eigenvalue λ^{lu} is real and simple and the saddle value σ (3.4.2) is negative, i.e. $\sigma = \text{Re}(\lambda^{\text{ls}}) + \lambda^{\text{lu}} < 0$.

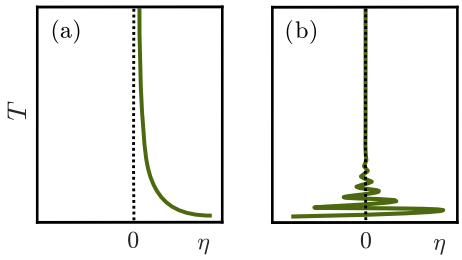

Figure 3.10: Periodic solutions with periods T bifurcating from a homoclinic solution at $\eta = 0$ in the case of (a) a tame saddle or (b) wild saddle focus or double focus.

Then a unique periodic solution $x_*(t;\eta)$ bifurcates from the homoclinic orbit; this periodic solution is hyperbolic and it bifurcates either for $\eta > 0$ or for $\eta < 0$, and $x_*(t,\eta)$ converges to $h(t)$ as $\eta \longrightarrow 0$ for each fixed t. Furthermore, $\dim W^s(x_*;\eta) = \dim W^s(x_0;\eta) + 1$.

In particular, if $\dim W^u(x_0;\eta) = 1$, this immediately implies the creation of a stable periodic solution for $\eta < 0$. Furthermore, for $\eta \longrightarrow 0$ the period of $x_*(t;\eta)$ goes to infinity. The periodic solution vanishes then at $\eta = 0$ by creating a homoclinic solution. Hence, we can think of a homoclinic solution as a periodic solution with an infinite period. Beyond that, the condition $|\mathrm{Re}(\lambda^{ls})| > \lambda^{lu}$ implies that the periodic solution approaches the homoclinic solution for $\eta \longrightarrow 0$ from one side. This is sketched in Figure 3.10, Panel (a). In particular, the negative saddle quantity implies that the dynamics near the saddle are area contracting, which in the end, delivers us the single periodic solution. Recall, that by reversing the time, one can also apply the theorem on equilibria with two complex conjugate leading unstable and one real leading stable eigenvalue, if it also has a positive saddle value. Consequently, the statement on the dimension of the stable manifold of the periodic solution is then made for the dimension of the unstable manifold. Especially, this implies the emergence of a family of periodic solutions from a homoclinic to a saddle of simple saddle-type (Hypothesis 3 (*2.*)), where both leading stable and unstable eigenvalues are real.

In the next theorem, we discuss the case of the saddle focus with a positive saddle value and a double focus equilibrium. In this case, the real leading eigenvalue dominates the complex conjugate leading eigenvalues. This leads to the occurrence of infinitely many periodic orbits of saddle-type arbitrarily close to the homoclinic, [Shi65]. This is visualized in Panel (b) of Figure 3.10. In particular, these periodic orbits are organized into infinitely many hyperbolic suspended horseshoes which accumulate onto the homoclinic, [Shi70]. Moreover, the unfolding of the homoclinic with positive saddle value leads to the existence of N-homoclinics, [Gas83; Gas84]. Hence, the case of a wild saddle focus or double focus leads to the presence of chaos.

Theorem 3 (Homoclinic bifurcation with wild saddle or double focus, see [HS10] Theorem 5.4)**.** *Suppose the system* (3.1.1) *has a homoclinic solution* $h(t)$ *to* x_0 *at* $\eta = \eta_*$*. Assume the non-degeneracy condition Hypothesis 2 for* $h(t)$ *is met. Further assume that the homoclinic is neither in an inclination flip nor orbit flip configuration (Hypothesis 4).*

Suppose that the equilibrium x_0 *satisfies one of the following conditions:*

1. (wild saddle) *(Hypothesis 3 (3.)): The leading unstable eigenvalue is unique, real and simple. There are precisely two leading stable eigenvalues* λ^{ls} *and* $\overline{\lambda^{\mathrm{ls}}}$*, and these are complex and simple. Additionally, the saddle value* (3.4.2) *is positive, i.e.* $\sigma = \mathrm{Re}(\lambda^{\mathrm{ls}}) + \lambda^{\mathrm{lu}} > 0$.

2. (double focus) *(Hypothesis 3 (4.)): The leading stable and unstable eigenvalues are unique (up to complex conjugation) and simple.*

Then, in an arbitrarily small neighbourhood of the homoclinic, there exist infinitely many saddle periodic orbits. At $\eta = 0$*, there are infinitely many suspended Smale horseshoes in each neighbourhood of the homoclinic solution. Furthermore, for each natural* $N > 0$*,* N*-homoclinic orbits exist for infinitely many parameter values which accumulate onto* $\eta = 0$ *from one side, say for* $\eta > 0$.

3.8 Homoclinic orbit flip

In Section 3.5, we discussed the so called orbit flip configuration. We have seen that in an orbit flip, the homoclinic orbit approaches the equilibrium along the strong stable or strong unstable eigendirection. In the following section, we examine the codimension-two bifurcation induced by the unfolding of a homoclinic in an orbit flip configuration. A detailed analysis of the results can be found in [San93].

In an orbit flip bifurcation, the orientation of the two-dimensional centre manifold changes its orientation, calling for a three-dimensional centre manifold in which the actual flip takes place. Recollecting Figure 3.7, it switches from orientable to non-orientable by passing through the orbit flip configuration. Another orientation-changing bifurcation is induced by the inclination flip. The orbit flip and inclination flip share the same bifurcation diagrams, although their prerequisites are different.

Again, suppose that the system (3.1.1) has a homoclinic solution to a saddle equilibrium x_0 at $\eta = \eta_*$. Since the unfolding of a generic homoclinic is of codimension-one, for the unfolding of the orbit flip a second parameter is necessary. That is, we need to consider here $\eta = (\eta_1, \eta_2) \in \mathbb{R}^2$. We suppose that Hypothesis 3 (*2.*) is satisfied, such that the leading eigenvalues of the matrix $\frac{\partial}{\partial x} f(x_0, \eta_*)$ are real and simple. Recall the definitons of the vectors ν^{s}, ν^{u}, ν^{s}_* and ν^{u}_* from Section 3.5 indicating the possible flip configurations of the homoclinic. We will examine an orbit-flip configuration within the stable manifold $W^{\mathrm{s}}(x_0; \eta)$.

Hypothesis 6 (Non-degenerate Orbit-Flip, see [HS10] Hypothesis 5.10)**.** *The stable manifold is in an orbit flip configuration, i.e.* $\nu^{\mathrm{s}}(\eta_*) = 0$*, while* ν^{u}*,* ν^{s}_**,* $\nu^{\mathrm{u}}_* \neq 0$ *at* $\eta = \eta_*$*. Additionally, it is* $\partial_{\eta_2} \nu^{\mathrm{s}}(\eta_*) \neq 0$*.*

Recall the strong stable eigenvalue λ^{ss} denoting the largest real part of the stable eigenvalues that lie strictly to the left of the leading stable eigenvalue λ^{ls}. Then we define the values

$$\alpha := -\frac{\lambda^{\mathrm{ss}}}{\lambda^{\mathrm{lu}}}, \quad \text{and} \quad \beta := -\frac{\lambda^{\mathrm{ls}}}{\lambda^{\mathrm{lu}}}.$$

Per definition, it is $\alpha > \beta > 0$. The value β is also known as *saddle quantity* and is equally used in the analysis of homoclinics instead of the saddle value σ (3.4.2). The unfolding can be categorized into three different cases:

$$\begin{aligned} &\text{Type A}: \ \beta > 1, \\ &\text{Type B}: \ \beta < 1 \text{ and } \alpha > 1, \\ &\text{Type C}: \ \alpha < 1. \end{aligned}$$

If the eigenvalues are of Type C, we need the following additional genericity assumption.

Hypothesis 7 (Nondegeneracy Condition for Type C, see [HS10] Hypothesis 5.11)**.** *The strong stable eigenvalue λ^{ss} giving the largest real part of the stable eigenvalues of $\frac{\partial}{\partial x} f(x_0, \eta_*)$, is also a unique, simple and real eigenvalue of $\frac{\partial}{\partial x} f(x_0, \eta_*)$, and the homoclinic orbit $h(t)$ satisfies $\lim_{t \longrightarrow \infty} e^{-\lambda^{ss} t} h(t) \neq 0$.*

For orbit flips of Type A the dynamics are simple: There is a curve of homoclinics in the parameter plane $(\eta_1, \eta_2) \in \mathbb{R}^2$. When moving across the curve, a single periodic orbit is created, cf. Theorem 2 of Section 3.7. In contrast to that, the dynamics in the case of Type B or C orbit flips are more complex.

Theorem 4 (Orbit flip Type B, see [HS10] Theorem 5.18)**.** *Assume that the nondegeneracy condition Hypothesis 2, is satisfied. Suppose further that x_0 is a simple saddle (Hypothesis 3 (2.)). Let the stable manifold be in an orbit flip configuration, such that Hypothesis 6 is satisfied.*

If the orbit-flip is of Type B, then the bifurcation diagram is as shown in Figure 3.11 with one-sided curves of saddle-node and period-doubling bifurcations of periodic orbits and a one-sided curve of 2-homoclinic orbits that emerge from the orbit-flip point at $\eta = \eta_*$ on the branch of primary homoclinic orbits.

Theorem 5 (Orbit flip Type C, see [HS10] Theorem 5.19)**.** *Assume that the nondegeneracy condition Hypothesis 2, is satisfied. Suppose further that x_0 is a simple saddle (Hypothesis 3 (2.)). Let the stable manifold be in an orbit flip configuration, such that Hypothesis 6 is satisfied.*

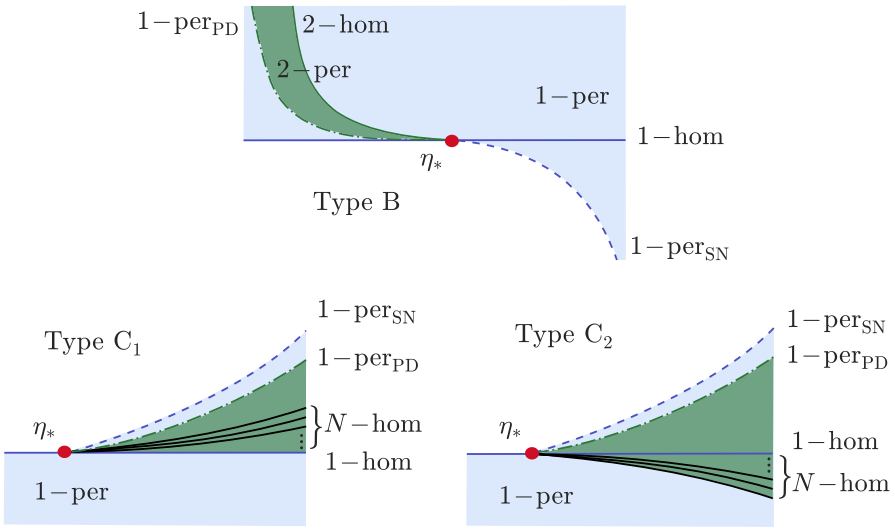

Figure 3.11: Unfolding of orbit flip bifurcation of Type B and C in the parameter plane $\eta \in \mathbb{R}^2$. Curve of 1-homoclinics (blue) together with stability region of periodic solutions (blue). At the flip point at $\eta = \eta_*$, further bifurcation curves of codimension-one emerge, leading to stable 2-periodic solutions (green area) and 2-homoclinics (Type B) and N-periodic solutions and N-homoclinics with $N > 1$ (Type C).

If the orbit flip is of Type C and Hypothesis 7 is met, then the bifurcation diagram is given by one of the two cases shown in Figure 3.11 with one-sided curves of saddle-node and period-doubling bifurcations of periodic orbits. The two cases differ by a global condition on the stable and unstable manifolds. In particular, infinitely many one-sided curves of N-homoclinic orbits emerge for each $N \geq 2$ from the orbit flip point at $\eta = \eta_*$ on the branch of primary homoclinic orbits.

In particular, in an open neighbourhood in parameter space of the unfolding

of Type C orbit flips, one can also find shift dynamics.

3.9 Degenerate homoclinc orbits

We will now discuss a bifurcation induced by a violation of the nondegeneracy condition in Hypothesis 2. The bifurcation is induced, if the intersection of the tangent spaces of the stable and unstable manifolds $W^{\mathrm{s}}(x_0;\eta_*)$ and $W^{\mathrm{u}}(x_0;\eta_*)$ along the homoclinic orbit $h(t)$ is a manifold of dimension more than one. Suppose that the intersection of $T_{h(0)}W^{\mathrm{s}}(x_0;\eta_*)\cap T_{h(0)}W^{\mathrm{s}}(x_0;\eta_*)$ is two-dimensional. This leads to a bifurcation of codimension-three, studied by [Van92].

To this end, we consider the system (3.1.1) with $x(t)\in\mathbb{R}^n$, where $n\geq 4$ and $\eta\in\mathbb{R}^3$. Suppose it possesses a homoclinic solution $h(t)$ to a saddle equilibrium x_0 at $\eta=\eta_*$.

Hypothesis 8 (Degenerate homoclinic orbit, see [HS10] Hypothesis 5.13)**.** *Assume that the intersection $T_{h(0)}W^{\mathrm{s}}(x_0;\eta_*)\cap T_{h(0)}W^{\mathrm{s}}(x_0;\eta_*)$ is two-dimensional and that the stable and unstable manifolds $W^{\mathrm{s}}(x_0;\eta_*)$ and $W^{\mathrm{u}}(x_0;\eta_*)$ of x_0 for $\dot{x}=f(x,\eta)$ intersect transversally along $h\times\{\eta_*\}$ in the product $\mathbb{R}^n\times\mathbb{R}^3$ of state and parameter space.*

This results in the following theorem.

Theorem 6 (see [HS10] Theorem 5.23)**.** *Suppose that $h(t)$ is a homoclinic solution to the hyperbolic equilibrium x_0 and assume that Hypothesis 8 is met, then the set of parameter values for which a single-round homoclinic orbit exists forms a Whitney umbrella in parameter space.*

Consider a degenerate homoclinic orbit $h(t)$ in $\mathbb{R}^4$ to saddle equilibrium that has a stable and unstable manifold of both dimension two. Choose a point $h(t)$ at $t=0$ and take a cross-section S. The stable and unstable manifold intersect the cross-section then along curves denoted with $W^{\mathrm{s}}_S(x_0;\eta)$ and $W^{\mathrm{u}}_S(x_0;\eta)$. If Hypothesis 8 is met, these curves then intersect at $\eta=\eta_*$ in a point. In particular, the curves intersect with a quadratic tangency, that is the intersection

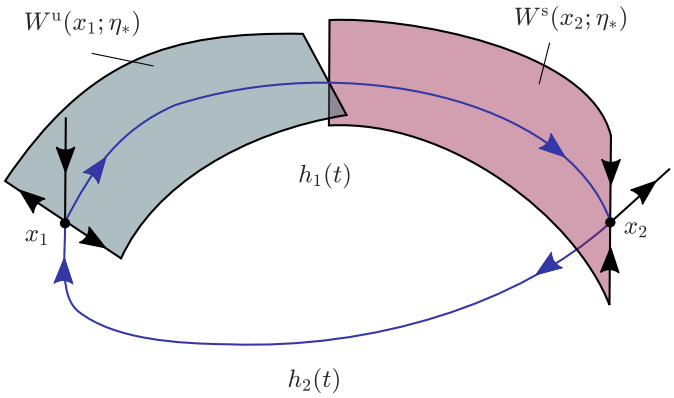

Figure 3.12: Schematic representation of a heteroclinic cycle corresponding to a Bykov T-point in $\mathbb{R}^3$.

is not transversal. Then, the set of parameters in $\mathbb{R}^3$ for which $W^{\mathrm{s}}_S(x_0;\eta)$ and $W^{\mathrm{u}}_S(x_0;\eta)$ intersect forms a Whitney umbrella.

3.10 Bykov T-points

In this section, we discuss the unfolding of a *Bykov T-point*. This is a bifurcation of codimension-two in which a heteroclinic cycle is generated, when a homoclinic connecting to a saddle equilibrium collides with an additional saddle. It was coined by Bykov [Byk93] and has further been studied in [GS84; GS86; KLW14]. A detailed discussion of heteroclinic cycles and their genericity conditions can be found in Section 2.3. of [HS10].

We consider system (3.1.1) with $x(t) \in \mathbb{R}^3$ and $\eta \in \mathbb{R}^2$ and let x_j, $j = 1, 2$, be two hyperbolic equilibria of this system for all η. We discuss the unfolding of a heteroclinic cycle consisting of two heteroclinic orbits h_1 and h_2 connecting

equilibria x_1 and x_2, such that

$$\lim_{t\longrightarrow-\infty} h_j(t) = x_j \quad \text{and} \quad \lim_{t\longrightarrow\infty} h_j(t) = x_{(j+1) \bmod 2},$$

for $j = 1, 2$. We assume that x_1 and x_2 are of saddle-type (Hypothesis 1). Then similarly to homoclinic orbits, the heteroclinic orbits h_1 and h_2 satisfy $h_j(t) \in W^{\mathrm{u}}(x_j;\eta_*) \cap W^{\mathrm{s}}(x_{(j+1) \bmod 2};\eta_*)$ for $j = 1, 2$. Although they can generically appear as robust codimension-zero objects, in order to create a heteroclinic solution one usually needs to adjust a sufficient number of parameters. To this end, consider the *Morse index* of an equilibrium x_j, which is defined as

$$\operatorname{ind}(x_j) := \dim W^{\mathrm{u}}(x_j;\eta).$$

In general, the equilibria do not share the same Morse index. Suppose that $\operatorname{ind}(x_j) > \operatorname{ind}(x_{(j+1) \bmod 2})$ for $j = 1$ or 2, then the intersections of the manifolds $W^{\mathrm{u}}(x_j;\eta)$ and $W^{\mathrm{s}}(x_{(j+1) \bmod 2};\eta)$, which are assumed to be transversal, form a manifold of dimension $\operatorname{ind}(x_j) - \operatorname{ind}(x_{(j+1) \bmod 2})$. If instead $\operatorname{ind}(x_j) - 1 \leq \operatorname{ind}(x_{(j+1) \bmod 2})$, then the codimension of the heteroclinic h_j is equal to $\operatorname{ind}(x_{(j+1) \bmod 2}) - \operatorname{ind}(x_j) + 1$.

T-points are heteroclinic cycles that generically involve saddles of different Morse indices. They are generated in homoclinic bifurcations of codimension-two. We will make the following assumption on the spectrum of the equilibria.

Hypothesis 9 (Saddle condition for T-points, see [HS10] Hypothesis 5.20)**.** *The linearization* $\frac{\partial}{\partial x} f(x_1, \eta_*)$ *has simple eigenvalues* $\lambda_1^{\mathrm{s}}, \lambda_1^{\mathrm{u}}, \tilde{\lambda}_1^{\mathrm{u}}$ *with* $\lambda_1^{\mathrm{s}} < 0 < \operatorname{Re}(\lambda_1^{\mathrm{u}}) \leq \operatorname{Re}(\tilde{\lambda}_1^{\mathrm{u}})$*, while the linearization* $\frac{\partial}{\partial x} f(x_2, \eta_*)$ *has simple eigenvalues* $\tilde{\lambda}_2^{\mathrm{s}}, \lambda_2^{\mathrm{s}}, \lambda_2^{\mathrm{u}}$ *with* $\operatorname{Re}(\tilde{\lambda}_2^{\mathrm{s}}) \leq \operatorname{Re}(\lambda_2^{\mathrm{s}}) < 0 < \lambda_2^{\mathrm{u}}$*. We assume that the saddle quantities*

$$\sigma_1 := -\frac{\operatorname{Re}(\lambda_1^{\mathrm{u}})}{\lambda_1^{\mathrm{s}}} \quad \text{and} \quad \sigma_2 := -\frac{\lambda_2^{\mathrm{u}}}{\operatorname{Re}(\lambda_2^{\mathrm{s}})}$$

satisfy $\sigma_j \neq 1$*, for* $j = 1, 2$.

The manifolds $W^{\mathrm{s}}(x_1;\eta)$ and $W^{\mathrm{u}}(x_2;\eta)$ are then one-dimensional, while $W^{\mathrm{u}}(x_1;\eta)$ and $W^{\mathrm{s}}(x_2;\eta)$ are two-dimensional. Suppose that the system (3.1.1) possesses a heteroclinic cycle at $\eta = \eta_*$ that consists of a heteroclinic orbit

$h_1(t) \in W^{\mathrm{u}}(x_1;\eta_*) \cap W^{\mathrm{s}}(x_2;\eta_*)$ of codimension-zero and a heteroclinic $h_2(t) \in W^{\mathrm{u}}(x_2;\eta_*) \cap W^{\mathrm{s}}(x_1;\eta_*)$ of codimension-two, see Figure 3.12. In order to provide for a generic unfolding of the heteroclinic cycle, there are several assumptions necessary, which are similar to the nondegeneracy assumptions of homoclinics. They cover a generic unfolding of the stable and unstable manifolds and exclude inclination and orbit flip configurations. For this reason, we will not discuss them here, but they can be gathered from [HS10], Section 2.3.

Hypothesis 10 (Genericity conditions for T-points, see [HS10] Hypothesis 5.21)**.** *We assume the following:*

1. *The heteroclinic orbit $h_1(t) \cap W^{\mathrm{u}}(x_1;\eta_*) \cap W^{\mathrm{s}}(x_2;\eta_*)$ is of codimension-zero, while the orbit $h_2(t) \in W^{\mathrm{u}}(x_2;\eta_*) \cap W^{\mathrm{s}}(x_1;\eta_*)$ is of codimension-two. Furthermore, the manifolds unfold generically with respect to the parameter $\eta = (\eta_1, \eta_2) \in \mathbb{R}^2$.*

2. *Neither h_1 nor h_2 are in an orbit-flip configuration.*

3. *If the eigenvalues of x_1 and x_2 are all real, we assume, in addition, that the heteroclinic cycle is not in an inclination-flip configuration: more precisely, we assume that the closure of $W^{\mathrm{s}}(x_2;\eta_*)$ is homeomorphic to a cylinder ($O := 1$) or to a Möbius strip ($O := -1$); in this case, the closure of $W^{\mathrm{u}}(x_1;\eta_*)$ is also homeomorphic to a cylinder if $O = 1$, and to a Möbius strip if $O = -1$.*

If all eigenvalues of the equilibria x_1 and x_2 are real, we obtain the following scenario, examined by Bykov in [Byk93], giving the eponymous bifurcation:

Theorem 7 (Bykov T-point with simple saddles, see [HS10] Theorem 5.31)**.** *Assume that Hypotheses 9 and 10 are met. If the eigenvalues of both equilibria x_1 and x_2 are all real, then the bifurcation diagrams near $\eta = \eta_*$ are as shown in Figure 3.13.*

In particular, two curves of 1-homoclinic orbits connecting to, respectively, x_1 and x_2 emerge from the T-point at $\eta = \eta_*$. On the other hand, if one of the equilibria is a saddle focus, cf. [Byk93; GS84; GS86], the situation is leading to complex dynamics:

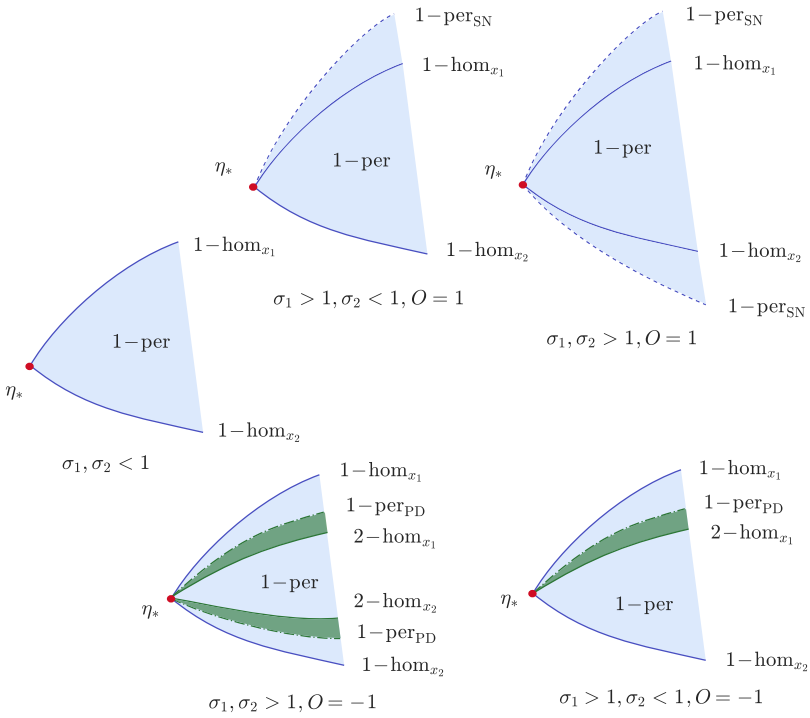

Figure 3.13: Unfolding of a Bykov T-point (red) at $\eta = \eta_*$ in the parameter plane, that consists of a heteroclinic cycle connecting to two simple saddle equilibria x_1 and x_2. From the T-point further codimension-one bifurcation curves emerge, depending on the saddle quantities defined in Hyp. 9 of the respective saddle equilibria and the orientations O given in Hyp. 10.

Theorem 8 (Bykov T-point with one saddle focus, see [HS10] Theorem 5.32)**.** *Assume that Hypotheses 9 and 10 (1.)–(2.) are met. Assume furthermore that the eigenvalues of x_2 are real, while x_1 is a saddle focus so that* $\mathrm{Im}(\lambda_1^{\mathrm{u}}) = -\mathrm{Im}(\tilde{\lambda}_1^{\mathrm{u}}) > 0$. *The bifurcation diagram of heteroclinic orbits and 1-homoclinic orbits is shown in Figure 3.14 (Panel (a)). In addition, for each η close to zero, there are infinitely many hyperbolic periodic orbits near the heteroclinic cycle and the dynamics contain a shift of two symbols.*

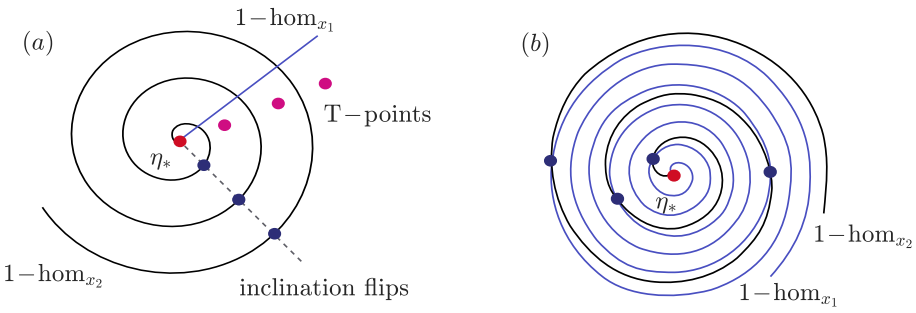

Figure 3.14: Some bifurcation curves in the parameter plane $\eta \in \mathbb{R}^2$ arising in the unfolding of a Bykov T-point (red) at $\eta = \eta_*$. Panel (a) shows the case when one equilibrium x_1 is of saddle focus type while the second, x_2, is a simple saddle. Panel (b) shows the case when both equilibria are either a saddle focus or double focus. Together with the curves of 1-homoclinics to x_1 and x_2, there are further T-points and inclination flips accumulating to $\eta = \eta_*$.

Also in this case, two curves of 1-homoclinic orbits connecting to, respectively, x_1 and x_2 emerge from the T-point at $\eta = \eta_*$. However, the curve of 1-homoclinics to x_2 forms a spiral.

Finally, we consider the situation where both x_1 and x_2 are foci, see also [Byk00; Byk99]. In the case of two saddle foci, the two curves of 1-homoclinic orbits, connecting respectively to x_1 and x_2, emerging from the T-point at $\eta = \eta_*$, spiral into the centre $\eta = \eta_*$ and we have the following:

Theorem 9 (Bykov T-point with two saddle or double foci, full theorem see [HS10] Theorem 5.33)**.** *Assume that Hypotheses 9 and 10 (1.-2.) are met. Assume that the unstable eigenvalues of x_1 and the stable eigenvalues of x_2 have non-vanishing imaginary parts. Under further assumptions, the following is true:*

First, the manifolds $W^{\mathrm{u}}(x_1;\eta_*)$ and $W^{\mathrm{s}}(x_2;\eta_*)$ intersect transversely at infinitely many different heteroclinic orbits. Second, the bifurcation diagram of 1-homoclinic orbits is as shown in Figure 3.14 (Panel (b)): in particular, there exists an infinite sequence of parameter values that accumulate at $\eta = \eta_*$, so that (3.1.1) *has a pair of coexisting homoclinic orbits to x_1 and x_2.*

Recall, that homoclinics to saddle-focus or double-focus type equilibria, can induce extremely complicated structures. In their neighbourhood in phase space and for nearby parameter values, they can give rise to chaotic motion, including N-periodic orbits and N-homoclinic orbits, see [GS84; SSTC01] or Sections 3.7. Accordingly, also the unfolding of Bykov T-points involving equilibria of saddle-focus or double-focus type can induce infinitely many secondary T-points involving infinitely many N-homoclinics for all $N \in \mathbb{N}$.

We have now reviewed certain genericity conditions of homoclinics in finite-dimensional vector fields and bifurcations induced by their violations. In particular, we have convinced ourselves that homoclinic solutions are always accompanied by a family of periodic solutions with large periods in a parameter neighbourhood of the homoclinic. Note, that these solutions are the ones that are the objects of interest for our further analysis of temporal dissipative solitons in DDE systems. In the following chapters, we will present the results of our research. Especially, we will show, how we can effectively analyse temporal dissipative solitons in the context of homoclinic bifurcation theory and gain substantial information on their dynamics and bifurcations.

CHAPTER 4

Theoretical analysis of temporal dissipative solitons as homoclinic solutions

In this chapter, we suggest a mathematical description of temporal dissipative solitons, aiming to verify analytically the relation to homoclinic solutions in the profile equation. In order to extend the existing theory to specific other localized solutions, like alternating pulse solutions, we then derive a novel equation with an innate symmetry, in which also these solutions can be identified with homoclinic orbits. Additionally, we analyse the Floquet problem for a critical multiplier corresponding to the period-doubling bifurcation and analyse its reappearance in the newly derived system. Furthermore, we develop a method to facilitate the numerical continuation of the period-doubling phenomenon. Beyond that, we present a system generalizing the newly introduced framework and providing a reappearance of general resonant Floquet multipliers. Lastly, we show how in the newly derived system for alternating pulse solutions, also square wave solutions can be identified with connecting orbits, thereby allowing an investigation of these localized states using homoclinic bifurcation theory.

4.1 Analytical definiton of temporal dissipative solitons

In this section, we suggest an analytical definition supplementary to the phenomenological introduction of temporal dissipative solitons in Chapter 2, in order to create a mathematical foundation for the existing theory.

To this end, we consider the general delay differential equation

$$\dot{x}(t) = f\left(x(t), x(t-\tau), \eta\right), \; x(t) \in \mathbb{R}^n, \tag{4.1.1}$$

where $f \in \mathcal{C}^1(\mathbb{R}^n \times \mathbb{R}^n \times \mathbb{R}, \mathbb{R}^n)$ and the delay τ is assumed to be large. For now, we assume the parameter $\eta \in \mathbb{R}$ to be fixed. Recall, that TDSs are a family of periodic solutions of (4.1.1) for all large enough delays τ, that spend most of the time near a stable background equilibrium x_0, thus exhibiting temporal localization. We will now formalize the basic characteristics of TDSs for our further analysis in the following way.

Definition 3 (Temporal dissipative solitons (TDS))**.** *Suppose the system* (4.1.1) *possesses an equilibrium x_0 that is stable for all nonnegative delays and a* 1*-parameter family of periodic solutions $x_*(t;\tau)$ for all $\tau > \tau_0 > 0$. Let $T(\tau)$ denote the minimal period of $x_*(t;\tau)$ and $T(\tau) > \tau$. Let the periodic solutions $x_*(t;\tau)$ be defined and uniformly bounded on $[-T(\tau)/2, T(\tau)/2]$. Define the* response time *as*

$$\delta(\tau) := T(\tau) - \tau. \tag{4.1.2}$$

Suppose δ is finite, positive and for $\tau, T \longrightarrow \infty$ it has a limit denoted with δ_∞.

Then the family of periodic solutions $x_*(t;\tau)$ are TDSs, if for all $\epsilon > 0$, there is a minimal delay $\tau_{\min}(\epsilon) > \tau_0$, an interval $I(\epsilon) := [t_1(\epsilon), t_2(\epsilon)] \subseteq [-T(\tau_{\min})/2, T(\tau_{\min})/2]$ with $t_1(\epsilon), t_2(\epsilon) \in \mathcal{O}(\log(\epsilon))$ and appropriate phase shifts $0 < s(\tau) < T(\tau)$, such that all periodic solutions $x_*(t;\tau)$ with $\tau > \tau_{\min}$ satisfy

$$||x_*(t + s(\tau);\tau) - x_0|| < \epsilon \text{ for all } t \notin I(\epsilon). \tag{4.1.3}$$

Additionally, it exists a $\zeta > 0$ and $\hat{t} \in I(\epsilon)$ such that all periodic solutions $x_*(t;\tau)$ with $\tau > \tau_{\min}$ satisfy

$$||x_*(\hat{t} + s(\tau);\tau) - x_0|| > \zeta. \tag{4.1.4}$$

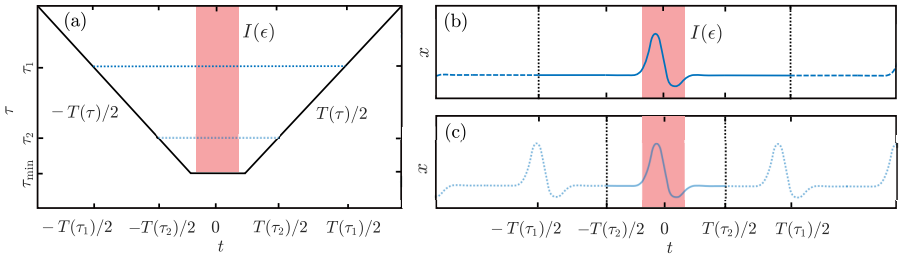

Figure 4.1: Sketch of Definition 3 of TDSs for an $\epsilon > 0$. The time interval $I(\epsilon)$ is displayed in red. Panel (a): domain of the family of TDSs for all $\tau > \tau_{\min}$. Panels (b) and (c): profiles of a soliton for two selected delay values τ_1 (dark blue), τ_2 (light blue) with respective periods $T(\tau_1)$, $T(\tau_2)$.

Note, that with $||\cdot||$ we measure the euclidean distance of the soliton $x_*(t,\tau)$ to the background equilibrium x_0 at time t in the system variables. In the infinite-dimensional phase space of the DDE system consisting of functions in $\mathcal{C}^0([-\tau,0],\mathbb{R}^n)$, the soliton never comes close to the background, as there is always a pulse contained in the history interval. Furthermore, recall, that an equilibrium that is stable for all $\tau \geq 0$ is referred to as *absolutely stable*, see Definition 1.

Figure 4.1 gives a motivation for Definiton 3 of TDSs. Let $x_*(t;\tau)$ be a family of solitons with corresponding periods $T(\tau)$. In Panel (a), we see the domain $[-T(\tau)/2, T(\tau)/2] \subset \mathbb{R}$ of the solitons in a diagram displaying the time t plotted versus the delay τ. For an $\epsilon > 0$, it indicates the minimal delay $\tau_{\min}$ and the time interval $I(\epsilon)$ (red), such that for all $\tau > \tau_{\min}$ the family of TDSs $x_*(t;\tau)$ satisfies the inequality (4.1.3) for all $t \notin I(\epsilon)$. In Panels (b) and (c), there are the profiles of periodic solutions belonging to the family of TDS, respectively, for delays τ_1 and τ_2 with $\tau_1 > \tau_2 > \tau_{\min}$. The periodic solutions are all supposed to be shifted using their corresponding phase shifts $s(\tau)$ such that the localization occurs during the same time interval $I(\epsilon)$. In Panel (a), the domains that belong to the solutions in Panels (b) and (c) are indicated with dotted lines of the corresponding colours. The set $I(\epsilon)$ gives the time interval where the soliton lies outside the ϵ-neighbourhood of the background x_0 and only takes up a small fraction of the whole domain for large delays in

which the pulse occurs. The length of the pulse remains constant maintaining its shape and only the time spent near the background increases. Indeed, since for $0 < \tilde{\epsilon} < \epsilon$, it is $I(\epsilon) \subset I(\tilde{\epsilon})$, the condition $t_1, t_2 \in \mathcal{O}(\log(\epsilon))$ for t_1, t_2, such that $I(\epsilon) := [t_1(\epsilon), t_2(\epsilon)]$, ensures the following: For decreasing ϵ, leading to an increase in the minimal delay $\tau_{\min}$, the interval $I(\epsilon)$ increases much slower than $T(\tau_{\min})$. It enables a temporal localization, such that outside of $I(\epsilon)$ the solitons decay exponentially to x_0. In fact, for small ϵ, we can think of t_1 as negative and t_2 as positive. There is then a $c_1 > 0$, such that $t_1 = c_1 \log(\epsilon)$ and hence $\epsilon = \exp(t_1/c_1)$ and similarly, there is a $c_2 < 0$, such that $t_2 = c_2 \log(\epsilon)$ and hence $\epsilon = \exp(t_2/c_2)$. On the other hand, for large ϵ, it is then $t_2 < t_1$, such that $I(\epsilon) = \emptyset$.

Finally, the nontriviality condition (4.1.4) excludes pulse families, whose pulses gradually vanish for $\tau \longrightarrow \infty$. Conversely, a family of periodic pulse solutions with unlimited growth of the pulses for $\tau \longrightarrow \infty$ is prohibited by assuming the uniform boundedness of the solutions.

4.2 Theoretical analysis of temporal dissipative solitons as homoclinic solutions

We are now able to prove the correspondance of temporal dissipative solitons to homoclinic solutions.

Recall from Chapter 2, that the profile of a soliton solution can be found not only as a periodic solution of the DDE (4.1.1) with large delay τ, but also for τ replaced by $-\delta$, as solutions of the profile equation

$$\dot{x}(t) = f\left(x(t), x(t+\delta), \eta\right), \tag{4.2.1}$$

cf. (2.4.3). This is due to the reappearance rule ([YP09]), see Section 2.4, stating that any T-periodic solution of a DDE with delay τ reappears as a solution for all $\tau_m := \tau + mT$, for all $m \in \mathbb{Z}$, (2.4.1) and by making use of the definition of the response time δ (4.1.2).

We will now prove, that in the profile equation (4.2.1), the stable background equilibrium of the DDE (4.1.1) turns into an equilibrium of saddle-type for all $\delta > 0$. In [YWPT22], the authors showed that stability of an equilibrium for large delays implies stability for all nonnegative delays, i.e. absolute stability of the equilibrium (Definition 1). This can be extended, such that we can show that the equilibrium is hyperbolic for all real delay values, i.e. all roots of the characteristic equation (2.1.2) have nonvanishing real part.

Theorem 10. *Suppose x_0 is an equilibrium of (4.1.1), that is stable for all $\tau \geq 0$. Then it is hyperbolic for all $\tau \in \mathbb{R}$.*

Proof. Whereas the background equilibrium of a soliton of the DDE (4.1.1) is trivially reappearing under varying delays, its stability alters in the following way. Consider an equilibrium x_0, which is stable for all positive delays $\tau \geq 0$. For $\tau \longrightarrow 0$ most of the eigenvalues disappear to $-\infty$ and n eigenvalues, equal to the dimension of the state space, remain and have negative real parts. The real parts of the stable eigenvalues at $\tau = 0$ remain negative, also for small negative delays $\tau < 0$. Additionally, for small negative delays, there are infinitely many eigenvalues of the pseudo-continuous spectrum appearing with positive real part from $+\infty$ and accumulate on the imaginary axis for $\tau \longrightarrow -\infty$. Suppose a pair of complex conjugated eigenvalues is crossing the imaginary axis for a negative delay $\tau_c < 0$. Then the characteristic equation

$$\det(i\omega\mathbb{I} - A - Be^{i\omega\tau}) = 0, \tag{4.2.2}$$

where $A = \partial_1 f(x_0, x_0)$, $B = \partial_2 f(x_0, x_0)$, and $\mathbb{I}$ being the identity matrix in $\mathbb{R}^{n\times n}$, has an imaginary root $i\omega$ for $\tau = \tau_c$. The characteristic equation is then also zero for infinitely many delays $\tau = \tau_c + 2\pi k/\omega$ where $k \in \mathbb{Z}$. Especially, the characteristic equation (4.2.2) is zero for k such that $\tau = \tau_c + 2\pi k/\omega$ is positive. This contradicts the stability of x_0 for positive delays. □

Based on the terminology in [YWPT22], we give the following definition:

Definition 4. *An equilibrium of the system (4.1.1) is said to be absolutely hyperbolic, if it is hyperbolic for all delays $\tau \geq 0$.*

Hence, we can say that the absolutely stable background equilibrium x_0 of (4.1.1), is absolutely hyperbolic in the profile equation (4.2.1). Thereby, it turns into an equilibrium of saddle-type in the profile equation, as displayed in Figure 2.3 in Section 2.4.

Recall from Section 2.4, that in the profile equation the solitons appear as a family of T-periodic solutions with $T \longrightarrow \infty$ for a finite $\delta \longrightarrow \delta_\infty$. Thereby, this allows, that they approach a homoclinic solution (2.4.4) at $\delta = \delta_\infty$. The homoclinic approaches the background equilibrium x_0, which is an equilibrium of saddle-type in the profile equation, that remains hyperbolic for all values of δ. We will now prove this relationship analytically with our previously suggested definition of TDSs.

Theorem 11. *Suppose there is a family of TDSs $x_*(t;\tau)$ as established in Definition 3, in the large delay DDE (4.1.1) for all delays $\tau > \tau_0$ with an absolutely stable background x_0. Let $T(\tau)$ denote the respective periods and response times $\delta(\tau) := T(\tau) - \tau$, with $\delta(\tau) \longrightarrow \delta_\infty$ as $\tau, T(\tau) \longrightarrow \infty$.*

Then, in the profile equation (4.2.1), the TDSs turn into a family of periodic solutions approaching a homoclinic solution (2.4.4) for $\delta \longrightarrow \delta_\infty$. The homoclinic limits to the background equilibrium x_0 for $t \longrightarrow \pm\infty$, which, in the profile equation, is absolutely hyperbolic.

Proof. From Theorem 10 it follows immediately, that the background x_0 is a saddle-type equilibrium in the profile equation (4.2.1) for all $\delta > 0$. We need to show that there is a solution $x_h(t)$ in the profile equation at $\delta = \delta_\infty$, and that solution is, indeed, a homoclinic solution.

In the first step, we create a solution at $\delta = \delta_\infty$ in the profile equation (4.2.1). To this end, we will first need to acquire an initial value to create the desired solution at $\delta = \delta_\infty$. Recalling that the profile equation (4.2.1) is an advanced delay system, note that the phase space consists of functions in $\mathcal{C}^0([0, \delta_\infty], \mathbb{R}^n)$.

Let $x_*(t;\tau)$ be the family of TDSs of (4.1.1). As discussed above, they correspond to a family of periodic solutions $x_*(t;\tau)$ in the profile equation (4.2.1) under the reappearance rule (2.4.1). Their corresponding periods $T(\tau)$ increase as $\delta \longrightarrow \delta_\infty$. Let $\epsilon > 0$, then by Definition 3, there is a $\tau_{\min} > 0$, an interval

$I(\epsilon) \subseteq [-T(\tau_{\min})/2, T(\tau_{\min})/2]$ and phase shifts $s(\tau) > 0$ and such that for all $x_*(t;\tau)$ with $\tau > \tau_{\min}$, it is $||x_*(t + s(\tau);\tau) - x_0|| < \epsilon$ for all $t \notin I(\epsilon)$.

In order to suppress the phase shift, we apply a Poincaré section in the phase space, i.e. the space of all history functions $\mathcal{C}^0([0, \delta_\infty], \mathbb{R}^n)$, through $x_*(t_0;\tau)$, for a fixed $t_0 \in I(\epsilon)$ and $\tau > \tau_{\min}$, such that it intersects with all the orbits of $x_*(\,\cdot\,;\tau)$ for all $\tau > \tau_{\min}$. Then it is possible to reparametrize all $x_*(t;\tau)$ such that the time of the intersection with the plane is set to $t = t_0$ of all $x_*(t;\tau)$ with $\tau > \tau_{\min}$.

Considering this family of periodic solutions $x_*(t;\tau)$ in the profile equation, we can reversely express τ as a solution parameter, obtained by

$$\tau(\delta) := T(\delta) - \delta. \tag{4.2.3}$$

Since the solutions are per definition uniformly bounded, the family of periodic solutions has a pointwise limit

$$\lim_{\delta \longrightarrow \delta_\infty} x_*(t_0; \tau(\delta)) =: x_h(t_0),$$

in the Poincaré section, which itself lies the phase space given by $\mathcal{C}^0([0, \delta_\infty], \mathbb{R}^n)$. The limit $x_h(t_0)$ is then a point in the phase space and thereby, the point $x_h(t_0)$ is actually a function $x_h(t_0) := x_h(t_0 + \theta)$ with $\theta \in [0, \delta_\infty]$ that is continuous. This suffices for an initial value in the profile equation (4.2.1).

We now create a solution through the initial value at $\delta = \delta_\infty$. Whereas backward integration is always feasible for equations with an advanced argument, forward integration is only possible under certain conditions, see e.g. [HL93] for an extensive functional analytical study. Recall that the soliton solutions are continuously differentiable periodic solutions and hence belong to a class of solutions that are backward as well as forward integrable for all $t \in \mathbb{R}$. This also transmits to the history function $x_h(t_0)$ obtained as the pointwise limit, which can, in consequence, be piecewise extended to a solution on $\mathbb{R}$. On that account, there is a trajectory through $x_h(t_0)$ at $\delta = \delta_\infty$ denoted with $x_h(t)$ and the family of periodic solutions converges pointwise to $x_h(t)$ for all $t \in \mathbb{R}$:

$$\lim_{\delta \longrightarrow \delta_\infty} x_*(t; \tau(\delta)) = x_h(t). \tag{4.2.4}$$

In the last step, we verify that the solution $x_h(t)$ at $\delta = \delta_\infty$ in the profile equation is a homoclinic solution to x_0, i.e. the trajectory through $x_h(t_0)$ converges to x_0 for $t \longrightarrow \pm\infty$. Indeed, from (4.2.4) we gather, that for all $\epsilon > 0$, there is a $\Delta(\epsilon) > 0$ and a minimal period $T_{\min}(\epsilon) > 0$ with $t \in [-T_{\min}/2, T_{\min}/2]$, such that for all periodic solutions $x_*(t;\tau(\delta))$ with periods $T = T(\delta) > T_{\min}$ for $\delta > 0$ with $||\delta - \delta_\infty|| < \Delta$, it is

$$||x_*(t;\tau(\delta)) - x_h(t)|| < \epsilon, \tag{4.2.5}$$

where $\tau(\delta) = T(\delta) - \delta$ (4.2.3). For this formulation, we took into account, that for a δ close to δ_∞, there can be more than one periodic solution, so $T(\delta)$ does not have to be unique and the periodic solutions with a smaller period do not necessarily satisfy the preceding inequality. The coexistence of infinitely many periodic solutions together with a homoclinic depends on the eigenvalues of the equilibrium x_0 in the profile equation, see Section 3.7.

Let us now rewrite Definition 3 for the reappeared soliton solutions in the profile equation, such that the delay is an additional parameter depending implicitly on δ, that is: For all $\epsilon > 0$, there is a $\tilde{\Delta}(\epsilon) > 0$ and a minimal period $\tilde{T}_{\min}(\epsilon) > 0$ and an interval $I(\epsilon) := [t_1(\epsilon), t_2(\epsilon)] \subseteq [-\tilde{T}_{\min}/2, \tilde{T}_{\min}/2]$ with $t_1, t_2 \in \mathcal{O}(\log(\epsilon))$, such that for all periodic solutions $x_*(t;\tau(\delta))$ with periods $T = T(\delta) > \tilde{T}_{\min}$ for $\delta > 0$ with $||\delta - \delta_\infty|| < \tilde{\Delta}$, it is

$$||x_*(t;\tau(\delta)) - x_h(t)|| < \epsilon, \qquad \text{for all } \; t \notin I(\epsilon), \tag{4.2.6}$$

where $\tau(\delta) = T(\delta) - \delta$ (4.2.3).

Equation (4.2.5) together with Equation (4.2.6) yields then the desired result: For all $\epsilon > 0$, there is a $\Delta_{\mathrm{M}}(\epsilon/2) := \min\{\Delta(\epsilon/2), \tilde{\Delta}(\epsilon/2)\}$, a minimal period $T_{\mathrm{M}}(\epsilon/2) := \max\{T_{\min}(\epsilon/2), \tilde{T}_{\min}(\epsilon/2)\}$ and an interval $I(\epsilon/2) := [t_1(\epsilon/2), t_2(\epsilon/2)] \subseteq [-T_{\mathrm{M}}/2, T_{\mathrm{M}}/2]$, such that for all periodic solutions $x_*(t;\tau(\delta))$ with periods $T(\delta) > T_{\mathrm{M}}$ for $\delta > 0$ with $||\delta - \delta_\infty|| < \Delta_{\mathrm{M}}$, it is

$$\begin{aligned} ||x_h(t) - x_0|| &\leq ||x_h(t) - x_*(t;\tau(\delta))|| + ||x_*(t;\tau(\delta)) - x_0|| \\ &< \epsilon/2 + \epsilon/2 = \epsilon \qquad\qquad \text{for all } t \notin I(\epsilon/2), \end{aligned}$$

where $\tau(\delta) = T(\delta) - \delta$. In particular, per definition, the size of $I(\epsilon/2)$ grows logarithmically with ϵ, such that for $\epsilon \longrightarrow 0$, $I(\epsilon/2)$ grows much slower than the interval $[-T(\tau_{\min})/2, T(\tau_{\min})/2]$ and, hence, remains nonempty. □

With this, we showed that a family of TDSs can be mapped to periodic solutions approaching a homoclinic orbit in the profile equation.

In the next part of this section, we want to show that, provided there is an absolutely stable equilibrium x_0 in the DDE, that is accordingly absolutely hyperbolic in the profile equation, then we also have the following: If there is a homoclinic to the saddle equilibrium x_0 in the profile equation, then there is a family of TDSs in the original large delay DDE system having x_0 as a stable background. To this end, the conditions on the homoclinic and its corresponding saddle have to be more specific.

In Section 3.7, we discussed, that under certain genericity conditions a family of periodic orbits bifurcates from a homoclinic solution for a varying parameter. To this end, we also need to consider the eigenvalues of the linearization of (4.1.1) at the saddle equilibrium limiting to the homoclinic. Recall from Section 3.4, that the leading eigenvalues generically dominating the asymptotics at the tails of the homoclinic, are given by the eigenvalues closest to the imaginary axis as they give the slowest exponential decay rates. Suppose there are real values that separate the leading eigenvalues from the remaining spectrum, which is referred to as the strong spectrum. The conditions for a homoclinic to be generic cover the following statements, thoroughly discussed e.g. in [SSTC01], or [HS10], see also Hypotheses 1–4 in the review on homoclinic bifurcation theory in Chapter 3:

Hypothesis 11 (Nondegeneracy conditions for homoclinic solutions)**.** *A homoclinic solution of* (4.1.1) *to a hyperbolic equilibrium x_0 is generic, if it satisfies the following conditions:*

1. (saddle equilibrium) *The equilibrium x_0 is hyperbolic and there are exactly one unstable and one stable leading eigenvalue up to complex conjugation. They are unique and simple and spectral gaps are separating the leading eigenvalues from the strong spectrum.*

2. (transversal intersection) *The stable and unstable manifold of the saddle equilibrium are assumed to intersect transversely.*

3. (generic unfolding) *The stable and unstable manifold of the saddle equilibrium unfold generically with respect to the parameter η.*

4. (no inclination flip) *The stable (unstable) manifold intersects transversally with the manifold generated by the unstable (stable) together with the leading stable (leading unstable) manifold along the homoclinic.*

5. (no orbit flip) *The homoclinic does not lie in the strong stable (strong unstable) manifold of the saddle.*

The existence of periodic solutions was then proven in the case of finite-dimensional vector fields in [SSTC01], see also [HS10] and references therein. Note that not only Hypothesis 11 has to be satisfied, certain proofs require a $\mathcal{C}^2$- vector field. Suppose the unfolding parameter is η and the homoclinic exists at $\eta = \eta_\infty$. The branch of periodic solutions can either bifurcate for $\eta > \eta_*$ or $\eta < \eta_*$ for real leading eigenvalues of the saddle. In the case of complex conjugate leading eigenvalues, the coexistence of infinitely many periodic solutions with the homoclinic at $\eta = \eta_*$ is also possible, depending on the ratio of the real parts of the leading eigenvalues (cf. Section 3.7).

In order to relate the existence of periodic solutions near a homoclinic orbit in a DDE system to results in finite dimensions, it is essential to reduce the dimensionality. A key tool for studying the dynamics of homoclinic solutions in higher dimensions is the centre manifold reduction. Through this method, one can construct a locally invariant, lower-dimensional manifold that contains the homoclinic solution and all nearby recurrent solutions. The construction of the centre manifold in finite dimensions is feasible under certain conditions related to the asymptotic behavior of the homoclinic orbit (see [HS10; San00] or the review in Section 3.6). The differentiability of the centre manifold is influenced by the size of the spectral gaps between the leading eigenvalues and the strong spectrum. For details on the construction and technical prerequisites of centre manifold reductions in delay equations, refer to [DG91; DVGLW95; VV87]. However, they only cover the centre manifold reduction for equilibria. A detailed analysis of the existence and smoothness conditions for centre manifolds in the context of homoclinic solutions in DDE systems remains lacking. This analysis is beyond the scope of this thesis. Instead, we assume the existence of a $\mathcal{C}^2$-smooth centre manifold for the homoclinic solution in order to match the necessary conditions for the following Theorem.

Theorem 12. *Suppose the DDE system* (4.1.1) *has an equilibrium* x_0 *that is absolutely stable in the DDE and absolutely hyperbolic in the profile equation* (4.2.1). *Suppose further that there is a generic homoclinic solution to* x_0 *in the profile equation* (4.2.1) *at* $\delta = \delta_\infty$. *Assume that Hypothesis 11 is satisfied and that the homoclinic is provided with a* $\mathcal{C}^2$*-centre manifold.*

Then there is a family of T*-periodic solutions bifurcating from the homoclinic for* $\delta \neq \delta_\infty$ *with* $T \longrightarrow \infty$ *for* $\delta \longrightarrow \delta_\infty$. *They correspond to a family of TDSs in the large delay DDE* (4.1.1) *at delays* $\tau := T - \delta > \tau_0$ *and have* x_0 *as stable background equilibrium. Moreover, for* $\tau, T \longrightarrow \infty$ *it is* $\delta \longrightarrow \delta_\infty$.

Proof. At first, we verify that there are periodic solutions bifurcating from the homoclinic in the profile equation: Let $x_h(t)$ be a homoclinic solution existing at a value $\delta = \delta_\infty$ to the saddle equilibrium x_0 in the profile equation (4.2.1). It is presumed, that there is a $\mathcal{C}^2$-centre manifold, reducing the dynamics near the homoclinic to finite dimensions. Homoclinic bifurcation theory ([HS10; SSTC01], or see Theorem 2 and 3 in Section 3.7) now implies the existence of periodic orbits nearby. Note, that depending on the saddle-type and its corresponding saddle value, at $\delta = \delta_\infty$ there can be infinitely many coexisting periodic solutions together with the homoclinic.

Let $x_*(t; \delta(T))$ be the corresponding family of T-periodic solutions of (4.2.1) with $T > T_0 > 0$. We apply a Poincaré section transversal to a point $x_h(t_0)$ for a $t_0 \in \mathbb{R}$, in order to neglect a phase shift in the profiles. Reparametrize all $x_*(t; \delta(T))$ such that the time of the intersection with the plane is set to $t = t_0$ and that $x_*(t; \delta(T))$ is defined on $[-T/2, T/2]$. Then for every $t \in \mathbb{R}$ and for all $\epsilon > 0$, there is a $\Delta(\epsilon) > 0$ and $T_{\min}(\epsilon) > T_0$ with $t \in [-T_{\min}/2, T_{\min}/2]$, such that for all $x_*(t; \delta(T))$ with periods $T > T_{\min}$ at a corresponding $\delta(T) > 0$ with $||\delta - \delta_\infty|| < \Delta$, it is

$$||x_h(t) - x_*(t; \delta(T))|| < \epsilon. \tag{4.2.7}$$

Since they bifurcate from the homoclinic, it is $T \longrightarrow \infty$ for $\delta \longrightarrow \delta_\infty$.

In the next step, we show that the family of periodic solutions bifurcating from the homoclinic corresponds to a family of solitons in the DDE: The homoclinic $x_h(t)$ satisfies (2.4.4), i.e. for all $\epsilon > 0$ there is a $t_0(\epsilon) > 0$ such that

$$||x_h(t) - x_0|| < \epsilon, \qquad \text{for all } |t| > t_0. \tag{4.2.8}$$

Similarly, for larger periods the bifurcating periodic solutions approach the homoclinic and hence spend most of the time close to the saddle equilibrium x_0. Indeed, with (4.2.7) and (4.2.8), for all $\epsilon > 0$, there exists a $\tau_{\min}(\epsilon) := T_{\min}(\epsilon/2) - \delta(T_{\min}) > T_0 - \delta(T_0)$ and an interval $I(\epsilon) := [t_1(\epsilon), t_2(\epsilon)]$ where $t_1 := \min\{-t_0(\epsilon/2), -T_{\min}(\epsilon/2)/2\}$ and $t_2 := \max\{t_0(\epsilon/2), T_{\min}(\epsilon/2)/2\}$, such that for all periodic solutions $x_*(t; \delta(t))$ with $\tau := T - \delta(T) > \tau_{\min}$, where $T > T_{\min}$ with $|\delta(T) - \delta_\infty| < \Delta(\epsilon/2)$, it is

$$||x_*(t;\delta(T)) - x_0|| \leq ||x_*(t;\delta(T)) - x_h(t)|| + ||x_h(t) - x_0|| < \epsilon/2 + \epsilon/2 = \epsilon,$$

for all $t \notin I(\epsilon)$.

It remains to verify, that $t_1(\epsilon), t_2(\epsilon) \in \mathcal{O}(\log(\epsilon))$. At the tails, the dynamics of a homoclinic can be approximated by the linearization of (4.2.1) at the saddle equilibrium x_0. Especially, for a homoclinic solution $x_h(t)$, it is $||x_h(t) - x_0|| \in \mathcal{O}(\mathrm{Re}(e^{\lambda^{\mathrm{ls,lu}} t}))$, where $\lambda^{\mathrm{ls}}, \lambda^{\mathrm{lu}} \in \mathbb{C}$ denote respectively the leading stable and unstable eigenvalues of the corresponding saddle x_0, cf. Section 3.4. This is equivalent to $t_0(\epsilon)$ being of order $\mathcal{O}(\log(\epsilon))$. This also transmits to the periodic solutions $x_*(t; \delta(T))$ close to the homoclinic, hence also $T_{\min}(\epsilon)$ is of order $\mathcal{O}(\log(\epsilon))$.

Setting $\tau := T - \delta(T)$ and applying the reappearance rule (2.4.1) gives then the desired result. Beyond that, since the periodic solutions reappear from large period periodic solutions that limit a homoclinic, the uniform boundedness, as well as the nontriviallity condition (4.1.4), is naturally satisfied. □

Hence, we proved that solitons can be associated with homoclinic solutions in the profile equation. Generically, homoclinic solutions are created in a bifurcation by varying one parameter and are thus of codimension-one. Solving the profile equation for a homoclinic solution, one needs to solve for the profile together with the parameter δ as the control parameter, tuning the parameter δ to δ_∞. In contrast to that, solitons are generic solutions of (4.1.1) for all large enough delays, persisting small parameter changes. The response time δ is an additional parameter that is already determined by the soliton. In order to study bifurcations of solitons induced by homoclinic bifurcations in the profile equation, one always has to adjust the parameter δ_∞, too, thus increasing the codimension of the bifurcation by one. Hence, homoclinic bifurcations of

codimension-two in the profile equation correspond to bifurcations of solitons of codimension-one in the DDE.

4.3 An alternated profile equation for alternating pulses

The framework presented for TDSs can be extended to other localized solutions by deriving a similar framework as the profile equation for these types of solutions. To this end, consider a family of periodic solutions of (4.1.1) for all large delays τ, consisting of alternating pulses, that have a period which is slightly larger than twice the delay τ. These are periodic solutions accomodating two pulses, which have a distance of approximately τ, that possibly differ in size and shape. For these kinds of solutions, we will suggest a definition, similar to Definition 3 for TDSs.

Definition 5 (Alternating pulse solutions)**.** *Suppose the system* (4.1.1) *possesses an equilibrium* x_0 *that is stable for all nonnegative delays and a* 1*-parameter family of periodic solutions* $x_*(t;\tau)$ *for all* $\tau > \tau_0 > 0$*. Let* $2T(\tau)$ *denote the period of* $x_*(t;\tau)$ *and* $T(\tau) > \tau$*. Let the periodic solutions* $x_*(t;\tau)$ *be defined and uniformly bounded on* $[-T(\tau), T(\tau)]$*. Define the* response time *as*

$$\delta(\tau) := T(\tau) - \tau. \tag{4.3.1}$$

Suppose δ *is finite, positive and for* $\tau, T \longrightarrow \infty$ *it has a limit denoted with* δ_∞*.*

Then the family of periodic solutions $x_*(t;\tau)$ *are* alternating pulse solutions*, if for all* $\epsilon > 0$*, there is a* $\tau_{min}(\epsilon) > \tau_0$*, a subset* $I(\epsilon) \subseteq [-T(\tau_{min}), T(\tau_{min})]$ *consisting of two disjoint subintervals* $I_1(\epsilon)$ *and* $I_2(\epsilon)$ *and appropriate phase shifts* $0 < s(\tau) < 2T(\tau)$*,* $0 < \tilde{s}(\tau) < 2T(\tau)$ *such that all periodic solutions* $x_*(t;\tau)$ *with* $\tau > \tau_{min}$ *satisfy*

$$||x_*(t + s(\tau);\tau) - x_0|| < \epsilon \text{ for all } t \notin I_1 \cup \{I_2 + \tilde{s}(\tau)\}.$$

Additionally, it exists a $\zeta > 0$ *and* $\hat{t} \in I(\epsilon)$ *such that all periodic solutions* $x_*(t;\tau)$ *with* $\tau > \tau_{\min}$ *satisfy*

$$||x_*(\hat{t} + s(\tau);\tau) - x_0|| > \zeta.$$

Here $I + s$ denotes the following: Let $I := [t_1, t_2] \subset \mathbb{R}$ and $s \in \mathbb{R}$, then $I + s := [t_1 + s, t_2 + s]$. Also in the context of alternating pulse solutions, we will call the equilibrium x_0 *background*. Note, that we defined the response time by the same formula as in (4.3.1), although T gives here only half the period. Our goal is to find an equation similar to the profile equation for solitons, that treats these types of pulse solutions as homoclinic solutions.

Based on earlier work by Mallet-Paret and Nussbaum on square wave solutions in DDEs in 1986 [MPN86], consider the following system of delay differential equations, based on the original large delay system (4.1.1), for $\sigma \in \mathbb{R}$:

$$\dot{x}(t) = f(x(t), y(t-\sigma), \eta), \tag{4.3.2}$$

$$\dot{y}(t) = f(y(t), x(t-\sigma), \eta). \tag{4.3.3}$$

The system (4.3.2)–(4.3.3) is equivariant with respect to the mirror symmetry

$$\gamma : (x, y) \longmapsto (y, x). \tag{4.3.4}$$

The corresponding subspace of fixed points of the symmetry γ is given by

$$\mathrm{Fix}(\gamma) := \{(x, y) \,|\, \gamma(x, y) = (x, y)\} = \{(x, y) \,|\, x = y\}. \tag{4.3.5}$$

The solutions in the symmetry subspace $x = y$ correspond to solutions of the original large delay system (4.1.1) for $\tau = \sigma$. An equilibrium x_0 of (4.1.1) reappears as the equilibrium (x_0, x_0) of (4.3.2)–(4.3.3) lying in $\mathrm{Fix}(\gamma)$. Especially, a T-periodic TDS solution $x_*(t)$ in (4.1.1) for a delay τ, corresponds to the T-periodic TDS solution $(x_*(t), x_*(t)) \in \mathrm{Fix}(\gamma)$ of (4.3.2)–(4.3.3) at $\sigma = \tau$.

But the system can also possess other solutions that do not lie in $\mathrm{Fix}(\gamma)$. Suppose that $x_*(t)$ is a periodic solution of the large delay DDE (4.1.1) with minimal period $2T$. This solution reappears in system (4.3.2)–(4.3.3) and does not lie in $\mathrm{Fix}(\gamma)$:

Let $x_*(t)$ be a $2T$-periodic solution of (4.1.1) for a delay τ. This yields with

$$(x(t), y(t)) := (x_*(t), x_*(t-T)), \tag{4.3.6}$$

a $2T$-periodic solution of system (4.3.2)–(4.3.3), whenever

$$\sigma = \sigma_m := \tau + (2m-1)T, \qquad m \in \mathbb{Z}. \tag{4.3.7}$$

Indeed, extracting τ from (4.3.7) and inserting it in (4.1.1) leads to

$$\dot{x}_*(t) = f(x_*(t), x_*(t-\sigma-T), \eta),$$

by taking in count the $2T$-periodicity of $x_*(t)$. With (4.3.6), $x_*(t)$ solves (4.3.2). Analogously, (4.3.3) is satisfied using $y(t) = x(t-T)$. Thereby, equation (4.3.7) gives us an alternated reappearance rule for the newly introduced system.

Correspondingly to the derivation of the profile equation (4.2.1) in Section 2.4, we make use of the definition of the response time δ (4.3.1). Here we choose $\sigma = \sigma_0$, which is equal to $-\delta$ and we call (4.3.2)–(4.3.3) for $\sigma = -\delta$ the *alternated profile equation (APE)*.

The APE system (4.3.2)–(4.3.3) is an equation with an advanced argument, with similar features as the profile equation. Firstly, the stable background equilibrium x_0 reappears to (x_0, x_0) and is naturally hyperbolic in the APE system for all $\delta > 0$.

Corollary 1. *Suppose the DDE system* (4.1.1) *possesses an equilibrium* x_0 *that is stable for all delays* $\tau \geq 0$. *Then, the corresponding equilibrium* (x_0, x_0) *in the system* (4.3.2)–(4.3.3) *is hyperbolic for all* $\sigma \in \mathbb{R}$.

Proof. Recall, that absolute stability of x_0 of (4.1.1) implies hyperbolicity for all delays $\tau \in \mathbb{R}$, see Theorem 10. Hence there is no $\tau_c \in \mathbb{R}$, such that the characteristic equation given by

$$\det\left(i\omega\mathbb{I} - A - Be^{i\omega\tau_c}\right) = 0, \tag{4.3.8}$$

where $A = \partial_1 f(x_0, x_0, \eta)$ and $B = \partial_2 f(x_0, x_0, \eta)$, has an imaginary root $i\omega$. The corresponding characteristic equation of system (4.3.2)–(4.3.3) is given by

$$\det\left(i\omega\begin{pmatrix}\mathbb{I} & \mathbb{O}\\ \mathbb{O} & \mathbb{I}\end{pmatrix} - \begin{pmatrix}A & \mathbb{O}\\ \mathbb{O} & A\end{pmatrix} - \begin{pmatrix}\mathbb{O} & B\\ B & \mathbb{O}\end{pmatrix}e^{i\omega\tau_c}\right) = 0. \tag{4.3.9}$$

Using that

$$\det\begin{pmatrix}M_1 & M_2\\ M_2 & M_1\end{pmatrix} = \det(M_1+M_2)\,\det(M_1-M_2),$$

for two matrices M_1,$M_2 \in \mathbb{R}^{n\times n}$, equation (4.3.9) is equivalent to

$$\det\left(i\omega\mathbb{I} - A - Be^{i\omega\tau_c}\right)\det\left(i\omega\mathbb{I} - A + Be^{i\omega\tau_c}\right) = 0.$$

Then with $e^{i\omega\tau_c} = -e^{i\omega(\tau_c-\pi/\omega)}$, one can see, that if there is no $\tau_c \in \mathbb{R}$, such that (4.3.8) has an imaginary root $i\omega$, then the same is true for the characteristic equation of system (4.3.9). The equilibrium (x_0, x_0) is consequently hyperbolic in system (4.3.2)–(4.3.3) for all $\sigma \in \mathbb{R}$. □

Recalling the innate stability properties of time-delayed systems, cf. Section 2.4, the equilibrium (x_0, x_0) is consequently of saddle-type in system (4.3.2)–(4.3.3) for all $\sigma \in \mathbb{R}$. Additionally, in the APE system, the alternating pulse solutions approach a homoclinic solution in the following familiar way. Suppose there is a family of alternating pulse solutions $x_*(t;\tau)$ in the large delay DDE with corresponding periods $2T(\tau)$ and background x_0. The response time δ (4.3.1) again satisfies $\delta(\tau) := T(\tau) - \tau \longrightarrow \delta_\infty$ for $\tau \longrightarrow \infty$. Applying the reappearance rule for alternating pulse solutions (4.3.7), they turn into a family of periodic solutions in the APE system (4.3.2)–(4.3.3) at $\sigma = -\delta$. For $\delta \longrightarrow \delta_\infty$, it is then $T \longrightarrow \infty$. Hence, the family of alternating pulses approach a homoclinic at $\delta = \delta_\infty$. Furthermore, the homoclinic approaches the equilibrium (x_0, x_0) for $t \longrightarrow \pm\infty$, which is a saddle equilibrium in the APE.

Corollary 2. *Suppose there is a family of alternating pulse solutions $x_*(t;\tau)$ in the large delay DDE* (4.1.1) *for all delays $\tau > \tau_0$ with an absolutely stable background x_0. Let $2T(\tau)$ denote their respective periods. The corresponding response times $\delta(\tau) := T(\tau) - \tau$ are finite and have a limit for $\tau, T(\tau) \longrightarrow \infty$, denoted with δ_∞.*

Then, in the alternated profile equation (4.3.2)–(4.3.3)*, the alternating pulses $x_*(t;\tau)$ turn into a family of periodic solutions $(x_*(t;\tau), x_*(t - T(\tau);\tau))$ that approach a homoclinic solution for $\delta \longrightarrow \delta_\infty$. The homoclinic approaches the equilibrium (x_0, x_0) for $t \longrightarrow \pm\infty$, which is an equilibrium of saddle-type in the alternated profile equation.*

Especially, if the periodic solutions $x_*(t;\tau)$ have minimal period $T(\tau)$, then the periodic solutions $(x_*(t;\tau), x_*(t-T(\tau);\tau))$ in the alternated profile equation approach a homoclinic orbit to (x_0, x_0) and the homoclinic lies in $\mathrm{Fix}(\gamma)$.

Proof. From Corollary 1 it follows, that the equilibrium (x_0, x_0) is of saddle-type in the APE system (4.3.2)–(4.3.3) for all $\delta > 0$.

The remaining part of the proof works analogously as for Theorem 11, using Definition 5 for alternating pulses instead of Definition 3 for TDSs. Thereby, with (4.3.6) and with the reappearance rule for alternating pulse solutions (4.3.7), the alternating pulse solutions $x_*(t)$ reappear to a family of periodic solutions $(x_*(t;\tau),\, x_*(t - T(\tau);\tau))$ in the APE system (4.3.2)–(4.3.3) that approach a homoclinic solution to (x_0, x_0).

If the periodic solutions $x_*(t;\tau)$ have a period $T(\tau)$, which is also the minimal period, this immediately implies that $x_*(t;\tau) = x_*(t - T(\tau);\tau)$. By Definition 5, the periodic solutions reappear to a family of periodic solutions $(x_*(t;\tau),\, x_*(t;\tau))$ in the APE system (4.3.2)–(4.3.3) lying in $\mathrm{Fix}(\gamma)$. Consequently, they approach a homoclinic solution $(x_h(t),\, x_h(t))$ that lies in $\mathrm{Fix}(\gamma)$, as well. □

Consequently, the alternating pulse solutions can be identified with homoclinic solutions in the APE system that do not lie in the symmetry subspace $\mathrm{Fix}(\gamma)$. In contrast to that, temporal dissipative solitons correspond to homoclinic solutions in the APE system that lie in $\mathrm{Fix}(\gamma)$.

4.4 The Floquet problem and the reappearance of the period-doubling in the APE

In order to study bifurcations of TDSs, it is useful to analyse the spectrum of the solution. In general, the spectrum of a periodic solution is given by solutions to the Floquet problem, cf. Chapter 2.5.

For a T-periodic solution $x_*(t)$ of (4.1.1) at a fixed value of τ and η, the Floquet problem (2.5.1)–(2.5.2) is given by

$$\dot{v}(t) = A(t)v(t) + B(t)v(t-\tau), \tag{4.4.1}$$

$$v(t+T) = \mu v(t), \tag{4.4.2}$$

where $A(t) = \partial_1 f\left(x_*(t), x_*(t-\tau), \eta\right)$ and $B(t) = \partial_2 f\left(x_*(t), x_*(t-\tau), \eta\right)$. Let $v_*(t)$ be the Floquet eigenfunctions to the Floquet multiplier μ of the solution $x_*(t)$ of (4.1.1), i.e. $v_*(t)$ and μ satisfy (4.4.1)–(4.4.2). The Floquet mode $\tilde{v}(t)$ can be expressed through $v_*(t) = \exp(\lambda t)\tilde{v}(t)$, where $\mu = \exp(\lambda T)$ for an exponent $\lambda \in \mathbb{C}$ and a T-periodic function $\tilde{v}(t)$.

In this section, we focus on the case

$$\mu = -1, \tag{4.4.3}$$

corresponding to a period-doubling bifurcation. Note, that the emergence of alternating pulse solutions discussed in the previous section can be associated with this bifurcation. In order for the Floquet problem (4.4.1)–(4.4.2) together with condition (4.4.3) to be a well-posed problem, a parameter has to be treated as an unknown. Indeed, if the system (4.1.1), together with (4.4.1)–(4.4.3) are solvable for a fixed delay τ, one obtains a T-periodic solution $x_*(t)$ with Floquet pair $(-1, v_*)$ at $\eta = \eta_*$. This renders the period-doubling into a bifurcation of codimension-one.

Applying the reappearance rule (2.4.1) on periodic solutions, their stability might change. In particular, the period-doubling bifurcation of a TDS in the large delay DDE (4.1.1) does not reappear in the profile equation (4.2.1). This can already be deduced from the computations for the derivation of the pseudo-continuous and interface spectrum provided in [YRSW19], cf. review in Section 2.5.

Remark 2 (No reappearance of the period-doubling in the profile equation)**.** *Suppose a T-periodic solution $x_*(t)$ of the DDE (4.1.1) at delay τ undergoes a period-doubling bifurcation. Although the profile of the periodic solution reappears in the profile equation (4.2.1) at $\delta = T - \tau$ (4.1.2), it does not undergo a period-doubling bifurcation anymore. Let (μ, v_*) be the corresponding Floquet pair solving (4.4.1)–(4.4.2). The solution $x_*(t)$ reappears in the profile equation (4.2.1); the corresponding Floquet problem in the profile equation is then*

$$\dot{v}(t) = A(t)v(t) + B(t)v(t+\delta), \tag{4.4.4}$$

$$v(t+T) = \mu v(t). \tag{4.4.5}$$

Note, that we used here the T-periodicity of the matrices $A(t)$ and $B(t)$.

On the other hand, using the Floquet condition (4.4.2)*, it is*

$$v(t-\tau) = \mu^{-1} v(t-\tau+T) = \mu^{-1} v(t+\delta).$$

Then the Floquet problem (4.4.1)–(4.4.2) *of the original large delay DDE* (4.1.1) *is equivalent to*

$$\dot{v}(t) = A(t)v(t) + \mu^{-1}B(t)v(t+\delta), \tag{4.4.6}$$

$$v(t+T) = \mu v(t). \tag{4.4.7}$$

By comparing (4.4.4) *with* (4.4.6)*, one can see that they are equivalent if and only if* $\mu = 1$*, which is just an immediate consequence of the reappearance rule* (2.4.1) *for* T*-periodic solutions. Hence only the Floquet pair* $(1, \dot{x}_*)$ *solves both the Floquet problem* (4.4.1)–(4.4.2) *of the DDE system and the Floquet problem* (4.4.4)–(4.4.5) *of the profile equation. Especially, the Floquet pair corresponding to a period-doubling* $(-1, v_*)$ *does not solve* (4.4.4)–(4.4.5)*.*

This also leads to Lemma 1 in [GR23], cf. Section 2.6.

Another viewpoint to this result lies in the following: Using the Floquet condition (4.4.2), then for a Floquet pair $(-1, v_*)$ it is $v_*(t+T) = -v_*(t)$. One can see that $v_*(t)$ is a $2T$-periodic solution of (4.4.1) and can hence not be mapped to the profile equation (4.2.1) by the reappearance rule (4.5.3) for T-periodic solutions. Recalling Chapter 4.3, we note that the APE system (4.3.2)–(4.3.3) accomodates these $2T$-periodic solutions. The Floquet problem to a periodic solution $(x_*(t), x_*(t)) \in \mathrm{Fix}(\gamma)$ in the APE system with minimal period T, is given by

$$\begin{pmatrix} \dot{v}_1(t) \\ \dot{v}_2(t) \end{pmatrix} = \begin{pmatrix} A(t) & \mathbb{O} \\ \mathbb{O} & A(t) \end{pmatrix} \begin{pmatrix} v_1(t) \\ v_2(t) \end{pmatrix} + \begin{pmatrix} \mathbb{O} & B(t) \\ B(t) & \mathbb{O} \end{pmatrix} \begin{pmatrix} v_1(t+\delta) \\ v_2(t+\delta) \end{pmatrix}, \tag{4.4.8}$$

$$\begin{pmatrix} v_1(t+T) \\ v_2(t+T) \end{pmatrix} = \mu \begin{pmatrix} v_1(t) \\ v_2(t) \end{pmatrix}. \tag{4.4.9}$$

The $2T$-periodic solution $v_*(t)$ of (4.4.1) also solves system (4.4.8) with

$$(v_1(t), v_2(t)) := (v_*(t), v_*(t-T)).$$

Especially, in contrast to $(x_*(t), x_*(t))$, it does not lie in Fix(γ). The period-doubling bifurcation in the APE hence appears together with a symmetry-breaking. We will demonstrate in the following, that the period-doubling bifurcation occurring in the large delay DDE does, indeed, reappear in the APE:

Theorem 13 (Reappearance of the period-doubling in the APE)**.** *Let $x_*(t)$ be a T-periodic solution of the DDE system* (4.1.1) *and the corresponding solution reappearing in the APE system* (4.3.2)–(4.3.3) *is given by $(x_*(t), x_*(t))$.*

Then $x_*(t)$ undergoes a period-doubling bifurcation in the DDE system at parameter $\eta = \eta_*$ if and only if $(x_*(t), x_*(t))$ undergoes a period-doubling bifurcation in the APE system at $\eta = \eta_*$:

The pair $(-1, v_*)$ solves the Floquet problem (4.4.1)–(4.4.2) *corresponding to $x_*(t)$ in the DDE if and only if $(-1, (v_*, -v_*))$ solves the Floquet problem* (4.4.8)–(4.4.9) *to the solution $(x_*(t), x_*(t))$ in the APE system.*

Proof. " $\Longrightarrow$ ": Define $v_1(t) := v_*(t)$ and $v_2(t) := v_*(t-T)$. Hence, they satisfy trivially (4.4.9) for $\mu = -1$. Since $v_*(t)$ solves (4.4.1), it can be rewritten for v_1, v_2. Using $\delta = T - \tau$ (4.1.2), it is then

$$\dot{v}_1(t) = A(t)v_1(t) + B(t)v_1(t-\tau) = A(t)v_1(t) + B(t)v_2(t+\delta), \tag{4.4.10}$$

$$\dot{v}_2(t) = A(t)v_2(t) + B(t)v_2(t-\tau) = A(t)v_1(t) + B(t)v_1(t+\delta), \tag{4.4.11}$$

which is (4.4.8).

" $\Longleftarrow$ ": Suppose the multiplier $\mu = -1$, together with $(v_1(t), v_2(t)) = (v_*(t), -v_*(t))$ solves the Floquet problem (4.4.8)–(4.4.9) of the T-periodic solution $(x_*(t), x_*(t))$ in the APE system. Setting $v_*(t) = v_1(t) = -v_2(t)$, it is then $v_*(t+T) = \mu v_*(t)$ with $\mu = -1$ (4.4.9). Recalling $\delta = T - \tau$ (4.1.2), equation (4.4.8) is then equivalent to

$$\dot{v}_*(t) = A(t)v_*(t) - B(t)v_*(t+\delta) = A(t)v_*(t) + B(t)v_*(t-\tau).$$

Hence $v_*(t)$ with $\mu = -1$ solves (4.4.1)–(4.4.2). □

An immediate consequence of Remark 2 based on [YRSW19] is the following Theorem, that serves as an alternative to Theorem 13.

Theorem 14 (An adapted variational equation for the period-doubling). *A T-periodic solution $x_*(t)$, together with an eigenmode $v_*(t)$ and exponent $\lambda_* \in \mathbb{C}$, at a parameter value η_*, solves the system*

$$\dot{x}(t) = f(x(t), x(t-\tau), \eta), \tag{4.4.12}$$
$$\dot{\tilde{v}}(t) = (A(t) - \lambda \,\mathrm{Id})\tilde{v}(t) + \exp(-\lambda\tau)B(t)\tilde{v}(t-\tau), \tag{4.4.13}$$
$$x(t+T) = x(t), \tag{4.4.14}$$
$$\tilde{v}(t+T) = \tilde{v}(t), \tag{4.4.15}$$
$$\exp(\lambda T) = -1, \tag{4.4.16}$$

if and only if, with $\delta := T - \tau$, it solves

$$\dot{x}(t) = f(x(t), x(t+\delta), \eta), \tag{4.4.17}$$
$$\dot{\tilde{v}}(t) = (A(t) - \lambda \,\mathrm{Id})\tilde{v}(t) - \exp(\lambda\delta)B(t)\tilde{v}(t+\delta), \tag{4.4.18}$$
$$x(t+T) = x(t), \tag{4.4.19}$$
$$\tilde{v}(t+T) = \tilde{v}(t), \tag{4.4.20}$$
$$\exp(\lambda T) = -1, \tag{4.4.21}$$

where $A(t) := \partial_1 f\,(x(t), x(t-\tau), \eta)$, and $B(t) := \partial_2 f\,(x(t), x(t-\tau), \eta)$.

Proof. Equations (4.4.12)–(4.4.15) are the Floquet problem (4.4.1)–(4.4.2) of (4.1.1) for Floquet mode $\tilde{v}(t)$ given by $v(t) = \exp(\lambda t)\tilde{v}(t)$, where $\mu = \exp(\lambda T)$. Using $\delta = T - \tau$, it is

$$\exp(-\lambda\tau) = \exp(\lambda(-T+\delta)). \tag{4.4.22}$$

Together with the general reappearance rule (2.4.1) for periodic solutions, equations (4.4.12)–(4.4.15) are equivalent to

$$\begin{aligned}
\dot{x}(t) &= f(x(t), x(t+\delta), \eta),\\
\dot{\tilde{v}}(t) &= (A(t) - \lambda \,\mathrm{Id})\tilde{v}(t) + \mu^{-1}\exp(\lambda\delta)B(t)\tilde{v}(t+\delta),\\
x(t+T) &= x(t),\\
\tilde{v}(t+T) &= \tilde{v}(t).
\end{aligned}$$

This is (4.4.17)–(4.4.20) if and only if $\mu = \exp(\lambda T) = -1$. □

We summarize now the results from Theorem 13 and 14 in the following corollary:

Corollary 3. *The following are equivalent:*

1. *(PD in DDE) a T-periodic solution $x_*(t)$ of the large delay DDE* (4.1.1) *with Floquet pair $(-1, v_*)$ solving the Floquet problem* (4.4.1)–(4.4.2).

2. *(PD in APE) a T-periodic solution $(x_*(t), x_*(t))$ of the alternated profile equation* (4.3.2)–(4.3.3) *with Floquet pair $(-1, (v_*, -v_*))$ solving the corresponding Floquet problem* (4.4.8)–(4.4.9).

3. *(PD in alternated variational equation) a T-periodic solution $x_*(t)$ of the profile equation* (4.2.1) *and $\tilde{v}_*(t) := \exp(-\lambda t) v_*(t)$ with $\lambda \in \mathbb{C}$ such that $\exp(\lambda T) = -1$ solves the adapted variational equation* (4.4.18),(4.4.20).

Whereas in the large-delay DDE system of case (*1.*), one has to deal with the singular limit $\tau \longrightarrow \infty$ for solitons, in the other two cases (*2.*) and (*3.*), this is replaced by the finite limit $\delta \longrightarrow \delta_\infty$. Additionally, the alternated variational equation of case (*3.*) provides for a robust numerical path-continuation of the period-doubling point, in those cases where case (*2.*) poses numerical difficulties.

4.5 An alternated profile equation for resonant Floquet multipliers

The alternated profile equation can also be generalized for other critical multipliers. Suppose $x_*(t)$ is a T-periodic solution of (4.1.1), having a resonant Floquet multiplier μ, cf. (2.6.1), such that

$$\mu^l = 1 \text{ for some } l \in \mathbb{N}, \text{ and } \mu^j \neq 1 \text{ for all } j < l.$$

Instabilities induced by resonant Floquet multipliers lead to resonant Neimark-Sacker bifurcations.

Theorem 15 (Subharmonic reappearance rule)**.** *Consider the following statements:*

1. *The T-periodic solution $x_*(t) \in \mathbb{R}^n$ of*

$$\dot{x}(t) = f\left(x(t), x(t-\tau)\right) \tag{4.5.1}$$

possesses a resonant Floquet multiplier μ s.t. there is an $l \in \mathbb{N}, l \geq 2$ with $\mu^l = 1$ and $\mu^j \neq 1$ for $j = 1, \ldots, l-1$.

2. *The T-periodic solution $(x_*(t), \ldots, x_*(t)) \in \mathbb{R}^{ln}$ of system*

$$\dot{x}_k(t) = f\left(x_k(t), x_{(k+1) \bmod l}\,(t-\sigma)\right), \quad k = 1, \ldots, l, \tag{4.5.2}$$

possesses a resonant Floquet multiplier μ with $l \in \mathbb{N}$, $l \geq 2$ satisfying $\mu^l = 1$ and $\mu^j \neq 1$ for $j = 1, \ldots, l-1$.

The statements (1.) and (2.) are equivalent if and only if

$$\sigma = \sigma_m = \tau + (ml - 1)T, \quad m \in \mathbb{Z}. \tag{4.5.3}$$

We call (4.5.2) *the* generalized alternated profile equation.

Proof. Recall the Floquet problem (4.4.1)–(4.4.2). Let $v_*(t)$ be the Floquet mode corresponding to the resonant Floquet multiplier μ of the periodic solution $x_*(t)$ of (4.5.1). The Floquet mode $v_*(t)$ is then lT-periodic, since (4.4.2) implies $v_*(t+lT) = \mu^l v_*(t)$ and $\mu^l = 1$. Set $v_1(t) := v_*(t)$ and define iteratively

$$v_{(k+1) \bmod l}(t) := v_k(t-T). \tag{4.5.4}$$

Then the Floquet pair (μ, v_*) of solution $x_*(t)$ of system (4.5.1) is equivalent to the Floquet pair $(\mu, (v_1, \ldots, v_l))$ of solution $(x_*(t), \ldots, x_*(t))$ of system (4.5.2):

The components of the Floquet problem of $(x_*(t), \ldots, x_*(t))$ of (4.5.2) for the Floquet mode $(v_1(t), \ldots, v_l(t))$ are given by

$$\dot{v}_k(t) = A(t)v_k(t) + B(t)v_{k+1 \bmod l}(t-\sigma), \text{ for } k = 1, \ldots, l, \tag{4.5.5}$$

where $A(t) = \partial_1 f\left(x_*(t), x_*(t-\sigma)\right)$ and $B(t) = \partial_2 f\left(x_*(t), x_*(t-\sigma)\right)$.

Every $v_k(t)$ is itself a Floquet mode of $x_k(t) = x_*(t)$ in (4.5.1) satisfying the Floquet problem (4.4.1) per definiton (4.5.4):

$$\dot{v}_k(t) = \partial_1 f\left(x_*(t), x_*(t-\tau)\right) v_k(t) + \partial_2 f\left(x_*(t), x_*(t-\tau)\right) v_k(t-\tau) \quad (4.5.6)$$

Hence $v_k(t)$ satisfies (4.5.5) and (4.5.6) if and only if (4.5.3) and (4.5.4) are satisfied. □

The case $l = 1$ is the general reappearance rule under which only the trivial Floquet multiplier $\mu = 1$ reappears. This case is trivially covered by the Theorem when neglecting the restriction $l \geq 2$.

The system (4.5.2) supports the study of TDSs undergoing resonant Neimark-Sacker bifurcations. Beyond that, the system is provided with a $\mathbb{Z}_l$-symmetry.

4.6 Square waves in the alternated profile equation

Finally, we want to extend the strategy developed for alternating pulse solutions in Section 4.3 to square waves (SWs). Similarly to solitons, these types of solutions are localized states which are characterized by sharp transitions between alternating plateaus. However, they have a period of approximately twice the delay. The approach is essentially analogous to the derivation in Chapter 4.3 for alternating pulse solutions and based on our publication [SKJGW23a].

Let us first consider the singular map of the system, cf. equation (2.3.1),

$$0 = f(x_{k+1}, x_k), \qquad k \in \mathbb{Z}.$$

In Section 2.3, this map was derived by rescaling the time in the DDE (4.1.1) by $t' = t/\tau$ and then applying formally the limit $\tau \longrightarrow \infty$. Recall, that a stable equilibrium x_0 of the singular map (2.3.1) is also a stable equilibrium of the DDE system (4.1.1) ([YWPT22]) and can serve as a background for solitons. Suppose the equilibrium x_0 undergoes a flip bifurcation and a stable period-two solution (x_1, x_2) is created, i.e. a solution of (2.3.1) satisfying

$$0 = f(x_1, x_2) = f(x_2, x_1).$$

Then these two values $x_{1,2}$ can serve as plateaus of a square waves in the large delay DDE (4.1.1). A square wave then corresponds to a periodic solution $x_*(t)$ with a period $2T$ slightly larger than 2τ having two plateaus $x_{1,2}$ of length approximately τ each.

Consider now the alternated profile equation from Section (4.3), given by

$$\dot{x}(t) = f(x(t), y(t-\sigma)), \tag{4.6.1}$$

$$\dot{y}(t) = f(y(t), x(t-\sigma)). \tag{4.6.2}$$

cf. (4.3.2)–(4.3.3). In this system, the period-two solution (x_1, x_2) of the singular map (2.3.1) induces two different equilibria $(x, y) = (x_1, x_2)$ and $(x, y) = (x_2, x_1)$. In particular, the $2T$-periodic square wave solution $x_*(t)$ of the DDE system (4.1.1) provides by (4.3.6), i.e.

$$(x(t), y(t)) := (x_*(t), x_*(t-T))$$

a solution of the system (4.6.1)–(4.6.2), whenever the alternated reappearance rule (4.3.7)

$$\sigma = \sigma_m := \tau + (2m-1)\,T, \text{ for all } m \in \mathbb{Z}.$$

is satisfied.

Also for the case of a $2T$-periodic square wave of (4.1.1) at delay τ, we will again define the response time as

$$\delta(\tau) := T(\tau) - \tau. \tag{4.6.3}$$

Thus, the profile of a square wave $x_*(t)$ of the DDE system can also be found as a periodic solution of (4.6.1)–(4.6.2) with $\sigma = \sigma_0 := -\delta$. Also the response time δ (4.6.3) for square waves is positive and is assumed to have a finite limit δ_∞ for a family of square waves of (4.1.1) where both τ and T are tending to infinity. Accordingly, the system (4.6.1)–(4.6.2) at $\sigma = -\delta$ serves as alternated profile equation for square waves.

Recall now the mirror symmetry γ (4.3.4) given by

$$\gamma : (x, y) \longmapsto (y, x),$$

intrinsic to the system (4.6.1)–(4.6.2). The corresponding subspace of fixed points (4.3.5) under the symmetry γ is given by

$$\mathrm{Fix}(\gamma) := \{(x, y) \mid \gamma(x, y) = (x, y)\} = \{(x, y) \mid x = y\}.$$

The equilibria (x_1, x_2) and (x_2, x_1) given by the period-two orbit of the singular map are hence identical with respect to γ. In particular, they are stable equilibria in the system (4.6.1)–(4.6.2) for all $\sigma > 0$, since the corresponding period-two orbit in the singular map is stable, see [YWPT22]. Consequently, they are both of saddle-type in the APE system (4.6.1)–(4.6.2) for $\sigma = -\delta$ (Corollary 1 in Section 4.3). For $\delta \longrightarrow \delta_\infty$ the period of the square wave increases and, in this case, the corresponding family of periodic solutions approaches a heteroclinic cycle, connecting to the symmetrical equilibria (x_1, x_2) and (x_2, x_1). Both heteroclinics in this cycle are related by γ, as well. Thus, for our computation of the square waves as connecting orbits, it suffices to compute just one of them. Hence, the square wave can be described by a single heteroclinic orbit $(x_h(t), y_h(t))$, $t \in \mathbb{R}$, with

$$\lim_{t \to \pm\infty} (x_h(t),\, y_h(t)) = (x_{1,2},\, x_{2,1}), \tag{4.6.4}$$

i.e. the orbit is connecting (x_1, x_2) with its symmetry twin (x_2, x_1). Accordingly, we call it a *relative homoclinic* with respect to γ. Consequently, we can treat square waves similarly to TDSs and analyse their dynamics by means of homoclinic bifurcation theory. The relative homoclinic together with its corresponding saddle does not lie in the symmetry subspace of γ. Note, that this is diverging from the alternating pulse solutions discussed in Section 4.3, where the homoclinics in the APE do not lie in the symmetry subspace, while their corresponding saddles lie in it.

Recall, that homoclinic solutions are generically objects of codimension-one. For a relative homoclinic (4.6.4), the codimension depends on the number of stable and unstable eigendirections of the corresponding saddles. Together with the symmetry relation here, the codimension is equal to one, as well. Also in the alternated profile equation (4.6.1)–(4.6.2), the response time δ acts as a system parameter and the relative homoclinic can only be found after adjusting one parameter. That is, to solve the alternated profile equation for

a relative homoclinic solution representing a square wave, one needs to solve for the connecting orbit (4.6.4) together with its response time δ_∞. Note that in contrast to solitons, for square waves in the large delay DDE (4.1.1) the response time δ (4.6.3) is given as the difference of half the period and the delay. Accordingly, also when studying the bifurcations of square waves induced by homoclinic bifurcations in the corresponding profile equation, one always has to adjust the parameter δ_∞, increasing the codimension of the associated bifurcation by one.

We have now proposed a mathematical description of temporal dissipative solitons, which allows us to analytically identify the TDSs in the large delay DDE to homoclinic solutions in the profile equation. Furthermore, we have expanded this theory to encompass alternating pulse solutions by deriving the alternated profile equation, which shares similar characteristics with the profile equation while also possessing an intrinsic symmetry. Within this equation, alternating pulse solutions can be analyzed as homoclinics that do not reside in the symmetry subspace, whereas TDSs manifest as homoclinics within the symmetry subspace. Moreover, we discussed the Floquet problem for a critical multiplier corresponding to the period-doubling bifurcation and showed its reappearance in the alternated profile equation. Especially, this framework of the alternated profile equation allows us, thereby, to study temporal dissipative solitons undergoing a period-doubling bifurcation with homoclinic bifurcation theory. Beyond that, we showed how we can also use the alternated profile equation to analyse square wave solutions as a relative homoclinic solution with respect to the mirror symmetry.

CHAPTER 5

The Morris-Lecar model

In this chapter, we introduce the Morris-Lecar model as a representative system showcasing diverse facets of neuronal behaviour due to different excitability types, and discuss the fundamental mechanism underpinning these behaviours, which is a codimension-two bifurcation known as the saddle-node separatrix loop bifurcation.

5.1 The model equations

A crucial role for the emergence of TDSs in time-delayed systems plays excitability. The Morris-Lecar (ML) system, a classical model for neuronal dynamics, offers a nuanced study ground and logical extension to the simpler excitable systems investigated in [YRSW19], cf. Chapter 2, due to its capacity to exhibit different excitability types reproducing different aspects of neuronal behaviour in great detail. The discussion of the Morris-Lecar model in this Chapter is based on our publication in [SW23].

The Morris-Lecar model, introduced in [ML81], is a biophysical model describing the dynamics of an action potential in a neuron. It is a conductance-based model that includes the influence of ionic currents on the voltage in the

cell. The model is given by the following set of ordinary differential equations

$$\begin{aligned}\dot{V}(t) = & -g_{\mathrm{l}}(V(t)-E_{\mathrm{l}}) - g_{\mathrm{K}}w(t)\ (V(t)-E_{\mathrm{K}}) \qquad (5.1.1a)\\ & - g_{\mathrm{Ca}}m_{\infty}(V(t))\ (V(t)-E_{\mathrm{Ca}}),\\ \dot{w}(t) = & \lambda(V(t))\ (w_{\infty}(V(t)) - w(t)), \qquad (5.1.1b)\end{aligned}$$

where V describes the membrane potential and w the recovery. Responsible for a depolarizing current, in this model, are Ca^{++}-ions. The recovery variable describes the fraction of open K^{+}-channels, as these ions are accountable for the production of the hyperpolarizing current. A leakage current involved in maintaining the resting potential is also included. The parameters g_{Ca}, g_{K} and g_{l} describe the instantaneous conductance values for the corresponding pathways, E_{Ca}, E_{K} and E_{l} the equilibrium potentials of the corresponding indicated ions. The voltage-dependent sigmoidal activation functions $m_{\infty}(V)$, $w_{\infty}(V)$ and the time scale $\lambda(V)$ are given as

$$\begin{aligned}m_{\infty}(V) &= \tfrac{1}{2}\left(1+\tanh\left(\tfrac{V-V_1}{V_2}\right)\right),\\ w_{\infty}(V) &= \tfrac{1}{2}\left(1+\tanh\left(\tfrac{V-V_3}{V_4}\right)\right),\\ \lambda(V) &= \tfrac{1}{3}\cosh\left(\tfrac{V-V_3}{2V_4}\right).\end{aligned}$$

The functions $m_{\infty}(V)$ and $w_{\infty}(V)$ describe the probability of open Ca^{++} and K^{+}- channels at equilibrium, respectively, and $\lambda(V)$ is the rate constant for the opening of K^{+}-channels. They involve further parameters V_1, V_2, V_3 and V_4, scaling and shifting the hyperbolic functions to suitable values of the model.

The model was derived in 1981 by C. Morris and H. Lecar [ML81] in their experimental study of the barnacle muscle fibre. The eponymous model emerged as a reduced system in order to facilitate the study of neuronal dynamics. In comparison to e.g. the Hodgkin-Huxley model [HH52], it has a two-dimensional phase space which simplifies the analysis and makes it more graphic. Due to its simplicity whilst retaining most of its dynamical features, this system serves as a computational framework for studying the dynamics of action potentials within neurons. It has been scrutinized, both from the mathematical [BR05; DZL11; ET10; Izh00; Izh07; RE98] and the neuroscientific [LLL13; ML81; TKYAK06] point of view. Notably, depending on the specific values of its

parameters, the Morris-Lecar model can exhibit different forms of excitability, like the Class I and Class II excitability as discussed in a neuroscientific context. They are responsible for the nonlinear response of the system to different kinds of input signals. For a review of the effects of noise in excitable systems, see [LGNS04]. These rich dynamics induced by the different types of excitability make it also interesting for our studies as it can serve as a showcase example for more complicated pulse dynamics compared to the simple excitable phase oscillator system studied in [YRSW19] and [MJG20]. The fundamental mechanism underpinning these behaviours is a bifurcation of codimension-two known as the *saddle-node separatrix loop bifurcation* (SNSL) [CL90; Den90; Sch87]. Below, we will give a detailed overview of this bifurcation.

5.2 The saddle-node separatrix loop bifurcation

The unfolding of the saddle-node separatrix loop bifurcation in the Morris-Lecar model (5.1.1a)–(5.1.1b) will be executed in the parameters V_4 and E_l, and all other parameters will be fixed to the values given in Table 5.1, following Izhikevich [Izh00]. The parameter E_l governs the unfolding of the saddle-node bifurcation of equilibria, i.e. it regulates the distance between the two equilibria. To understand the role of the parameter V_4, consider the nullclines,

$$\mathrm{null}_V(V) = \left(-g_\mathrm{l}(V-E_\mathrm{l}) - g_\mathrm{Ca} m_\infty(V)(V-E_\mathrm{Ca})\right) / (g_\mathrm{K}(V-E_\mathrm{K})), \quad (5.2.1)$$

$$\mathrm{null}_w(V) = w_\infty(V), \quad (5.2.2)$$

which can be computed by setting respectively $\dot{V}=0$ and $\dot{w}=0$. The curves are sigmoidal and can intersect in a variety of ways. Their intersections give the equilibria of the system. Here, V_4 only appears in $w_\infty(V)$. Thus, we see that the parameter V_4 is responsible for the slope of the nullcline $\mathrm{null}_w(V)$.

Figure 5.1 displays schematically the unfolding of a saddle-node separatrix loop bifurcation. The unfolding consists of three codimension-one bifurcation curves meeting in one point, the codimension-two SNSL-point. These curves separate the parameter space into four regions, represented in the sketch by

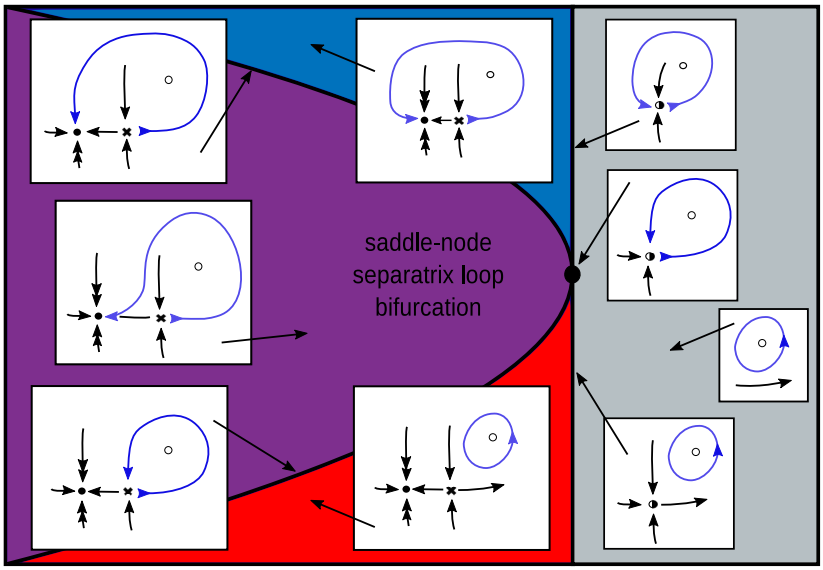

Figure 5.1: Sketch of the general unfolding of a saddle-node separatrix loop bifurcation. Coloured parameter regions correspond to different dynamical regimes. Sketched phase portraits in the insets indicate qualitative dynamics in the regions and at the bifurcations. In the case of the Morris-Lecar model, such an unfolding can be found in the parameters E_l and V_4, see also Fig. 6.5. Figure and Caption taken from [SW23].

different colours, such that each colour displays a different dynamical regime. The vertical bifurcation curve represents a saddle-node bifurcation of equilibria. In the grey region to its right, there is only an unstable equilibrium of saddle focus type and a stable periodic orbit present. To its left, a stable equilibrium

V_1	V_2	V_3	E_K	E_Ca	g_l	g_K	g_Ca
0	0.15	0.1	-0.7	1	0.5	2	1.2

Table 5.1: Parameters for the Morris-Lecar model (5.1.1a)–(5.1.1b) (cf. Izikevich [Izh00]).

and an unstable equilibrium of simple saddle-type appear. Especially, on the upper part of the saddle-node curve above the SNSL point, there is a saddle-node on invariant circle (SNIC) bifurcation. The periodic orbit disappears while a saddle-node appears on it forming a non-generic homoclinic solution. In the blue region, the saddle-node is split into the stable and saddle equilibrium and two heteroclinic orbits are created connecting the saddle equilibrium with the stable one, forming an invariant circle. On the lower half of the saddle-node curve, the saddle-node appears outside the periodic solution (fold off limit cycle). In the red region, there is then a stable periodic solution together with a stable and saddle equilibrium. The parameter space underlying the red coloured area is thusly a regime with bistability.

In the purple region, one finds a regime that displays the same solution types as the blue region, but the course of the heteroclinic orbit with the longer trajectory in phase space has changed. Specifially, one finds a so called heteroclinic orbit flip, located on the codimension-one curve separating the blue from the purple region. This bifurcation has been discussed in detail for homoclinic orbits in Section 3.5 and 3.8 in the introductory part on homoclinic bifurcation theory Chapter 3. Recall from Section 3.4, that the leading eigendirections are given by those eigenvalues closest to the imaginary axis. Generically, a connecting orbit approaches its corresponding equilibria along the leading eigendirections, since they belong to the eigenmodes with the slowest exponential decay rates. In an orbit flip, this condition is violated, and the trajectory approaches its equilibrium along the strong eigendirection. Numerically computed phase portraits of the heteroclinic orbit in the Morris-Lecar model (5.1.1a)–(5.1.1b) undergoing the flip bifurcation are provided in Figure 5.2. Panels (a)–(c) show the heteroclinic orbits before, directly at, and after the flip bifurcation. One can see how the trajectory passes through the leading stable eigendirections (single arrows) of the stable equilibrium in the generic cases in (a) and (c), but "flips" between both configurations by passing through the strong stable eigendirection (double arrows) at the bifurcation (b).

The bifurcation curve separating the purple and red region is a homoclinic bifurcation in the plane. This bifurcation has been discussed in detail for finite dimensions in Section 3.7. The corresponding phase portraits of the homoclinic

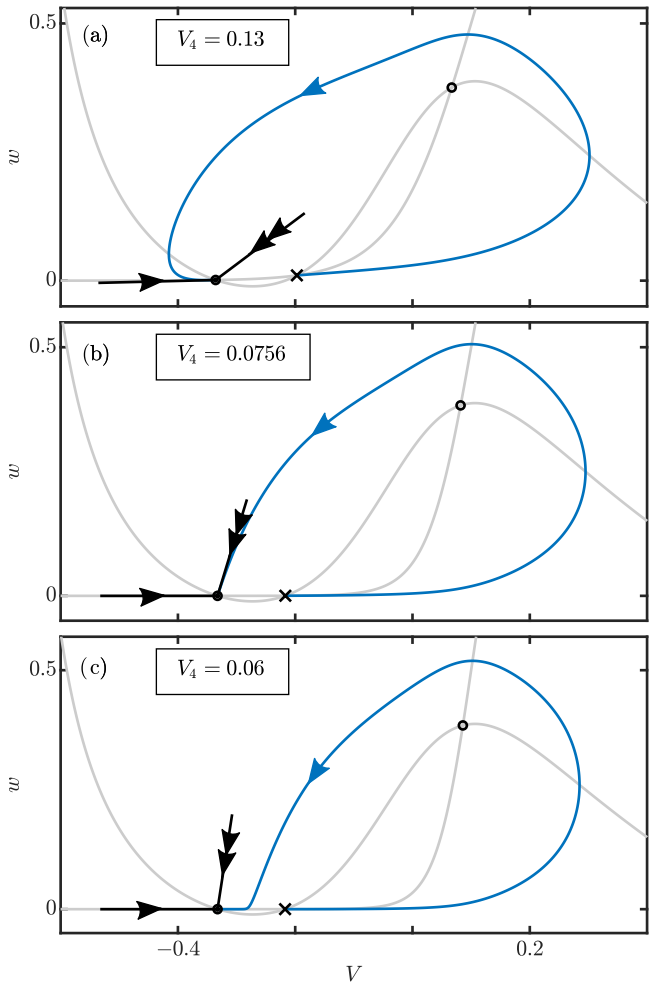

Figure 5.2: Phase portraits of heteroclinic orbits (blue) involved in the heteroclinic orbit flip for the Morris-Lecar model (5.1.1a)–(5.1.1b) without feedback. The different choices of parameter V_4 in panels (a)–(c) represent the situation before, directly at, and after the orbit flip, respectivley. Grey lines: nullclines (5.2.1)–(5.2.2). Stable, saddle and unstable equilibrium are indicated by black dot, cross, and circle, respectively. Leading stable eigendirection of stable equilibrium indicated with one arrow, strong stable eigendirection with two arrows. Other parameters as in Fig. 6.1. Figure and Caption taken from [SW23].

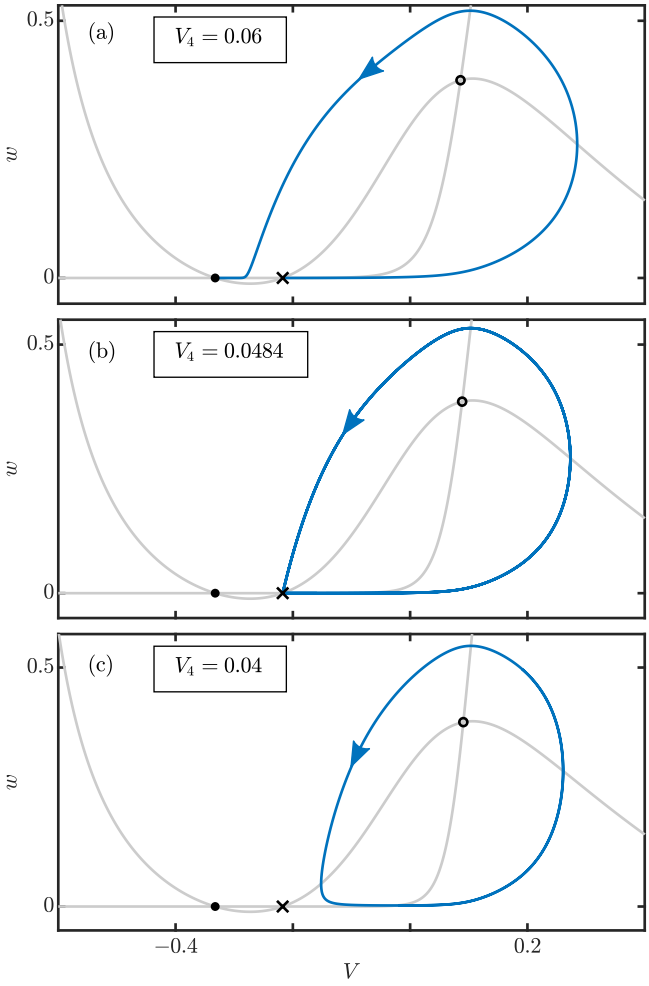

Figure 5.3: Phase portraits of the solutions (blue) involved in the homoclinic bifurcation in the Morris-Lecar model (5.1.1a)–(5.1.1b) without feedback. The different choices of parameter V_4 in panels (a)–(c) represent the situation before, directly at, and after the creation of the homoclinic orbit, respectivley. Grey lines: nullclines (5.2.1)–(5.2.2). Stable, saddle and unstable equilibrium are indicated by black dot, cross, and circle, respectively. Other parameters as in Fig. 6.1.

bifurcation in the Morris-Lecar model are given in Figure 5.3. The stable periodic solution existing in the red region approaches the saddle equilibrium when moving closer to the bifurcation curve (Panel (c)). At the bifurcation curve presented in Panel (b), it intersects with the stable and unstable manifold of the saddle equilibrium and creates a homoclinic orbit. The homoclinic dissolves in the purple region and forms a heteroclinic connection linking the saddle with the stable equilibrium (Panel (a)).

In the next chapter, we will see how the introduction of time-delayed feedback creates different types of solitons in the excitable regime to the left of the saddle-node bifurcation. Their dynamics are strongly influenced by the different parameter regimes and lead to different types of solitons as much as their disappearance.

We have now introduced the Morris-Lecar model and explored the underlying SNSL-bifurcation, which governs the excitability properties in the system. In the following chapter, we intend to study the emergence of TDSs due to the excitability in the Morris-Lecar model when adding a time-delayed feedback. Moving forward, our focus will shift to examining the bifurcations of TDSs in the Morris-Lecar model under time-delayed feedback and establish connections between the dynamics of the solitons and the codimension-one bifurcations stemming from the SNSL-point.

CHAPTER 6

Temporal dissipative solitons in the Morris–Lecar model with time-delayed feedback

In this chapter, we explore the dynamics and bifurcations of temporal dissipative solitons (TDSs) within an excitable system subjected to time-delayed feedback. Utilizing the Morris-Lecar model as a representative system showcasing diverse pulse solutions due to different excitability types, we leverage the large delay limit to treat soliton-like solutions as homoclinic solutions of an equation with an advanced argument. Employing classical homoclinic bifurcation theory, we investigate various pulse solutions and elucidate their dependence on system parameters. Notably, we reveal how a homoclinic orbit flip of a single-pulse soliton triggers the destabilization of equidistant multi-pulse solutions, giving rise to stable pulse packages. Mirroring the excitability properties inherent in the Morris-Lecar model, this transition is intricately linked to a heteroclinic orbit flip in the feedback-absent system. Furthermore, we observe a delocalization of solitons, induced by a heteroclinic bifurcation called Bykov T-point.

6.1 Introduction

This chapter delves into the dynamics of TDSs within the Morris-Lecar model, examining their emergence as a consequence of the interplay between excitability and time-delayed feedback. We utilize the Morris-Lecar model, introduced in Chapter 5, as a prototypical model that demonstrates various types of excitability, making it a promising candidate for the emergence of TDSs that display rich dynamics related to the SNSL-bifurcation. The results presented in this chapter are based on our publication [SW23].

Before exploring the model's rich properties and the employed time-delayed feedback, a brief overview on the different coexisting pulse patterns in Figure 6.1 highlights the main dynamical phenomena appearing in the Morris-Lecar model under time-delayed feedback for different parameter values. There are parameter regions where stable solutions with one or several equidistant pulses per delay interval coexist (blue profiles in Panels (a), (c), and (d)). Stable pulse packages (bursts) appear (purple profiles in Panels (c) and (d)) in a different parameter regime, where those equidistant pulses with more than one pulse per delay interval are unstable. Lastly, there is also a parameter regime, in which all localized solutions are unstable and a rapidly oscillating solution is the only attractor (red trajectory in Panel (b)).

The dynamical behaviour in the different regimes from equidistant pulses to stable pulse packages and, ultimately, to oscillatory solutions are demonstrated in Figure 6.2. It illustrates the slow temporal evolution of the profiles from round-trip to round-trip in a so called space-time representation introduced by [GP96], see also Section 2.2. It gives a coordinate change in which the horizontal axis represents the time within one round-trip, while the vertical axis corresponds to the number of round-trips as discrete time steps. In the parameter region corresponding to stable equidistant pulses in Figure 6.1, we display a single-pulse soliton in Panel (a). In the same regime, an initial condition with two non-equidistant pulses transitions to the stable equidistant configuration, shown in Panel (c). For the parameter regime of stable pulse packages an initial condition similar to an equidistant two-pulse solution approaches a stable two-pulse package solution, see Panel (d). An initial condition with a single pulse in the parameter regime of stable oscillations, see Panel (b),

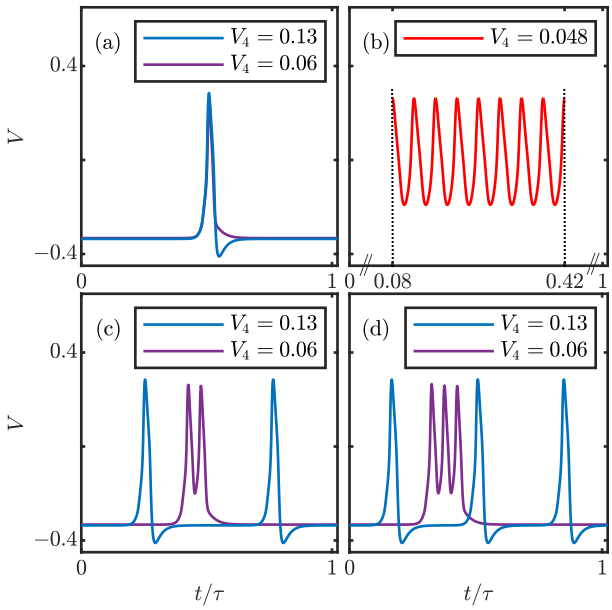

Figure 6.1: Different types of stable periodic solutions of the Morris-Lecar model with time-delayed feedback (6.2.1) for different choices of the parameter V_4. At $V_4 = 0.13$ the single-pulse soliton coexists with equidistant multi-pulse solutions (blue trajectories in panels (a),(c), and (d)). At $V_4 = 0.06$ the single pulse soliton coexists with pulse packages (purple trajectories in panels (a),(c), and (d)). At $V_4 = 0.048$ (b) there is only a stable rapid oscillation. Other parameters: $\tau = 100$, $E_l = -0.37$, $\kappa_V = 0.2$ and as given in Tab. 5.1. Figure and Caption taken from [SW23].

develops a trailing-edge instability. Additional pulses appear over time until the whole delay interval is filled with oscillations.

The primary objective of this chapter is to comprehend these diverse feedback-induced pulse dynamics within the excitable regime. The chapter is structured to first explore the introduction of a time-delayed feedback, elucidating how it engenders TDSs. Before analyzing in detail the different bifurcation scenarios, we give an overview of the stability region and its boundaries in the

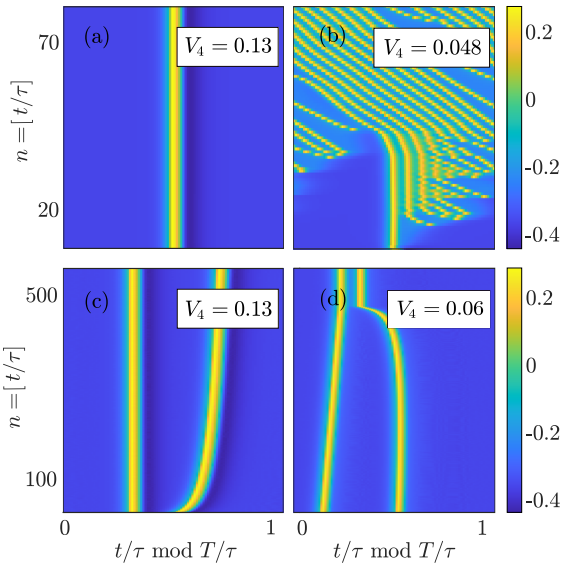

Figure 6.2: Space-time representation of solutions in the Morris-Lecar model with time-delayed feedback (6.2.1): (a) stable soliton at $V_4 = 0.13$, (c) at $V_4 = 0.13$ a two-pulse solution approaches a stable equidistant configuration, (d) at $V_4 = 0.06$ a two-pulse solution approaches a stable pulse package, (b) at $V_4 = 0.048$ the single pulse has a trailing edge instability. Parameters: $\tau = 50$, other parameters as in Fig. 6.1. Figure and Caption taken from [SW23].

Morris-Lecar model under time-delayed feedback in Section 6.3. The ensuing section 6.4 unravels how a heteroclinic orbit flip in the system without time-delayed feedback induces a homoclinic orbit flip in the profile equation. Exploring classical homoclinic bifurcation theory, we deduce the emergence of multi-pulse homoclinics from the bifurcation point, leading to the various pulse dynamics displayed in Figures 6.1 and 6.2. Furthermore, we present in Section 6.5 the delocalization of the solitons caused by a heteroclinic bifurcation called Bykov T-point, leading to a loss of stability of the solitons. This gives rise to the stable rapidly oscillating solutions in Figures 6.1 and 6.2. The corresponding stability boundary induced by the Bykov T-point is then discussed in Section 6.6.

The study applies numerical methods, employing the DDE-BIFTOOL software [ELR02; SELSR16] for path continuation and stability calculations.

6.2 Emergence of solitons in Morris–Lecar model with time-delayed feedback

We want to study the dynamics in the Morris-Lecar model under time-delayed feedback. To this end, set $x := (V, w)$ and let $\tilde{f}(x)$ represent the right-hand side of system (5.1.1a)–(5.1.1b). Then we add a feedback of Pyragas-type, such that the time-delayed Morris-Lecar model is given by

$$\dot{x}(t) = \tilde{f}(x(t)) + \kappa(x(t-\tau) - x(t)), \tag{6.2.1}$$

where the coupling κ is given by a matrix $\kappa \in \mathbb{R}^{n\times n}$ with nonnegative entries.

Feedback terms like this were introduced in [Pyr92] by K. Pyragas in the context of the control of chaos as a method to stabilize an unstable periodic solution. It is a continuous controlling signal that is injected into the system, described by a time-delayed feedback term, where the delay τ is chosen to be equal to the period of the addressed periodic solution. The feedback does not act invasively on the system as it vanishes on this periodic solution, but also equilibria. On that account, the equilibria, and also their saddle-node bifurcations, are preserved for all feedback parameters κ and τ. However, the stability of the solutions in the system might have changed under this type of feedback.

In contrast to that, we intend to use it here to create soliton solutions, where the delay does not exactly coincide with the period of the resulting periodic solution. First, we choose parameters such that the system is excitable, i.e. to the left of the SNIC-bifurcation curve in Figure 5.1. Then we introduce the time-delayed feedback of Pyragas-type in the Morris-Lecar system (5.1.1a)–(5.1.1b) such that the resulting system is of the form (6.2.1) with a delay $\tau > 0$ that is substantially larger than the duration of a pulse. Moreover, we choose

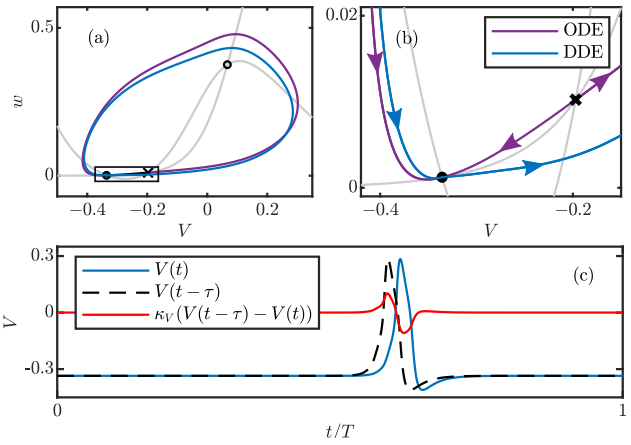

Figure 6.3: (a) Phase portrait of a soliton solution at $\kappa_V = 0.2$ (blue) and of the heteroclinic orbits without feedback at $\kappa_V = 0$ (purple) in the Morris-Lecar model. (b) Enlargement of framed region in (a) close to the background equilibrium. (c) Time traces of the soliton and of the feedback-term. Parameters: $V_4 = 0.13$, other parameters as in Fig. 6.1. Figure and Caption taken from [SW23].

a coupling strength κ, such that the stability of the equilibria persists. To this end, we choose

$$\kappa = \begin{pmatrix} \kappa_V & 0 \\ 0 & 0 \end{pmatrix}, \tag{6.2.2}$$

and set $\kappa_V = 0.2$, keeping it fixed for our entire bifurcation analysis in Chapter 6. Introducing a time-delayed feedback generates an infinite dimensional phase space. On the spectral level, this induces the appearance of infinitely many additional stable eigenvalues from $-\infty$ for small $\tau > 0$, which accumulate at the imaginary axis for $\tau \longrightarrow \infty$. For our choice of coupling strength κ, the stable equilibrium from the ODE remains stable also for arbitrarily large delay, i.e. it is absolutely stable, see [YWPT22] and Definition 1 in Section 2.4. This equilibrium will serve us as background for the solitons.

The threshold of excitation of this system is given by the stable manifold

of the saddle equilibrium appearing through the fold. Note, that the stable manifold is infinite-dimensional in the system with time-delayed feedback. A small perturbation away from the stable equilibrium can lead the trajectory across the threshold and result in the generation of a spike before returning to the stable equilibrium. The time-delayed feedback now can induce an excitation pulse, that instead of decaying to the stable equilibrium, triggers a subsequent pulse. This leads to periodic solutions, where each of the subsequent pulses is triggered by the previous one entering the feedback loop. Figure 6.3 (a) displays the trajectories of the ODE consisting of the two heteroclinic orbits (purple trajectories) and a soliton of the DDE (blue). The trajectories lie close in the phase plane, but the zoom in Panel (b) reveals that close to the equilibria, the trajectories point in opposing directions. This is exactly the moment, when the feedback term $\kappa(x(t-\tau)-x(t))$ is nonzero (cf. Panel (c)), leading the trajectory across the excitation threshold. Thereby, in the present case, the Pyragas control is an invasive feedback term, as it does not entirely vanish on the corresponding targeted TDS. For a sufficiently large delay, the above-described mechanism leads to the generation of TDSs and, especially, it then works for all large enough delays. The appropriate choice of κ to obtain stable TDSs is related to the distance of the two equilibria created in the saddle-node bifurcation. If the equilibria are closer together, i.e. closer to the saddle-node bifurcation, also smaller values of the feedback can trigger an excitation pulse inducing TDSs. Beyond that, the influence of different dynamics induced by the excitability remains strong for our choice of a small coupling strength κ_V.

Our intention now is to use the large delay limit as an approximation for the case of large but finite values of the delay. Recall the following details on TDSs from the introductory part in Chapter 2. Solitons in time-delayed systems appear as families of periodic solutions parametrized by the delay τ with corresponding periods $T(\tau)$. The response time, cf. Equation (2.1.3) in Section 2.1, is given by $\delta(\tau) := T(\tau) - \tau$, which is always positive and has a finite limit δ_∞ for $\tau \longrightarrow \infty$. It was demonstrated in Section 2.4, that the profile of a soliton can be calculated not only as a periodic solution of the DDE with large delay τ, but also for τ replaced by $-\delta$, giving us the profile equation, cf. equation (2.4.3). Thereby, the family of solitons turns into a family of periodic

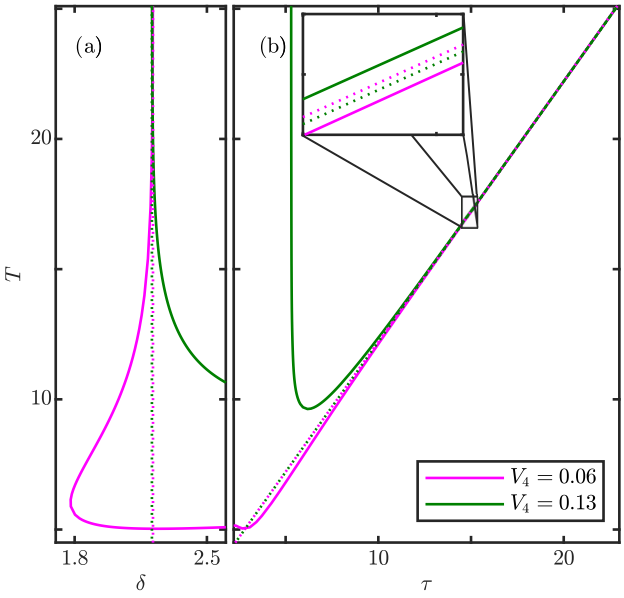

Figure 6.4: Branches of periodic solutions in the profile equation (a) and in the large delay DDE (b) for two different choices of V_4. In the DDE (b), the branches approach the lines $T(\tau) = \tau + \delta_\infty$ (dashed), while both T and τ become infinite. In the profile equation (a), each branch approaches a vertical line at $\delta = \delta_\infty$ with $T \longrightarrow \infty$ in a homoclinc bifurcation. Other parameters as in Fig. 6.1. Figure and Caption taken from [SW23].

solutions, which in the limit, approach a homoclinic orbit. The homoclinic approaches the background equilibrium for $t \longrightarrow \pm\infty$ which is of saddle-type in the profile equation.

Figure 6.4 exhibits the connection between the original DDE with large delay and the profile equation. Panel (b) shows typical branches of solitons: a branch of periodic solutions that exists for all large τ, while its period $T(\tau)$ approaches the line $T(\tau) = \tau + \delta_\infty$ (dotted lines). Note that the figure shows two branches of solitons for two different V_4 values, displayed in magenta and green and their limiting response times δ_∞ are slightly distinct. Panel (a) shows the situation in the profile equation. Each branch of solitons reappears to a

branch of periodic solutions, whose periods increase when δ approaches their corresponding critical δ_∞. The large-period periodic solutions belong to a generic homoclinic bifurcation. The homoclinic orbits limiting to the branches of periodic solutions for different V_4-values both approach the background equilibrium, which turns naturally into a saddle in the profile equation.

The soliton solutions on the branches for the two different V_4-parameters in Figure 6.4 represent the two different regimes of the Morris-Lecar model without feedback, shown in Figure 5.1, respectively in purple and blue. The profiles differ by the undershoot in V (hyperpolarization), which is not present in the purple region. This different shape of the trajectory comes together with a qualitative difference in the response time $\delta(\tau)$. Whereas in the blue region, the response time $\delta(\tau)$ for finite τ is bigger than its asymptotic value δ_∞, in the purple region it is smaller. In Section 6.4, it will be revealed, how this difference is connected to the heteroclinic orbit flip in the ODE and how it leads to the appearance of different multi-pulse solutions.

6.3 SNSL-bifurcation under time-delayed feedback

We will study now the existence and bifurcations of TDSs using the profile equation of the Morris-Lecar model (5.1.1a)–(5.1.1b). To this end, one can apply standard methods of numerical path-continuation, see also [GR23]. We will study the resulting system using the continuation package DDE-BIFTOOL ([ELR02; SELSR16]). This toolkit allows the numerical computation of periodic solutions treated as boundary value problems with periodic boundary conditions. Periodic solutions can be continued by varying a parameter and adjusting the period accordingly. To continue a periodic solution with a fixed period, an additional parameter must be varied as well. The package allows additionally for the computation of connecting orbits, which are implemented as boundary value problems within a finite time domain. These boundary conditions use projections into the spectral eigenspaces of the corresponding saddle equilibria, as described in more detail in references [Bey90; SER02]. Recall, that generic homoclinics are objects of codimension-one, meaning that

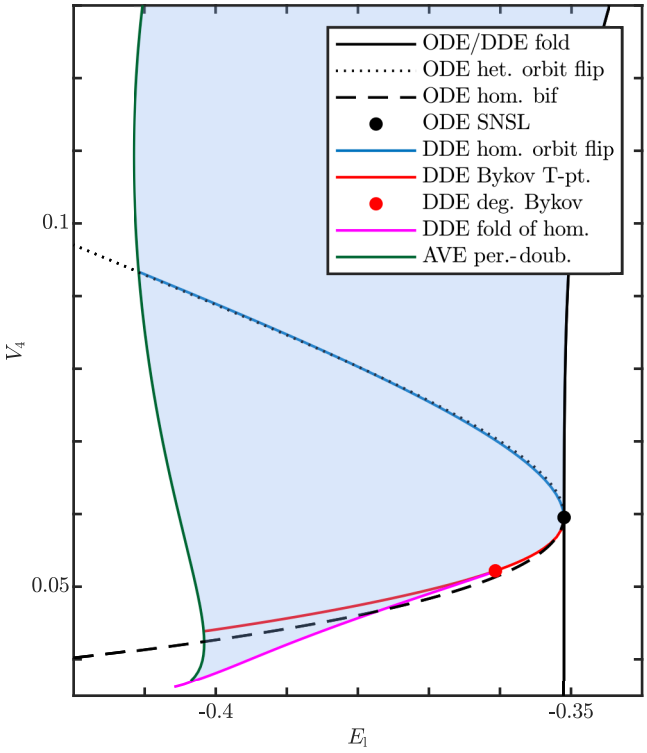

Figure 6.5: Stability region (blue) and bifurcation curves (coloured) of the single-pulse soliton in the DDE system $\kappa_V = 0.2$ and bifurcations of the ODE system $\kappa_V = 0$ (black) with SNSL point in the (E_l, V_4)-parameter plane, cf. schematic picture in Fig. 5.1. Other parameters as in Fig. 6.1. Figure and Caption taken from [SW23].

for their computation solving for one parameter suffices. For a continuation of generic homoclinics one needs to free yet another parameter. Furthermore, it is important to note that when dealing with systems featuring an advanced argument, a time reversal is necessary for an implementation in DDE-BIFTOOL.

In Figure 6.5, we show the bifurcation diagram of the solitons in the neighbourhood of the SNSL point in the (E_l, V_4)-parameter plane. The existence region of the stable solitons is given in blue and lies in the excitable regime

of the system without time-delayed feedback. It depends on the choice of coupling strength κ_V and the distance to the saddle-node bifurcation. Moving away from the saddle-node, the distance between the stable and saddle equilibrium grows until the given feedback strength is no longer sufficient to overcome the excitation threshold and sustain the generation of subsequent pulses. Then again, for decreasing values of κ_V, the distance of the stability boundary from the saddle-node becomes smaller. The left stability boundary is given by a subcritical period-doubling (green curve in Figure 6.5). Remarkably, the period-doubling bifurcation cannot be found in the profile equation, see Remark 2 in Section 4.4. We will discuss this bifurcation further in Chapter 7, employing the alternated profile equation, developed in Section 4.3, that covers period-doublings of solitons in the framework of homoclinic bifurcations. For the computation of this stability boundary here, we use an alternative to the profile equation given by the alternated variational equation (AVE) (4.4.17)–(4.4.21) in Section 4.4. This tool gives qualitatively the same result as the path-continuation of solitons in the original large delay DDE, which was used at this point in the publication [SW23].

Notably, the other bifurcations are induced by the bifurcations from the Morris-Lecar model without feedback, described in Section 5. They are given by the black lines in Figure 6.5 and correspond to the codimension-one bifurcations emanating from the SNSL-point, cf. Figure 5.1. Close to the homoclinic bifurcation of the Morris-Lecar model without feedback (black dashed line) there is another stability boundary of the solitons. It originates from bifurcation curves connected to the unfolding of a Bykov T-point (red) in the profile equation. This is a particular homoclinic bifurcation of codimension-two, involving a structurally unstable heteroclinic cycle between two hyperbolic equilibria, studied in [Byk93; GS86; KLW14], see also [HS10] or Section 3.10 of the review part on homoclinic bifurcation theory in Chapter 3. This bifurcation will be further discussed in Section 6.5 and the resulting stability boundary for TDSs in Section 6.6. The boundary value problem for the numerical computation of the heteroclinic cycle created in the Bykov T-point is developed in [Bey90; SER02] and we provide some details to it in the Appendix A.1.

In the interior of the stability region, there is the heteroclinic orbit flip

(black dotted line) of the system without feedback. It is accompanied by a homoclinic orbit flip of the system with feedback (blue curve). The homoclinic orbit flip is a bifurcation of codimension-two, cf. [San93] or Section 3.8. It can be computed by a continuation of a connecting orbit with the corresponding asymptotic behaviour in the profile equation. The corresponding boundary value problem, that we implemented for the numerical continuation of the orbit flip is presented in the Appendix A.3. The unfolding of the homoclinic orbit flip induces intriguing dynamics involving solutions consisting of multi-pulses and will be discussed in detail in the following section.

6.4 Homoclinic orbit flip in the profile equation induces pulse packages in the original DDE

Figure 6.6 depicts the phase portraits of the trajectories in the profile equation. Similarly to the ODE case, cf. Figure 5.2, it shows connecting orbits undergoing a flip bifurcation. Recall, that in the profile equation, the background equilibrium x_0 is of saddle-type. The eigendirections of the saddle equilibrium are given by the eigenfunctions of the linear delay operator. The projection of the stable eigendirections to the (V, w)-phase plane is shown by the black arrows, where the single arrows indicate the leading eigendirection and the double arrow the strong stable eigendirection. For $t \longrightarrow -\infty$ the homoclinic approaches the equilibrium along the leading unstable eigendirection. Recall, that in the eigenvalue spectrum of the linearized profile equation, infinitely many unstable eigenvalues appear from $+\infty$ for small $\delta > 0$. Their projection is not included in the figures for reasons of visibility. Panel (a) shows a homoclinic before the flip when the trajectory approaches the saddle along the leading stable eigendirection from the left. At the orbit flip in Panel (b), the homoclinic passes through the strong stable eigendirection. Then, the trajectory passes to the other side and the homoclinic orbit approaches its saddle again along the corresponding leading stable eigendirection from the right in Panel (c).

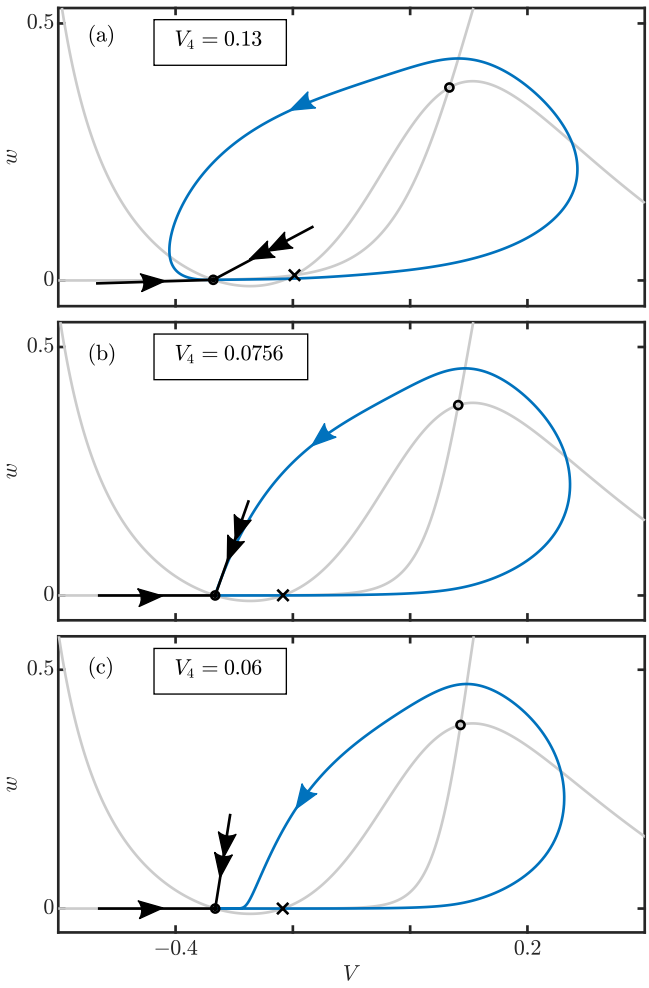

Figure 6.6: Homoclinic orbit flip in the profile equation. The different choices of parameter V_4 in panels (a)–(c) represent the situation before, directly at, and after the orbit flip, respectivley. The corresponding saddle equilibrium of the homoclinics is given by the black dot. Projection of leading stable eigendirection of stable equilibrium indicated with single arrow, of strong stable eigendirection indicated with double arrow. Nullclines are given by the grey curves. Black cross and circle refer to the saddle and unstable equilibrium of the ODE. Parameters: $\kappa_V = 0.2$, $T = 100$, other parameters as in Fig. 6.1. Figure and Caption taken from [SW23].

In the two-dimensional ODE case without feedback the heteroclinic orbit flip is of codimension-one. Its unfolding does not generate more structures than the ones given in Figure 5.2. Yet in general, the homoclinic orbit flip is a codimension-two phenomenon occuring in an at least three-dimensional phase space, see [San93] or the review in Section 3.5. The time-delayed feedback induces infinitely many further dimensions to the phase space and makes the generation of more complex structures possible. For the analysis of high dimensional structures, one usually applies then a centre manifold reduction. This tool to reduce the dimensions has already been discussed for the finite dimensional case in Section 3.6. For the construction of a centre manifold of an equilibrium in DDE systems, see [DG91; DVGLW95; VV87]; however, theory for the construction of a centre manifold around a homoclinic solution in DDE systems is still missing. Nonetheless, the principal dynamics appear to be three-dimensional and, therefore, we will *assume* that, in this case, a sufficiently smooth centre manifold of the homoclinic solution can also be obtained, allowing us to apply the results of the finite-dimensional case of orbit flips to the present case. The continuation of the connecting orbit together with an orbit flip condition (blue curve in Figure 6.5) in the profile equation is applied including the parameters V_4, E_1, and δ. The corresponding boundary value problem is presented in the Appendix A.3.

The branches of periodic solutions corresponding to the homoclinics displayed in Panels (a) and (c) of Figure 6.6 were shown in Panel (a) of Figure 6.4. In contrast to the branch at $V_4 = 0.13$ (green), the branch corresponding to $V_4 = 0.06$ (magenta) displays a fold of limit cycles. Approaching the homoclinic orbit flip, the fold of limit cycles on the corresponding branch of periodic solutions occurs for increasing periods until it collides with the homoclinic bifurcation and disappears. Indeed, according to general homoclinic bifurcation theory, see e.g. [HS10] and references therein or the review in Section 3.5, a homoclinic orbit flip can be accompanied by further codimension-one bifurcations emanating from the bifurcation point. The unfolding of the orbit flip in the present case induces infinitely many branches of N-homoclinics. Moreover, similarly to the fold bifurcation, there are period-doublings and resonant Neimark-Sacker bifurcations of the accompanying periodic orbits with

large periods that collide with the homoclinic bifurcation at the critical parameter of the flip bifurcation. These bifurcations are related to the creation of the multi-pulse solutions, presented in Figure 6.1 in the following way: As discussed in Section 6.2, periodic solutions of a delay equation are also solutions at other delay values, which are given by the reappearance rule (2.4.1). This induces multi-pulse solutions in a natural way. Indeed, applying the reappearance rule (2.4.1) with $m \geq 1$ to a soliton solution with a single pulse at delay τ ($m = 0$), we obtain multi-pulse solutions with several pulses within one delay interval of length $\tau_m = \tau + mT$, that are equidistant. The distance between neighbouring pulses is T, corresponding to the minimal period of the multi-pulse solution as well as the primary soliton. For a soliton with a single pulse per delay interval, each pulse is triggered by its preceding pulse. In contrast to that, in these multi-pulse solutions, a pulse is triggered by the m-th preceding pulse. This is corresponding to the pulse in the delay interval which has a distance of exactly mT to the current pulse. Regardless of the stability of the primary soliton, the multi-pulse solutions can be stable or unstable. In particular, the stability of the multi-pulse solutions depends on the stability with respect to their relative distance, causing pulses to be either attracting or repelling. The N-homoclinics in the profile equation, however, correspond to soliton solutions with a localized pulse package consisting of N pulses. Formally, they can be treated analogously to single-pulse solitons in the sense of Definition 3 from Chapter 4.1. On the other hand, for the equidistant N-pulses one can adapt Definition 5 of Chapter 4.3 to these kinds of solutions. Therefore, one mainly has to replace the delay τ with $\tau + (N-1)T$ and the subset $I(\epsilon)$, giving the time intervals in which the pulse occurs, consists of N subintervals. Since the equidistant N-pulse solutions are related by the reappearance rule for all $N \in \mathbb{Z}$, these solutions then correspond to a 1-homoclinic in the profile equation.

Figure 6.7 displays branches of multi-pulse solutions obtained from numerical continuations with varying parameter V_4, in a parameter neighbourhood of the orbit flip bifurcation. Whereas the orbit flip is not affecting the soliton solution, it has drastic consequences on the stability of the multi-pulse solutions. The equidistant multi-pulse solutions turn out to be stable to the right

of the orbit flip. This corresponds to the parameter regime associated with the blue region in Figure 5.1. At the orbit flip point, the equidistant multi-pulse solutions become unstable and the pulses start to attract each other. Accordingly, branches of stable non-equidistant multi-pulse solutions emerge. This loss of stability is connected to the other codimension-one bifurcations. The equidistant 2-pulse solutions lose their stability through a period-doubling bifurcation; resonant Neimark-Sacker bifurcations destabilize the equidistant pulse solutions accommodating larger numbers of pulses. This can be explained by the reappearance of critical Floquet multipliers in Lemma 1 of [GR23], see also Section 2.6.

The pulse packages emerging from the orbit flip are packed tighter the more one moves away from the orbit flip, see insets in Figure 6.7. In Panels (a) and (b), two different distance measures are used to display the branches. The value

$$N_{x_0} = ||h - x_0||_{L^2}^2 \tag{6.4.1}$$

measures the L^2-distance of a solution profile h to the background equilibrium x_0. In this measure, the branches of N-pulse solutions are distinguishable. Similarly, the branches of unstable equidistant pulses (dashed) and corresponding stable pulse packages become visible. With

$$N_h = ||h - h_{V_{flip}}||_{L^2}, \tag{6.4.2}$$

a different measure is used in Panel (b). It computes the distance of a solution profile h to the corresponding profile with N equidistant pulses from the orbit flip. Panel (b) reveals that the pulse packages become equidistant at the orbit flip and the shapes of the pulses coincide with the single pulse solution. For large delay, the N-pulse packages emerge from the profile corresponding to the degenerate homoclinic at the critical value at $V_4 = V_{flip}$. This implies the coexistence of stable equidistant N-solitons for $V_4 > V_{flip}$ and stable N-pulse packages for $V_4 < V_{flip}$ in the large delay DDE.

Recall that homoclinic bifurcation theory predicts the emergence of an infinite number of N-homoclinics from the orbit flip point, for all natural numbers $N \in \mathbb{N}$. These homoclinics come together with a family of large period periodic

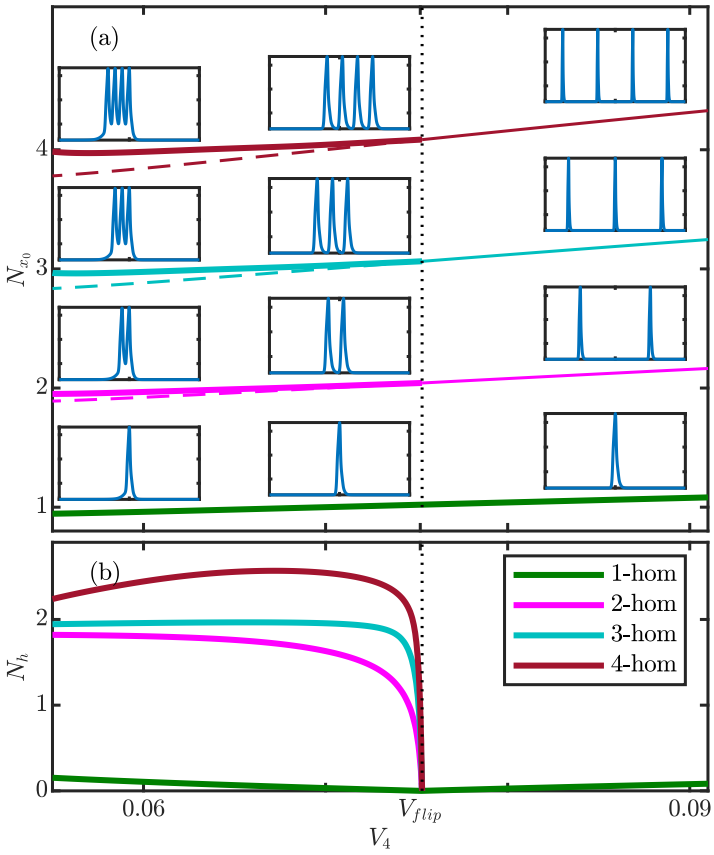

Figure 6.7: Homoclinic orbit flip along the branch of single pulse solitons (green curves) induces bifurcations along the branches of multi-pulse solutions (curves of other colours). For $V_4 > V_{flip}$ the equidistant multi-pulse solutions are stable. For $V_4 < V_{flip}$ the equidistant multi-pulse solutions are unstable (dashed curves) and stable non-equidistant multi-pulse solutions bifurcate (solid curves). Along the branch they turn into pulse packages with decreasing spacing of the pulses (see insets). The quantities N_{x_0} and N_h, used in panels (a) and (b) are given in (6.4.1) and (6.4.2), respectively. Parameters: $\kappa_V = 0.2$, $T = 100$, other parameters as in Fig. 6.1. Figure and Caption taken from [SW23].

solutions, consisting in this case of multi-pulse solutions. For approximations of the homoclinics by large-period periodic solutions, however, the number N of existing multi-pulse solutions is then finite and equal to the number of the possible pulses that fit within an interval of the length of a period. After applying the reappearance rule in the reversed direction, we obtain then multi-pulse solutions in the large delay DDE. When we increase now the delay, the number of possible pulses gradually increases. This reminds of a similar scenario of multi-pulse solutions discussed in a detailed bifurcation analysis of the Yamada model with delayed feedback [TKB17; TPKBB21]. Treating the delay as the main bifurcation parameter and using classical numerical bifurcation analysis, their approach is restricted to moderate values of τ and gives a detailed picture of the effects caused by the finite delay and the changing number of admissible pulses for varying delay.

6.5 Bykov T-point in the profile equation induces delocalization of TDSs in the large delay DDE

When passing from the purple parameter regime to the red separated by the homoclinic bifurcation in the ODE system, cf. Figure 5.1, also the dynamics of TDSs in the Morris-Lecar model under time-delayed feedback change. Then, the TDSs, including the pulse packages that appeared through the orbit flip discussed in the previous section, experience a delocalization that leads to a destabilization of the solutions. This is due to a so called Bykov T-point in the profile equation. For details to this bifurcation see [Byk93; GS86; KLW14], or the review in Section 3.10. It refers to a homoclinic bifurcation of codimension-two, in which a homoclinic orbit to a hyperbolic equilibrium collides with a secondary hyperbolic equilibrium and creates a structurally unstable heteroclinic cycle connecting to both equilibria. In its unfolding, there are two curves of homoclinics to either one of the two equilibria that meet at the T-point corresponding to the heteroclinic cycle. This bifurcation is only possible in dimensions three or higher. Similarly to the orbit flip case, we need

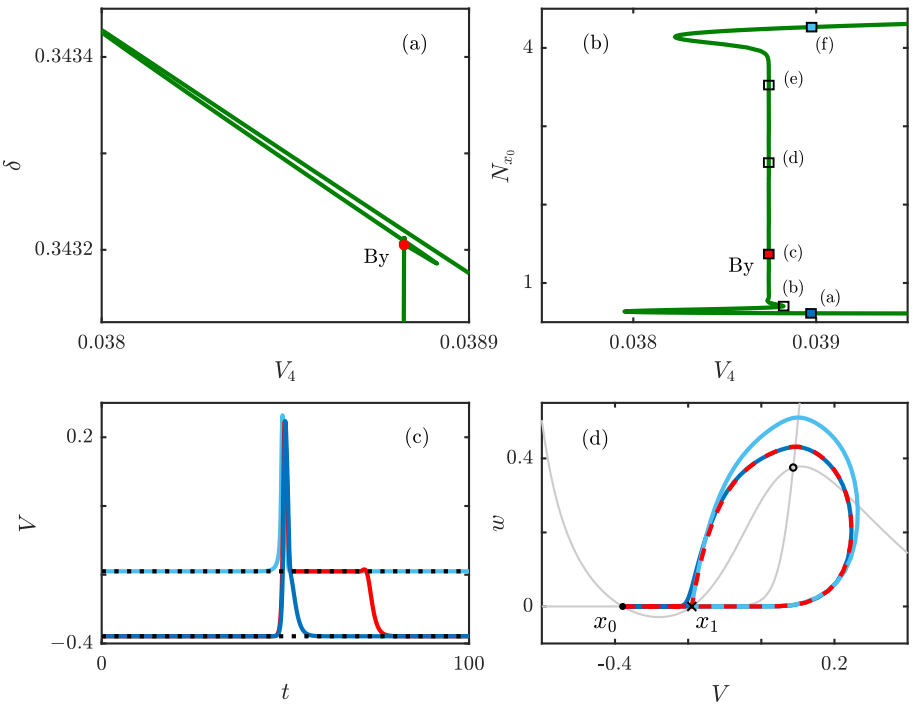

Figure 6.8: Panel (a) Branch of periodic solutions (green) accompanying homoclinic solutions passing through a Bykov T-point (red), (b) plotted versus N_{x_0} given in (6.4.1). Profiles of selected solutions along the branch are given in Panel (c), their corresponding phase portrait in Panel (d). Colours indicate the position along the branch in (b). The Floquet spectrum of selected periodic solutions (a)–(f) in the large delay DDE is given in Fig. 6.9. Parameters: $E_\mathrm{l} = -0.4$, $\kappa_V = 2$, $T = 100$, and as in Fig. 6.1.

to reduce the dimensionality of the system in order to apply the results from the finite-dimensional case, presented in Section 3.10. In the case presented here, the principal dynamics appear to be also three-dimensional, and therefore, we assume, that there is a sufficiently smooth, three-dimensional centre manifold, containing the corresponding connecting orbits and all recurring dynamics nearby.

Recall, that the stable background equilibrium x_0 in the Morris-Lecar system is created in a saddle-node bifurcation, cf. solid black line in Figure 6.5. Let us refer to the saddle equilibrium emerging from this bifurcation with x_1. Note that in the profile equation, these two equilibria are of saddle-type, yet only the background equilibrium x_0 is stable in the original DDE system. Figure 6.8 presents an overview of the unfolding of the Bykov T-point. Using large-period periodic solutions as an approximation of the homoclinic in the profile equation, the branch of periodic solutions (green) undergoes a number of folds, see Panel (a) or Panel (b) for an unwrapped version of the spiral in a snaking scenario. To this end, we use N_{x_0} (6.4.1) to measure the L^2-distance of a solution profile h to the background equilibrium x_0. Panel (c) displays the profiles of selected solutions along the branch indicated by the squares filled with the same colour in Panel (b). They correspond to a periodic solution from the bottom of the branch (blue), at the T-point (red), and top of the branch (light blue). In Panel (d), we show the solutions in the phase portrait. Whereas the solutions from the bottom of the branch spend most of the time near the equilibrium x_0, the periodic solutions along the branch spend an increasing amount of time near the equilibrium x_1. That is, the corresponding homoclinic orbits in the profile equation along the branch exchange their respective saddle equilibria. Using the reappearance rule (2.4.1), the periodic solutions from the bottom of the branch in the profile equation are mapped to solitons in the large delay DDE having x_0 as background, that is a stable equilibrium in the DDE. In contrast to that, the solutions from the top reappear to solitons with the saddle equilibrium x_1 as background, which is unstable in the DDE. Moreover, the periodic solutions approaching the heteroclinic cycle (red) corresponds to a solution that has plateaus near both equilibria. Hence, the solitons gradually exchange their background from a stable to a saddle equilibrium along the branch. The switch of background through the Bykov T-point induces a loss of stability of the soliton in the present case.

In Section 2.5, it was presented that the Floquet spectrum of a soliton can be subdivided into the interface spectrum and the pseudo-continuous spectrum. Whereas the interface spectrum consists of a finite number of multipliers and is governed by the profile of the soliton, the pseudo-continuous spectrum,

given by (2.5.7), is entirely determined by the corresponding background. For $\tau \longrightarrow \infty$ an increasing number of multipliers accumulate at the limiting curve. Instabilites and bifurcations of solitons can be induced by a critical point spectrum and homoclinic bifurcations. A critical pseudo-continuous spectrum is related to the instabilities of the background and a possible delocalization of the soliton. Accordingly, one can also observe the switch of the background in the spectrum of the large delay DDE.

Figure 6.9 (a)–(f) shows the Floquet spectrum computed in the large delay DDE of selected profiles along the branch in Figure 6.8 (b) indicated by the same labels. Panel (a) depicts the spectrum of a stable soliton corresponding to a periodic solution from the bottom of the branch. All Floquet multipliers lie inside the unit circle (grey), besides the trivial multiplier at 1, and accumulate at the pseudo-continuous spectrum (blue) with respect to the background equilibrium, which is here the stable equilibrium x_0. Computing the pseudo-continuous spectrum, given by (2.5.7), with respect to the saddle equilibrium x_1 yields a curve (purple), that leaves the unit circle. Recall, that in Figure 6.8 the branch undergoes a cascade of folds in the unfolding of the Bykov T-point. After every fold, a simple real eigenvalue crosses the unit circle until the T-point is reached, see Panels (b)–(c). Afterwards, they rearrange, and two-by-two, form complex conjugate pairs. These move towards the pseudo-continuous spectrum determined by the saddle equilibrium x_1, see Panels (d)–(e). In Panel (f), we see then the spectrum of a periodic solution that has fully transitioned to a soliton which has the saddle equilibrium x_1 as background. Finally, in the present case, where one equilibrium is of saddle focus type, the branch obtained for period $T \longrightarrow \infty$ corresponding to homoclinics to the simple saddle equilibrium, undergoes infinitely many folds.

In Figure 6.10, we show the eigenfunctions (red) of a multiplier from the Floquet spectrum presented in Figure 6.9. To this end, we selected a multiplier from the pseudo-continuous spectrum in Panel (a), indicated by the black asterisk, and tracked its change of position in Panels (b)–(f), as it moves outside the unit circle and settles at the pseudo-continuous spectrum associated with the saddle equilibrium x_1. In Panels (a)–(f), we present then a selected eigenfunction of the corresponding multiplier from the panels in Figure 6.9, identified by

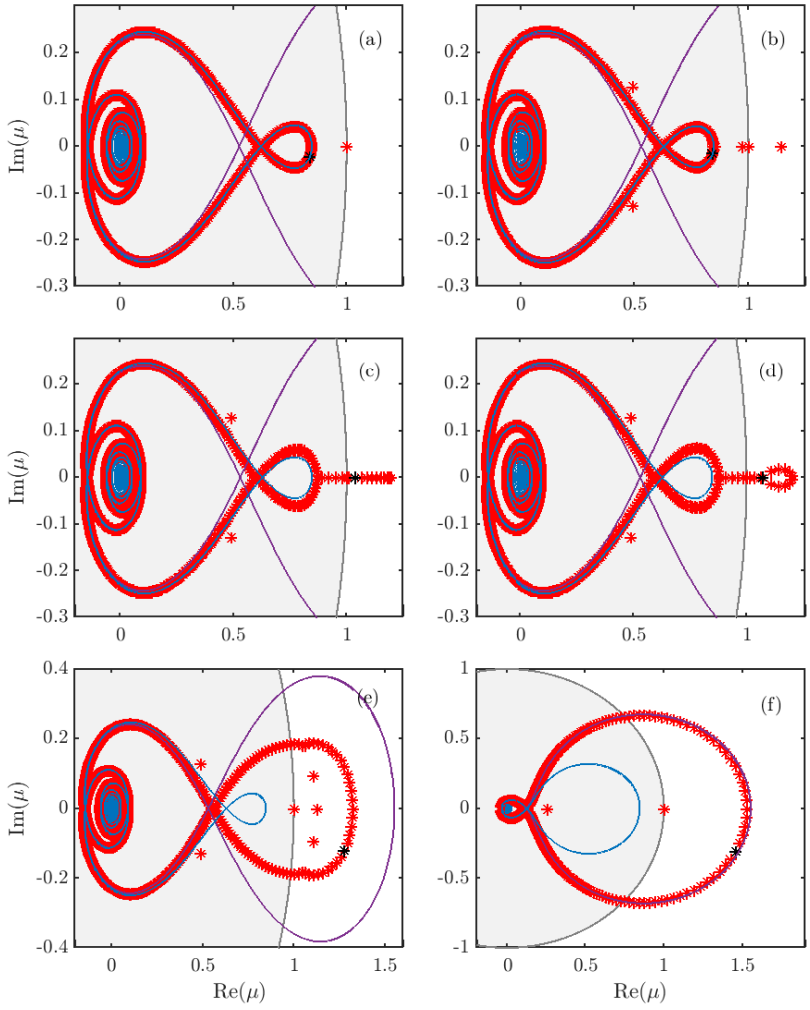

Figure 6.9: The Floquet spectrum in the large delay DDE of selected profiles from Panel (b) of Fig. 6.8 indicated correspondingly with (a)–(f). Numerical computed multipliers (red), PCS to stable background x_0 (blue), PCS to saddle equilibrium x_1 (purple), unit circle (grey). Floquet eigenfunction of selected multipliers (black asterisks) given in Fig. 6.10. Parameters: $E_l = -0.4$, $\kappa_V = 2$, $T = 100$, and as in Fig. 6.1.

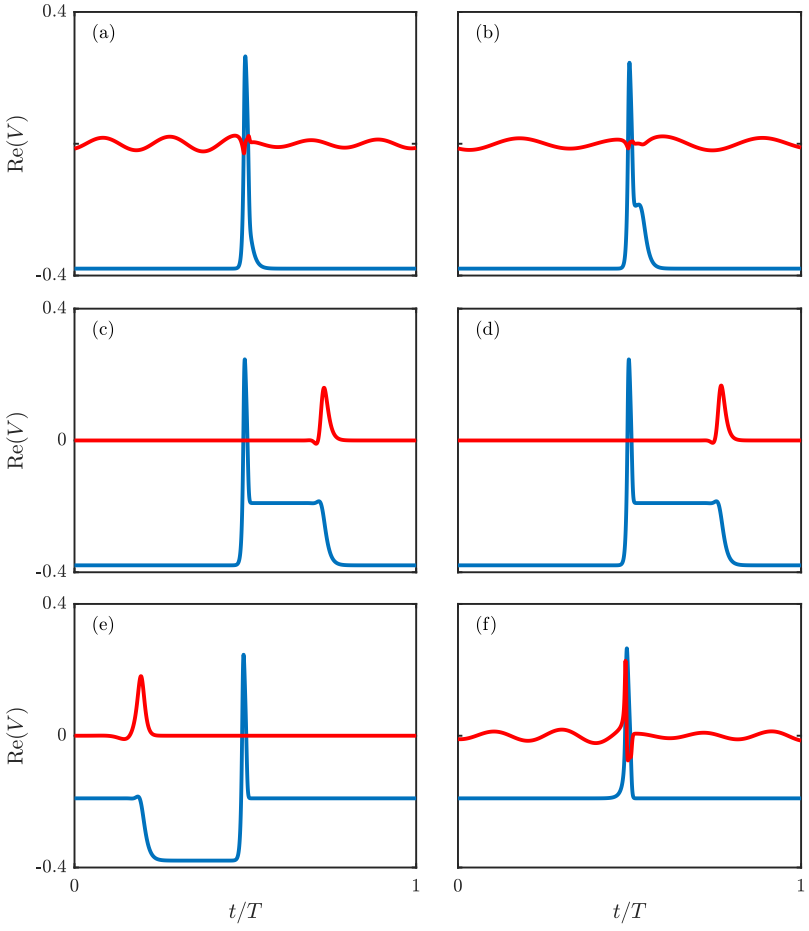

Figure 6.10: Profiles of Floquet eigenfunctions (red) in the large delay DDE of a selected multiplier (black asterisks) in spectrum presented in Fig. 6.9, together with the profile of the corresponding TDS (blue) along the branch in Fig. 6.8, assigned correspondingly with (a)–(f). Parameters: $E_1 = -0.4$, $\kappa_V = 2$, $T = 100$, and as in Fig. 6.1.

the same label. Whereas the profile of the eigenfunction in Panel (a) shows the fast oscillations, typical of a multiplier from the pseudo-continuous spectrum, the oscillations vanish, when the mutliplier becomes real and passes through 1. At this stage, the eigenfunction develops a pulse around the shoulder of the profile of the corresponding TDS (blue). Finally, the eigenfunction shows rapid oscillations again as the multiplier becomes complex once more and realigns at the pseudo-continuous spectrum of x_1.

Note, that for the results in Figures 6.8 and 6.9, we used a larger coupling strength than for the other Figures. In the original parameter regime, the saddle equilibrium is strongly unstable but weakly stable, following the terminology of [LWY11]. That is, the eigenvalue spectrum of the saddle equilibrium x_1 has a pseudo-continuous spectrum, that is lying entirely to the left of the imaginary axis. For the solitons, this leads to a corresponding pseudo-continuous spectrum, that lies entirely inside the unit circle. For the larger coupling strength presented in the Figures, the saddle equilibrium is weakly unstable. Hence, the pseudo-continuous spectrum in the eigenvalue spectrum of the saddle also crosses the imaginary axis. Now the pseudo-continuous spectrum of the corresponding soliton does not lie entirely inside the unit circle. In this case, the transition of the background of the soliton can be more coherently observed in the spectrum, justifying our parameter choice.

6.6 Stability boundary of TDSs in the DDE given by Bykov T-point in profile equation

At the T-point, a heteroclinic cycle connecting to two saddle equilibria is created. In its unfolding, two curves of homoclinics to either one of the two equilibria meet at the T-point, cf. Section 3.10. Their particular structure depends on the leading eigenvalues of the two equilibria being real or complex conjugate pairs. The curve of Bykov T-points can be computed in the profile equation by a path continuation of the codimension-two heteroclinic, connecting the saddle equilibrium x_1 and the original background equilibrium x_0 of

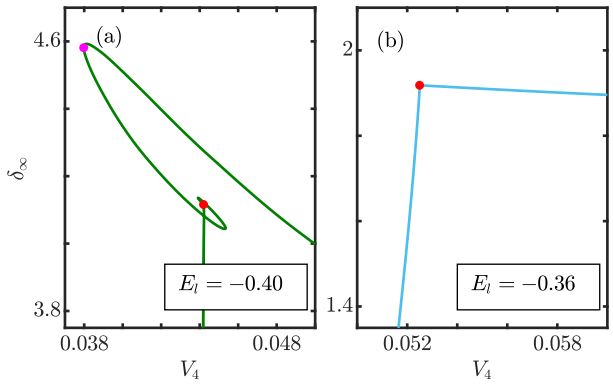

Figure 6.11: Branches of large-period periodic solutions in the profile equation for varying parameter V_4. (a) For $E_\mathrm{l} = -0.4$, unfolding of Bykov T-point (red dot) with the saddle equilibrium of saddle focus type and fold point (magenta). (b) For $E_\mathrm{l} = -0.36$ unfolding of Bykov T-point (red dot) with simple saddle. Parameters: $\kappa_V = 0.2$, $T = 100$, other parameters as in Fig. 6.1. Figure and Caption taken from [SW23].

the soliton. Details of the numerics are provided in [Bey90; SER02], see also Appendix A.1. Recall the special role of the response time δ (2.1.3) discussed in Chapter 4. Then by including the asymptotic response time δ_∞ as a free parameter in the continuation, we obtain a codimension-one curve in the original system parameters of the large delay DDE. This way, we obtain the red curve of Bykov T-points in Figure 6.5. The background equilibrium x_0 does not change its saddle configuration in the profile equation. However, at the red point located on the branch of Bykov T-points in Figure 6.5, the saddle equilibrium x_1 has a double eigenvalue in the linearized profile equation and changes from a simple saddle (two real leading eigenvalues) to a saddle focus (one complex conjugate pair and one real leading eigenvalue). This changes the structure of the unfolding of the Bykov T-point as displayed in Figure 6.11: In the case of real leading eigenvalues, the branches of homoclinics display a kink at the Bykov T-point, see Panel (b). When the saddle equilibrium is of saddle-focus type, the branch has a spiralling shape and undergoes a sequence

of folds (see Panel (a)) before hitting the T-point in the centre of the spiral. Hence, to the left of this degenerate Bykov T-point, the stability boundary of the TDSs with the stable background x_0 is given by a fold of solitons (magenta curve in Figure 6.5). Along this fold curve, the manifold of homoclinic solutions in the profile equation is folded with respect to the parameter δ_∞.

In this chapter, we examined various pulse solutions and elucidated their emergence and dynamics, focusing on the underlying mechanisms related to a saddle-node separatrix loop bifurcation occurring in the system without feedback. By employing the profile equation, we demonstrated the effective application of homoclinic bifurcation theory to gain a better understanding of the dynamics of TDSs. Specifically, we unveiled how a homoclinic orbit flip of a single-pulse soliton leads to the destabilization of equidistant multi-pulse solutions, resulting in the formation of stable pulse packages. Finally, we observed that these stable pulse packages undergo a delocalization at a Bykov T-point.

CHAPTER 7

Period-doubling of temporal dissipative solitons in the Morris-Lecar model with time-delayed feedback

In this chapter, our primary focus is on investigating temporal dissipative solitons undergoing a period-doubling bifurcation. To achieve this, we utilize the alternated profile equation, derived in Chapter 4, which accommodates the periodic solutions associated with a period-doubling bifurcation and enables us to identify them as homoclinic solutions. This new approach inherently incorporates a symmetry relation, linking the period-doubling bifurcation to the unfolding of a degenerate homoclinic together with a symmetry-breaking in the alternated profile equation. We illustrate our results by using the Morris-Lecar model under time-delayed feedback.

7.1 Introduction

In the previous chapters, we elaborated that a particular characteristic of solitons is that they can be identified with homoclinic solutions in the profile equation. However, there are limitations to this method concerning the period-doubling bifurcation or, more general, resonant Neimark-Sacker bifurcations. As displayed in Remark 2 in Section 4.4, these bifurcations do not reappear in the profile equation. This chapter is devoted to the analysis of temporal

dissipative solitons undergoing a period-doubling bifurcation. Therefore, we will use the alternated profile equation, introduced in Chapter 4 in which not only the solitons appear as homoclinics, but also the alternating pulse solutions emerging in this bifurcation. Moreover, in this system, also the period-doubling reappears together with the profile of the corresponding solitons.

To this end, we study the dynamics in the Morris-Lecar model under time-delayed feedback given by

$$\dot{x}(t) = \tilde{f}(x(t)) + \kappa(x(t-\tau) - x(t)), \tag{7.1.1}$$

where $x := (V, w)$ and $\tilde{f}(x)$ represent the right-hand side of system (5.1.1a)–(5.1.1b) and the coupling

$$\kappa \;=\; \begin{pmatrix} \kappa_V & 0 \\ \kappa_w & 0 \end{pmatrix}, \tag{7.1.2}$$

where κ_V and κ_w are nonnegative real numbers. In Chapter 6, cf. [SW23], we supplied the time-delayed model (7.1.1) with a coupling (7.1.2), where $\kappa_w = 0$, leading to a feedback only in the V variable. It was shown that this induces the emergence of TDSs in the regime of excitability for large enough κ_V and τ. In Section 6.2, it was established that the solitons in this system lose their stability in a subcritical period-doubling. This bifurcation is induced when the feedback term is not large enough to trigger any subsequent pulse. In this chapter, we choose a coupling (7.1.2), such that there is a feedback term in both variables. Furthermore, we fix the parameters to the regime of excitability, given in Table 5.1. This leads to the emergence of stable TDSs for $\kappa_w = 0$, which also remain stable for some $\kappa_w \geq 0$. For a critical coupling $\kappa_w > 0$, they lose their stability in a supercritical period-doubling. This facilitates the analysis and demonstration of the results on the period-doubling bifurcation of TDSs using the Morris-Lecar model, since the emerging period-doubled solutions are stable.

For this new choice of coupling strength, we give now an overview of TDS solutions in the DDE and the corresponding periodic solutions in the profile equation of the Morris-Lecar model under time-delayed feedback (7.1.1) in Figure 7.1. Recall that both systems are related by the reappearance rule (2.4.1).

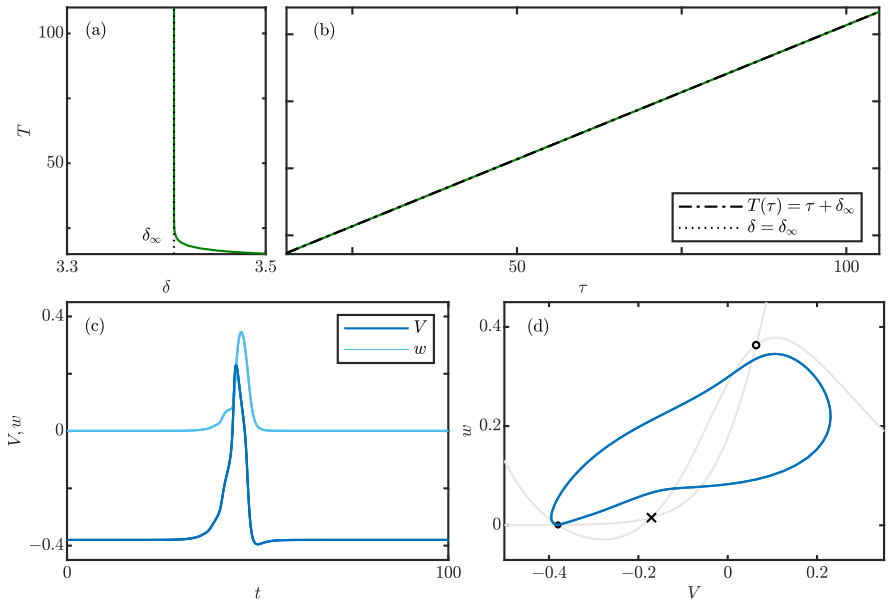

Figure 7.1: Branches of periodic solutions: (a) in the profile equation (4.2.1) and (b) in the DDE (4.1.1) of the Morris-Lecar system under time-delayed feedback (7.1.1). Profile of a soliton with period $T = 100$ displayed in (c), corresponding phase portrait of the soliton in (d). Parameters: $V_4 = 0.13$, $E_l = -0.4$, $\kappa_V = 0.32$, $\kappa_w = 0.115$ and as in Table 5.1.

Together with the definition of the response time δ (2.1.3), we see also in this regime, that the branches show the characteristic asymptotic behaviour of the branches with soliton periodic solutions. In Panel (a), there is a branch of periodic solutions (green) in the profile equation with periods $T \longrightarrow \infty$ for $\delta \longrightarrow \delta_\infty$. In (b) there is a branch of periodic solutions (green) approaching a line $T(\tau) = \tau + \delta_\infty$ (dashed-dotted) for $\tau \longrightarrow \infty$. The profile of a soliton for a selected period is given in Panel (c) and its corresponding orbit in the phase portrait in Panel (d). The background of the soliton lies approximately at $(V, w) \approx (-0.39, 0)$ indicated by the black dot. The other equilibria correspond to a saddle equilibrium (cross) and a saddle focus (circle) in the DDE. All equilibria lie on the intersections of the nullclines (grey) (5.2.1)–(5.2.2) of

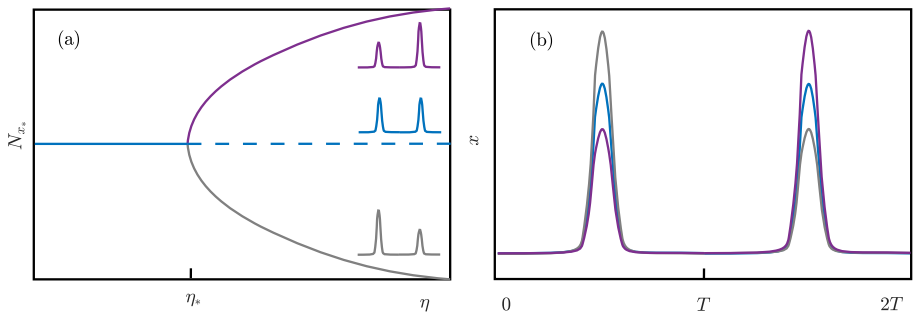

Figure 7.2: (a) Sketch of a supercritical period-doubling bifurcation: (blue) branch of periodic solutions undergoing a period-doubling at $\eta = \eta_*$, (purple, grey) branches of stable periodic solutions with twice the period bifurcating from it in parameter η plotted versus N_{x_*} (7.2.1). Solid lines represent stable solutions, dashed unstable. (b) Profiles of solutions involved in a period-doubling at a value $\eta > \eta_*$.

the system. Note, that the parameter regime and coupling strengths are chosen such that the solitons are stable, and the stable background is absolutely stable (Definition 1).

This chapter is structured as follows. In order to examine the period-doubling bifurcations of TDSs, we firstly give a short recap on the period-doubling bifurcation in Section 7.2. and present then in Section 7.3 the alternating pulses emerging in the alternated profile equation. In Section 7.4, we analyze the underlying homoclinic bifurcation in this novel system and reveal the relation to the unfolding of a degenerate homoclinic with a symmetry breaking. As in the previous Chapter, we apply a numerical analysis by using DDE-BIFTOOL.

7.2 Period-doubling bifurcations in the context of TDSs

A period-doubling bifurcation in a continuous dynamical system describes the codimension-one phenomenon, where a periodic orbit with twice the period

of the original orbit is either created or destroyed.

A sketch of the unfolding of a period-doubling is given in Figure 7.2 (a). Suppose, that there is a branch of periodic solutions (blue) of (4.1.1) that is stable for $\eta < \eta_*$. Assume for consistency that period $T \approx \tau$ large. At $\eta = \eta_*$ the periodic solution becomes unstable by generating a periodic solution with twice the period: Suppose, that at the critical value, the periodic solution $x_*(t)$ on the primary branch has period T, then the periodic solution bifurcating from it at $\eta = \eta_*$ has period $2T$. With

$$N_{x_*} = \int_0^T ||\tilde{x}(t) - x_*(t)||^2 \mathrm{d}t \tag{7.2.1}$$

we display the distance of a $2T$-periodic solution $\tilde{x}(t)$ to the primary T-periodic solution $x_*(t)$ for varying η. At $\eta = \eta_*$, two branches of periodic solutions (purple and grey) emerge. There are two different scenarios possible, that are referred to as supercritical and subcritical. In the first case, the branches bifurcating from the primary branch for $\eta > \eta_*$ are stable. In the latter case, the branches bifurcate for $\eta < \eta_*$ and are unstable. For simplicity, we will focus on the supercritical case throughout the paper. The profiles of the stable periodic solutions of approximately twice the period are given in Panel (b) in purple and grey and consist of alternating pulses. The unstable primary solution is displayed in blue. Approaching η_* with $\eta > \eta_*$, the alternating pulse solutions approach the regular solution and coincide at the period-doubling point. Thus, a solution on the purple branch shares the same profile shifted by T as one from the grey branch at the same parameter value.

Since solitons are a phenomenon for all large delays, the following applies. If a soliton at a delay value $\tau = \tau_*$ undergoes a period-doubling at $\eta = \eta_*$, then also solitons at larger delays $\tau > \tau_*$ undergo a period-doubling bifurcation at a parameter $\eta = \eta_*(\tau)$ close to η_*. We can think of a period-doubling of solitons in the following way: A family of TDSs $x_*(t;\tau)$ undergoes a period-doubling bifurcation at $\eta = \eta_\infty$, if for all $\epsilon > 0$, there is a minimal delay $\tau_{\min} > 0$ such that for all $\tau > \tau_{\min}$ there is a TDS $x_*(t;\tau)$ undergoing a period-doubling bifurcation at $\eta = \eta_*(\tau)$ where $||\eta_*(\tau) - \eta_\infty|| < \epsilon$.

Figure 7.3 supports this description. It shows a branch of period-doublings in the Morris-Lecar model (7.1.1) for varying delay τ and κ_w. For increasing

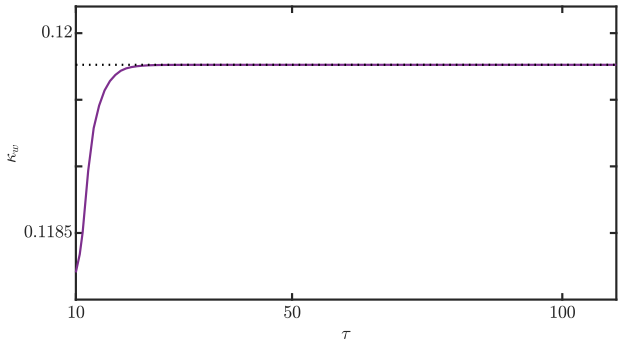

Figure 7.3: Branch of period-doubling points in the Morris-Lecar model under time-delayed feedback (7.1.1). Parameters as in Fig. 7.1.

delay, the parameter value of the period-doubling in κ_w stays bounded and has a limit at approximately $\kappa_w \approx 0.1198$ for $\tau \longrightarrow \infty$. Moreover, we can see from this, that the TDSs displayed in Figure 7.1 are all stable. However, for slightly larger κ_w, these solitons turn unstable in a period-doubling bifurcation and thereby creating stable alternating pulse solutions.

7.3 Alternating pulse solutions in the APE

As mentioned in Section 7.1, for larger values of κ_w the TDSs lose their stability in a period-doubling bifurcation, which is supercritical for our choice of parameters. Moving on, we will analyse the period-doubling and the emerging alternating pulse solutions using the alternated profile equation, introduced in Section 4.3.

Figure 7.4 displays a family of alternating pulse solutions in the Morris-Lecar model under time-delayed feedback (7.1.1). Panel (a) displays a branch of alternating pulses (green) in the alternated profile equation (4.3.2)–(4.3.3) with varying parameter δ and resulting period $2T$. The branch limits a homoclinic orbit for $\delta \longrightarrow \delta_\infty$ (dashed-dotted). In the large delay DDE system (7.1.1)

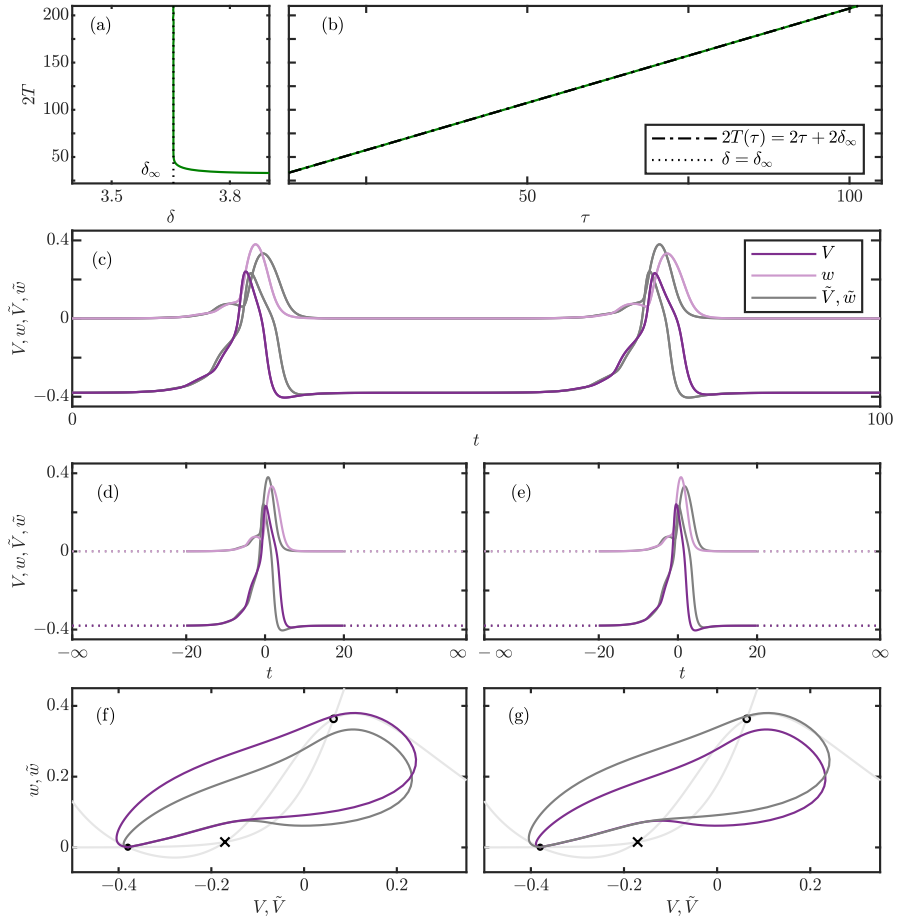

Figure 7.4: Branches of alternating pulse solutions: (a) in the alternated profile equation (4.3.2)–(4.3.3) and (b) in the DDE (4.1.1) of the Morris-Lecar system under time-delayed feedback (7.1.1). Profile of an alternating pulse with period $2T = 100$ displayed in (c). Profiles of the limiting homoclinic solutions in (d) and (e), the corresponding phase portrait of the respective homoclinics in (f) and (g). Parameters: $\kappa_w = 0.124$ and as in Fig. 7.1.

displayed in Panel (b), the solutions reappear to a branch of alternating pulses that approaches the line $2T(\tau) = 2\tau + 2\delta_\infty$ (dashed-dotted) for $\tau \longrightarrow \infty$. For a fixed value of the period, Panel (c) displays the profile of an alternating pulse solution. Note that the variables $\tilde{V}$ and $\tilde{w}$ (grey) are copies of V and w (purple and light purple), respectively, shifted by half the period, where the tuple $(\tilde{V}, \tilde{w})$ gives the newly introduced variable y in the alternated profile equation (4.3.2)–(4.3.3). Accordingly, the profile of the alternating pulse solution shows the relation (4.3.6). The corresponding profiles of the limiting homoclinic solutions are displayed in (d) and (e) in a numerical representation (see Apendix A.1), and their phase portraits in (f) and (g).

Recall, that the APE system (4.3.2)–(4.3.3) is equivariant with respect to the mirror symmetry γ (4.3.4). The stable background equilibrium x_0 reappears to (x_0, x_0) in the symmetry subspace $\mathrm{Fix}(\gamma)$ and is naturally of saddle-type in the APE system (Corollary 1 in Section 4.3). Beyond that, the alternating pulse solutions, as displayed in Figure 7.4, are identical up to symmetry γ (4.3.4) and do not lie in $\mathrm{Fix}(\gamma)$. Also the limiting homoclinic solutions do not lie in $\mathrm{Fix}(\gamma)$, but the homoclinics themselves approach an equilibrium (x_0, x_0) lying in the symmetry subspace. In contrast to that, the soliton solutions in Figure 7.1 lie entirely in $\mathrm{Fix}(\gamma)$, as well as their limiting homoclinics with corresponding saddle (x_0, x_0).

7.4 Degenerate homoclinic orbit with a symmetry breaking

Consider a soliton $x_*(t;\tau)$ in (4.1.1) for a fixed, large value of the delay τ and with corresponding period $T(\tau)$. Suppose it undergoes a period-doubling bifurcation. That is, it loses its stability and a solution with period $2T(\tau)$ emerges consisting of alternating pulses. Thereby, soliton solutions and alternating pulse solutions are related by a period-doubling. Both reappear in the APE system (4.3.2)–(4.3.3), together with the period-doubling bifurcation. In particular, the soliton solutions lie in the symmetry subspace $\mathrm{Fix}(\gamma)$, while the alternating pulse solutions do not. Consequently, in the APE system, the period-doubling is additionally related to a symmetry-breaking bifurcation.

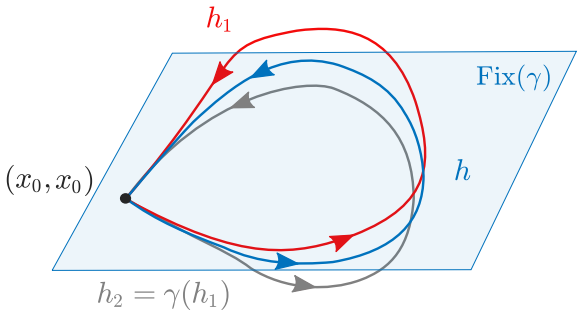

Figure 7.5: Sketch of the two different kinds of homoclinic solutions in the APE system (4.3.2)–(4.3.3): (blue) homoclinic h lying in Fix(γ), (red, grey) homoclinics h_1, h_2 outside of Fix(γ), related by the symmetry γ (4.3.4). All homoclinics connect to the saddle equilibrium (x_0, x_0). The symmetry subspace Fix(γ) is given by the blue plane.

A sketch of the homoclinics, treated in Corollary 2 of Section 4.3, is given in Figure 7.5. The homoclinic h (blue) to the saddle equilibrium (x_0, x_0) is contained in the symmetry subspace Fix(γ), indicated by the blue plane. The two homoclinics h_1 (red) and its symmetry twin h_2 (grey) do not lie in Fix(γ). The homoclinics h_1 and h_2 connect to (x_0, x_0), as well, and form so called *homoclinic bellows* ([HS10]). In order for a homoclinic h and its accompanying periodic solutions lying in Fix(γ) to leave the subspace, the homoclinic h and periodic solutions must pass through a symmetry-breaking bifurcation. Note, that bellows can only exist in dimensions four or higher. Figure 7.6 shows analogously the homoclinic solutions in the Morris-Lecar model under time-delayed feedback in a representation, where the creation of the homoclinic bellows through the symmetry-breaking bifurcation becomes visible.

In general, homoclinic bifurcations can be induced by either qualitative changes in the spectrum of the equilibrium, or by the violation of a genericity condition involving the stable or unstable manifold along the homoclinic. The symmetry-breaking bifurcation here comes together with the unfolding of a degenerate homoclinic orbit, see [Van92] or [HS10], cf. Section 3.9. Consider the stable and unstable manifold of the saddle equilibrium, whose intersec-

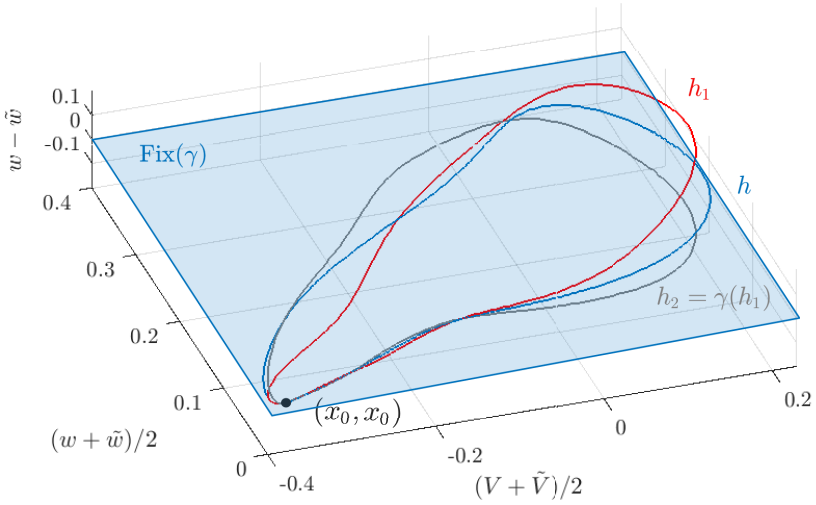

Figure 7.6: Homoclinic solitions in the APE system (4.3.2)–(4.3.3) of the Morris-Lecar model under time-delayed feedback (7.1.1). The symmetrical homoclinic h lying in Fix(γ) is given in blue. The two homoclinics h_1 and h_2 (red and grey) lying outside of Fix(γ) are related by γ (4.3.4). All homoclinics connect to the saddle equilibrium (x_0, x_0). The symmetry subspace Fix(γ) is given by the blue plane. Parameters: $\kappa_w = 0.124$ and as in Fig. 7.1.

tion creates the homoclinic structure joining the saddle to itself. The generic configuration of the homoclinic requires the transverse intersection of the corresponding tangent spaces along the homoclinic (Hypothesis 2 (*1.*) in Section 3.3). In the present case, this condition is not satisfied. The tangent spaces of the stable and unstable manifold intersecting along the homoclinic orbit have a quadratic tangency. This can only be obtained in dimensions four or higher and requires at least two-dimensional stable and unstable manifolds. In order to obtain this configuration, three parameters have to be adjusted and the para-

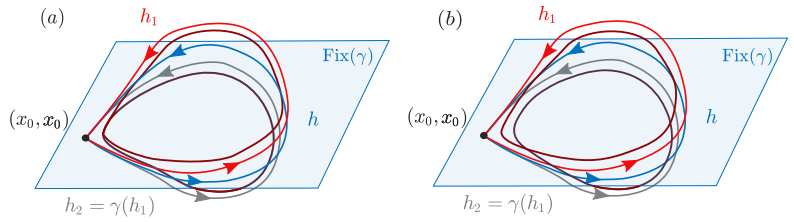

Figure 7.7: Sketch of the two different kinds of periodic solutions (dark red) bifurcating from the degenerate homoclinic bifurcation in the APE system (4.3.2)–(4.3.3): (a) periodic solution with alternating pulses, (b) periodic solution twin with components that are not related by a time-shift and its symmetry. Other curves: (blue) homoclinic h lying in Fix(γ), (red, grey) homoclinics h_1, h_2 outside of Fix(γ), related by the symmetry γ (4.3.4). The symmetry subspace Fix(γ) is given by the blue plane.

meter set where a homoclinic exists forms a Whitney umbrella, [Van92]. Since in our case, the system incorporates a symmetry, the codimension is reduced to two. To our knowledge, this homoclinic bifurcation with $\mathbb{Z}_2$-equivariance has not yet been studied in the rich literature on homoclinic bifurcations. Below we report some numerical observations, which could be the starting point for an extensive rigorous investigation of this interesting bifurcation scenario.

From the bifurcation point of the degenerate homoclinic with symmetry breaking, various codimension-one bifurcations of periodic solutions emerge. One of them is the period-doubling, discussed above. There is also a pitchfork bifurcation curve of periodic orbits appearing, which involves very special kinds of solutions. Recall, that the $2T$-periodic alternating pulses in the APE system satisfy

$$(x, y) = (x_*(t), y_*(t)) \quad \text{with} \quad y_*(t) = x_*(t - T). \tag{7.4.1}$$

Considering, that the underlying state space has to be at least four-dimensional, the two components can be connected without crossing the plane Fix(γ) which has half the dimension. They approach two homoclinics, that are related by γ. In the unfolding of the pitchfork bifurcation, emerging from the degenerate

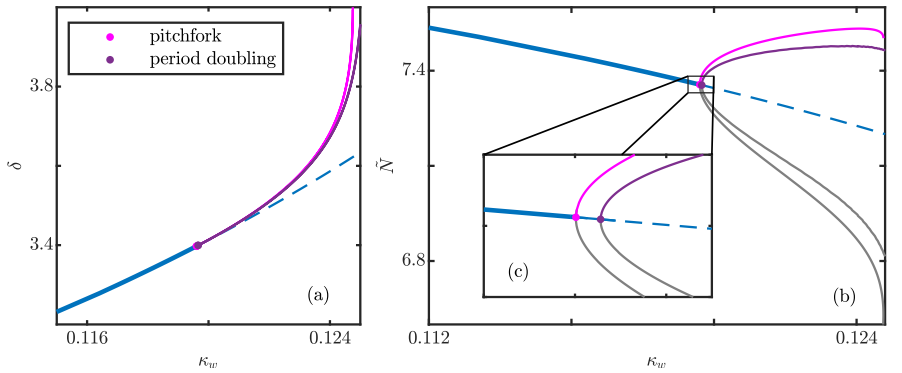

Figure 7.8: Branches of periodic solutions in the APE system of the time-delayed Morris-Lecar model (7.1.1) emerging from the degenerate homoclinic bifurcation: (blue) branch of periodic solutions corresponding to TDSs in the DDE, (magenta) branch of periodic solutions emerging from the pitchfork, (purple) branch of periodic solutions corresponding to alternating pulses in the DDE, branches containing the symmetry twins (grey). Panel (b): branches plotted versus $\tilde{N}$ (7.4.2). Parameters: (blue and magenta) $T = 20$, (purple) $T = 40$. Other parameters as in Fig. 7.1.

homoclinic bifurcation with a symmetry breaking, periodic solutions (7.4.1) of a minimal period T are created from the primary T-periodic soliton solution, but the x and y component are not related by any time shift. The trajectory of the periodic solution and the trajectory of the symmetry twin lie in two disjoint subspaces separated by the hyperplane $\mathrm{Fix}(\gamma)$ and are not connected. Note that these solutions do not reappear in the large delay DDE and only exist in the APE system. These two different kinds of periodic solutions (dark red) are visualized in Figure 7.7. In Panel (a), one sees the periodic solution corresponding to an alternating pulse in the large delay DDE. Panel (b) displays a periodic solution that has components which are not related by a time shift (dark red) together with its symmetry twin (grey). Both solutions lie in separate subspaces.

Figure 7.8 (a) shows a branch of T-periodic solutions (blue) with a fixed

period T in the APE system of the time-delayed Morris-Lecar model (7.1.1) corresponding to TDSs in the large delay DDE. The branch undergoes a pitchfork (magenta) and a period-doubling (purple) bifurcation. The branch bifurcating from the pitchfork (magenta) consists of T-periodic solutions with non-connected components (cf. Panel (b) of Figure 7.7). The branch bifurcating from the period-doubling (purple) consists of $2T$-periodic solutions with connected components (cf. Panel (a) of Figure 7.7), corresponding to alternating pulses in the large delay DDE. In Panel (b) and Inlet (c), we use

$$\tilde{N} = \int_0^T ||\tilde{x}(t)||^2 \mathrm{d}t, \tag{7.4.2}$$

where $\tilde{x}(t)$ denotes a $2T$-periodic solution, for a visualization of the branches emerging from the pitchfork and period-doubling bifurcation containing the symmetry twins (grey) given by (4.3.4). For $T \longrightarrow \infty$ the pitchfork and period-doubling meet in the degenerate homoclinic point.

We have undertaken an examination of the period-doubling bifurcation of solitons within the framework of homoclinic bifurcation theory, utilizing the alternated profile equation. Although the profile equation does not encompass this specific bifurcation type, this newly introduced system enables us to investigate TDSs as homoclinic solutions, along with the resultant alternating pulse solutions. Furthermore, considering the inherent symmetry of the system, we have illustrated that the underlying dynamics are linked to the creation of a degenerate homoclinic orbit with a symmetry breaking.

CHAPTER 8

Square waves and Bykov T-points in a delay algebraic model for the Kerr–Gires–Tournois interferometer

In this chapter, we investigate the mechanisms governing the formation of square waves in a delay-algebraic model of the Kerr-Gires-Tournois interferometers. By utilizing the alternated profile equation, introduced in Chapter 4 for the analysis of periodic solutions in DDEs having periods of approximately twice the delay, the square waves can be treated as connecting orbits. Thereby, we can examine the dynamics of square wave solutions and their bifurcations leveraging classical homoclinic bifurcation theory. Specifically, we elucidate the mechanism underlying the collapsed snaking scenario of square waves leading to the emergence of complex-shaped multistable square wave solutions in the Kerr-Gires-Tournois interferometers through a Bykov T-point.

8.1 Introduction

Besides temporal dissipative solitons, studied in the previous chap- ters, yet another typical phenomenon induced by large delay is the formation of square wave (SW) oscillations. From a mathematical perspective square waves have been studied extensively, see e.g. [HH94; HH96; MPN86; Niz03]. Typically, square waves emerge in the regime of large delay via a supercritical Hopf

bifurcation with a period of approximately twice the delay.

Finding applications in signal processing, communication systems [KAM10; SWX13], and optical sensing [USNA11], they have been observed experimentally and analyzed theoretically in various optical and optoelectronic systems, like in vertical-cavity surface-emitting lasers [MGJB07; MJBGB13], edge-emitting diode lasers [FVDE14; Gav+06], semiconductor ring lasers [Li+16; Mas12], and quantum dot lasers [Dil+19]. In certain systems, e.g. in a broadband bandpass optoelectronic oscillator [Wei+12], asymmetrical SWs and SWs with periods close to once the delay have also been observed.

Recently, a novel mechanism for the formation of square waves has been detected in nonlinear vertical external-cavity Gires-Tournois interferometers [GT64], enclosed within a long external feedback cavity and subjected to anti-resonant injection. Utilizing either Kerr [KSGJ22] or semiconductor quantum well [KSJG23] nonlinearities, it was demonstrated that SWs can emerge via a collapsed snaking scenario [BK07; KW05] in the normal dispersion regime. Thereby, complex-shaped multistable square wave solutions are created. Notably, the dispersive microcavity [Sch+19] induces oscillatory tails. In this way, moving fronts between different plateau solutions can become locked at various positions near a point, where the two fronts have the same speed and their dynamics are bound. This point is also referred to as Maxwell point. In a similar optical setup with resonant optical feedback, so called dark and bright temporal dissipative solitons emerge through the locking of domain walls between bistable continuous wave background states [SGJ22; SJG22; SPVJG19]. These TDSs possess a period slightly larger than the delay, that is given by one round-trip in the external cavity. Similarly to square waves, they can lock at different positions, resulting in a collapsed snaking bifurcation scenario. This phenomenon has been observed in various physical systems, spanning from thin liquid films and flame propagation to vegetation patterns and optical pulses [GK21; LBK17; PRAL21; PRFO20; TGT14; YBK06].

In this chapter, we present our results published in [SKJGW23a]. We will apply the alternated profile equation, developed in Section 4.3 and 4.6, to the square waves emerging in a time-delayed model of the Kerr-Gires-Tournois (KGTI) interferometer, allowing us to treat SWs as relative homoclinic orbits

with respect to a mirror symmetry. Additionally, we show that the snaking scenario and the corresponding Maxwell point can be analyzed as a Bykov T-point [Byk93; GS86; KLW14]. This bifurcation of homoclinic orbits can also be tracked in parameter space using numerical path-continuation techniques, as conducted before in Chapters 6 and 7.

This chapter is structured as follows. At first, we will introduce the delay-algebraic equations modelling vertical external-cavity Kerr-Gires-Tournois interferometers. We recall the mechanisms of the emergence of square waves in this system and the phenomenon of collapsed snaking. In Section 8.3, we apply the alternated profile equation developed in Section 4.6 to the solutions in this system related to the collapsed snaking. In Section 8.4, we analyze the dynamics of the solutions involved in the collapsed snaking and connect it to a Bykov T-point. The intricate dynamics induced by secondary Bykov T-points in a different parameter regime are then further discussed in Section 8.5.

8.2 The DAE-equations modelling the Kerr-Gires-Tournois interferometers

The setup of a Kerr-Gires-Tournois interferometer is schematically displayed in Figure 8.1 (a), see also [KSGJ22; SJG22; SPVJG19] for more details. It constitutes of a single-mode micro-cavity of a few micrometres in length and radius up to 100 μm; its round-trip time is given by τ_c. The micro-cavity includes a thin layer of the Kerr material such as silicon nitride acting as a nonlinear medium that is situated at the anti-node of the field. It is enclosed by two distributed Bragg mirrors with reflectivities $r_{1,2}$. The micro-cavity is coupled to a long external cavity of a few centimetres. Its round-trip time is given by $\tau \gg \tau_c$ and it is closed by a mirror with reflectivity η and the feedback phase ϕ.

The system is subjected to a continuous wave (CW) injection with amplitude Y_0 and frequency ω_0. The total external cavity phase $\varphi = \phi + \omega_0\tau$ is the sum of the propagation phase in the external cavity and of the phase shift

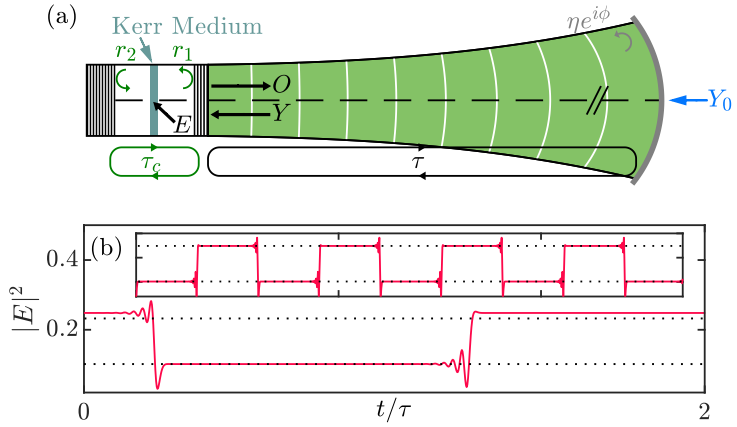

Figure 8.1: (a) Schematic of a micro-cavity containing a Kerr medium coupled to a long external cavity which is closed by a mirror with reflectivity η and phase ϕ, and driven by a CW beam with amplitude Y_0. (b) An exemplary SW solution obtained from a direct numerical time integration of the KGTI system (8.2.1)–(8.2.2). The black dotted lines correspond to the period-two orbit of the singular map (2.3.1). The inset shows the dynamics over several round-trips. Parameters are $(\tau, d, h, \eta, \varphi) = (300, 0.2, 2, 0.9, \pi)$. Figure and Caption taken from [SKJGW23a].

induced by the feedback mirror. It describes the detuning with respect to the nearest external cavity mode. Let ω_c denote the micro-cavity resonance, then the detuning is given by $d = \omega_c - \omega_0$. The case where the injection frequency is set exactly in between two external cavity modes corresponds to setting $\varphi = \pi$. In that situation trains of SWs with a periodicity slightly larger than 2τ, as displayed in the inset of Figure 8.1 (b), can be generated for a range of Y_0 and of the detuning d.

By using methods developed in [MB05; SJG22; SPVJG19], in this setup the evolution of the slowly varying field envelopes in the micro-cavity E and the external cavity Y is modelled by the set of delay algebraic equations (DAE):

$$\dot{E}(t) = \left[i\left(|E(t)|^2 - d\right) - 1\right] E(t) + hY(t), \tag{8.2.1}$$

$$Y(t) = \eta e^{i\varphi}\left(E\left(t-\tau\right) - Y\left(t-\tau\right)\right) + \sqrt{1-\eta^2}\, Y_0, \tag{8.2.2}$$

see also [KSGJ22]. The factor $h = h(r_1, r_2) = (1 + |r_2|)(1 - |r_1|)/(1 - |r_1||r_2|)$ is the light coupling efficiency. For $h(r_1, 1) = 2$, we obtain a perfectly reflective bottom mirror which is also called the Gires-Tournois interferometer regime [GT64]. This system covers second and third-order dispersion effects. Figure 8.1 (b), shows a time trace of a square wave obtained from time integration of the KGTI system (8.2.1)–(8.2.2). It displays strong oscillatory tails resulting from third-order dispersion terms becoming the leading part around resonance.

In order to conduct a bifurcation analysis of delay-algebraic systems and delay equations of neutral type, we make use of a recently developed extension of DDE-BIFTOOL [ELR02; SELSR16]. A resulting bifurcation diagram of the KGTI system (8.2.1)–(8.2.2) for varying Y_0 and other parameters as in Figure 8.1 (b), cf. also [KSGJ22] is presented in Figure 8.2 (a). Exemplary profiles of the different solutions along the branch are displayed in Panels (b)–(d), respectively. Note that the solution in Panel (b) is the same as in Figure 8.1 (b).

Figure 8.2 shows a branch of equilibria (black) consisting of CW states, that are unstable (dashed-dotted) between two Hopf bifurcations $\mathrm{H}_{1,2}$. For higher injection values, a branch of periodic solutions (green) emerges from the CW state in a supercritical Hopf-bifurcation at H_2. It consists of stable SWs on the upper branch part, see Figure 8.2 (b). The branch enters into a region of collapsed snaking around a vertical line $Y_0 = Y_{0,MP}$, the so called Maxwell point, located in the regime of bistability between the SWs and the stable CW state. Therein the branch experiences a sequence of fold bifurcations, before vanishing in a subcritical Hopf-bifurcation point H_1, see the inset in Figure 8.2 (a). In the snaking regime, the branch consists of multiple coexisting solutions having fronts not only between the plateaus of the SW state but also connecting the CW state with one of the other plateaus, corresponding to stable mixed-type solutions as shown in Figure 8.2 (c). On the lower part of the branch, we find unstable alternating pulse solutions consisting of two localized pulses with the CW state as background equilibrium, cf. Figure 8.2 (d).

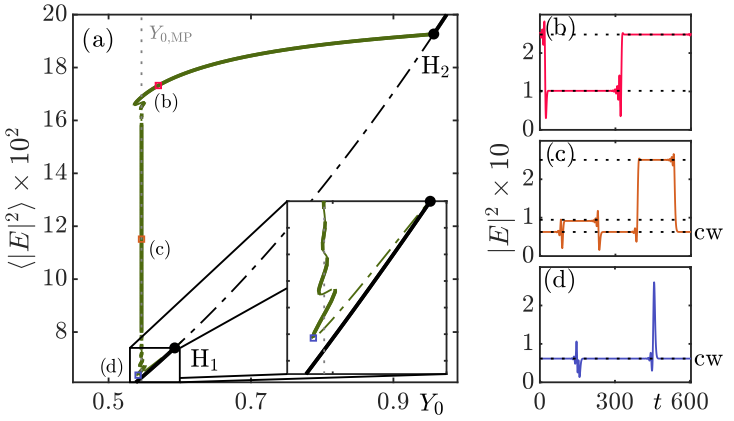

Figure 8.2: (a) Branch of periodic solutions (green) and CW states (black) for varying Y_0 obtained by path-continuation of Eqs. (8.2.1)–(8.2.2). Stable (unstable) solutions are depicted in solid (dashed-dotted), respectively. $\mathrm{H}_{1,2}$ are a subcritical and a supercritical Hopf-bifurcation of the CW state. The branch consists of SW solutions (b) in the upper part, mixed-type solutions (c) around the Maxwell point $Y_{0,\mathrm{MP}} \approx 0.54625$ (dotted grey), and unstable alternating pulse solutions (d) close to the subcritical Hopf-bifurcation point H_1. Exemplary profiles (b)–(d) are marked in (a). Parameters as in Fig. 8.1. Figure and Caption taken from [SKJGW23a].

8.3 Finding square waves in the KGTI as connecting orbits

Applying the approach discussed in Section 4.6 to the square waves of the Kerr-Gires-Tournois interferometer (8.2.1)–(8.2.2), we obtain the following alternated profile equation (APE) of the system:

$$\dot{E}(t) = \left[i\left(|E(t)|^2 - d\right) - 1\right] E(t) + hY(t), \tag{8.3.1}$$

$$Y(t) = \eta e^{i\varphi}\left(F\left(t+\delta\right) - Z\left(t+\delta\right)\right) + \sqrt{1-\eta^2}\, Y_0, \tag{8.3.2}$$

$$\dot{F}(t) = \left[i\left(|F(t)|^2 - d\right) - 1\right] F(t) + hZ(t), \tag{8.3.3}$$

$$Z(t) = \eta e^{i\varphi}\left(E\left(t+\delta\right) - Y\left(t+\delta\right)\right) + \sqrt{1-\eta^2}\, Y_0. \tag{8.3.4}$$

Note, that the KGTI system is a delay-algebraic model. However, the theory developed in Chapter 4.6 for simple delay differential equations with a single delay can still be applied to the more general setting of delay-algebraic equations, considering that they can, in general, be expressed by (4.1.1) by multiplying the left-hand side with a singular mass matrix M.

As in previous analyses, we will investigate the resulting system using the DDE-BIFTOOL path-continuation package, allowing for a numerical computation of periodic solutions and connecting orbits treated as boundary value problems with periodic boundary conditions. Although it is often feasible to approximate homoclinic orbits using nearby periodic solutions with fixed large periods, spectral projection boundary conditions are generally considered more robust and efficient. Recall, that generic homoclinics are objects of codimension-one, meaning that for their computation, solving for one parameter suffices. For a continuation of generic homoclinics one needs to free yet another parameter, for which the response time comes into play. For the computation of all connecting orbits in this chapter, we use our extension implemented in the software, see Appendix A.2 for the corresponding boundary value problem of the computation of connecting orbits to double foci. An example of the continuation of connecting orbits and Bykov T-points discussed in this paper can be found in [SKJGW23b].

We want to analyze the different kinds of solutions and their relations appearing in the DAE system (8.2.1)–(8.2.2) and its equivalent in the APE system (8.3.1)–(8.3.4), see Figure 8.3. Starting with the stationary solutions of the DAE system, there is a branch of CW states $x_{\mathrm{cw}} = (E_{\mathrm{cw}}, Y_{\mathrm{cw}})$, which are equilibria in the DAE system, but also fixed points of the singular map (black line) (2.3.1). The CW states are unstable in the interval between the two flip bifurcations $\mathrm{H}_{1,2}$ of the singular map. From these points emerges a branch of period-two orbits $(x_1, x_2) = ((E_1, Y_1), (E_2, Y_2))$ of the singular map (grey line in Figure 8.3). While the flip bifurcation at the point H_2 is supercritical, in the parameter regime presented in Figure 8.3, the other at H_1 is subcritical. This thereby leads to a fold (red point) on the branch of period-two orbits in the DAE system.

In the APE system (8.3.1)–(8.3.4) the CW state corresponds to an equi-

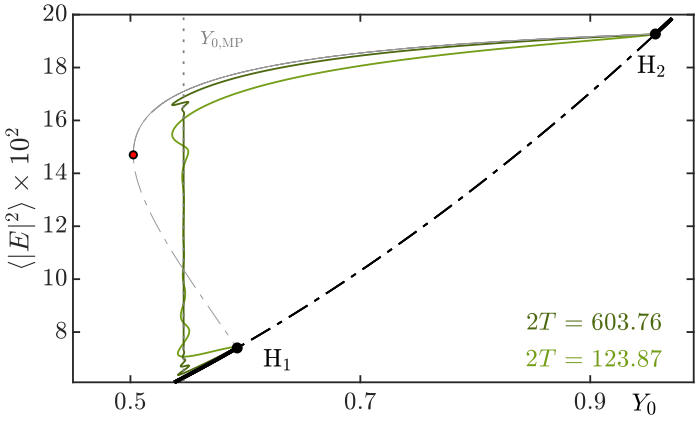

Figure 8.3: Black curve: branch of fixed points of the singular map (2.3.1) of the DAE system (8.2.1)–(8.2.2) with flip bifurcations at $\mathrm{H}_{1,2}$. Grey curve: Branch of period-two orbits of the singular map bifurcating in the flip bifurcations and changing its stability in a fold point (red). Solid and dash-dotted parts of black and grey curves indicate stable and unstable solutions, respectively. Light and dark green curve: branches of periodic solutions of the APE system (8.3.1)–(8.3.4) with fixed periods $2T = (603.76, 123.87)$ and varying δ. Dotted grey line $Y_{0,\mathrm{MP}}$ indicates the position of the Maxwell point. Other parameters as in Fig. 8.2. Figure and Caption taken from [SKJGW23a].

librium lying in the subspace of fixed points $\mathrm{Fix}(\gamma)$ (4.3.5) under the symmetry γ (4.3.4) and is given by

$$(x_{\mathrm{cw}}, x_{\mathrm{cw}}) = (E, Y, F, Z) = (E_{\mathrm{cw}}, Y_{\mathrm{cw}}, E_{\mathrm{cw}}, Y_{\mathrm{cw}}),$$

whereas the period-two orbit of the singular map gives rise to two equilibria

$$(x_1, x_2) = (E, Y, F, Z) = (E_1, Y_1, E_2, Y_2),$$
$$(x_2, x_1) = (E, Y, F, Z) = (E_2, Y_2, E_1, Y_1),$$

which are related by γ. The stability properties of the solutions in the APE system differ from the DAE system. Especially, all these equilibria of the APE system are saddle equilibria of double focus type, i.e. with two complex

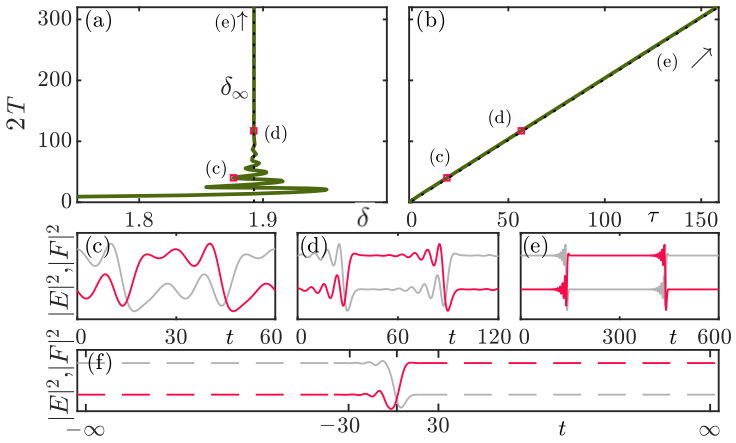

Figure 8.4: Branches of SWs in the (a) APE system (8.3.1)–(8.3.4), and (b) DAE system (8.2.1)–(8.2.2). In (b) the branch approaches the line $2T(\tau) = 2\tau + 2\delta_\infty$ (dashed), for $\tau, T \longrightarrow \infty$. In (a) the branch approaches a vertical line (dashed) at $\delta = \delta_\infty$ with $T \longrightarrow \infty$ in a homoclinic bifurcation. Panels (c)–(e) show profiles for the periods $2T \approx 60, 120, 600$, respectively. For $\delta \longrightarrow \delta_\infty$ in the APE system, the SWs approximate the relative homoclinic given in (f). Parameters as in Fig. 8.1 and $Y_0 = 0.7$. Figure and Caption taken from [SKJGW23a].

conjugate pairs of leading eigenvalues. Near the flip bifurcations in the singular map, there are Hopf-bifurcations located at $H_{1,2}$ in the APE system. We obtain the emanating branches (cf. green curves in Figure 8.3) containing the different kinds of periodic solutions by fixing the period $2T$ and solving simultaneously for the corresponding value of δ.

Near the Hopf-point H_2, the periodic solutions have the shape of square waves. Just as the stable period-two solutions of the singular map, the corresponding square waves in the DAE system (8.2.1)–(8.2.2) are stable as well. The formation of square waves near a supercritical flip bifurcation of the singular map has been studied in detail from a mathematical perspective in [HH94; HH96; MPN86].

Figure 8.4 gives an overview of the square wave solutions, in both the APE

system (8.3.1)–(8.3.4) and the DAE system (8.2.1)–(8.2.2) obtained for fixed Y_0 close to H_2. Panel (a) shows a branch of square waves in the APE system with varying parameter δ and resulting period $2T$. One can see that $T \longrightarrow \infty$ as $\delta \longrightarrow \delta_\infty$, accordingly the square wave periodic solutions in the APE approach a connecting orbit (4.6.4) at $\delta = \delta_\infty$. Recall from Section 4.6 that this is a relative homoclinic with respect to the mirror symmetry γ (4.3.4) which approaches the saddle equilibria $(x_{1,2}, x_{2,1})$ for $t \longrightarrow \pm\infty$. In the DAE system, see Panel (b), the branch reappears to a branch of stable square wave solutions with $\tau, T \longrightarrow \infty$ and they approach a line $2T(\tau) = 2\tau + 2\delta_\infty$. The intensity profiles of selected square wave solutions of the APE system along this branch with increasing periods are given in Panels (c)–(e). Note that the newly introduced variable F is equal to the field E shifted by half the period. In Panel (f), there is the limiting connecting orbit of the branch of periodic solutions in the APE system corresponding to the relative homoclinic (4.6.4) in a numerical representation (see Appendix A). The corresponding boundary value problem is based on spectral projections to the stable and unstable manifold of the saddle equilibria $(x_{1,2}, x_{2,1})$ at the endpoints of a sufficiently long computational interval. As a consequence of the complex conjugated leading eigenvalues at the saddle equilibria $(x_{1,2}, x_{2,1})$, we can observe oscillatory tails of the relative homoclinic. Accordingly, the frequency of these damped oscillations in the tails remains unchanged for the different values of the period $2T$ and the corresponding delay times τ and the plateaus of different lengths of the SW solutions in Panels (c)–(f) carry different numbers of such oscillations. Note, that the complex conjugated leading eigenvalues at the saddle equilibria $(x_{1,2}, x_{2,1})$ also induce the snaking shape of the branch of periodic solutions in Panel (a), as discussed in Section 3.7 or [SSTC01].

Close to the other Hopf-point H_1, the period-two orbit of the singular map is unstable. In contrast to the square wave solutions near H_2, the branches of periodic solutions do not lie close to the branch of period-two solutions of the singular map, but follow the branch of stable CW states instead and approach it for large periods. The corresponding periodic solutions consist of alternating pulses. These types of solutions in DDE systems have been discussed in Section 4.3 and Chapter 7 in the context of period-doubling bifurcations. The

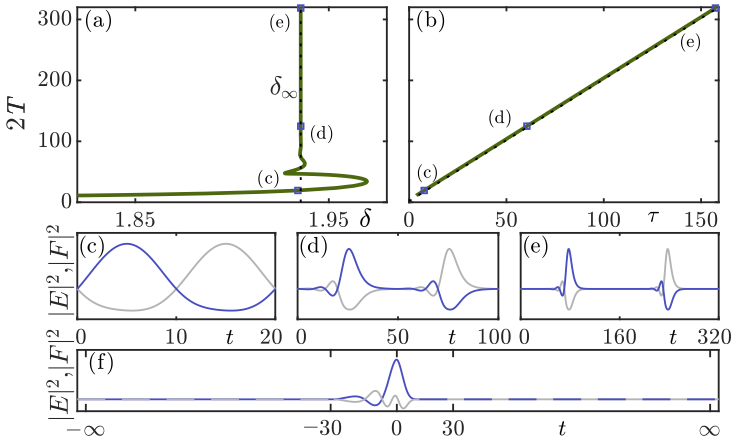

Figure 8.5: Branches of alternating pulse solutions in the (a) APE system (8.3.1)–(8.3.4), and (b) DAE system (8.2.1)–(8.2.2). In (b) the branch approaches the line $2T(\tau) = 2\tau + 2\delta_\infty$ (dashed), for $\tau, T \longrightarrow \infty$. In (a) the branch approaches a vertical line (dashed) at $\delta = \delta_\infty$ with $T \longrightarrow \infty$ in a homoclinic bifurcation. Panels (c)–(e) show profiles for the periods $2T = 20, 100, 320$. For $\delta \longrightarrow \delta_\infty$ the periodic solutions approximate the homoclinic given in (f). Parameters as in Fig. 8.1 and $Y_0 = 0.58$. Figure and Caption taken from [SKJGW23a].

pulses have an approximate distance of half the period and spend most of the time near the stable CW state. In the DAE system (8.2.1)–(8.2.2) these alternating pulse solutions are unstable. A mathematical analysis of the emergence of alternating pulse solutions close to a subcritical flip bifurcation in the singular map can be found in [HH94; HH96]. Note, that we here have another example of alternating pulse solutions in the APE system, although in contrast to the case studied in Chapter 7, the alternating pulse solutions here are unstable. Their emergence in the context of a period-doubling of TDSs is not induced by a bifurcation of fixed points in the singular map.

Figure 8.5 gives similarly an overview of the alternating pulse solutions for a fixed value of Y_0 close to H_1. Panel (a) shows a branch of alternating pulse solutions in the APE system (8.3.1)–(8.3.4) with varying parameter δ and

resulting period $2T$. Also, these types of solutions display the property, that for $\delta \longrightarrow \delta_\infty$ it is $T \longrightarrow \infty$ and consequently they approach a homoclinic. The respective branch in the DAE system (8.2.1)–(8.2.2) is given in Panel (b) and it lies asymptotically to the line $2T(\tau) = 2\tau + 2\delta_\infty$. The intensity profiles of the fields E (blue) and F (grey) from the APE system of selected periodic solutions are given in Panels (c)–(e). Panel (f) displays the limiting solution which is a homoclinic solution to $(x_{\mathrm{cw}}, x_{\mathrm{cw}})$ in a numerical representation. The saddle equilibrium limiting to the homoclinic orbit lies in the symmetry subspace $\mathrm{Fix}(\gamma)$, in contrast to the homoclinic orbit itself. The pulse shapes in the two components of the homoclinic in the APE are different. Consequently, this leads to a corresponding limiting family of periodic solutions consisting of alternating pulses.

The branches of square waves emanating from H_2 presented in Figure 8.3, follow the branch of stable period-two solutions of the singular map only up to a certain region of bistability with the CW state. In this regime of bistability, the branches of square wave solutions detach from the branch of stable period-two solutions of the singular map and induce a snaking of the branches of periodic solutions. Also, the branches of alternating pulse solutions emanating from H_1 detach from the branch of CW states in this regime and enter the snaking structure from the other side. This leads to the creation of solutions that are a mixed-type combination of square waves and alternating pulse solutions. The number of folds along the branches increases for larger periods, or correspondingly for larger delay and induces multiple stable mixed-type solutions to coexist. This dynamical phenomenon will be discussed in detail with homoclinic bifurcation theory in the following section.

Finally, note, that already the Hopf bifurcations $\mathrm{H}_{1,2}$ belong to a homoclinic bifurcation in the APE system, that we will not discuss here further.

Remark 3. *The Hopf points* $\mathrm{H}_{1,2}$ *arise through a Takens-Bogdanov bifurcation with* $\mathbb{Z}_2$*-symmetry in the APE, see [AAIS94].*

8.4 Appearance of mixed-type solutions in a Bykov T-point

In order to obtain a qualitative understanding of the organization of the different kinds of solutions in the snaking structure, we will now study the connecting orbits that limit the periodic solutions for increasing periods in the APE. Figure 8.6 displays the two branches of solutions emanating from the points $H_{1,2}$, respectively, within the snaking region (Panel (a)), computed in the APE system (8.3.1)–(8.3.4) as connecting orbits with varying parameters Y_0 and δ_∞. Note that in comparison to Figure 8.3, instead of the intensity, we display the delay parameter $\delta = \delta_\infty$ on the vertical axis, leading to the spiralling shape. Furthermore, the parameter range of Y_0 is restricted to the snaking region in this plot. The square waves here are approximated by the relative homoclinic orbits (4.6.4) (red) to the equilibria ($x_{1,2}$, $x_{2,1}$), corresponding to the period-two orbit of the singular map. When entering the snaking region, the branch undergoes infinitely many folds. In the representation of the branch in the (Y_0, δ_∞)-plane, the branch spirals into a centre $(Y_0^\star, \delta_\infty^\star) \approx (0.546, 1.926)$ (black dot). Panels (b)–(d) show the intensity profiles of E (red) and F (grey) of selected solutions along the red branch, (cf. corresponding points in shades of red in Figure 8.6 (a)). Note that the numerically obtained profiles span varying time intervals. This stems from the calculation process being conducted solely beyond a certain distance from the limiting equilibria. Consequently, different solutions require differing times to traverse this distance.

Before the first fold, the solutions on the red branch (cf. Panel (b)) correspond to SW-type solutions that are stable in the DAE system (8.2.1)–(8.2.2). They become unstable after the first fold, but after a second fold restabilize in the DAE system. Thereby, solutions are created that perform a single oscillation around the CW state $(x_{\mathrm{cw}}, x_{\mathrm{cw}})$ when switching from (x_1, x_2) to (x_2, x_1) (Panel (c)) in the APE system. These two types of solutions coexist as stable solutions in the DAE system (8.2.1)–(8.2.2). Moving further along the branch into the spiral, the time of the solutions spent near the CW state increases and also the number of damped oscillations around the CW state, see Panel (d). At the same time the length of the parameter interval of Y_0, where these solutions exist, decreases. These mixed-type solutions are connecting orbits from (x_1, x_2) to (x_2, x_1) with plateaus of increasing length at the CW state.

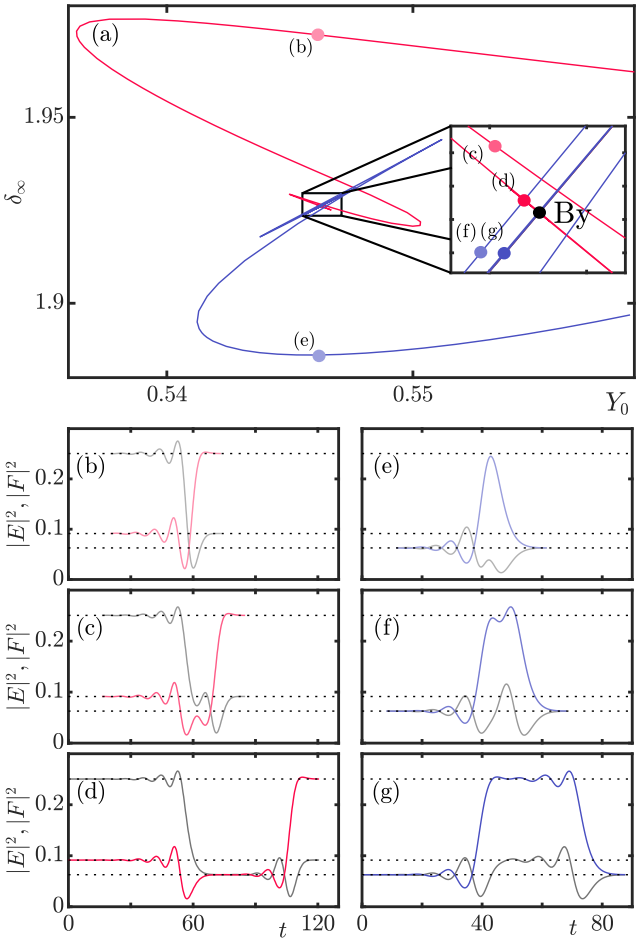

Figure 8.6: Branches of connecting orbits for the APE system (8.3.1)–(8.3.4) with varying parameters Y_0 and δ_∞. Red curve in (a): relative homoclinic orbits connecting the equilibria $(x_{1,2}, x_{2,1})$ corresponding to the period-two orbit of the singular map. Panels (b)–(d) show selected profiles (red points in (a)) from this branch (red: $|E(t)|^2$, grey: $|F(t)|^2$). Blue curve in (a): homoclinic orbits to the equilibrium $(x_{\mathrm{cw}}, x_{\mathrm{cw}})$ corresponding to the CW state. Panels (e)–(g) show selected profiles from this branch (blue points in (a)). Both branches are spiralling into a Bykov T-point (black dot). Other parameters as in Fig. 8.1. Figure and Caption taken from [SKJGW23a].

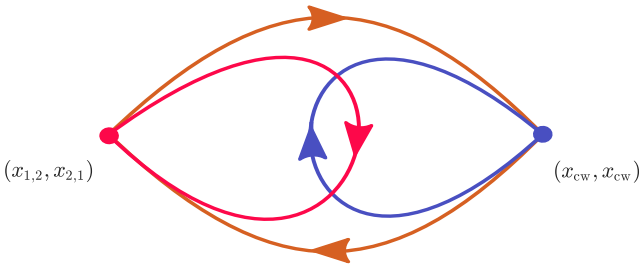

Figure 8.7: Sketch of connecting orbits involved in the unfolding of a Bykov T-point. A homoclinic switches its saddle by transitioning through a heteroclinic cycle (orange). The homoclinic solutions involved in the unfolding are a relative homoclinic to $(x_{1,2}, x_{2,1})$ (red) and to $(x_{\mathrm{cw}}, x_{\mathrm{cw}})$ (purple), representing the SW solutions and alternating pulse solutions respectively. Figure and Caption taken from [SKJGW23a].

The blue branch shown in Figure 8.6 (a) consists of homoclinic orbits to the equilibrium $(x_{\mathrm{cw}}, x_{\mathrm{cw}})$ corresponding to the alternating pulse solutions. It displays a similar behaviour and spirals into the centre $(Y_0^\star, \delta_\infty^\star)$ by passing through infinitely many folds. The profiles of the alternating pulse solutions along this branch behave complementary to the square wave solutions, see Figure 8.6 (e)–(g). Before the first fold, they consist of regular alternating pulse solutions (Panel (e)), that are unstable in the DAE system (8.2.1)–(8.2.2). They turn stable after the first fold. The alternating pulses perform an oscillation around the plateaus x_1 and x_2 of the square waves corresponding to the stable period-two orbit of the singular map when connecting $(x_{\mathrm{cw}}, x_{\mathrm{cw}})$ with itself (Panel (f)). Moving closer to the centre along the branch, we get further stable solutions which show an increasing number of damped oscillations around the plateaus of the square waves and the time spent near the plateaus increases (Panel (g)). The obtained mixed-type solutions are homoclinics to $(x_{\mathrm{cw}}, x_{\mathrm{cw}})$, that develop a plateau of increasing length at the equilibrium (x_1, x_2). Again, with the increasing length of the plateaus, the parameter intervals of their existence become smaller.

The two branches of connecting orbits terminate at a so called Bykov T-

point [Byk93; GS86; KLW14], see also the review in Section 3.10, located at the centre of the spiral $(Y_0^\star, \delta_\infty^\star)$. Such scenarios arise as homoclinic bifurcations of codimension-two and describe the situation when a homoclinic orbit collides with another saddle equilibrium. Thereby, a family of homoclinic orbits switches its corresponding saddle by creating a heteroclinic cycle. Figure 8.7 presents a sketch of the setup given in a Bykov T-point. The bifurcation point itself constitutes of a heteroclinic cycle connecting two different saddle equilibria (orange arrows). There are two families of homoclinic orbits connecting to each saddle in a parameter neighbourhood of the T-point (cf. red and blue lines in Figure 8.7). Identifying the equilibrium (x_1, x_2) with its symmetry twin (x_2, x_1), we can see that the scenario discussed here also matches with this schematic representation. Depending on the leading eigenvalues of the saddles being real or complex conjugate pairs, the unfolding of the Bykov T-points can have different shapes. Figure 8.7 gives a sketch of a Bykov T-point where the saddles have only real leading eigenvalues. This situation can already be realized for a planar ordinary differential equation. In general, the analysis of a Bykov T-point requires a three dimensional centre manifold. Details about the construction and technical prerequisites for centre manifold reductions for equilibria in delay equations can be found in [DG91; DVGLW95; VV87]. For the finite-dimensional case, see [HS10; San00] or the Section 3.6 in the introductory part on homoclinic bifurcation theory. For the APE system of the KGTI model discussed here, both saddle equilibria $(x_{\mathrm{cw}}, x_{\mathrm{cw}})$ and (x_1, x_2) are of double focus type, i.e. the leading stable and unstable eigenvalues are both unique up to complex conjugation. In this case, a four-dimensional centre manifold is required and we will assume that it exists and is sufficiently smooth. In either bifurcation scenario, there are two branches of homoclinic orbits emanating from the T-point, each of them corresponding to a branch of homoclinics to one of the two equilibria. In the present case of two double focus equilibria, both branches form a spiral, cf. Figure 8.6 (a).

Examples of Bykov T-points appearing in the context of temporal dissipative solitons in time-delayed systems have been discussed in [SW23], cf. Chapter 6, but also in [GR23; RKB20]. In particular, we have seen in Section 6.5, that a Bykov T-point is a possible way of the disappearance of solitons:

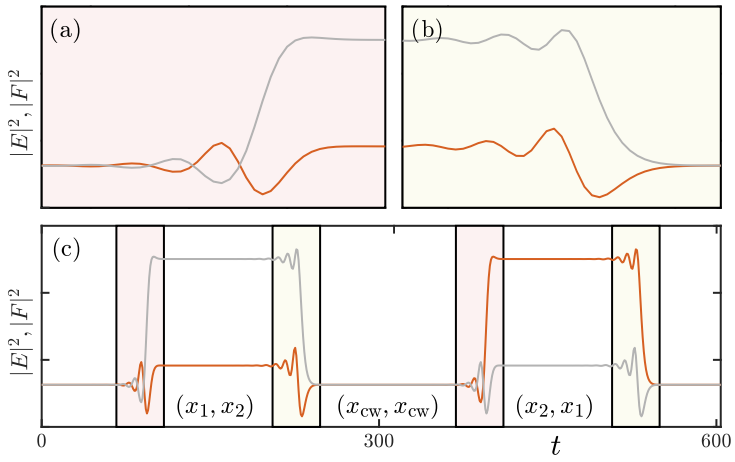

Figure 8.8: Profiles of the two heteroclinic solutions at the Bykov T-point: (a) heteroclinic solution connecting $(x_{\mathrm{cw}}, x_{\mathrm{cw}})$ to (x_1, x_2); (b) heteroclinic solution connecting (x_1, x_2) to $(x_{\mathrm{cw}}, x_{\mathrm{cw}})$; (c) profile of a periodic solution of mixed-type with $2T \approx 600$, composed by the heteroclinc solutions and plateaus at the equilibria. Intensity profiles of the fields E (orange) and F (grey) are shown. Parameters as in Fig. 8.1. Figure and Caption taken from [SKJGW23a].

when the corresponding homoclinic orbit of the profile equation collides with another equilibrium, a Bykov T-point is formed and the branch of stable TDSs terminates. If the second equilibrium is unstable in the original DDE, the T-point induces a delocalization and destabilization of the solution. In the case discussed here, both equilibria involved in the T-point are stable objects in the singular map. This leads to stable mixed-type solutions in the DAE system originating from the collision of the square waves with the stable CW state. Similarly, the alternating pulse solutions that form plateaus at the square waves coming from the stable period-two orbit also create stable mixed-type solutions. They correspond to the periodic orbits approaching the homoclinic orbits in the APE system ending at the T-Point. Hence, the unfolding of the T-point leads to various periodic orbits that can spend arbitrarily long times near each saddle equilibrium.

Figure 8.8 shows the relation of the profiles of these periodic orbits corresponding to the different mixed-type solutions with the heteroclinic solutions at the T-point. Panels (a) and (b) display the interface segments of the two heteroclinic solutions connecting $(x_{\mathrm{cw}}, x_{\mathrm{cw}})$ and (x_1, x_2) and vice versa which are symmetric under γ (4.3.4). For the same parameters, we give a periodic solution with $2T \approx 600$ close to the heteroclinic cycle in Panel (c). We can see, that such a square wave solution can be well-approximated by using the segments of the heteroclinic solutions from the panels (a) and (b) at the interface (red and yellow shaded regions, respectively), and inserting plateaus at $(x_{\mathrm{cw}}, x_{\mathrm{cw}})$ and $(x_{1,2},\, x_{2,1})$ in between transitions, which can be of arbitrary length (white regions).

The numerical approach to the computation of the snaking branches in a neighbourhood of the Bykov T-point is either achieved by path-continuation of periodic solutions with a large but fixed period, which are close to the connecting orbits, as executed in Figure 8.3. Qualitatively equivalent results can be achieved by the continuation of the connecting orbit itself as presented in Figure 8.6. The continuation of the T-point itself is only possible as a connecting orbit. Generically, a Bykov T-point is a bifurcation of codimension-two. In the APE system (8.3.1)–(8.3.4) both saddle equilibria have the same saddle index, i.e. the same number of unstable eigenvalues. Thereby, in this case, each heteroclinic solution connecting to either equilibria is of codimension-one. In order to find the codimension-two T-point, we compute both heteroclinic connections that yield the heteroclinic cycle, simultaneously. For its continuation a third parameter is necessary. To this end, we exploit the special role of the parameter δ in the APE system (8.3.1)–(8.3.4), which is not a control parameter in the DAE system (8.2.1)–(8.2.2). In this way, a continuation of the Bykov T-point is possible.

Figure 8.9 shows a bifurcation diagram in the parameter plane (Y_0, d), cf. Figure 3 in [KSGJ22]. It depicts the Hopf bifurcations of the CW state (solid and dotted black for supercritical and subcritical points, respectively), the fold of the period-two orbit of the singular map (grey), and the two first fold bifurcations along the branch of SWs (red) and alternating pulse solutions (blue). It can now be extended by the branch of Bykov T-points (orange)

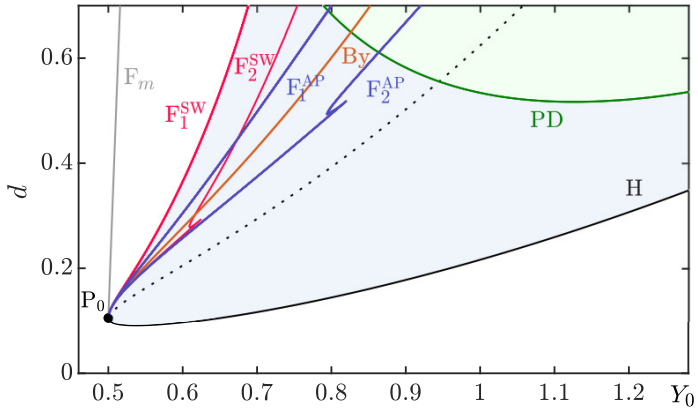

Figure 8.9: Bifurcation diagram for KGTI system (8.2.1)–(8.2.2) in the (Y_0, d)-plane: continuation of the Bykov T-point (orange), branch of supercritical (solid black) and subcritical (dotted black) Hopf points, first two folds along the branch of SWs (red), first two folds along the branch of alternating pulse solutions (blue). Fold of the equilibrium period-two orbit of the singular map (grey). All lines terminate in the point P_0 of the branch of Hopf points. Green line corresponds to period-doubling bifurcation of SWs. Other parameters as in Fig. 8.1. Figure and Caption taken from [SKJGW23a].

computed in the APE system (8.3.1)–(8.3.4), keeping in mind that at each point on the curve, our calculations also compute a response time δ_∞, that is not represented in the plot here. The branch of T-points is located among the branches of fold curves, at the centre of the snaking region, providing for a calculation of the position of the Maxwell point. The existence regime of the stable SW solutions, identified in [KSGJ22], is given by the blue-shaded region. It is bounded by the first fold of the square waves F_1^{SW} (red), the Hopf-curve H (black), together with a period-doubling of the singular map PD (green), which appears for larger values of Y_0 and d.

Between fold curve F_1^{SW}, that is the limiting curve for stable square waves, and the fold of the period-two orbit of the singular map F_m, there is a region where stable period-two solutions of the singular map exist but no stable SW

solutions. In this regime, the stable period-two orbit coexists with the stable CW state. This forms an obstruction that hinders the trajectory from passing immediately from one level of the period-two orbit to the other. The branch of T-points has to lie in the regime of bistability between the CW state and period-two solution in the singular map. This is localized between the fold-curve F_m and the subcritical part of the Hopf-curve (black dotted). All bifurcation curves emanate from the point $\mathrm{P}_0 \approx (0.500, 0.105)$. At this point in the singular map, the flip bifurcation switches between sub- and supercritical. In the APE system, this creates some type of degenerate Bykov T-point. This is a homoclinic bifurcation of codimension-three, which we are not going to study in more detail in this work. For values of d below the point P_0, the scenario for varying Y_0 is much simpler. The Hopf bifurcations are both supercritical and between them a branch of stable SWs without any bistability and hence no T-point.

8.5 Multiple T-points

In the preceding paragraphs, we analyzed a single Bykov T-point involving the stable period-two orbit of the singular map and the CW state. This is accompanied by a branch of periodic solutions, which links the two Hopf-bifurcations $\mathrm{H}_{1,2}$ as presented in Figure 8.2. Yet, homoclinics to saddle-focus or double-focus type equilibria, i.e. with complex conjugate leading eigenvalues, can induce extremely complicated structures. In their neighbourhood in phase space and for nearby parameter values, they can give rise to chaotic motion, including further periodic orbits and so-called N-homoclinic orbits, see [GS84; SSTC01] or Sections 3.7 and 3.10 in the introduction to homoclinic bifurcation theory. Analogously, the unfolding of Bykov T-points involving equilibria of saddle-focus or double-focus type can lead to infinitely many other T-points involving infinitely many N-homoclinics for all $N \in \mathbb{N}$. These N-homoclinics all lead to solutions that are unstable in the original system (8.2.1)–(8.2.2) and did not need to be explored for the theory presented in the previous sections.

Yet, the dynamics of the given APE system (8.3.1)–(8.3.4) can also be influenced by an additional equilibrium. This equilibrium corresponds to the

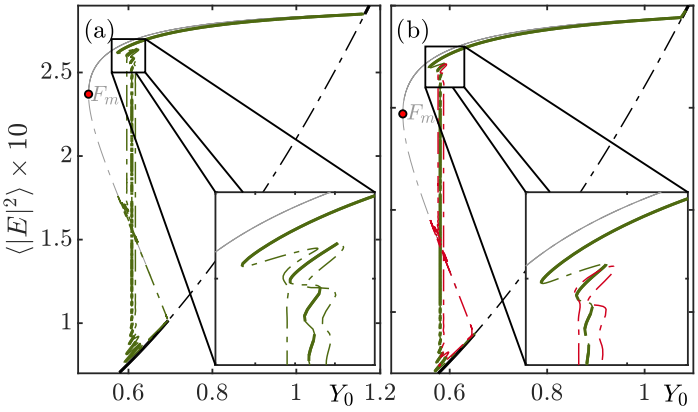

Figure 8.10: Branches of periodic solutions (coloured) and fixed points of the singular map (grey, black), compare Fig. 8.3: (a) For $d = 0.29$ the branches of periodic solutions have reconnected, creating a complex structure of multiple T-points along a single branch (green). Panel (b) For the lower value $d = 0.25$ this structure is detached and fully unstable (red). It contains another unstable SW regime which has the unstable period-two orbit of the singular map as its background. Other parameters as in Fig. 8.1. Figure and Caption taken from [SKJGW23a].

unstable period-two orbit emerging from the fold of period-two solutions of the singular map (dashed-dotted grey branch in Figure 8.3). It leads to unstable equilibria in the APE system and results in unstable square waves in the original system consisting of plateaus corresponding to these solutions. This additional equilibrium can also get entangled with the dynamics of the homoclinic orbits and T-points in the regime of bistability of the other two equilibria. An example of a T-point involving a saddle equilibrium corresponding to a stable background, whereas the other saddle corresponds to an unstable background was discussed in [SW23], cf. Sections 6.5–6.6. We will see that these additional branches of homoclinics and T-points, involving also the unstable period-two orbit, play a role here for larger values of the detuning parameter d.

Figure 8.10 (a) displays a branch of periodic solutions in the DAE sys-

tem (8.2.1)–(8.2.2) for $d = 0.29$. In contrast to the scenarios studied in the preceding sections, this branch shows an even more intricate structure. This elicits from four T-points, one of which lies near the Hopf-bifurcation point and is not visible in the figure here. This branch of periodic solutions features also unstable SWs to plateaus induced by the unstable period-two orbit of the singular map (dash-dotted grey curve in Figure 8.10), see also [KSGJ22] for an analytical derivation of the map. Two of the four T-points involve these unstable equilibria corresponding to such unstable period-two orbits. The remaining two T-points entail only the two stable equilibria. However, there is only one that displays also stable regions (middle curve of the three vertical green snaking curves in Figure 8.10 (a)). The branches corresponding to the other T-points consist of unstable solutions only, see the inset in Figure 8.10 (a).

If we decrease the detuning parameter d back to lower values, one can observe a recombination of the branches, see the inset of Figure 8.10 (b). As a consequence, we can observe the formation of two separate branches in Figure 8.10 (b). One of them builds a closed loop that is not connected to $H_{1,2}$. It contains the T-points involving the unstable background and the entire branch is unstable. In this parameter regime, it lies separate from the primary branch (green). The primary branch connecting to $H_{1,2}$ is in the familiar configuration as discussed before, carrying the stable square waves and stable mixed-type solutions created in a single T-point.

However, the reconnection of the branches does not influence the scenario for stable square wave solutions. The branch of stable square waves remains close to the branch of stable period-two orbits of the singular map until it reaches the vicinity of the Maxwell point indicated by the primary Bykov T-point. It also does not interfere with the creation of stable mixed-type solutions. Near the primary T-point, we find the nested intervals of stable mixed-type solutions. The recombination of the branches also does not hinder the continuation of the T-point and sticks to the primary T-point connected to the branches carrying the stable mixed-type solutions also for higher values of d.

In this chapter, we showed how the dynamics of square waves can be analysed similarly to TDSs in the context of homoclinic bifurcation theory by making use of the tools created in the previous chapters for temporal dissipative solitons and alternating pulse solutions. Thereby, we could ascribe the underlying mechanisms responsible of the collapsed snaking phenomenon of square waves in the KGTI-system to a Bykov T-point.

In particular, we find here an example covering both the supercritical and subcritical flip bifurcation in the singular map leading to the formation of stable square waves and unstable alternating pulse solutions in the large delay DDE. Their limiting homoclinics and corresponding saddles in the alternated profile equation interact in the Bykov T-point.

CHAPTER 9

Conclusion

This chapter gives an overview and discussion of the results presented in this thesis on the bifurcations and instabilities of temporal dissipative solitons in large delay DDE systems. It terminates by giving an outlook on possible applications of our study and further intriguing phenomena promising interesting results on the dynamics of TDSs.

9.1 Overview and discussion

In this thesis, we have demonstrated how the intricate dynamics exhibited by temporal dissipative solitons in systems with a large time delay can be thoroughly analysed leveraging classical concepts from homoclinic bifurcation theory within the framework of the profile equation. This methodology is reminiscent of the approach employed in the study of pulse and wave solutions in spatially extended systems, see for example [Kir88]. Thereby, it offers a new dimension to understanding the interplay between time-delayed and spatially extended systems [GP96]. The advanced nature of the profile equation, mirroring the causality principle in the original large delay DDE, removes the singular nature inherent to the limit of large delay. It facilitates numerical treatment and bifurcation analysis, which is especially valuable when the original system with large delay poses numerical challenges. The homoclinics calculated

through this approach not only approximate the soliton solutions but also faithfully reproduce the bifurcation structure. The large-period periodic solutions accompanying the homoclinic solution in the profile equation correspond to the soliton solutions for the large delay and share the same profile. Similarly to spatial dynamical systems, the stability properties of solutions concerning the linearized profile equation differ from those of the soliton in the linearized original large delay DDE. Establishing a straightforward relationship between specific homoclinic bifurcations and the corresponding bifurcations and instabilities of TDSs requires careful consideration, particularly of the response time δ as an additional parameter in the profile equation.

The homoclinic orbit flip scenario, studied in Chapter 6, leads to the coexistence of stable pulse packages akin to bound states in PDEs. A coexistence of stable pulse packages can usually be associated with a homoclinic snaking scenario observed in spatially extended systems, see [BK07]. Another example for the coexistence of bound states can be found in the cubic-quintic complex Ginzburg-Landau equation, see [Mal91]. In this context, the different bound state solutions are related to the oscillatory tails of the pulse. They are organized on separate branches possibly with different coexistent spacing [SSM18] and can lead to very complicated dynamics [TVZ12]. However, our presented scenario deviates remarkably from the homoclinic snaking. It does not feature an increasing number of pulses along one single branch, that are added to the profile after consecutive folds in pulse-adding scenarios or through oscillatory tails. Instead, the stable pulse packages emerge from the equidistant pulses, that lose their stability in the homoclinic orbit flip. The stable pulse packages then lose their stability in connection with a Bykov T-point, where the pulse solutions collide with another unstable equilibrium. Beyond this stability boundary, the pulse packages exhibit a trailing edge instability, resulting in the generation of additional pulses until a rapidly pulsating solution is attained, see Figure 6.2 (b).

Our calculations in Chapter 6 considered a relatively small feedback strength. Interestingly, for this regime, or even smaller values of κ, the bifurcations transitioning between the different types of excitability in the Morris-Lecar model are strongly connected with the dynamics of solitons and multi-pulse solutions.

For larger feedback strength or feedback involving the activation variable w, one can anticipate more complex and diverse dynamical scenarios.

While the method of analysing TDSs as homoclinic solutions in the profile equation has proven effective, it encounters limitations in the case of TDSs undergoing a period-doubling or resonant Neimark-Sacker bifurcation. With the alternated profile equation, derived and analyzed in Chapter 4, we have suggested an effective solution to the problem. This newly introduced framework allows us to analyze also period-doubling bifurcations of TDSs and the resulting alternating pulse solutions with homoclinic bifurcation theory. The system is provided with an innate symmetry that comes naturally from the profile of the periodic solutions with a period of approximately twice the delay, cf. [MPN86]. In Chapter 7, we demonstrated that the underlying dynamics are related to the unfolding of a degenerate homoclinic with a symmetry breaking.

Note, that the period-doubling has no analogue in spatially extended systems. The travelling wave solutions in the spatially extended systems are stationary solutions with respect to a comoving frame and hence cannot undergo such a bifurcation. However a period-doubling in a reduced system of purely spatial dynamics, can lead to alternating pulses in the original PDE. In contrast to that, in the case of DDEs, where there is no explicit spatial variable, there can be period-doublings of pulse solutions. Although period-doublings can only appear in systems having three dimensions or higher, this is already possible for a one-dimensional space of system variables, because the delay term induces an infinite dimensional phase space.

For general TDSs, every pulse is triggered by the preceding one. This is also the case for the alternating pulse solutions created in a period-doubling. In the case of the orbit flip scenario treated in Chapter 6, cf. [SW23] or [GR23], also a period-doubling emerges. However, the period-doubling presented there deals with equidistant pulses. In these scenarios, each pulse is triggered not by the preceding pulse, but the pulse before the preceding one. This is related to the reappearance of critical Floquet multipliers, cf. Lemma 1 in [GR23]. Note, that whereas a one-pulse solution can be mapped to an equidistant two-pulse by the reappearance rule, their respective period-doubled solutions cannot be mapped to each other by the reappearance rule.

Beyond that, we provided a desingularized alternative for the computation of the period-doubling, which we could effectively apply for the continuation of the subcritical period-doubling curve in [SW23], cf. green curve in Figure 6.5.

Finally, the extension of the profile equation to encompass alternating pulse solutions or square waves presents opportunities for further exploration of complex bifurcation scenarios. Thereby, we elucidated the underlying mechanisms driving the collapsed snaking phenomenon of square waves in vertical external-cavity Kerr-Gires-Tournois interferometers by a Bykov T-point in Chapter 8. Beginning with a model based on delay-algebraic equations in the long delay limit, we applied the alternated profile equation to square waves. Notably, this equation eliminates the influence of large delay, allowing for the identification of square waves with periodic solutions of arbitrarily high periods near connecting orbits at finite parameter values. These connecting orbits can be interpreted as relative homoclinic orbits with respect to a mirror symmetry, thereby facilitating a qualitative understanding of the various profile shapes and their organization in parameter space emerging in the collapsed snaking scenario. Specifically, we illustrate that the position of the limiting Bykov T-point, resulting from homoclinic bifurcations of codimension-two when a homoclinic orbit collides with another equilibrium, corresponds to the position of the Maxwell point in the centre of the snaking region.

In Chapter 8, we encounter a scenario where both the supercritical and subcritical flip bifurcation of a fixed point in the singular map leading to the formation of square waves and alternating pulse solutions in the large delay DDE can be observed. The limiting homoclinics and corresponding saddles in the alternated profile equation interact at the Bykov T-point. In contrast to that, the alternating pulses arising from the period-doubling, as discussed in Chapter 7, do not stem from a bifurcation of fixed points within the singular map.

The study applied a numerical analysis, using DDE-BIFTOOL for path continuation and stability calculations. For certain bifurcations presented in this thesis, we provided an implementation as extensions in the software package and present the corresponding boundary value problems in Appendix A.

9.2 Outlook

Studying TDSs as homoclinic solutions in the profile equation provides a promising methodology for analyzing a variety of bifurcation scenarios of temporal dissipative solitons. Additionally, we presented a similar framework such that this theory can be applied to a wider class of periodic solutions in time-delayed systems like periodic solutions consisting of alternating pulses or plateaus. The alternated profile equation can be further expanded to encompass $N\tau$ periodic solutions with multiple alternating plateaus or pulses and may provide clarity on the intricate bifurcation scenarios involved.

This theory finds a wide range of applications in optical and optoelectronic systems. A particular example form laser systems subject to strong time-delayed feedback in long cavity regimes like the Kerr-Gires Tournois interferometers discussed in Chapter 8. The methodology presented in this thesis supports the detection of the existence regions of stable TDSs, square waves or other structures appearing in the system. For instance, it assists the identification of those regions with collapsed snaking, which could lead to regions characterized by the multistability of periodic solutions consisting of intricate multiple localized structures which can be of significance in experiments. Moreover, it offers potential applications such as the generation of high-power tunable optical frequency combs in systems subject to strong time-delayed feedback in long cavity regimes.

This methodology shows potential for the analysis of the dynamics in diverse scenarios. For example, it reveals that the mechanism lying behind the coexistence regions of dark and bright temporal dissipative solitons observed in the Kerr-Gires-Tournois interferometers involved in a collapsed snaking scenario, as evidenced in prior research [SGJ22; SJG22; SPVJG19] can also be linked to a Bykov T-point in the profile equation.

Having said that, homoclinic bifurcation theory also proposes other scenarios that could lead to intriguing dynamics for TDSs. Similarly to the homoclinic orbit flip, an inclination flip bifurcation in the profile equation is expected to induce the coexistence of TDSs in large delay DDEs with stable pulse packages. Other homoclinic bifurcations promise the emergence of possibly stable two-pulse packages. For example, the occurrence of a non-orientable resonant

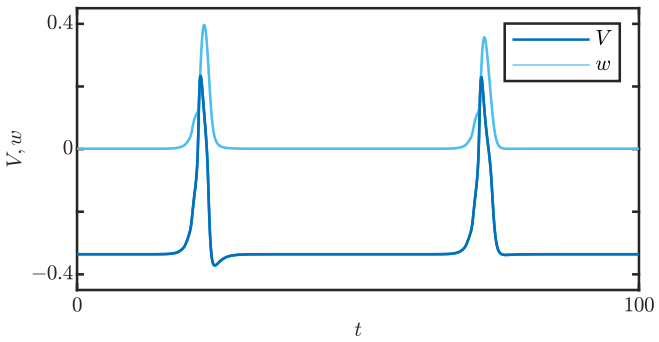

Figure 9.1: Profile of an alternating pulse solution in time-delayed Morris-Lecar model (7.1.1) discussed in Chapter 7. Parameters: $E_1 = -0.37$, $\kappa_V = 0.35$ and $\kappa_w = 0.1912$. Other parameters as in Fig. 7.1.

homoclinic orbit seems likely to result in the formation of stable pulse packages. In particular, exploring the consequences of a Belyakov transition could yield interesting dynamics where two-pulse packages emerge.

Finally, time-delayed systems offer a rich variety of dynamical phenomena. A peculiar effect can be observed in the formation of a profile containing alternating pulses as depicted in Figure 9.1, where only one pulse exhibits a hyperpolarization. In this scenario, a pulse without overshoot triggers another pulse with overshoot, while a pulse with overshoot triggers one without. It was found in the time-delayed Morris-Lecar model discussed in Chapter 7, induced by a feedback including also the activation variable w. Studying these kinds of solutions using homoclinic bifurcation theory could lead to interesting results on the complex dynamics of TDSs.

APPENDIX A

Boundary value problems for the numerical computation of connecting orbits in delay differential equations

In this chapter, we give an overview of the determining systems used for the numerical computations of the various homoclinic bifurcations used in the preceding chapters. We present the boundary value problem used for the numerical computation of connecting orbits in DDE-BIFTOOL. Furthermore, we suggest an equivalent system providing for the numerical computation of heteroclinic orbits connecting between certain saddle or double foci. Finally, we provide for the boundary value problem, that we used for the computation and continuation of the homoclinic orbit flip.

A.1 General boundary value problem for the numerical computation of connecting orbits

In Chapters 6 and 7, we analyzed temporal dissipative solitons in large delay DDE systems as homoclinic solutions in an equation with an advanced argument called the profile equation. We supported our results with a numerical analysis using the path-continuation software DDE-BIFTOOL [ELR02; SELSR16]. The computation of the connecting orbits is based on the boundary value problem (BVP) from [SER02]. The authors provide a detailed derivation

of the restraints and also the collocation method used for the computation of the profile of the connecting orbit. The discretization of the boundary value problem can then be computed numerically by using the Newton method. In this section, we present the boundary conditions used for the numerical computation of connecting orbits taken from [SER02].

We begin by setting up some notations used in the derivation. To this end, consider the delay differential equation

$$\dot{x}(t) = f(x(t), x(t-\tau), \eta), \tag{A.1.1}$$

where $f \in \mathcal{C}^1(\mathbb{R}^n \times \mathbb{R}^n \times \mathbb{R}^p, \mathbb{R}^n)$, with parameter $\eta \in \mathbb{R}^p$ and delay $\tau > 0$. Theory on these kinds of differential equations can be found in [DVGLW95; HL93]. Delay differential equations require an infinite-dimensional phase space consisting of continuous functions on $[-\tau, 0]$ into $\mathbb{R}^n$. These functions are characterized in the following way: Let $x_*(t)$ be a solution of (A.1.1) and define for any $t \in \mathbb{R}$ a segment $x_t(\theta)$ of this solution with $x_t(\theta) := x_*(t+\theta)$, where $-\tau \leq \theta \leq 0$. For any $s \in \mathbb{R}$, the segment x_s uniquely determines a solution $x_*(t)$ for all $t \geq s$.

A heteroclinic solution is a solution $h(t)$ of (A.1.1) at $\eta = \eta_*$ that satisfies

$$\lim_{t\to-\infty} h(t) = x^-, \quad \text{and} \quad \lim_{t\to\infty} h(t) = x^+,$$

where x^- and x^+ are two equilibria of (A.1.1). Note, that this includes homoclinic solutions as a special case, where $x^- = x^+$. Theory on these kinds of solutions can be reviewed in Chapter 3 or [HS10; SSTC01].

The asymptotic decay rates of these kinds of solutions can be determined by the stability around the corresponding saddle equilibria. To this end, we need to consider the linearization of (A.1.1) around an equilibrium x_0, given by

$$\dot{v}(t) = Av(t) + Bv(t-\tau), \tag{A.1.2}$$

with $A = A(x_0, \eta) = \partial_1 f(x_0, x_0, \eta)$ and $B = B(x_0, \eta) = \partial_2 f(x_0, x_0, \eta)$, and $\mathbb{I}$ denotes the identity in $\mathbb{R}^{n\times n}$. Define the matrix

$$\Delta(x_0, \lambda, \eta) := \lambda\mathbb{I} - A - Be^{-\lambda\tau},$$

and the characteristic equation is then given by

$$\det(\Delta(x_0, \lambda, \eta)) = 0.$$

Thereby, we can compute the eigenvalues λ of the linearization of x_0, which are given by the roots of the corresponding characteristic equation. The eigenvalues together with the corresponding eigenvector v can be found as solutions of

$$\Delta(x_0, \lambda, \eta)v = 0, \tag{A.1.3}$$
$$||v|| = 1, \tag{A.1.4}$$

where the last condition provides for a unique eigenvector such that v is normalized. The adjoint variational equation to (A.1.2) is given by

$$\dot{w}(t) = -A^{\mathrm{H}}w(t) - B^{\mathrm{H}}w(t+\tau),$$

where M^{H} denotes here the adjoint of matrix M. The eigenvalues together with the unique adjoint eigenvectors can then be found by solving

$$\Delta^{\mathrm{H}}(x_0, \lambda, \eta)w = 0, \tag{A.1.5}$$
$$||w|| = 1. \tag{A.1.6}$$

The corresponding eigenfunctions are given by

$$\phi(\theta) = ve^{\lambda\theta}, \quad \theta \in [-\tau, 0],$$

where $\phi(\theta) \in C([-\tau, 0], \mathbb{C}^n)$ and the adjoint eigenfunctions by

$$\psi(\theta) = w^{\mathrm{H}}e^{-\lambda\theta}, \quad \theta \in [0, \tau],$$

where $\psi(\theta) \in C([0, \tau], \mathbb{C}^{1\times n})$. The duality pairing is given by

$$\langle\psi|\phi\rangle = \psi(0)\phi(0) + \int_{-\tau}^{0} \psi(\xi+\tau)B(x_0, \theta)\phi(\xi)\mathrm{d}\theta. \tag{A.1.7}$$

If ϕ and ψ belong to different eigenvalues, then the duality pairing vanishes.

We will now present the conditions for the numerical computation of a heteroclinic solution. A heteroclinic is a solution $h(t)$ defined on the entire real line $t \in \mathbb{R}$. For a numerical computation of a connecting orbit of (A.1.1), it

is necessary to truncate the profile of the solution to a finite interval. To this end, we rescale the time with $t \longmapsto t/T$ in system (A.1.1) and obtain

$$(I.) \qquad \dot{y}(t) = Tf(y(t), y(t-\tau/T), \eta), \quad t \in [0,1].$$

The equilibria x^- and x^+ are given by

$$(II.) \qquad f(x^-, x^-, \eta) = 0,$$
$$(III.) \qquad f(x^+, x^+, \eta) = 0.$$

We want to impose now boundary conditions for a heteroclinic solution $h(t)$ at $t = 0$ and $t = 1$. To this end, we use projections onto the spectral eigenspaces of the corresponding equilibria. Assume, that both equilibria x^- and x^+ are hyperbolic, that is all eigenvalues do not have a vanishing real part and assume they have multiplicity one. Note that in DDE systems, in the spectrum of an equilibrium one finds infinitely many eigenvalues lying to the left of the imaginary axis, yet only a finite number lying to the right. Suppose the equilibrium x^- has s^- unstable eigenvalues λ_k^- with corresponding eigenvectors v_k^-, for $k = 1, \ldots, s^-$. Using (A.1.3)–(A.1.4), they can be found as solutions of

$$(IV.) \qquad \Delta(x^-, \lambda_k^-, \eta) v_k^- = 0, \qquad k = 1, \ldots, s^-,$$
$$(V.) \qquad ||v_k^-|| = 1, \qquad k = 1, \ldots, s^-.$$

The initial function segment at $t = 0$ can then be written as

$$y_0(\theta/T) = x^- + \epsilon \sum_{k=1}^{s^-} \alpha_k v_k^- e^{\lambda_k^- \theta}, \quad \theta \in [-\tau, 0] \tag{A.1.8}$$

with $\sum_{k=1}^{s^-} |\alpha_k|^2 = 1$, and a suitable $\epsilon > 0$ (small, but fixed), cf. [DVGLW95; SER02]. The constraint on the left boundary at $t = 0$ is then given by

$$(VI.) \qquad y(0) = x^- + \epsilon \sum_{k=1}^{s^-} \alpha_k v_k^-,$$

$$(VII.) \qquad \sum_{k=1}^{s^-} |\alpha_k|^2 = 1.$$

A similar condition on the right boundary $t = 1$ cannot be imposed, since it would require the computation of infinitely many stable eigenvalues and corresponding vectors. Instead, we impose conditions on the projections into the stable eigenspace with respect to the duality pairing (A.1.7). Suppose that x^+ has s^+ unstable eigenvalues, denoted with λ_k^+, and we denote the corresponding adjoint eigenvectors with w_k^+, and eigenfunctions $\psi_k(\theta)$, for $k = 1, \ldots, s^+$. Using (A.1.5)–(A.1.6), they are found as solutions to

$$\begin{aligned} (VIII.) \qquad & \Delta^H(x^+, \lambda_k^+, \eta) w_k^+ = 0, && k = 1, \ldots, s^+, \\ (IX.) \qquad & ||w_k^+|| = 1, && k = 1, \ldots, s^+. \end{aligned}$$

We impose that the projections of the desired solution along the unstable eigendirections at the right boundary vanish with respect to the duality pairing, that is

$$\left\langle \psi_k | y(1) - x^+ \right\rangle = 0, \qquad k = 1, \ldots, s^+. \tag{A.1.9}$$

Then we can write the projections (A.1.9) of the desired solution as

$$\begin{aligned} &(X.)\ w_k^{+H}(y(1) - x^+) \\ &\quad + \int_{-\tau}^{0} w_k^{+H} e^{-\lambda_k^+(\theta+\tau)} B(x^+, \eta)(y(1 + \theta/T) - x^+) \mathrm{d}\theta = 0, \qquad k = 1, \ldots, s^+. \end{aligned}$$

Finally, in order to remove the translational invariance of the heteroclinic solution, we also include a condition, which minimizes the phase shift with respect to some solution $\tilde{y}$, such that

$$(XI.) \qquad p(y, \eta) = \int_0^1 y(t) \tilde{y}'(t) \mathrm{d}t = 0.$$

Usually one picks the solution, that has been computed in the previous step inside the Newton solver.

Hence, the boundary value problem for the computation of a heteroclinic solution is given by

$$(I.) \qquad \dot{y}(t) = T f(y(t), y(t - \tau/T), \eta),$$

$$
\begin{aligned}
(II.) \qquad & 0 = f(x^-, x^-, \eta), \\
(III.) \qquad & 0 = f(x^+, x^+, \eta), \\
(IV.) \qquad & 0 = \Delta(x^-, \lambda_k^-, \eta) v_k^-, && k = 1, \ldots, s^-, \\
(V.) \qquad & 0 = ||v_k^-|| - 1, && k = 1, \ldots, s^-, \\
(VI.) \qquad & 0 = y(0) - (x^- + \epsilon \sum_{k=1}^{s^-} \alpha_k v_k^-), \\
(VII.) \qquad & 0 = \sum_{k=1}^{s^-} |\alpha_k|^2 - 1, \\
(VIII.) \qquad & 0 = \Delta^{\mathrm{H}}(x^+, \lambda_k^+, \eta) w_k^-, && k = 1, \ldots, s^+, \\
(IX.) \qquad & 0 = ||w_k^+|| - 1, && k = 1, \ldots, s^+, \\
(X.) \qquad & 0 = w_k^{+H}(y(1) - x^+) \\
& \quad + \int_{-\tau}^{0} w_k^{+H} e^{-\lambda_k^+(\theta+\tau)} \, B(x^+, \eta) \, (y(1 + \theta/T) - x^+) \mathrm{d}\theta, \\
& && k = 1, \ldots, s^+, \\
(XI.) \qquad & 0 = p(y, \eta) - \int_0^1 y(t) \tilde{y}'(t) \mathrm{d}t.
\end{aligned}
$$

Note that equation $(I.)$ needs to be implemented using a collocation method, provided in [SER02].

Connecting orbits can be found by solving equations $(I.) - (XI.)$. The system is well-posed with $s^+ - s^- + 1$ free parameters, where s^+ and s^- denote the number of unstable eigenvalues of x^+ and x^- respectively. Especially, for homoclinics, it is $x^+ = x^-$ and hence, we need to adjust one parameter in order to find the homoclinic.

A.2 Boundary value problem for connecting orbits in case of saddle or double foci

In general, numerical computations require systems of real equations. Since the eigenvalue problem presented in the previous section can provide solutions in $\mathbb{C}$, the equations defining the boundary value problem for the computation of a connecting orbit might be $\mathbb{C}$-valued, as well. Unfortunately, the numerical computation of the connecting orbit with this boundary value problem only works when the provided eigenvalues and corresponding eigenvectors are real. Note that this only concerns the unstable eigenvalues of the equilibria, since the boundary conditions presented in the previous section do not require stable eigenvalues.

In the case treated in Chapter 8, the eigenvalues of the linearization of the system (8.3.1)–(8.3.4) at the equilibria all appear as complex conjugated pairs. For the computation of the relative homoclinic solutions connecting these equilibria of double focus type, we implemented a different boundary value problem. It can be found in [SKJGW23b], where we give an exemplary continuation of the connecting orbits discussed in Chapter 8. In this section, we present the adapted boundary value problem for this special case. Additionally, since this system belongs to a DAE system, we will now generalize the case treated in the previous section to these kinds of systems.

To this end, we consider here a system

$$M\dot{x}(t) = f(x(t), x(t-\tau), \eta), \tag{A.2.1}$$

where $f \in \mathcal{C}^1(\mathbb{R}^n \times \mathbb{R}^n \times \mathbb{R}^p, \mathbb{R}^n)$, with parameter $\eta \in \mathbb{R}^p$ and delay $\tau > 0$ and especially $M \in \mathbb{R}^{n\times n}$ is a, possibly singular, mass matrix. Also here, we want to find a heteroclinic solution of (A.2.1) at $\eta = \eta_*$ satisfying

$$\lim_{t\to-\infty} h(t) = x^- \quad \text{and} \quad \lim_{t\to\infty} h(t) = x^+,$$

where x^- and x^+ are two equilibria of (A.2.1). The linearization of (A.2.1) around an equilibrium x_0 is given by

$$M\dot{v}(t) = Av(t) + Bv(t-\tau), \tag{A.2.2}$$

with $A = A(x_0, \eta) = \partial_1 f(x_0, x_0, \eta)$ and $B = B(x_0, \eta) = \partial_2 f(x_0, x_0, \eta)$. Let

$$\Delta(x_0, \eta, \lambda) = \lambda M - A - Be^{-\lambda\tau}.$$

We obtain the eigenvalues λ of the linearization at x_0 and a unique corresponding eigenvector v by solving

$$\Delta(\lambda, \eta)v = 0, \tag{A.2.3}$$

$$||v|| = 1. \tag{A.2.4}$$

Since these equations can have complex solutions, we need to replace them with real conditions. Note that if λ and v is a solution, then so is $\overline{\lambda}$ and $\overline{v}$. Setting $\lambda := \gamma + i\omega$ and $v := r + iq$. Using that $\mathbb{C} \cong \mathbb{R}^2$, then it can be shown by $v \longmapsto (r, q)$, that (A.2.3) is equivalent to

$$\begin{aligned} &- \begin{pmatrix} \gamma\mathbb{I} & -\omega\mathbb{I} \\ \omega\mathbb{I} & \gamma\mathbb{I} \end{pmatrix} \begin{pmatrix} M & \mathbb{O} \\ \mathbb{O} & M \end{pmatrix} \begin{pmatrix} r \\ q \end{pmatrix} + \begin{pmatrix} A & \mathbb{O} \\ \mathbb{O} & A \end{pmatrix} \begin{pmatrix} r \\ q \end{pmatrix} \\ &\quad + \begin{pmatrix} B & \mathbb{O} \\ \mathbb{O} & B \end{pmatrix} e^{-\gamma\tau} \begin{pmatrix} \cos(\omega\tau)\mathbb{I} & \sin(\omega\tau)\mathbb{I} \\ -\sin(\omega\tau)\mathbb{I} & \cos(\omega\tau)\mathbb{I} \end{pmatrix} \begin{pmatrix} r \\ q \end{pmatrix} = 0. \end{aligned} \tag{A.2.5}$$

As a normalization condition, we replace (A.2.4) by

$$\|(r, q)\| = 1. \tag{A.2.6}$$

However, the eigenvector v is unique up to multiplication with a complex number. To guarantee uniqueness, we then chose the vector with vanishing imaginary part in the first entry,

$$q^1 = 0, \tag{A.2.7}$$

where q^1 denotes the first entry of the vector q. This initial condition can always be obtained by multipling the vector with a complex number rotating the first coordinate to the real line.

Analogously, we obtain a unique adjoint eigenvector w by

$$\Delta^{\mathrm{H}}(\lambda, \eta)w = 0, \tag{A.2.8}$$

$$||w|| - 1 = 0. \tag{A.2.9}$$

Setting $w := R + iQ$, (A.2.8) is then equivalent to

$$-\begin{pmatrix} \gamma\mathbb{I} & \omega\mathbb{I} \\ -\omega\mathbb{I} & \gamma\mathbb{I} \end{pmatrix}\begin{pmatrix} M & \mathbb{O} \\ \mathbb{O} & M \end{pmatrix}\begin{pmatrix} R \\ Q \end{pmatrix} + \begin{pmatrix} A^{\mathrm{H}} & \mathbb{O} \\ \mathbb{O} & A^{\mathrm{H}} \end{pmatrix}\begin{pmatrix} R \\ Q \end{pmatrix} + \begin{pmatrix} B^{\mathrm{H}} & \mathbb{O} \\ \mathbb{O} & B^{\mathrm{H}} \end{pmatrix} e^{-\gamma\tau}\begin{pmatrix} \cos(\omega\tau)\mathbb{I} & -\sin(\omega\tau)\mathbb{I} \\ \sin(\omega\tau)\mathbb{I} & \cos(\omega\tau)\mathbb{I} \end{pmatrix}\begin{pmatrix} R \\ Q \end{pmatrix} = 0, \tag{A.2.10}$$

and we replace the normalization condition (A.2.9) with

$$\|(R, Q)\| = 1, \tag{A.2.11}$$

$$Q^1 = 0. \tag{A.2.12}$$

The corresponding eigenfunctions are given by

$$\phi(\theta) = ve^{\lambda\theta}, \quad \theta \in [-\tau, 0],$$

where $\phi(\theta) \in C([-\tau, 0], \mathbb{C}^n)$ and the adjoint eigenfunction by

$$\psi(\theta) = w^{\mathrm{H}} e^{-\lambda\theta}, \quad \theta \in [0, \tau],$$

where $\psi(\theta) \in C([0, \tau], \mathbb{C}^{1\times n})$. The duality pairing is given here by

$$\langle\psi|\phi\rangle = \psi(0)M\phi(0) + \int_{-\tau}^{0} \psi(\theta + \tau)MB(x_0, \eta)\phi(\theta)\mathrm{d}\theta. \tag{A.2.13}$$

This duality pairing now vanishes, if ϕ and ψ belong to different eigenvalues.

We will now present the conditions for the numerical computation of a heteroclinic solution connecting to equilibria of saddle foci or double foci type. A heteroclinic is a solution $h(t)$ defined on the entire real line $t \in \mathbb{R}$. Firstly, we need to truncate the profile of the solution to a finite interval. To this end, we rescale the time with $t \longmapsto t/T$ in system (A.2.1) and obtain

$$(i.) \qquad M\dot{y}(t) = Tf(y(t), y(t - \tau/T), \eta), \quad t \in [0, 1].$$

The equilibria x^- and x^+ are given by

$$(ii.) \qquad f(x^-, x^-, \eta) = 0,$$

$$(iii.) \qquad f(x^+, x^+, \eta) = 0,$$

and are both assumed to be hyperbolic.

We want to impose now boundary conditions for a heteroclinic solution $h(t)$ at $t = 0$ and $t = 1$. Suppose the linearization (A.2.2) at the equilibrium x^- has s^- unstable eigenvalues $\lambda_k^- := \gamma_k^- + i\omega_k^-$ with corresponding eigenvectors $v_k^- := r_k^- + iq_k^-$, and $\omega_k^- \neq 0$, $q_k^- \neq 0$ for $k = 1, \ldots, s^-$. Assume further that the eigenvalues λ_k^- are all complex conjugate pairs such that $\overline{\lambda}_{2k-1} = \lambda_{2k}$, for $k = 1, \ldots, s^-$. From (A.2.5)–(A.2.7), we obtain then the eigenvalues and corresponding unique eigenvectors as solutions of

$$(iv.) \qquad -\begin{pmatrix} \gamma_k^-\mathbb{I} & -\omega_k^-\mathbb{I} \\ \omega_k^-\mathbb{I} & \gamma_k^-\mathbb{I} \end{pmatrix} \begin{pmatrix} M & \mathbb{O} \\ \mathbb{O} & M \end{pmatrix} \begin{pmatrix} r_k^- \\ q_k^- \end{pmatrix} + \begin{pmatrix} A & \mathbb{O} \\ \mathbb{O} & A \end{pmatrix} \begin{pmatrix} r_k^- \\ q_k^- \end{pmatrix}$$
$$+ \begin{pmatrix} B & \mathbb{O} \\ \mathbb{O} & B \end{pmatrix} e^{-\gamma_k^-\tau} \begin{pmatrix} \cos(\omega_k^-\tau)\mathbb{I} & \sin(\omega_k^-\tau)\mathbb{I} \\ -\sin(\omega_k^-\tau)\mathbb{I} & \cos(\omega_k^-\tau)\mathbb{I} \end{pmatrix} \begin{pmatrix} r_k^- \\ q_k^- \end{pmatrix} = 0,$$

$$(v.) \qquad \left\| (r_k^-, q_k^-) \right\| = 1,$$

$$(vi.) \qquad {q_k^-}^1 = 0.$$

Recall from the previous section, that for a suitable $\epsilon > 0$ the initial function segment (A.1.8) is given by

$$y_0(\theta/T) = x^- + \epsilon \sum_{k=1}^{s^-} \alpha_k v_k^- e^{\lambda_k^-\theta}, \quad \theta \in [-\tau, 0], \tag{A.2.14}$$

$$\sum_{k=1}^{s^-} |\alpha_k|^2 = 1. \tag{A.2.15}$$

Recall, that for a vector with entries in $\mathbb{C}$, it is $v + \bar{v} \in \mathbb{R}$ and $v - \bar{v} \in i\mathbb{R}$. Note that we can replace the vector v_k^-, forming the basis of the stable eigenspace with respect to the eigenvalue λ_k^-, by a new basis given by the linear combinations $\frac{1}{2}(v_{2k-1}^- + v_{2k}^-)$ and $\frac{1}{2i}(v_{2k-1}^- - v_{2k}^-)$ for $k = 1, \ldots, s^-$. What is more, we can also replace the eigenfunctions $\phi_k(\theta) = v_k^- e^{\lambda_k^-\theta}$ that appear in this expression with $\frac{1}{2}(\phi_{2k-1}(\theta) + \phi_{2k}(\theta))$ and $\frac{1}{2i}(\phi_{2k-1}(\theta) - \phi_{2k}(\theta))$, for $k = 1, \ldots, s^-$. Note that $\overline{v_{2k-1}^-} = v_{2k}^-$ and $\overline{\phi_{2k-1}^-} = \phi_{2k}^-$.

We can then replace the initial function segment A.2.14 with the following

real expression,

$$\begin{aligned} y(\theta/T) = x^- + \epsilon \sum_{k=1}^{s^-/2} & \frac{1}{2}\alpha_{2k-1}\left(\phi_{2k-1}(\theta) + \phi_{2k}(\theta)\right) \\ & + \frac{1}{2i}\alpha_{2k}\left(\phi_{2k-1}(\theta) - \phi_{2k}(\theta)\right) \\ = x^- + \epsilon \sum_{k=1}^{s^-/2} & \alpha_{2k-1} e^{\gamma^-_{2k}\theta}\left(\cos(\omega^-_{2k}\theta) r^-_{2k} - \sin(\omega^-_{2k}\theta) q^-_{2k}\right) \\ & + \alpha_{2k} e^{\gamma^-_{2k}\theta}\left(\sin(\omega^-_{2k}\theta) r^-_{2k} + \cos(\omega^-_{2k}\theta) q^-_{2k}\right). \end{aligned}$$

The restraint on the left boundary at $t = 0$ is then given by

$$(vii.) \qquad y(0) = x^- + \epsilon \sum_{k=1}^{s^-/2} \alpha_{2k-1} r^-_{2k} + \alpha_{2k} q^-_{2k},$$

$$(viii.) \qquad \sum_{k=1}^{s^-} |\alpha_k|^2 = 1.$$

For the right boundary, we impose conditions on the projections with respect to the duality pairing for DAEs (A.2.13).

Suppose that the linearization (A.2.2) at x^+ has s^+ unstable eigenvalues, denoted with $\lambda^+_k := \gamma^+_k + i\omega^+_k$, and $\omega^+_k \neq 0$, $Q^+_k \neq 0$ for $k = 1, \ldots, s^-$. We denote the corresponding adjoint eigenvectors with $w^+_k := R^+_k + iQ^+_k$, and eigenfunctions $\psi_k(\theta)$, for $k = 1, \ldots, s^+$. Assume further that the eigenvalues λ^+_k are all complex conjugate pairs such that $\overline{\lambda}^+_{2k-1} = \lambda^+_{2k}$, for $k = 1, \ldots, s^+$.

They can be obtained by solving

$$\begin{aligned} (ix.) \qquad & -\begin{pmatrix} \gamma^+_{2k}\mathbb{I} & \omega^+_{2k}\mathbb{I} \\ -\omega^+_{2k}\mathbb{I} & \gamma^+_{2k}\mathbb{I} \end{pmatrix} \begin{pmatrix} M & \mathbb{O} \\ \mathbb{O} & M \end{pmatrix} \begin{pmatrix} R^+_{2k} \\ Q^+_{2k} \end{pmatrix} + \begin{pmatrix} A^{\mathrm{H}} & \mathbb{O} \\ \mathbb{O} & A^{\mathrm{H}} \end{pmatrix} \begin{pmatrix} R^+_{2k} \\ Q^+_{2k} \end{pmatrix} \\ & + \begin{pmatrix} B^{\mathrm{H}} & \mathbb{O} \\ \mathbb{O} & B^{\mathrm{H}} \end{pmatrix} e^{-\gamma^+_{2k}\tau} \begin{pmatrix} \cos(\omega^+_{2k}\tau)\mathbb{I} & -\sin(\omega^+_{2k}\tau)\mathbb{I} \\ \sin(\omega^+_{2k}\tau)\mathbb{I} & \cos(\omega^+_{2k}\tau)\mathbb{I} \end{pmatrix} \begin{pmatrix} R^+_{2k} \\ Q^+_{2k} \end{pmatrix} = 0, \end{aligned}$$

$$(x.) \qquad \left\|(R^+_k, Q^+_k)\right\| = 1,$$

$$(xi.) \qquad Q^{+\,1}_k = 0.$$

We impose that the projections of the desired solution along the unstable eigendirections at the right boundary vanish with respect to the duality pairing,

$$\left\langle \psi_k | y(1) - x^+ \right\rangle = 0, \qquad k = 1, \ldots, s^+. \tag{A.2.16}$$

Then we can write the projections (A.2.16) of the desired solution as

$$\begin{aligned} & w_k^{+H} M(y(1) - x^+) \\ & + \int_{-\tau}^{0} w_k^{+H} e^{-\lambda_k^+(\theta+\tau)} MB(x^+, \eta)(y(1+\theta/T) - x^+) \mathrm{d}\theta = 0, \quad k = 1, \ldots, s^+. \end{aligned} \tag{A.2.17}$$

Similarly as before, we set $\lambda^+ := \gamma_k^+ + i\omega_k^+$ and $w_k^+ := R_k^+ + iQ_k^+$ and use that $v + \bar{v} \in \mathbb{R}$ and $v - \bar{v} \in i\mathbb{R}$. For $k = 1, \ldots, s^+$, it is then

$$\begin{aligned} & \left\langle \frac{1}{2}(\psi_{2k-1} + \psi_{2k}) | y(1) - x^+ \right\rangle \\ & = \frac{1}{2}(\psi_{2k-1}(0) + \psi_{2k}(0))^{\mathrm{H}} M(y(1) - x^+) \\ & \qquad + \int_{-\tau}^{0} \frac{1}{2}(\psi_{2k-1}(\theta) + \psi_{2k}(\theta))^{\mathrm{H}} MB(x^+, \eta)(y(1+\theta/T) - x^+) \mathrm{d}\theta \\ & = R_{2k}^{+H} M(y(1) - x^+) \\ & \qquad + \int_{-\tau}^{0} (R_{2k}^+ \cos(\omega_{2k}\theta))^{\mathrm{H}} e^{-\gamma_{2k}^+ \theta} MB(x^+, \eta)(y(1+\theta/T) - x^+) \mathrm{d}\theta \\ & \qquad + \int_{-\tau}^{0} (Q_{2k}^+ \sin(\omega_{2k}^+ \theta))^{\mathrm{H}} e^{-\gamma_{2k}^+ \theta} MB(x^+, \eta)(y(1+\theta/T) - x^+) \mathrm{d}\theta, \end{aligned}$$

and

$$\begin{aligned} & \left\langle \frac{1}{2i}(\psi_{2k-1} - \psi_{2k}) | y(1) - x^+ \right\rangle \\ & = \frac{1}{2i}(\psi_{2k-1}(0) - \psi_{2k}(0))^{\mathrm{H}} M(y(1) - x^+) \\ & \qquad + \int_{-\tau}^{0} \frac{1}{2i}(\psi_{2k-1}(\theta) - \psi_{2k}(\theta))^{\mathrm{H}} MB(x^+, \eta)(y(1+\theta/T) - x^+) \end{aligned}$$

$$
\begin{aligned}
= &- Q_{2k}^{+\,H} M(y(1) - x^+) \\
&+ \int_{-\tau}^{0} (R_{2k}^+ \sin(\omega_{2k}\theta))^{\mathrm{H}} e^{-\gamma_{2k}^+\theta} MB(x^+, \eta)(y(1+\theta/T) - x^+)\mathrm{d}\theta \\
&- \int_{-\tau}^{0} (Q_{2k}^+ \cos(\omega_{2k}^+\theta))^{\mathrm{H}} e^{-\gamma_{2k}^+\theta} MB(x^+, \eta)(y(1+\theta/T) - x^+)\mathrm{d}\theta.
\end{aligned}
$$

Then, the right boundary condition can be replaced by

$$
\begin{aligned}
(xii.) \qquad 0 = &R_{2k}^{+\,H} M(y(1) - x^+) \\
&+ \int_{-\tau}^{0} (R_{2k}^+ \cos(\omega_{2k}\theta))^{\mathrm{H}} e^{-\gamma_{2k}^+\theta} MB(x^+, \eta)(y(1+\theta/T) - x^+)\mathrm{d}\theta \\
&+ \int_{-\tau}^{0} (Q_{2k}^+ \sin(\omega_{2k}^+\theta))^{\mathrm{H}} e^{-\gamma_{2k}^+\theta} MB(x^+, \eta)(y(1+\theta/T) - x^+)\mathrm{d}\theta, \\
&\qquad\qquad\qquad\qquad\qquad\qquad\qquad\qquad k = 1, \ldots, s^+,
\end{aligned}
$$

$$
\begin{aligned}
(xiii.) \qquad 0 = &- Q_{2k}^{+\,H} M(y(1) - x^+) \\
&+ \int_{-\tau}^{0} (R_{2k}^+ \sin(\omega_{2k}\theta))^{\mathrm{H}} e^{-\gamma_{2k}^+\theta} MB(x^+, \eta)(y(1+\theta/T) - x^+)\mathrm{d}\theta \\
&- \int_{-\tau}^{0} (Q_{2k}^+ \cos(\omega_{2k}^+\theta))^{\mathrm{H}} e^{-\gamma_{2k}^+\theta} MB(x^+, \eta)(y(1+\theta/T) - x^+)\mathrm{d}\theta, \\
&\qquad\qquad\qquad\qquad\qquad\qquad\qquad\qquad k = 1, \ldots, s^+.
\end{aligned}
$$

Finally, we use a phase condition, which minimizes the phase shift with respect to some solution $\tilde{y}$, such that

$$
(xiv.) \qquad p(y, \eta) = \int_0^1 y(t)\tilde{y}'(t)\mathrm{d}t = 0.
$$

in order to remove the translational invariance of the heteroclinic solution. As before, one usually picks the solution, that has been computed in the previous step inside the Newton solver.

Hence, the boundary value problem for the computation of a heteroclinic solution is given by

$$
(i.) \quad M\dot{y}(t) = Tf(y(t), y(t - \tau/T), \eta), \quad t \in [0, 1],
$$

$$(ii.) \qquad 0 = f(x^-, x^-, \eta),$$

$$(iii.) \qquad 0 = f(x^+, x^+, \eta),$$

$$(iv.) \qquad 0 = -\begin{pmatrix} \gamma_k^- \mathbb{I} & -\omega_k^- \mathbb{I} \\ \omega_k^- \mathbb{I} & \gamma_k^- \mathbb{I} \end{pmatrix} \begin{pmatrix} M & \mathbb{O} \\ \mathbb{O} & M \end{pmatrix} \begin{pmatrix} r_k^- \\ q_k^- \end{pmatrix} + \begin{pmatrix} A & \mathbb{O} \\ \mathbb{O} & A \end{pmatrix} \begin{pmatrix} r_k^- \\ q_k^- \end{pmatrix} + \begin{pmatrix} B & \mathbb{O} \\ \mathbb{O} & B \end{pmatrix} e^{-\gamma_k^- \tau} \begin{pmatrix} \cos(\omega_k^- \tau)\mathbb{I} & \sin(\omega_k^- \tau)\mathbb{I} \\ -\sin(\omega_k^- \tau)\mathbb{I} & \cos(\omega_k^- \tau)\mathbb{I} \end{pmatrix} \begin{pmatrix} r_k^- \\ q_k^- \end{pmatrix}, \quad k = 1, \ldots, s^-,$$

$$(v.) \qquad 0 = \left\| (r_k^-, q_k^-) \right\| - 1, \qquad k = 1, \ldots, s^-,$$

$$(vi.) \qquad 0 = q_k^{-\,1}, \qquad k = 1, \ldots, s^-,$$

$$(vii.) \qquad 0 = y(0) - (x^- + \epsilon \sum_{k=1}^{s^-/2} \alpha_{2k-1} r_{2k}^- + \alpha_{2k} q_{2k}^-),$$

$$(viii.) \qquad 0 = \sum_{k=1}^{s^-} |\alpha_k|^2 - 1,$$

$$(ix.) \qquad 0 = -\begin{pmatrix} \gamma_{2k}^+ \mathbb{I} & \omega_{2k}^+ \mathbb{I} \\ -\omega_{2k}^+ \mathbb{I} & \gamma_{2k}^+ \mathbb{I} \end{pmatrix} \begin{pmatrix} M & \mathbb{O} \\ \mathbb{O} & M \end{pmatrix} \begin{pmatrix} R_{2k}^+ \\ Q_{2k}^+ \end{pmatrix} + \begin{pmatrix} A^{\mathrm{H}} & \mathbb{O} \\ \mathbb{O} & A^{\mathrm{H}} \end{pmatrix} \begin{pmatrix} R_{2k}^+ \\ Q_{2k}^+ \end{pmatrix} + \begin{pmatrix} B^{\mathrm{H}} & \mathbb{O} \\ \mathbb{O} & B^{\mathrm{H}} \end{pmatrix} e^{-\gamma_{2k}^+ \tau} \begin{pmatrix} \cos(\omega_{2k}^+ \tau)\mathbb{I} & -\sin(\omega_{2k}^+ \tau)\mathbb{I} \\ \sin(\omega_{2k}^+ \tau)\mathbb{I} & \cos(\omega_{2k}^+ \tau)\mathbb{I} \end{pmatrix} \begin{pmatrix} R_{2k}^+ \\ Q_{2k}^+ \end{pmatrix}, \quad k = 1, \ldots, s^+,$$

$$(x.) \qquad 0 = \left\| (R_k^+, Q_k^+) \right\| - 1, \qquad k = 1, \ldots, s^+,$$

$$(xi.) \qquad 0 = Q_k^{+\,1}, \qquad k = 1, \ldots, s^+,$$

$$(xii.) \qquad 0 = R_{2k}^{+\,H} M(y(1) - x^+) + \int_{-\tau}^{0} (R_{2k}^+ \cos(\omega_{2k}\theta))^{\mathrm{H}} e^{-\gamma_{2k}^+ \theta} MB(x^+, \eta)(y(1 + \theta/T) - x^+) \mathrm{d}\theta + \int_{-\tau}^{0} (Q_{2k}^+ \sin(\omega_{2k}^+ \theta))^{\mathrm{H}} e^{-\gamma_{2k}^+ \theta} MB(x^+, \eta)(y(1 + \theta/T) - x^+) \mathrm{d}\theta, \quad k = 1, \ldots, s^+,$$

$$(xiii.) \qquad 0 = -Q_{2k}^{+\,H} M(y(1) - x^+)$$
$$+ \int_{-\tau}^{0} (R_{2k}^{+} \sin(\omega_{2k}\theta))^{\mathrm{H}} e^{-\gamma_{2k}^{+}\theta} MB(x^+, \eta)(y(1+\theta/T) - x^+)\mathrm{d}\theta$$
$$- \int_{-\tau}^{0} (Q_{2k}^{+} \cos(\omega_{2k}^{+}\theta))^{\mathrm{H}} e^{-\gamma_{2k}^{+}\theta} MB(x^+, \eta)(y(1+\theta/T) - x^+)\mathrm{d}\theta,$$
$$k = 1, \ldots, s^+,$$

$$(xiv.) \qquad 0 = p(y, \eta) - \int_0^1 y(t)\tilde{y}'(t)\mathrm{d}t.$$

A.3 Boundary value problem for the numerical computation of a homoclinic orbit flip

In Chapter 6, we discussed the dynamics of TDSs induced by a homoclinic orbit flip in the profile equation. In this section, we will present now the boundary value problem, that we implemented for its detection and continuation. Recall that generically, the asymptotic decay rates of a homoclinic solution are dominated by those eigenvalues nearest to the imaginary axis as they give the slowest exponential decay rates. These eigenvalues are called the leading eigenvalues. A generic homoclinic solution approaches its equilibrium along the leading eigendirections. In contrast to that, in an orbit flip, the homoclinic solution approaches its saddle along the strong stable eigendirection.

Recall now the boundary value problem $(I.)$–$(XI.)$ for computation of generic heteroclinic solutions presented in Section A.1. In the case of a homoclinic solution, the equilibria x^- and x^+ coincide and for its computation, one parameter has to be adjusted. Without loss of generality, suppose the linearization (A.1.2) at the equilibrium x^- has exactly two unstable eigenvalues λ_k^- with corresponding eigenvectors v_k^-, for $k = 1, 2$. Assume further that the eigenvalues can be ordered, such that

$$\lambda_1 > \lambda_2.$$

Then, the leading eigendirection is given by λ_2 and the strong eigendirection by λ_1. In case the unstable manifold is in an orbit flip configuration, we can compute and continue this bifurcation by adding the following constraint to the boundary value problem presented in Section A.1, by setting

$$(XII.) \qquad \alpha_1 = 1.$$

In order for system $(I.)$–$(XII.)$ to be a well-posed problem, for its computation we need to free an additional parameter. This way, the number of free parameters is equal to two, reflecting the codimension of the homoclinic orbit flip bifurcation.

Note, that the homoclinic orbit flip discussed in Chapter 6 is with respect to the stable manifold in the profile equation, i.e. a differential equation with an advanced argument. We compute them by reversing the time and obtain then a homoclinic orbit flip in the unstable manifold in the time-reversed profile equation.

References

[AA08] N. Akhmediev and A. Ankiewicz. 'Dissipative Solitons: From Optics to Biology and Medicine Series'. In: *Lecture Notes in Physics*. Vol. 751. Springer Berlin Heidelberg, 2008.

[AAIS94] V. I. Arnold, V. Afrajmovich, Y. S. Il'yashenko and L. Shil'nikov. *Dynamical systems V: bifurcation theory and catastrophe theory*. Vol. 5. Springer Science & Business Media, 1994.

[AJMRJ95] L. Arnold, C. K. Jones, K. Mischaikow, G. Raugel and C. K. Jones. 'Geometric singular perturbation theory'. In: *Dynamical Systems: Lectures Given at the 2nd Session of the Centro Internazionale Matematico Estivo (CIME) held in Montecatini Terme, Italy, June 13–22, 1994* (1995), pp. 44–118.

[ALGM73] A. Andronov, E. Leontovich, I. Gordon and A. Maĭer. *Theory of Bifurcations of Dynamic Systems on a Plane*. Halsted Press, 1973.

[Bey90] W.-J. Beyn. 'The Numerical Computation of Connecting Orbits in Dynamical Systems'. In: *IMA Journal of Numerical Analysis* 10 (1990), pp. 379–405.

[BK07] J. Burke and E. Knobloch. 'Homoclinic snaking: Structure and stability'. In: *Chaos: An Interdisciplinary Journal of Nonlinear Science* 17 (2007), p. 037102.

[BLZ98] P. W. Bates, K. Lu and C. Zeng. *Existence and persistence of invariant manifolds for semiflows in Banach space*. Vol. 645. American Mathematical Soc., 1998.

[Bou71] J. Boussinesq. 'Théorie de l'intumescence liquide appelée onde solitaire ou de translation se propageant dans un canal rectangulaire'. In: *CR Acad. Sci. Paris* 72 (1871), pp. 755–759.

[BR05] A Borisyuk and J Rinzel. 'Understanding neuronal dynamics by geometrical dissection of minimal models'. In: *Methods and Models in Neurophysics (1st Ed., Elsevier, 2005)* (2005), pp. 17–72.

[Byk00] V. Bykov. 'Orbit structure in a neighborhood of a separatrix cycle containing two saddle-foci'. In: *Translations of the American Mathematical Society-Series 2* 200 (2000), pp. 87–98.

[Byk93] V. V. Bykov. 'The Bifurcations of Separatrix Contours and Chaos'. In: *Physica D* 62 (Jan. 1993), 290–299.

[Byk99] V. Bykov. 'On systems with separatrix contour containing two saddle-foci'. In: *Journal of Mathematical Sciences* 95 (1999), pp. 2513–2522.

[CDF90] S.-N. Chow, B. Deng and B. Fiedler. 'Homoclinic bifurcation at resonant eigenvalues'. In: *Journal of Dynamics and Differential Equations* 2 (1990), pp. 177–244.

[CL90] S.-N. Chow and X.-B. Lin. 'Bifurcation of a homoclinic orbit with a saddle-node equilibrium'. In: *Differential Integral Equations* 3 (1990), 435–466.

[Den90] B. Deng. 'Homoclinic Bifurcations with Nonhyperbolic Equilibria'. In: *SIAM Journal on Mathematical Analysis* 21 (1990), pp. 693–720.

[DG91] O. Diekmann and S. A. van Gils. 'The center manifold for delay equations in the light of suns and stars'. In: *Singularity Theory and its Applications*. Ed. by M. Roberts and I. Stewart. Berlin, Heidelberg: Springer Berlin Heidelberg, 1991, pp. 122–141.

[Dil+19] M. Dillane, B. Tykalewicz, D. Goulding, B. Garbin, S. Barland and B. Kelleher. 'Square wave excitability in quantum dot lasers under optical injection'. In: *Opt. Lett.* 44.2 (Jan. 2019), pp. 347–350.

[DVGLW95] O. Diekmann, S. A. Van Gils, S. M. Lunel and H.-O. Walther. *Delay equations: functional-, complex-, and nonlinear analysis.* Vol. 110, Applied Mathematical Sciences. Springer-Verlag, New York, 1995.

[DZL11] L. Duan, D. Zhai and Q. Lu. 'Bifurcation and Bursting in Morris-Lecar Model for Class I and Class II Excitability'. In: *Dynamical Systems and Differential Equations, AIMS Proceedings 2011 Proceedings of the 8th AIMS International Conference (Dresden , Germany)* (2011).

[ELR02] K. Engelborghs, T. Luzyanina and D. Roose. 'Numerical Bifurcation Analysis of Delay Differential Equations Using DDE-BIFTOOL'. In: *ACM Trans. Math. Softw.* 28 (2002), pp. 1–21.

[ET10] G. B. Ermentrout and D. H. Terman. 'Mathematical Foundations of Neuroscience'. In: *Interdisciplinary Applied Mathematics* (2010).

[Fen79] N. Fenichel. 'Geometric singular perturbation theory for ordinary differential equations'. In: *Journal of differential equations* 31 (1979), pp. 53–98.

[FVDE14] G. Friart, G. Verschaffelt, J. Danckaert and T. Erneux. 'All-optical controlled switching between time-periodic square waves in diode lasers with delayed feedback'. In: *Opt. Lett.* 39 (2014), pp. 6098–6101.

[Gas83] P. Gaspard. 'Generation of a countable set of homoclinic flows through bifurcation'. In: *Physics Letters A* 97 (1983), pp. 1–4.

[Gas84] P. Gaspard. 'Generation of a countable set of homoclinic flows through bifurcation in multidimensional systems'. In: *Bulletins de l'Académie Royale de Belgique* 70 (1984), pp. 61–83.

[Gav+06] A. Gavrielides, T. Erneux, D. W. Sukow, G. Burner, T. McLachlan, J. Miller and J. Amonette. 'Square-wave self-modulation in diode lasers with polarization-rotated optical feedback'. In: *Opt. Lett.* 31 (2006), pp. 2006–2008.

[GH83] J. Guckenheimer and P. Holmes. *Nonlinear Oscillations, Dynamical Systems, and Bifurcations of Vector Fields*. Vol. 42. Springer, 1983.

[GJTB15] B. Garbin, J. Javaloyes, G. Tissoni and S. Barland. 'Topological solitons as addressable phase bits in a driven laser'. In: *Nature Communications* 6 (2015), pp. 1–7.

[GK21] D. Gomila and E. Knobloch. 'Curvature effects and radial homoclinic snaking'. In: *IMA Journal of Applied Mathematics* 86 (2021), pp. 1094–1111.

[GP96] G. Giacomelli and A. Politi. 'Relationship between Delayed and Spatially Extended Dynamical Systems'. In: *Phys. Rev. Lett.* 76 (1996), pp. 2686–2689.

[GR23] A. Giraldo and S. Ruschel. 'Pulse-adding of temporal dissipative solitons: Resonant homoclinic points and the orbit flip of case B with delay'. In: *Nonlinearity* 36 (2023), p. 7105.

[GS84] P. Glendinning and C. Sparrow. 'Local and global behavior near homoclinic orbits'. In: *Journal of Statistical Physics* 35 (1984), pp. 645–696.

[GS86] P. Glendinning and C. Sparrow. 'T-points: A codimension two heteroclinic bifurcation'. In: *Journal of Statistical Physics* 43 (1986), pp. 479–488.

[GT64] F. Gires and P. Tournois. 'Interferometre utilisable pour la compression d'impulsions lumineuses modulees en frequence'. In: *C. R. Acad. Sci. Paris* 258 (1964), pp. 6112–6115.

[Gus+15] F. Gustave, L. Columbo, G. Tissoni, M. Brambilla, F. Prati, B. Kelleher, B. Tykalewicz and S. Barland. 'Dissipative phase solitons in semiconductor lasers'. In: *Physical Review Letters* 115 (2015), p. 043902.

[Hei+11] S. Heiligenthal, T. Dahms, S. Yanchuk, T. Jüngling, V. Flunkert, I. Kanter, E. Schöll and W. Kinzel. 'Strong and Weak Chaos in Nonlinear Networks with Time-Delayed Couplings'. In: *Phys. Rev. Lett.* 107 (2011), p. 234102.

[HGJ21] D. Hessel, S. V. Gurevich and J. Javaloyes. 'Wiggling instabilities of temporal localized states in passively mode-locked vertical external-cavity surface-emitting lasers'. In: *Optics Letters* 46 (2021), pp. 2557–2560.

[HH52] A. L. Hodgkin and A. F. Huxley. 'A quantitative description of membrane current and its application to conduction and excitation in nerve'. In: *The Journal of Physiology* 117 (1952), pp. 500–544.

[HH94] J. K. Hale and W. Huang. 'Period doubling in singularly perturbed delay equations'. In: *Journal of Differential Equations* 114 (1994), pp. 1–23.

[HH96] J. K. Hale and W. Huang. 'Periodic solutions of singularly perturbed delay equations'. In: *Zeitschrift für angewandte Mathematik und Physik ZAMP* 47 (1996), pp. 57–88.

[HL93] J. K. Hale and S. M. V. Lunel. *Introduction to Functional Differential Equations*. Vol. 99. Springer-Verlag, 1993.

[HMO06] J. K. Hale, L. T. Magalhães and W. Oliva. *Dynamics in infinite dimensions*. Vol. 47. Springer Science & Business Media, 2006.

[Hom96] A. J. Homburg. *Global aspects of homoclinic bifurcations of vector fields*. Vol. 578. American Mathematical Soc., 1996.

[HS10] A. J. Homburg and B. Sandstede. 'Homoclinic and Heteroclinic Bifurcations in Vector Fields'. In: *Handbook of Dynamical Systems*. Ed. by H. Broer, B. Hasselblatt and F. Takens. Vol. 3. North-Holland, Elsevier Science, 2010. Chap. 8, pp. 379–524.

[Izh00] E. M. Izhikevich. 'Neural excitability, Spiking and bursting'. In: *Int. J. Bifurc. Chaos* 10 (2000), pp. 1171–1266.

[Izh07] E. M. Izhikevich. *Dynamical Systems in Neuroscience: The Geometry of Excitability and Bursting*. The MIT Press, 2007.

[KA03] Y. S. Kivshar and G. P. Agrawal. *Optical solitons: from fibers to photonic crystals*. Academic press, 2003.

[KAM10] A. M. Kaplan, G. P. Agrawal and D. N. Maywar. 'Optical Square-Wave Clock Generation Based on an All-Optical Flip-Flop'. In: *IEEE Photonics Technology Letters* 22 (2010), pp. 489–491.

[KDV95] D. J. Korteweg and G. De Vries. 'XLI. On the change of form of long waves advancing in a rectangular canal, and on a new type of long stationary waves'. In: *The London, Edinburgh, and Dublin Philosophical Magazine and Journal of Science* 39 (1895), pp. 422–443.

[Kir88] K. Kirchgässner. 'Nonlinearly Resonant Surface Waves and Homoclinic Bifurcation'. In: *Advances in Applied Mechanics* 26 (1988), pp. 135–181.

[KLW14] J. Knobloch, J. S. Lamb and K. N. Webster. 'Using Lin's method to solve Bykov's problems'. In: *Journal of Differential Equations* 257 (2014), pp. 2984–3047.

[KSGJ22] E. R. Koch, T. G. Seidel, S. V. Gurevich and J. Javaloyes. 'Square-wave generation in vertical external-cavity Kerr-Gires-Tournois interferometers'. In: *Opt. Lett.* 47 (2022), pp. 4343–4346.

[KSJG23] E. R. Koch, T. G. Seidel, J. Javaloyes and S. V. Gurevich. 'Temporal localized states and square-waves in semiconductor micro-resonators with strong time-delayed feedback'. In: *Chaos: An Interdisciplinary Journal of Nonlinear Science* 33 (2023). 043142.

[Kue+15] C. Kuehn et al. *Multiple time scale dynamics*. Vol. 191. Springer, 2015.

[KW05] J. Knobloch and T. Wagenknecht. 'Homoclinic snaking near a heteroclinic cycle in reversible systems'. In: *Physica D: Nonlinear Phenomena* 206 (2005), pp. 82–93.

[LBK17] D. Lo Jacono, A. Bergeon and E. Knobloch. 'Spatially localized radiating diffusion flames'. In: *Combustion and Flame* 176 (2017), pp. 117–124.

[LGNS04] B. Lindner, J. García-Ojalvo, A. Neiman and L. Schimansky-Geier. 'Effects of noise in excitable systems'. In: *Physics Reports* 392 (2004), pp. 321–424.

[Li+16] S.-S. Li, X.-Z. Li, J.-P. Zhuang, G. Mezosi, M. Sorel and S.-C. Chan. 'Square-wave oscillations in a semiconductor ring laser subject to counter-directional delayed mutual feedback'. In: *Opt. Lett.* 41 (2016), pp. 812–815.

[Lin90] X.-B. Lin. 'Using Melnikov's method to solve Silnikov's problems'. In: *Proceedings of the Royal Society of Edinburgh Section A: Mathematics* 116 (1990), pp. 295–325.

[LLL13] C. Liu, X. Liu and S. Liu. 'Bifurcation analysis of a Morris–Lecar neuron model'. In: *Biological Cybernetics* 108 (2013), pp. 75–84.

[LWY11] M. Lichtner, M. Wolfrum and S. Yanchuk. 'The Spectrum of Delay Differential Equations with Large Delay'. In: *SIAM J. Math. Anal.* 43 (2011), pp. 788–802.

[Mal91] B. A. Malomed. 'Bound solitons in the nonlinear Schrödinger/Ginzburg-Landau equation'. In: *Large Scale Structures in Nonlinear Physics*. Ed. by J.-D. Fournier and P.-L. Sulem. Springer Berlin Heidelberg, 1991, pp. 288–294.

[Mas12] Mashal, Lilia and Van der Sande, Guy and Gelens, Lendert and Danckaert, Jan and Verschaffelt, Guy. 'Square-wave oscillations in semiconductor ring lasers with delayed optical feedback'. In: *Opt. Express* 20 (2012), pp. 22503 –22516.

[MB05] J. Mulet and S. Balle. 'Mode locking dynamics in electrically-driven vertical-external-cavity surface-emitting lasers'. In: *Quantum Electronics, IEEE Journal of* 41 (2005), pp. 1148–1156.

[Mel63] V. K. Mel'nikov. 'On the stability of a center for time-periodic perturbations'. In: *Trudy moskovskogo matematicheskogo obshchestva* 12 (1963), pp. 3–52.

[MGB14] F. Marino, G. Giacomelli and S. Barland. 'Front Pinning and Localized States Analogues in Long-Delayed Bistable Systems'. In: *Phys. Rev. Lett.* 112 (2014), p. 103901.

[MGJB07] J. Mulet, M. Giudici, J. Javaloyes and S. Balle. 'Square-wave switching by crossed-polarization gain modulation in vertical-cavity semiconductor lasers'. In: *Phys. Rev. A* 76 (2007), p. 043801.

[MJBG14] M. Marconi, J. Javaloyes, S. Balle and M. Giudici. 'How Lasing Localized Structures Evolve out of Passive Mode Locking'. In: *Phys. Rev. Lett.* 112 (2014), p. 223901.

[MJBGB13] M. Marconi, J. Javaloyes, S. Barland, M. Giudici and S. Balle. 'Robust square-wave polarization switching in vertical-cavity surface-emitting lasers'. In: *Phys. Rev. A* 87 (2013), p. 013827.

[MJG20] L. Munsberg, J. Javaloyes and S. V. Gurevich. 'Topological localized states in the time delayed Adler model: Bifurcation analysis and interaction law'. In: *Chaos: An Interdisciplinary Journal of Nonlinear Science* 30 (2020), p. 063137.

[ML81] C. Morris and H. Lecar. 'Voltage oscillations in the barnacle giant muscle fiber'. In: *Biophysical Journal* 35 (1981), pp. 193–213.

[MPN86] J. Mallet-Paret and R. Nussbaum. 'Global continuation and asymptotic behaviour for periodic solutions of a differential-delay equation'. In: *Annali di Matematica Pura ed Applicata* 145 (1986), pp. 33–128.

[Niz03] M. Nizette. 'Front dynamics in a delayed-feedback system with external forcing'. In: *Physica D: Nonlinear Phenomena* 183 (2003), pp. 220 –244.

[NRVW06] M. Nizette, D. Rachinskii, A. Vladimirov and M. Wolfrum. 'Pulse interaction via gain and loss dynamics in passive mode locking'. In: *Physica D: Nonlinear Phenomena* 218 (2006), pp. 95–104.

[PBA10] H.-G. Purwins, H. Bödeker and S. Amiranashvili. 'Dissipative soli-tons'. In: *Advances in Physics* 59 (2010), pp. 485–701.

[PRAL21] P. Parra-Rivas, C. M. Arabí and F. Leo. 'Dark quadratic localized states and collapsed snaking in doubly resonant dispersive cavity-enhanced second-harmonic generation'. In: *Phys. Rev. A* 104 (6 2021), p. 063502.

[PRFO20] P. Parra-Rivas and C. Fernandez-Oto. 'Formation of localized states in dryland vegetation: Bifurcation structure and stability'. In: *Phys. Rev. E* 101 (2020), p. 052214.

[Pyr92] K. Pyragas. 'Continuous control of chaos by self-controlling feedback'. In: *Physics Letters A* 170 (1992), pp. 421–428.

[RAFBJ16] B Romeira, R Avó, J. M. L. Figueiredo, S Barland and J Javaloyes. 'Regenerative memory in time-delayed neuromorphic photonic resonators'. In: *Scientific reports* 6 (2016), p. 19510.

[Ray76] J. W. Rayleigh. 'XXXII. On waves'. In: *The London, Edinburgh, and Dublin Philosophical Magazine and Journal of Science* 1.4 (1876), pp. 257–279.

[RE98] J. Rinzel and G. Ermentrout. 'Analysis of neural excitability and oscillations'. In: *Methods in neuronal modeling*. Ed. by C. Koch and I. Segev. 2nd ed. MIT Press, 1998. Chap. 7, pp. 251–291.

[RKB20] S. Ruschel, B. Krauskopf and N. G. R. Broderick. 'The limits of sustained self-excitation and stable periodic pulse trains in the Yamada model with delayed optical feedback'. In: *Chaos: An Interdisciplinary Journal of Nonlinear Science* 30 (2020), p. 093101.

[Rus45] J. S. Russell. *Report on Waves: Made to the Meetings of the British Association in 1842-43*. 1845.

[San00] B. Sandstede. 'Center manifolds for homoclinic solutions'. In: *Jour- nal of Dynamics and Differential Equations* 12 (2000), pp. 449–510.

[San02] B. Sandstede. 'Stability of travelling waves'. In: ed. by B. Fiedler. Vol. 2. Handbook of Dynamical Systems. North-Holland, Elsevier Science, 2002, pp. 983–1055.

[San93] B. Sandstede. 'Verzweigungstheorie homokliner Verdopplungen'. In: *WIAS Report* 7 (1993).

[Sch+19] C. Schelte, P. Camelin, M. Marconi, A. Garnache, G. Huyet, G. Beaudoin, I. Sagnes, M. Giudici, J. Javaloyes and S. V. Gurevich. 'Third Order Dispersion in Time-Delayed Systems'. In: *Phys. Rev. Lett.* 123 (2019), p. 043902.

[Sch87] S. Schecter. 'The Saddle-Node Separatrix-Loop Bifurcation'. In: *SIAM J. Math. Anla.* 18 (1987), pp. 1142–1157.

[SELSR16] J. Sieber, K. Engelborghs, T. Luzyanina, G. Samaey and D. Roose. 'DDE-BIFTOOL Manual - Bifurcation analysis of delay differential equations'. In: *arXiv preprint* (2016).

[SER02] G. Samaey, K. Engelborghs and D. Roose. 'Numerical computation of connecting orbits in delay differential equations'. In: *Numerical Algorithms* 30 (2002), pp. 335–352.

[SGJ22] T. G. Seidel, S. V. Gurevich and J. Javaloyes. 'Conservative Solitons and Reversibility in Time Delayed Systems'. In: *Phys. Rev. Lett.* 128 (2022), p. 083901.

[Shi63] L. P. Shilnikov. 'Some cases of generation of period motions from singular trajectories'. In: *Matematicheskii Sbornik* 103 (1963), pp. 443–466.

[Shi65] L. Shilnikov. 'A case of the existence of a countable number of periodic motion'. In: *Sov. Math. Dokl.* Vol. 6. 1965, pp. 163–166.

[Shi68] L. P. Shilnikov. 'On the generation of a periodic motion from trajectories doubly asymptotic to an equilibrium state of saddle type'. In: *Mathematics of the USSR-Sbornik* 6 (1968), p. 427.

[Shi70] L. Shilnikov. 'A contribution to the problem of the structure of an extended neighborhood of a rough equilibrium state of saddle-focus type'. In: *Mathematics of the USSR-Sbornik* 10 (1970), p. 91.

[SJG18] C. Schelte, J. Javaloyes and S. V. Gurevich. 'Dynamics of temporally localized states in passively mode-locked semiconductor lasers'. In: *Phys. Rev. A* 97 (2018), p. 053820.

[SJG22] T. G. Seidel, J. Javaloyes and S. V. Gurevich. 'A normal form for frequency combs and localized states in Kerr–Gires–Tournois interferometers'. In: *Opt. Lett.* 47 (2022), pp. 2979–2982.

[SKJGW23a] M. Stöhr, E. R. Koch, J. Javaloyes, S. V. Gurevich and M. Wolfrum. 'Square waves and Bykov T-points in a delay algebraic model for the Kerr-Gires-Tournois interferometer'. In: *Chaos: An Interdisciplinary Journal of Nonlinear Science* 33 (2023), p. 113105.

[SKJGW23b] M. Stöhr, E. R. Koch, J. Javaloyes, S. V. Gurevich and M. Wolfrum. 'Supplementary Code: Square Waves and Bykov T-points in a Delay Algebraic Model for the Kerr- Gires-Tournois Interferometer'. Version 1.0. In: *Zenodo* (2023).

[SM18] V. V. Semenov and Y. L. Maistrenko. 'Dissipative solitons for bistable delayed-feedback systems'. In: *Chaos: An Interdisciplinary Journal of Nonlinear Science* 28 (2018).

[SPVJG19] C. Schelte, A. Pimenov, A. G. Vladimirov, J. Javaloyes and S. V. Gurevich. 'Tunable Kerr frequency combs and temporal localized states in time-delayed Gires-Tournois interferometers'. In: *Opt. Lett.* 44 (2019), pp. 4925–4928.

[SSM18] H. Sakaguchi, D. V. Skryabin and B. A. Malomed. 'Stationary and oscillatory bound states of dissipative solitons created by third-order dispersion'. In: *Opt. Lett.* 43 (2018), pp. 2688–2691.

[SSTC01] L. P. Shilnikov, A. L. Shilnikov, D. V. Turaev and L. O. Chua. *Methods of Qualitative Theory in Nonlinear Dynamics - Part II.* Ed. by L. O. Chua. Vol. 5. World Scientific, 2001.

[SSTC98] L. P. Shilnikov, A. L. Shilnikov, D. V. Turaev and L. O. Chua. *Methods Of Qualitative Theory in Nonlinear Dynamics - Part I.* Ed. by L. O. Chua. Vol. 4. World Scientific, 1998.

[SW23] M. Stöhr and M. Wolfrum. 'Temporal dissipative solitons in the Morris-Lecar model with time-delayed feedback'. In: *Chaos: An Interdisciplinary Journal of Nonlinear Science* 33 (2023), p. 023117.

[SWLY13] J. Sieber, M. Wolfrum, M. Lichtner and S. Yanchuk. 'On the stability of periodic orbits in delay equations with large delay'. In: *Discrete and Continuous Dynamical Systems* 33 (2013), 3109–3134.

[SWX13] J. Sheng, J. Wang and M. Xiao. 'Synchronous control of dual-channel all-optical multistate switching'. In: *Opt. Lett.* 38 (2013), pp. 5369–5372.

[TGT14] D. Tseluiko, M. Galvagno and U. Thiele. 'Collapsed heteroclinic snaking near a heteroclinic chain in dragged meniscus problems'. In: *The European Physical Journal E* 37 (2014), p. 33.

[TKB17] S. Terrien, B. Krauskopf and N. G. Broderick. 'Bifurcation analysis of the Yamada model for a pulsing semiconductor laser with saturable absorber and delayed optical feedback'. In: *SIAM Journal on Applied Dynamical Systems* 16 (2017), pp. 771–801.

[TKYAK06] K. Tsumoto, H. Kitajima, T. Yoshinaga, K. Aihara and H. Kawakami. 'Bifurcations in Morris–Lecar neuron model'. In: *Neurocomputing* 69 (2006), pp. 293–316.

[TPKBB21] S. Terrien, V. A. Pammi, B. Krauskopf, N. G. R. Broderick and S. Barbay. 'Pulse-timing symmetry breaking in an excitable optical system with delay'. In: *Phys. Rev. E* 103 (2021), p. 012210.

[TV10] F. Takens and A. Vanderbauwhede. 'Local invariant manifolds and normal forms'. In: *Handbook of dynamical systems* 3 (2010), pp. 89–124.

[TVZ12] D. Turaev, A. G. Vladimirov and S. Zelik. 'Long-Range Interaction and Synchronization of Oscillating Dissipative Solitons'. In: *Phys. Rev. Lett.* 108 (2012), p. 263906.

[USNA11] S. Ura, S. Shoda, K. Nishio and Y. Awatsuji. 'In-line rotation sensor based on VCSEL behavior under polarization-rotating optical feedback'. In: *Opt. Express* 19 (2011), pp. 23683–23688.

[Van92] A. Vanderbauwhede. 'Bifurcation of degenerate homoclinics'. In: *Results in Mathematics* 21 (1992), pp. 211–223.

[Vla22] A. G. Vladimirov. 'Short- and long-range temporal cavity soliton interaction in delay models of mode-locked lasers'. In: *Physical Review E* 105 (2022).

[VT05] A. G. Vladimirov and D. Turaev. 'Model for passive mode locking in semiconductor lasers'. In: *Physical Review A* 72 (2005), p. 033808.

[VV87] A Vanderbauwhede and S. Van Gils. 'Center manifolds and contractions on a scale of Banach spaces'. In: *Journal of Functional Analysis* 72 (1987), pp. 209–224.

[Wei+12] L. Weicker, T. Erneux, O. D'Huys, J. Danckaert, M. Jacquot, Y. Chembo and L. Larger. 'Strongly asymmetric square waves in a time-delayed system'. In: *Phys. Rev. E* 86 (2012), p. 055201.

[Wig03] S. Wiggins. *Introduction to Applied Nonlinear Dynamical Systems and Chaos*. Texts in Applied Mathematics. Springer New York, 2003.

[YBK06] A. Yochelis, J. Burke and E. Knobloch. 'Reciprocal Oscillons and Nonmonotonic Fronts in Forced Nonequilibrium Systems'. In: *Phys. Rev. Lett.* 97 (2006), p. 254501.

[YG14] S. Yanchuk and G. Giacomelli. 'Pattern formation in systems with multiple delayed feedbacks'. In: *Physical Review Letters* 112 (2014), p. 174103.

[YG15] S. Yanchuk and G. Giacomelli. 'Dynamical systems with multiple long-delayed feedbacks: Multiscale analysis and spatiotemporal equivalence'. In: *Phys. Rev. E* 92 (2015), p. 042903.

[YG17] S. Yanchuk and G. Giacomelli. 'Spatio-temporal phenomena in complex systems with time delays'. In: *Journal of Physics A: Mathematical and Theoretical* 50 (2017), p. 103001.

[YP09] S. Yanchuk and P. Perlikowski. 'Delay and periodicity'. In: *Phys. Rev. E* 79 (2009), p. 046221.

[YRSW19] S. Yanchuk, S. Ruschel, J. Sieber and M. Wolfrum. 'Temporal Dissipative Solitons in Time-Delay Feedback Systems'. In: *Phys. Rev. Lett.* 123 (2019), p. 053901.

[YWPT22] S. Yanchuk, M. Wolfrum, T. Pereira and D. Turaev. 'Absolute stability and absolute hyperbolicity in systems with discrete time-delays'. In: *Journal of Differential Equations* 318 (2022), pp. 323–343.

Publications

1. [SW23] M. Stöhr and M. Wolfrum. 'Temporal dissipative solitons in the Morris-Lecar model with time-delayed feedback'.

   This article may be downloaded for personal use only. Any other use requires prior permission of the author and AIP Publishing. This article appeared in *Chaos* 1 February 2023; 33 (2): 023117, and may be found at `https://doi.org/10.1063/5.0134815`.

2. [SKJGW23a] M. Stöhr, E. R. Koch, J. Javaloyes, S. V. Gurevich and M. Wolfrum. 'Square waves and Bykov T-points in a delay algebraic model for the Kerr-Gires-Tournois interferometer'.

   This article may be downloaded for personal use only. Any other use requires prior permission of the author and AIP Publishing.

   This article appeared in *Chaos* 1 November 2023; (33) 11: 113105, and may be found at `https://doi.org/10.1063/5.0173320`.

   Supplementary code of a minimal reproducable example computing the square waves discussed in Publication 2 :

3. [SKJGW23b] M. Stöhr, E. R. Koch, J. Javaloyes, S. V. Gurevich and M. Wolfrum. 'Supplementary Code: Square Waves and Bykov T-points in a Delay Algebraic Model for the Kerr-Gires-Tournois Interferometer'. Version 1.0. *Zenodo* (2023): `https://doi.org/10.5281/zenodo.8375471`.

Index

$\mathcal{C} = \mathcal{C}(I, \mathbb{R}^n)$	space of continuous functions on $I \subset \mathbb{R}$
$\mathcal{C}^k = \mathcal{C}^k(I, \mathbb{R}^n)$	space of k-times continuously differentiable functions on $I \subset \mathbb{R}$
$\mathcal{C}^{K,\alpha}$	Hölder space $\mathcal{C}^{K,\alpha} = \mathcal{C}^K$, s.t. the K-th partial derivatives are Hölder continuous with exponent α.
$f \in \mathcal{O}(g)$	(big O-notation) f grows at most as fast as g
$f \in \mathcal{O}(1)$	(big O-notation) f is bounded
$\mathrm{Re}(\lambda)$	real part of $\lambda \in \mathbb{C}$
$\mathrm{Im}(\lambda)$	imaginary part of $\lambda \in \mathbb{C}$
M^{tr}	transpose of matrix M
M^{H}	hermetian of matrix M
$\langle \cdot, \cdot \rangle$	euclidean scalar product
$\| \cdot \|$	euclidean norm
$A + B$	direct sum of A and B

Selbstständigkeitserklärung

Name: Stöhr
Vorname: Mina

Ich erkläre gegenüber der Freien Universität Berlin, dass ich die vorliegende Dissertation selbstständig und ohne Benutzung anderer als der angegebenen Quellen und Hilfsmittel angefertigt habe. Die vorliegende Arbeit ist frei von Plagiaten. Alle Ausführungen, die wörtlich oder inhaltlich aus anderen Schriften entnommen sind, habe ich als solche kenntlich gemacht. Diese Dissertation wurde in gleicher oder ähnlicher Form noch in keinem früheren Promotionsverfahren eingereicht.

Mit einer Prüfung meiner Arbeit durch ein Plagiatsprüfungsprogramm erkläre ich mich einverstanden.

Berlin, den 15. April 2024